

OBSERVATIONS AND MODELING OF PROCESSES IN ARTIFICIALLY INITIATED  
(TRIGGERED) LIGHTNING

By

CHRISTOPHER JOHN BIAGI

A DISSERTATION PRESENTED TO THE GRADUATE SCHOOL  
OF THE UNIVERSITY OF FLORIDA IN PARTIAL FULFILLMENT  
OF THE REQUIREMENTS FOR THE DEGREE OF  
DOCTOR OF PHILOSOPHY

UNIVERSITY OF FLORIDA

2011

© 2011 Christopher John Biagi

To my mother and father

## ACKNOWLEDGMENTS

First and foremost, I would like to thank my advisor, Dr. Martin Uman, for providing me with the best academic guidance at every step of my Ph.D. studies. His generous support made this work possible, and I will always be grateful for his mentorship. I would also like to thank Dr. Vladimir Rakov for so often lending his encyclopedic knowledge to me. I am grateful for the considerable experimental assistance of Dr. Douglas Jordan, and the help of Dr. Robert Moore. I am indebted and grateful to Dr. Jay Gopalakrishnan for contributing his expertise in numerical modeling. I thank Dr. William Beasley for his assistance, and Michael Stapleton for helping me with electronics design. I would like to acknowledge and give thanks to Julia Jordan for being an excellent assistant. Many other people have contributed in various ways to this work that I would like to acknowledge and thank, including Terry Ngin, Dimitris Tsalikis, Dr. Amitabh Nag, Paul Anderson, George Schnetzer, Rob Olsen III, and Shreeharsh Mallick. I would like to express special gratitude to Dr. Joseph Howard and Jonathan Hill, not only for their considerable contributions to this work, but for helping me transition to the field of electrical engineering, and for being great friends. Finally, I would like to say that it has been a great honor and privilege to work with all of the talented people in the Lightning Research Group at the University of Florida.

## TABLE OF CONTENTS

	<u>page</u>
ACKNOWLEDGMENTS .....	4
LIST OF TABLES .....	8
LIST OF FIGURES .....	10
ABSTRACT.....	14
CHAPTER	
1 INTRODUCTION .....	16
2 LITERATURE REVIEW .....	20
2.1 The Lightning Discharge.....	20
2.2 Photography of Lightning .....	27
2.2 Rocket-Triggered Lightning .....	30
2.2.1 Classical-Triggered Lightning .....	31
2.2.1.1 Precursors .....	33
2.2.1.2 The sustained upward positive leader.....	35
2.2.2 Altitude-Triggered Lightning.....	37
2.3 Corona Space Charge Layer at Ground .....	41
2.4 The Stepping Mechanisms of Long Negative Laboratory Discharges and Their Relationship to Lightning.....	45
3 EXPERIMENT DESCRIPTION .....	58
3.1 Experiment Control.....	61
3.1.1 PICs.....	62
3.1.2 Fiber-Optic Links.....	63
3.1.3 Control Computers.....	65
3.1.4 Rocket Launching Apparatus.....	66
3.2 Waveform Digitization and Storage .....	68
3.2.1 Yokogawa DL716 .....	68
3.2.2 Yokogawa DL750 .....	69
3.2.3 LeCroy LT344 Waverunner.....	70
3.2.4 LeCroy LT734 Waverunner 2.....	70
3.2.5 Lecroy 44Xi .....	70
3.2.6 MSE DSO Network .....	71
3.2.7 Positive Lightning Experiment DSO Network .....	71
3.3 Electric Field Mills.....	73
3.4 Broadband Electric Field and $dE/dt$ .....	74
3.4.1 The Flat-Plate Antenna .....	74
3.4.2 Electric Field Sensor .....	80

3.4.3	dE/dt Sensor .....	83
3.5	Channel-Base Currents.....	84
3.6	High-Speed Video Cameras.....	87
3.6.1	Photron SA1.1 .....	87
3.6.2	Phantom V7.1.....	90
4	DATA .....	118
4.1	Summary of Collected Data.....	118
4.2	Data Processing.....	118
4.2.1	Waveform Data .....	119
4.2.2	Image Data .....	120
5	OBSERVATIONS OF LIGHTNING LEADERS WITH HIGH-SPEED VIDEO AND CORRELATED CHANNEL-BASE CURRENT, REMOTE ELECTRIC FIELDS, AND X-RAY EMISSION.....	127
5.1	Observations of a Stepped Upward Positive Leader Initiating Triggered Lightning ..	128
5.2	Observations of Leader Stepping Mechanisms.....	132
5.2.1	Dart Stepped Leaders in Classical Triggered Lightning.....	132
5.2.2	Downward Negative Stepped Leader in Altitude Triggered Lightning.....	135
5.3	Upward Positive Connecting Leaders .....	139
5.4	Discussion .....	142
6	TRANSIENT CURRENT PULSES IN ROCKET-EXTENDED WIRES USED TO TRIGGER LIGHTNING.....	171
6.1	Data and Observations .....	172
6.1.1	Luminosity Associated with Precursor Current Pulses.....	172
6.1.2	Precursor Current and Electric Field Signatures.....	172
6.1.3	Precursor Rates.....	174
6.1.4	Negative-Polarity Precursors .....	175
6.2	Analysis.....	176
6.2.1	Propagation Speed.....	176
6.2.2	Precursor Charge and Current.....	177
6.3	Modeling .....	178
6.3.1	Model Input.....	178
6.3.2	Model Description.....	179
6.3.3	Model Predictions .....	185
6.4	Discussion .....	189
7	DETERMINATION OF THE ELECTRIC FIELD INTENSITY AND SPACE CHARGE DENSITY VERSUS HEIGHT PRIOR TO TRIGGERED LIGHTNING.....	210
7.1	The Wire Shielding Effect .....	212
7.2	Data .....	213
7.2.1	Rocket Height and Wire Extension Rate .....	213
7.2.2	Ground-Level Quasi-Static Electric Field Measurements .....	214

7.2.3	Precursor Current in the Wire and Corresponding Charge Transfer.....	217
7.3	Modeling .....	219
7.3.1	Model Description.....	219
7.3.2	Model Predictions .....	221
7.3.3	Model Fit.....	222
7.3.4	Model Predicted Line Charge Density .....	223
7.4	Discussion .....	224
8	SUMMARY OF RESULTS AND RECOMMENDATIONS FOR FUTURE RESEARCH .....	242
8.1	Summary .....	242
8.2	Recommendations for Future Research .....	249
	LIST OF REFERENCES .....	251
	BIOGRAPHICAL SKETCH .....	268

## LIST OF TABLES

<u>Table</u>	<u>page</u>
3-1 Sensor locations at the ICLRT.....	92
3-2 Makes, models, and salient specifications of the DSO used at the ICLRT. ....	94
3-3 PLE DSO channel assignment.....	94
3-4 Electric field sensor configuration.....	95
3-5 2008 channel-base current measurements configurations. ....	95
3-6 2009 channel-base current measurements. ....	96
3-7 OU Photron configurations in 2008.....	96
3-8 UF Photron configurations in 2008.....	97
3-9 UF Photron configurations in 2009.....	97
3-10 Photron framing rates, specified and actual.....	98
3-11 Phantom configurations 2009.....	99
4-1 Summary of triggering in 2008 and 2009.....	122
4-2 Summary of data acquired in 2008.....	122
4-3 Summary of data acquired in 2009.....	123
4-4 Summary of the triggered lightning flash from 2010. ....	123
4-5 Summary of return stroke times and peak currents in 2008. ....	124
4-6 Summary of return stroke times and peak currents in 2009.. ....	125
5-1 Salient information for the stepped upward positive leader of UF09-30.....	149
5-2 Lengths and distances for the space stems and space leaders observed in event UF09-25.....	150
5-3 Lengths and distances for the space stems and space leaders observed in event UF09-13.....	150
5-4 Upward positive connecting leader lengths.....	151

6-1	Precursor information, triggering-wire transmission-line parameters corresponding to the model-predicted precursor signatures that best match the measured precursor signatures, and the amplitude scaling factor of the input current pulse.....	195
7-1	Salient values of the quasi-static ground-level electric fields and the upward positive leader (UPL) initiation height. ....	230
7-2	The number of precursors, the height at which they first occurred, and the total ground-level field change they produced.....	230
7-3	The initial stage (IS) duration, the time interval between the end of the IS and the first return stroke, and the duration of the return stroke stage.. ....	231
7-4	Salient statistics of precursor charge and electric field change (sample size of 96).....	231
7-5	Model parameters, the corresponding space charge density at ground, and the electric field and the electric potential at the triggering height. ....	231

## LIST OF FIGURES

<u>Figure</u>	<u>page</u>
2-1 The four types of cloud to ground lightning, defined by the charge transfer to ground and direction of the leader.....	53
2-2 The sequence of events in a natural, downward negative cloud-to-ground lightning flash.....	54
2-3 The sequence of events in a classical triggered lightning.....	55
2-4 Sequence of events in altitude triggered lightning.....	56
2-5 Schematics illustrating the stepped development of the negative leader.....	57
3-1 The launch tower with the current interceptor installed. ....	100
3-2 The layout of stations and buildings at the ICLRT.....	101
3-3 The 2001 PIC controller.....	102
3-4 The 2006 PIC controller.....	103
3-5 Schematic of the typical 2001 PIC installation.....	103
3-6 Schematic of a typical 2006 PIC installation.....	104
3-7 The launch tube apparatus. ....	105
3-8 The bottom of the launch tubes showing a loaded rocket installation.....	106
3-9 A Campbell Scientific field mill installation (LC field mill).....	107
3-10 A field deployed flat-plate antenna sensor.....	108
3-11 The frequency-domain Norton equivalent circuit for the flat-plate antenna. ....	108
3-12 Schematic of an electric field sensor configuration.....	109
3-13 Picture of an RC box.....	109
3-14 Circuitry of the amplifier used in the electric field and II-VLS current sensors. . ....	110
3-15 Amplifier circuit board mounted inside a Pomona box.....	111
3-16 Flat-plate antenna covered with a plastic dome.....	112
3-17 Schematic of the dE/dt measurement configuration. ....	112

3-18	Inside the 2008 shunt box. ....	113
3-19	Current schematic for the 2008 current setup. ....	114
3-20	The 2009 tower current measurement configuration. ....	115
3-21	Schematic of the 2009 tower current configuration. ....	116
3-22	The high-speed video cameras setup in the office trailer. ....	117
3-23	The Phantom V7.2 and the Photron SA1.1. ....	117
5-1	High-speed video images of the channel during the initial stage of UF09-30. ....	152
5-2	The sequence of 60 Photron images containing the UPL for UF09-30, along with the synchronized wire-base current. ....	153
5-3	The wire-base current associated with the ten upward positive leader steps in UF09-30 that were imaged with high-speed video. ....	154
5-4	High-speed video images, and correlated electric field and current pulses for the dart-stepped leader preceding return stroke 8 of UF08-18. ....	155
5-5	Ten high-speed video frames depicting the leader for the fifth stroke of UF09-25 developing from 150 m height to ground during a time of 41.7 $\mu$ s. ....	156
5-6	Expanded and contrast-enhanced reproductions of the bottom of the downward-extending leader channel seen in the first nine frames in Figure 5-5. ....	157
5-7	The x-ray emission, dE/dt, and tower current that were recorded during the time when the 10 images shown in Figures 5-5 and 5-6 were recorded. ....	158
5-8	An image of the lower 200 m of channel for UF09-13 recorded by the HD camera. ....	159
5-9	A sequence of 64 images recorded at 108 kfps (9.3 $\mu$ s per image) showing the first downward negative stepped leader in UF09-13. ....	160
5-10	The leader tip seen in Images 7 through 11 from Figure 5-9 enlarged by a factor of 4. ....	160
5-11	The leader tip seen in images 33 through 37 from Figure 5-9 enlarged by a factor of 4. ....	161
5-12	The tip of a leader branch seen in images 56 through 59 from Figure 5-9 enlarged by a factor of 4. ....	161
5-13	The dE/dt record from dE-5 during the time when the downward negative stepped leader in UF09-13 was imaged. ....	162
5-14	High-speed video images of the leader preceding return stroke 1 of UF08-08. ....	163

5-15	High-speed video images of the leader preceding return stroke 2 of UF08-08. ....	164
5-16	High-speed video images of the leader preceding return stroke 2 of UF08-11. ....	165
5-17	High-speed video images of the leader preceding return stroke 3 of UF08-11. ....	166
5-18	High-speed video images of the leader preceding return strokes 1 through 8 of UF08-18. ....	167
5-19	High-speed video images of the leader preceding return stroke 9 of UF09-13. ....	168
5-20	High-speed video images of the leader preceding return stroke 2 of UF09-17. ....	169
5-21	High-speed video images of the leader preceding stroke seven of UF09-27. ....	170
6-1	Current signature of a precursor in which the first current pulse, and subsequent current pulses resulting from reflections from the wire base and wire top, are clearly separated in time and easily distinguishable. ....	196
6-2	Current and electric field signatures produced by a precursor that exhibited an initial low-level, steady current, and corresponding electric field ramp. ....	197
6-3	The wire-base current, and respective electric field measured by E2 at 156 m for three precursor signatures from event UF09-11. ....	198
6-4	The wire-base current, and respective electric field measured by E2 at 156 m for three precursor signatures for wire launch UF09-11 on a 2 s time scale. ....	199
6-5	The wire-base current, and respective electric field measured by E2 at 156 m for UF09-12 on a 1.3-s time scale. ....	200
6-6	An expanded view of the wire-base current and electric field of the precursors in UF09-11 viewed at 300 ms full scale. ....	201
6-7	Wire-base current and electric field signatures of negative-polarity precursors during wire launch UF09-01. ....	202
6-8	A scatter plot showing the measured current propagation speeds (the ratio of wire-top height to one-half of the average peak-to-peak times) versus wire-top heights for 271 precursors. ....	203
6-9	A scatter plot of the current-peak ratios. ....	204
6-10	A scatter plot of the charge transferred to ground during the initial precursor current pulse versus the total charge transferred to ground by the end of the precursor current signature. ....	205
6-11	The incident current pulses that are used as inputs to the distributed-circuit model shown in Figure 6-12. ....	206

6-12	The distributed circuit used to model the current propagation on the triggering wire, ground-lead, and ground rod.....	207
6-13	Measurement and modeling results for three precursors for two model grounding configurations.. .....	208
6-14	The model predictions for precursor 3 with varied values of $G_{TW}$ and $R_{TW}$ . .....	209
7-1	Schematic illustrations of the ambient electric field before and after the extension of a triggering wire.....	232
7-2	The model wire trajectory.....	233
7-3	The ground-level electric field changes and wire-top heights versus time for Launches 1 through 6.....	234
7-4	Field change versus wire-top heights for Launches 1 through 6. ....	235
7-5	An example of a precursor that produced a static electric field change. ....	236
7-6	The vertical profiles of space charge density, electric field magnitude, and electric potential for the nine combinations of $d$ and $E_{\infty}$ values and $E_0 = 6 \text{ kV m}^{-1}$ .....	237
7-7	The model-predicted ground-level field changes for no space charge and the nine cases of exponentially decaying space charge density for $E_0 = 6 \text{ kV m}^{-1}$ .....	238
7-8	The model predictions that best fit the measured electric field changes for Launches 1 through 6. ....	239
7-9	Examples of the model-predicted height profiles of the radial electric field 5 m from the wire and equivalent approximate line charge density.....	240
7-10	Triggering height versus initial ground-level electric field magnitude. ....	241

Abstract of Dissertation Presented to the Graduate School  
of the University of Florida in Partial Fulfillment of the  
Requirements for the Degree of Doctor of Philosophy

OBSERVATIONS AND MODELING OF PROCESSES IN ARTIFICIALLY INITIATED  
(TRIGGERED) LIGHTNING

By

Christopher John Biagi

August 2011

Chair: Martin A. Uman  
Cochair: Vladimir A. Rakov  
Major: Electrical and Computer Engineering

From 2008 to 2010, data were obtained for 38 artificially initiated lightning flashes. Images from high-speed framing cameras and synchronized remote electric fields and currents are employed to study lightning leader initiation and propagation: (1) Optical images and wire-base currents recorded during the development of a stepped upward positive leader from the tip of an extending triggering wire are examined and compared with positive polarity long laboratory discharges. (2) The space stem and space leader, processes known to play a significant role in the step-wise propagation of long, negative polarity long laboratory discharges, have been observed for the first time in association with steps in two downward negative dart-stepped leaders in classical triggered lightning flashes, and in a downward negative stepped leader in an altitude triggered flash. These observations confirm a previous hypothesis that the lightning leader and the long laboratory leader develop in a similar manner, albeit on different scales of length, time, and voltage. (3) Prior to the attachment phase, high-speed framing cameras imaged a total of 15 upward positive connecting leaders and their associated downward negative leaders within tens of meters of each other. Their development and eventual attachment are examined.

In addition to the primarily optical measurements noted above, inferences are made of the vertical profiles of space charge density and electric field intensity above ground, as well as the line charge density that forms along the extending triggering wire in response to the ambient electric field. These inferences are made by comparing modeling and measurements of the ground-level electric field changes caused by the vertical extension of six grounded lightning-triggering wires that initiated lightning. The sustained upward positive leader inception heights and the ground-level electric field intensity at the wire launch time were linearly correlated with a correlation coefficient of -0.85. The transient current, electric field, and optical signatures produced by the sudden electrical breakdown processes (precursors) that occur at the top of the upward-extending lightning-triggering wires are examined. The lightning-triggering wire and its grounding system are modeled as uniform transmission lines with model predictions that are consistent with the measured wire-base precursor current signatures.

## CHAPTER 1 INTRODUCTION

The work presented in this dissertation represents the culmination of four years of research by the author on artificially initiated (triggered) lightning at the University of Florida/Florida Institute of Technology International Center for Lightning Research and Testing (ICLRT) at Camp Blanding in north-central Florida. The purpose of the research was three-fold: (1) To use high-speed video images and synchronized current and remote electric field waveforms to build upon the existing knowledge pertaining to the initiation and propagation mechanisms of lightning leaders. An ancillary goal was to demonstrate the utility of modern digital high-speed video cameras, a research tool that is facilitating a new era of lightning research that will help unravel some of the long standing mysteries of lightning physics. (2) To examine the electrical environment into which the grounded, lightning-triggering wires are launched. This examination involved comparing measurements and modeling of the ground-level electric field change during the vertical extension of the wire in order to infer vertical profiles of ambient electric field, space charge density, and the charge density that forms along the wire in response to the ambient electric field. (3) To characterize the sudden electrical breakdown processes (precursors) that occur at the top of the grounded lightning-triggering wires through analysis of the current, electric field, and optical signatures they produce. Part of this characterization involved modeling the propagation of the current pulses on the triggering wire to determine the wire's transmission-line characteristics.

Chapter 5 presents new observations and discoveries pertaining to lightning leaders, including their propagation and initiation, and attachment mechanisms made from the high-speed video images and synchronized waveform data. The most important contributions in Chapter 5 are summarized as follows: (1) The lower 12 m of an upward positive leader developing in a

stepped manner from the tip of a triggering wire was imaged at 300 kfps (3.3  $\mu$ s per frame) with synchronized current pulses detected at the wire base, and the currents and charges associated with positive leader steps were measured. (2) Individual steps in two downward negative dart-stepped leaders in separate classically triggered lightning flashes, and in a downward negative stepped leader in virgin air in an altitude triggered lightning flash, were resolved temporally and spatially in high-speed video images. The high-speed video images show that the negative leader step in lightning develops via similar mechanisms as do negative leaders steps in laboratory sparks, namely through the formation of space stems and space leaders in the streamer zone below the previously formed leader tip. (3) Upward positive connecting leaders and their corresponding downward negative leaders just prior to the attachment phase in triggered lightning were observed in high-speed video images. The lengths of upward positive connecting leaders in triggered lightning have been measured, and it was observed that attachment heights can vary from stroke to stroke in a flash. Channel-base current and remote electric field observations indicate that the observed upward positive connecting leaders did not develop stepwise. In one image, the streamer zone of a downward negative dart-stepped leader appears to be in contact with the upward positive connecting leader.

Chapter 6 presents new observations of precursors and an examination of the propagation of transient current pulses on a triggering wire, and the transmission-line characteristics of the wire itself. The most important new contributions in Chapter 6 are as follows: (1) Luminous leader channels associated with the precursors to the sustained upward positive leader were resolved for the first time, some of which reached 8 m in length. (2) Measurements of the wire-base precursor current signatures have shown that transient current pulses propagate on the vertically extending triggering wire with a speed that is 10 to 20% slower than that of light, and

with a speed that decreases with increasing wire lengths. (3) Precursors were observed to sometimes occur rapidly (every few hundreds of microseconds) with a rate that is inversely related to their peak current amplitudes throughout the wire extension. (4) Negative-polarity electrical breakdown was detected at the tip of triggering wires launched in electric fields consistent with predominately positive charge was overhead. (5) The triggering wire and its grounding system were modeled as uniform transmission lines, and the model predictions of the wire-base precursor current signatures were consistent with the measured wire-base precursor current signatures. The model was used to infer the distributed-circuit characteristics of the triggering wire and the grounding system. The current reflection coefficient at the connection of the triggering wire to ground was found to be about 0.9, and the attenuation constant for a current pulse propagating on the wire was found to be about  $8.2 \times 10^{-4}$  Neper  $m^{-1}$ .

In Chapter 7, inferences are made of the vertical profiles of electric field and space charge density, and the line charge density contained in the corona sheath along a triggering wire is examined. The most important new contributions found in Chapter 7 are as follows: (1) Finite-element modeling yielded ground-level electric field changes that were consistent with measurements during several wire launches with ground-level charge densities between 1.5 and 7  $nC m^{-3}$ , space charge exponential height decay constants ranging from 67 to 200 m, and uniform electric field intensities far above the space-charge layer ranging from 20 to 60  $kV m^{-1}$ . (2) Finite-element modeling predicted that the radial electric field along the wire increased with height and was of sufficient strength to produce a corona sheath having a radius of up to 5 m. The predicted radial electric field would require the charge per unit length contained by the corona sheath to increase steadily from less than 1  $\mu C m^{-1}$  to about 60  $\mu C m^{-1}$  at wire heights from 1 m to 285 m. (3) A strong inverse correlation was found between the triggering height and

the ground-level electric field magnitude at the time that the wire was launched for six wire launches.

In addition to the new contributions to lightning research presented in Chapters 5, 6 and 7, a review of relevant literature is given in Chapter 2, and the experimental setup and equipment are described in Chapter 3. Chapter 4 summarizes the data, and describes how it was processed. Finally, a summary of the results presented in this work, and suggestions for future research are given in Chapter 8.

## CHAPTER 2 LITERATURE REVIEW

### 2.1 The Lightning Discharge

The term lightning is applied to transient, high-current electric discharges in the atmosphere with a length on the order of kilometers [Uman, 1987]. Thunderstorms are the primary source of lightning, although lightning is known to originate from volcanic plumes [e.g., Thomas *et al.*, 2007] and nuclear explosions as well [e.g., Uman *et al.*, 1972]. All references to lightning herein refer to the type involved with thunderclouds. The vast majority of lightning, as much as 75%, occurs within clouds (intracloud) or between clouds (intercloud) [e.g., Williams *et al.*, 1989; Rakov and Uman, 2003]. Cloud-to-ground (CG) lightning is the most deleterious type to humans; it kills an estimated 100 people and causes several hundred million dollars worth property damage per annum in the United States alone [Rakov and Uman, 2003]. Given its impact on humans, it is understandable that the CG lightning discharge (also called CG flash) is by far the most studied form of lightning.

There are four types of CG flashes, illustrated in Figure 2-1, and these can be characterized by the direction of the initial leader and the overall charge transferred to ground [Berger *et al.*, 1975; Rakov and Uman, 2003]: (1) downward negative, (2) upward negative, (3) downward positive, and (4) upward positive. Note that for the upward negative type, the initial upward leader is of positive polarity, and for the upward positive type, the initial upward leader is of negative polarity. Nearly all lightning is the downward type, and upward lightning of either polarity is believed to only begin from the tips of tall structures or mountain tops where the electric field can be enhanced by the local topography. It is estimated that 90% of all CG flashes are of the downward negative type, with the remaining 10% being the downward positive type [e.g., Rakov and Uman, 2003].

The downward negative CG lightning apparently begins with a distinct process known as preliminary breakdown or initial breakdown that leads to the development of a downward-moving stepped leader. Evidence for initial breakdown consists of observations of cloud luminosity lasting for a hundred or more milliseconds prior to a stepped-leader emerging from the cloud, and relatively long electric field changes exceeding 100 ms in duration [Rakov and Uman, 2003]. The initial breakdown is likely the development of a channel between the negative and lower positive charge regions of a cloud [Clarence and Malan, 1957], or multiple discharges with significant horizontal extent originating from the main negative charge region [Krehbiel et al., 1979; Rhodes and Krehbiel, 1989]. The stepped leader inception is associated with a train of bipolar electric field pulses having an initial half cycle polarity that is the same as that of the following return stroke field change [Kitagawa and Brook, 1960; Weidman and Krider, 1979; Beasley et al., 1982; Rakov et al., 1996; Nag and Rakov, 2009]. The train of bipolar pulses typically lasts for about 1 millisecond, and precedes the first return strokes by several tens of milliseconds. The electric field pulses have durations of 20 to 40  $\mu\text{s}$  and occur on time intervals between 70 and 130  $\mu\text{s}$  [Rakov et al., 1996].

The sequence of events in a typical downward negative CG lightning flash after a stepped leader has emerged from the cloud is illustrated in Figure 2-2. A leader is defined as a self-propagating electrical discharge that creates a channel with electrical conductivity of the order of  $10^4 \text{ S m}^{-1}$  [Rakov and Uman, 2003]. The first downward negative leader in a CG flash is called a stepped leader because it develops intermittently, extending in length seemingly through a sequence of steps. The intermittent progression of downward-propagating, negatively-charged stepped and dart-stepped leaders was first reported by Schonland [1935], motivating further studies of the development of stepped leaders. Stepped leader speeds have been found to

typically be in the range from about  $10^5$  to  $10^6$  m s<sup>-1</sup> [e.g., *Schonland*, 1956; *Berger and Vogelsanger*, 1966; *Orville and Idone*, 1982; *Chen et al.*, 1999; *Proctor et al.*, 1988; *Shao et al.*, 1995]. Lengths of stepped leaders have been observed ranging from a few meters up to 200 m, and interstep intervals are typically between 5 and 100  $\mu$ s [e.g., *Schonland*, 1956; *Berger and Vogelsanger*, 1966; *Krider et al.*, 1977; *Chen et al.*, 1999]. The total charge deposited by a stepped leader just before ground contact is around 5 C, the line charge density ranges from  $10^{-4}$  to  $10^{-3}$  C m<sup>-1</sup>, and the average current is tens to hundreds of amperes [e.g., *Rakov and Uman*, 2003]. Electric field waveforms have indicated that peak stepped leader currents are on average about 1 kA, but can reach levels as high as 8 kA [e.g., *Krider et al.*, 1977; *Krehbiel*, 1981; *Thomson et al.*, 1985]. *Howard et al.* [2011], using transmission line modeling to reproduce measured electric field waveforms from leader steps, inferred peak currents for leader steps ranging from 5 to 7 kA, and a step charge of about 300 mC. *Howard et al.* [2011] also demonstrated that leader step currents likely have a slow front that is similar to the slow front in return stroke currents.

When the downward-moving negative stepped leader reaches a height of several tens of meters, the electric field at ground is significantly enhanced due to the potential difference between the leader and ground, on the order of tens of megavolts, and probably on the order of the cloud potential [*Bazelyan et al.*, 1978]. In response to the enhanced electric field, one or more upward positive leaders develop from local ground objects or the ground itself, beginning the attachment process. It is thought that the relatively low-conductivity streamers at the tips of the downward negative and upward leader meet to form a common streamer zone in which the two leaders accelerate towards each other [*Rakov and Uman*, 2003]. The breakthrough phase occurs when the two leaders meet, which can be viewed as a switch-closing operation that

launches return stroke waves in both directions [e.g., *Wagner and Hileman, 1958; Uman et al., 1973; Weidman and Krider, 1978; Willett et al., 1988; Willett et al., 1989; Leteinturier et al., 1990; Rakov and Uman, 2003; Jerauld et al., 2007*]. The upward leader that connects to the downward leader is called an upward connecting leader.

*Yokoyama et al. [1990]* reported time-resolved optical observations, using the ALPS optical imaging system, of upward connecting leaders ranging from 25 to 150 m in length from an 80-m tall communications tower in Japan, and estimated that their speeds ranged from  $0.8 \times 10^5$  to  $2.7 \times 10^5$  m s<sup>-1</sup>. *Wang et al. [1999a]*, also using the ALPS system, estimated a propagation speed of  $2 \times 10^7$  m s<sup>-1</sup> for one upward positive connecting leader in a triggered lightning stroke. Several researchers have reported observing in streak photography a return stroke beginning while the downward leader was some 20 to 50 m above ground, and inferred that an upward connecting leader too faint to be imaged intercepted the downward leader [*Golde, 1947; Berger and Vogelsanger, 1966; Wagner, 1967; Orville and Idone, 1982*]. Observations of loops and upward branches in lightning channels a few tens of meters above ground [e.g., *Golde, 1967; Orville, 1968; Hagenguth, 1947*] or unconnected upward discharges in the vicinity of a the ground strike point of lightning channels [e.g., *Krider and Ladd, 1975; Rakov and Uman, 2003*] indicate that upward connecting leaders play a significant role in the attachment process.

Upward connecting leaders a few tens of meters in length have been inferred in several triggered lightning strokes, which are similar to subsequent strokes in natural lightning [*Idone et al., 1984; Idone, 1990*]. Using the ALPS optical imaging system, *Wang et al. [1999a]* observed in triggered-lightning strokes in Florida one upward connecting leader that was 7 to 11 m in length, and inferred the existence of another one that was 4 to 7 m in length. The observed upward connecting leader lasted several hundred nanoseconds and had a luminosity that was an

order of magnitude lower than that of its associated downward dart leader. Connecting leaders are not always observed for subsequent strokes, and they are typically shorter in length than those for first strokes. From streak photography in Florida and New Mexico, *Orville and Idone* [1982] observed 21 dart leaders and 3 dart-stepped leaders that showed no indication of upward connecting leaders. New observations of upward positive leaders in triggered lightning are presented in Chapter 5 of this work.

When the downward-moving leader meets with an upward-connecting leader, the return stroke phase begins. Initially, there is an upward-propagating return stroke wave and a downward-propagating return stroke wave. The downward-propagating return stroke wave quickly reaches ground, and a reflected, upward-propagating wave is produced. Since the reflected wave propagates up in a return-stroke-conditioned channel, it likely travels faster than and catches up to the initial upward propagating return stroke wave [*Rakov, 1998*]. The bi-directional return stroke waves are short lived, and a single upward moving wave quickly forms [*Rakov and Uman, 2003*].

Of all the processes comprising a lightning flash, return strokes cause the most damage, produce the brightest luminosity and a distinct electromagnetic signature [*Rakov and Uman, 2003*]. Thus, the return stroke has been observed and studied extensively. Return strokes in negative cloud-to-ground lightning typically: have a peak current of 30 kA, transfer a charge of 5 C, propagate at speeds ranging from  $1 \times 10^8$  to  $2 \times 10^8$  m s<sup>-1</sup>, and have a peak channel temperature on the order of 30,000 K [*Rakov and Uman, 2003, Table 1.1*]. Return strokes are one of three ways charge is transferred by lightning from the cloud to the earth, the other two being continuing current and M-components.

In about 80% of downward negative lightning, subsequent leader/return stroke sequences follow the first return stroke. *Kitagawa et al.* [1962] observed in New Mexico a CG flash containing 26 return strokes. However, CG flashes typically have 3 to 5 leader/return stroke sequences, and 1.7 ground contact points [*Rakov et al.*, 1994; *Rakov and Uman*, 2003]. About half of CG flashes in New Mexico and Florida have more than one ground contact point [*Kitagawa et al.*, 1962; *Rakov and Uman*, 1990]. *Biagi et al.* [2007], based on 16.7-ms time resolution video observations, reported that 444 of 2338 (19%) and 126 of 338 (37%) of subsequent strokes in Southern Arizona and Texas/Oklahoma, respectively, struck ground at new locations. *Saraiva et al.*, [2010] reported that 49% of 344 flashes observed in Arizona and near Sao Paulo, Brazil had more than one ground contact point.

Subsequent return strokes that follow channels to ground that have been pre-conditioned by previous strokes are preceded by dart leaders or dart-stepped leaders. The dart leader appears to develop continuously, that is, without stepping. Optical measurements show that dart leaders propagate faster than stepped leaders, with speeds typically on the order of  $10^6$  to  $10^7$  m s<sup>-1</sup> in natural lightning [e.g., *Schonland et al.*, 1935; *McEachron*, 1939; *Orville and Idone*, 1982; *Jordan et al.*, 1992; *Mach and Rust*, 1997] and in triggered lightning [e.g., *Hubert and Mouget*, 1981; *Idone et al.*, 1984; *Jordan et al.*, 1992; *Mach and Rust*, 1997]. Dart leader speeds have been observed to increase or decrease near ground [e.g., *Schonland et al.*, 1935; *Orville and Idone*, 1982; *Jordan et al.*, 1992; *Wang et al.*, 1999b]. *Jordan et al.* [1992] observed in Florida that dart leader speeds and the following return stroke peak currents are positively correlated. These observations led *Rakov* [1998] to infer that the dart-leader propagation characteristics are determined primarily by the leader current wave magnitude, as opposed to the channel conditions ahead of the wavefront.

The occurrence of dart-stepped leaders preceding subsequent strokes is apparently related to the cumulative conditioning (or the lack of it) of the lightning channel, as first hypothesized by *Rakov et al. (1994)*. *Rakov and Uman [1990]* gave a histogram showing the percentage of dart-stepped leaders occurring after an interstroke interval of 100 ms or less as a function of stroke order for 76 negative CG flashes near Tampa, Florida. The histogram shows that second strokes are initiated by dart-stepped leaders more often than all other stroke orders combined. The geometric mean of the interstroke interval preceding the 13 second strokes initiated by dart-stepped leaders was 54 ms. *Davis [1999]* observed in  $dE/dt$  measurements in Florida that dart-stepped leaders that initiated second strokes occurred after a typical interstroke interval of 61 ms. *Davis [1999]* found that dart-stepped leaders initiating strokes of higher order were preceded by a typical interstroke interval of 140 ms. The six dart-stepped leaders discussed by *Schonland [1956]* preceded second strokes. Dart-stepped leader develop with speeds on the order of  $10^6 \text{ m s}^{-1}$  and, like the dart leader, the dart-stepped leader apparently may increase or decrease its speed as it approaches ground [*Orville and Idone, 1982; Davis, 1999; Wang et al., 1999b*]. *Davis [1999]* reported a clear tendency for the downward dart-stepped leader speed to decrease with decreasing altitude, from a mean of  $1.6 \times 10^7 \text{ m s}^{-1}$  at heights between 3 and 6 km, to  $3.5 \times 10^6 \text{ m s}^{-1}$  below heights of 1 km. *Schonland [1956]* reported that leader step lengths in natural dart-stepped leaders near ground were on average 10 m, and the interstep time interval was typically 10  $\mu\text{s}$ . *Orville and Idone [1982]* analyzed four dart-stepped leaders in detail, and reported step lengths from a few meters to several tens of meters, interstep time intervals from several to tens of microseconds. In one stroke analyzed by *Orville and Idone [1982]* the interstep time interval increased and the propagation speed decreased with decreasing height, and in another the opposite was observed. *Idone and Orville [1984]* reported for two dart-stepped

leaders in triggered lightning dart-stepped leader that step lengths ranged from 5 to 10 m, and interstep time intervals ranged from 2 to 8  $\mu\text{s}$ .

*Krider et al.*, [1977], from electric field pulses 200  $\mu\text{s}$  before the return-stroke onset, found that the mean interstep time interval for dart-stepped leaders in Florida and Arizona was 6.5 and 7.8  $\mu\text{s}$ , respectively. These times are shorter than the mean interstep time interval for stepped leaders reported in the same study, 16 and 25  $\mu\text{s}$  for Florida and Arizona, respectively. *Davis* [1999] reported that interstep time intervals increased with decreasing altitude, from 1.6  $\mu\text{s}$  near the leader origin to 4.1  $\mu\text{s}$  near ground. *Wang et al.* [1999b] reported that luminosity waves that began at the leader tip and traveled up the leader channel were associated with dart-stepped leader steps. *Rakov et al.* [1998] estimated for a dart-stepped leader in triggered lightning that the charge and current associated with each step is a few millicoulombs and a few kiloamperes, respectively. New observations of a dart-stepped leader in triggered lightning are presented in Chapter 5 of this work.

## 2.2 Photography of Lightning

The first quantitative measurements of lightning were made with photography in the late nineteenth century. *Kayser* [1884], in a still photograph of a single flash, spatially resolved return strokes in a flash that were separated by a strong wind. *Hoffert* [1889] and *Weber* [1889] were the first researchers to attain photographs of lightning with crude temporal resolution by moving cameras photographing lightning. *Hoffert* [1889] managed to observe that the first return stroke was branched, that there was continuing luminosity between return strokes, and was able to estimate interstroke interval times. These features, and their causes, are still studied today. *Walter* [1902, 1903, 1910, 1912, and 1918] using time resolved photography, was apparently the first to photograph the leader preceding a first return stroke. *Larsen* [1905], using a moving camera in the United States, measured interstroke time intervals and imaged what

appeared to be 40 return strokes in a single flash, although many of these were likely M-components.

The invention of the two-lens streak camera by Boys [Boys, 1926; Boys, 1928; Boys, 1929] led to significant advances in lightning research made by B. F. J. Schonland, D. J. Malan, and their co-workers in the 1930's in South Africa. A detailed review of these findings is given in Uman [1969], but some are worth mentioning here. Schonland and Collens [1934] provided the first evidence in streak photography of return strokes moving from the ground to the cloud, with a mean speed of  $3.8 \times 10^7 \text{ m s}^{-1}$ . They also reported a mean dart leader speed of  $1.1 \times 10^7 \text{ m s}^{-1}$ . Schonland *et al.* [1935] reported the first observations of the stepped leader preceding the first stroke in a flash, and the existence of dart-stepped leaders. They measured an effective stepped leader speed of  $1.5 \times 10^5 \text{ m s}^{-1}$ . Schonland [1956] reported that step lengths varied from 10 to 200 m. M-components were studied by Malan and Collens [1937] and Malan and Schonland [1947]. Schonland [1956] reported a cumulative frequency distribution of the number of return strokes per flash in 1,800 cloud-to-ground flashes showing that 50% of them consisted of four or more return strokes. Other researchers have performed similar studies of natural lightning using streak photography [e.g., Hagenguth, 1947; Workman *et al.*, 1960; Kitagawa *et al.*, 1962, Brook *et al.*, 1962; Orville and Idone, 1982; Jordan *et al.*, 1992, 1995, 1997].

Streak photography has been used to study lightning to tall buildings and towers that are known to be struck multiple times each year. McEachron [1939, 1941], and Hagenguth and Anderson [1952] studied lightning to the Empire State Building in New York City, NY, using photographic observations with simultaneous oscilloscopic measurements of lightning currents. McEachron [1939] reported the discovery of the upward-stepped leader, and continuing currents and corresponding luminosities lasting 0.5 s or longer. A majority of the flashes to the Empire

State Building were found to be the upward type, beginning with a stepped leader that developed from the building to the cloud, with the tower currents increased steadily to smooth continuous currents. Dart-leader/return-stroke sequences sometimes occurred during the continuous current in different channels (branches). *Berger and Vogelsanger* [1966] studied lightning striking instrumented towers on Monte San Salvatore using streak photography. They observed that stepped leaders of both polarities can travel upwards from towers/buildings, or downward from the clouds, and that there are distinct differences between negative and positive polarity steps. In some streak photographs of upward-negative stepped leaders, *Berger and Vogelsanger* [1966] reported observing corona-like discharge up to 3 m in length extending from the leader tip.

Streak photography has helped to elucidate the sequence of events that occur in rocket-and-wire triggered lightning [e.g., *Fieux et al.*, 1978; *Horii*, 1982; *Hubert et al.*, 1984; *Laroche et al.*, 1988; *Idone*, 1992; *Lalande et al.*, 1998; *Rakov et al.*, 2003; *Olsen et al.*, 2006]. *Fieux et al.* [1978], using streak photography, were the first to resolve the upward positive leader, the wire destruction, the initial stage current, and return strokes in triggered lightning in France. Several other studies of triggered lightning with streak photography have examined upward connecting discharges [*Idone*, 1990], the relationship between luminosity and channel-base current [*Idone and Orville*, 1985], channel tortuosity [*Idone and Orville*, 1988; *Idone*, 1995], and dart leader speeds [*Jordan et al.*, 1992].

Another photographic instrument that has been used to study lightning is the high-speed framing camera, which are often called high-speed ‘video’ cameras because the images can be displayed as a video sequence. *Kito et al.* [1985] used a high-speed framing camera operating at 1,000 frames per second (1 kfps) to study triggered lightning during the winter season in Japan. *Evans and Walker* [1963] photographed lightning an area of about 8 m x 11 m at a tower top on

Mount Bigelow near Tucson, AZ from a distance of about 110 m using a high speed framing camera operating with a 2- $\mu$ s exposure time (with 77  $\mu$ s between frames). Their images provided data on lightning-channel radius, luminosity verses time, and changes in channel geometry during and between return strokes. In the past decade or so, digital high-speed video cameras have played an important role in observations of lightning-related transient luminous events above cloud tops [e.g., *Stanley et al.*, 1999; *Cummer and Stanley*, 1999; *Moudry et al.*, 2002; *Cummer et al.*, 2006; *Marshall and Inan*, 2005; *Stenback-Nielsen and McHarg*, 2008], and researchers have been making new observations of cloud-to-ground lightning [e.g., *Ballarotti et al.*, 2005; *Qie and Kong*, 2007; *Saba et al.*, 2008; *Zhang et al.*, 2009; *Kong et al.*, 2009; *Warner et al.* 2011].

## 2.2 Rocket-Triggered Lightning

The method of triggering lightning by quickly extending a thin wire using a rocket was first advanced by *Newman* [1958]. *Brook et al.* [1961] demonstrated that rapidly introducing a thin wire into the electric field of a laboratory spark gap could trigger a discharge, whereas having the same wire stationary in the gap did not produce a spark. The first triggered lightning discharges were produced by *Newman et al.* in 1960 by using rockets to quickly extend thin wires into the air from a boat off the west coast of Florida [*Newman*, 1965; *Newman et al.*, 1967; *Newman and Robb*, 1967]. The first triggered lightning over land was done in 1973 at Saint-Privat d'Allier in France [*Fieux et al.*, 1975; *Fieux et al.*, 1978]. These ground breaking experiments led to similar triggered lightning programs, as summarized in Table 7.1 in *Rakov and Uman* [2003, pg. 266] in Japan [e.g., *Horii*, 1982; *Kito et al.*, 1985; *Nakamura et al.* 1991; *Nakamura et al.*, 1992], at Langmuir Laboratory in New Mexico [e.g., *Hubert et al.*, 1984; *Idone et al.*, 1984], at the Kennedy Space Center in Florida [e.g., *Eybert-Berard et al.*, 1986; *Willet*, 1992], at various sites in China [e.g., *Liu et al.*, 1994; *Liu and Zhang*, 1998], at Camp Blanding,

Florida [e.g., *Uman et al.*, 1997; *Rakov et al.*, 1998], and at Cachoeira Paulista, Brazil [e.g., *Saba et al.*, 2000; *Saba et al.*, 2005].

Triggered lightning is relatively easy to study since researchers can essentially control the time and place in which it occurs. Further, direct channel-base current measurements can be made for triggered lightning [e.g., *Hubert et al.*, 1984; *Horii and Ikeda*, 1985; *Leteinturier et al.*, 1991; *Fisher et al.*, 1993; *Depasse*, 1994; *Uman et al.*, 2002; *Kodali et al.*, 2005; *Wang et al.*, 2005; *Schoene et al.*, 2009; *Schoene et al.*, 2010], in contrast to the current measurements for natural lightning that have been made on tall towers [e.g., *Berger et al.*, 1975] or inferred from the radiated fields. The tower currents can be influenced, or ‘contaminated’ by the transient process that occur in the tower due to transmission-line effects [e.g., *Gorin and Shkilev*, 1984; *Zundl*, 1994; *Rakov*, 2001]. Triggered lightning also provides the means to study lightning’s effect on structures, such as buildings and power transmission lines [e.g., *Nakamura et al.*, 1991; *Rakov et al.*, 2002; *DeCarlo et al.*, 2008]. Triggered lightning can be used to validate models with current being a parameter [e.g., *Rakov and Uman*, 1998], and to validate location systems like the U.S. National Lightning Detection Network (NDLN) [*Jerauld et al.*, 2005; *Nag et al.*, 2011].

In the following, the classical and altitude types of rocket-and-wire triggered lightning are described. In the classical type, the triggering wire is attached to ground. In the altitude type, the triggering wire is extended so that its bottom end is up to several hundred meters above ground. Literature regarding triggered lightning experiments and observations will be reviewed with emphasis placed on reports of the leader process.

### **2.2.1 Classical-Triggered Lightning**

The sequence of events in classical triggered lightning is depicted in Figure 2-3. The triggering process begins with the launching of a rocket trailing a grounded, thin metallic wire

into a thunderstorm environment when at ground intensified electric fields are observed. The rocket quickly accelerates to a maximum speed of about 160 to 200 m s<sup>-1</sup>. After extending for a time of 1 to 3 s, with the wire-tip reaching a height between about 100 and 300 m, the electric field at the wire tip is sufficiently enhanced to launch a sustained upward positive leader (UPL) from the triggering wire tip that develops upward with a speed between 10<sup>4</sup> to 10<sup>6</sup> m s<sup>-1</sup> [e.g., *Fioux et al.*, 1978; *Kito et al.*, 1985; *Laroche et al.*, 1988; *Idone*, 1992; *Biagi et al.*, 2009; *Yoshida et al.*, 2010]. The upward positive leader establishes a conductive channel between the cloud and ground, and leads to the initial continuous current (ICC) phase. The triggering wire explodes from Joule heating several milliseconds to tens of milliseconds after the upward positive leader inception, effectively disconnecting the upward positive leader from ground. The wire explosion is typically associated with the so-called initial current variation (ICV) [e.g., *Wang et al.*, 1999c; *Rakov et al.*, 2003; *Olsen et al.*, 2006]. The ICV is preceded by a rise in current of several hundred amperes over a time of milliseconds, followed a rapid drop in current over a few hundred microseconds, sometimes to zero or near zero. The resultant current cut-off (or nearly cut-off) is followed by a leader/return-stroke-like process that re-establishes the current flow. Following the wire explosion and its replacement by a plasma channel, the initial continuous current flows for some hundreds of milliseconds, with a geometric mean current of about 100 A [*Wang et al.*, 1999c; *Miki et al.*, 2005]. *Yoshida et al.* [2010] reported maximum initial stage current of 18 kA for a flash triggered in an intense thunderstorm. Often, impulsive current features (ICC pulses) that resemble the M-component mode of charge transfer occur during the ICC [*Wang et al.*, 1999a; *Rakov et al.*, 2003; *Miki et al.*, 2005; *Yoshida et al.*, 2010].

After the ICC, there is typically an interval lasting some tens of milliseconds with no channel-base current. Then, one or more downward-leader/upward-return-stroke sequences may

occur that are guided to ground by the channel that has been established by the initial stage current. These leader/return-stroke sequences are similar to subsequent strokes in natural lightning [e.g., *Rakov and Uman*, 2003]. In some cases the downward negative leaders are dart-stepped (some cases are presented in Chapter 5 of this work). Dart-stepped leaders in triggered lightning can exhibit some similarities to stepped leaders in natural lightning, including discrete  $dE/dt$  pulse bursts and x-ray emission [e.g., *Howard et al.*, 2010].

### **2.2.1.1 Precursors**

In rocket-and-wire triggered lightning, transient current pulses in the triggering wires are observed at ground before the development of a sustained upward positive leader from the wire tip. The current pulses are caused by electrical breakdown at the tip of wire where the electric field is significantly enhanced. The triggering wire behaves like a transmission line with the precursor-pulse round-trip propagation time on the wire being greater than the pulse width. Current-pulse reflections are produced at the ground and at the wire tip. As a result, the current signature from a single precursor observed at ground is a sequence of pulses of alternating polarity and decreasing amplitude.

*Horii* [1982] identified “pre-discharge” current pulses that were recorded at a 5-kHz sampling rate. *Horii’s* current pulses occurred both as isolated events and in groups (two or more pulses occurring with intervals of several tens of microseconds) and had amplitudes between 0.1 A to 100 A. *Laroche et al.* [1988] observed current pulses and associated electric field pulses occurring prior to the inception of a sustained upward positive leader with intervals of some tens of milliseconds in isolation, or in groups, with the pulses within groups occurring about every 25  $\mu$ s. Higher-magnitude current pulses exhibited damped-oscillatory behavior, and the oscillation period increased with increasing wire length, leading *Laroche et al.* [1988] to hypothesize that the current-pulse oscillations represented the transient response of the triggering

wire. *Lalande et al.* [1998] observed that damped-oscillatory current pulses were separated in time by 5 ms on average and lowered to ground several tens of microcoulombs. *Willett et al.* [1999] gave examples of damped-oscillatory current pulses before the initiation of a sustained upward positive leader, along with corresponding damped-oscillatory electric field signatures resulting in a static electric field change. *Willett et al.* [1999] reported that the pulses occurred roughly every 10 ms, and sometimes occurred in groups in which individual pulses occurred roughly every 30  $\mu$ s. The electrical breakdown that produces the current pulses preceding the inception of a sustained upward positive leader were first termed “precursors” by *Willett et al.* [1999].

*Lalande et al.* [1998] speculated that the damped-oscillatory current waveforms are caused by aborted leader channels developing from the wire tip. The leader channels stop elongating when the electric field intensity above the leader channel is below the level required to sustain the leader’s propagation. *Biagi et al.* [2009] reported observations of two luminous channels at the triggering wire tip that were time-correlated with two wire-base current pulses, confirming that the observed current pulses were associated with aborted leader channels at the wire tip. The aborted leader channels had observed lengths of 1.5 and 8 m at heights of 128 and 158 m above ground level, respectively, and had luminosity similar to that of the sustained upward positive leader. *Biagi et al.* [2009] noted that no luminosity could be detected in association with several other precursor current pulses in the same triggering wire launch, perhaps indicating that lower luminosity processes such as corona or corona streamers produce at least some of the observed current pulses. New observations of luminous channels in association with precursor current pulses are given in Section 6.2.1.

### 2.2.1.2 The sustained upward positive leader

There are few reports in the literature of highly time-resolved optical observations of the development of the sustained upward positive leader in artificially triggered lightning [Rakov and Uman, 2003]. Laroche *et al.* [1988] reported observing in streak photography stepped upward positive leader developing with a mean step length of 14 m, a mean interstep period of 20- $\mu$ s interstep, and a mean speed of  $5 \times 10^5 \text{ m s}^{-1}$ . The upward positive leader discussed in Laroche *et al.* [1998] was only imaged for heights above 1 km. A streak photograph of an upward positive leader in triggered lightning was taken by Dr. Vincent Idone at the Kennedy Space Center in 1988, and is presented in Rakov and Uman [2003, pg. 271]. The streak photograph shows the upward positive leader developing with pronounced stepping, and increasing speed and luminosity with increasing height. The upward positive leader image by Idone apparently switched from a stepped to a continuous propagation mode and back. Luminosity waves evidently began from the leader tip and traveled down the channel. Rakov and Uman [2003] note that for Idone's upward positive leader, the interstep period was about 20  $\mu$ s, the speed was  $1.2 \times 10^5 \text{ m s}^{-1}$  when it was first imaged, and  $6.5 \times 10^5 \text{ m s}^{-1}$  when it exited the field of view. Idone's leader was apparently first imaged when it was about 300 m above the triggering wire, and when the leader was imaged, the wire length was unknown. Horii and Nakano [1995] gave an example of an upward positive leader propagating continuously.

Yoshida *et al.* [2010], using VHF interferometry, give observations of two upward positive leaders in a relatively intense thunderstorm. The VHF sources for the first upward positive leader (in flash UF09-29) moved from an altitude of 1.1 km to 2.4 km and over a horizontal distance of 1.4 km with an average 3-D speed of  $2.2 \times 10^6 \text{ m s}^{-1}$ . The lower few hundred meters of the second upward positive leader was observed in high-speed video. The 2-D speed of the second leader increased in speed, from  $1.2 \times 10^4 \text{ m s}^{-1}$  to  $2.1 \times 10^5 \text{ m s}^{-1}$  for

heights from 123 m to 325 m above ground. The newly-added channel segments for the second leader increased in length and luminosity in successive high-speed video frames, indicating the step lengths were increasing, or that steps were occurring with an increasing rate. The VHF source locations for the second leader (in flash UF09-30) moved from an altitude of 1.5 km to 3.7 km and over a horizontal distance of 2.7 km with an average 3-D speed of  $3.3 \times 10^6 \text{ m s}^{-1}$ . *Yoshida et al.* [2010] argued that the increasing speed with increasing altitude was likely due to the decrease in air pressure and increase in electric field with altitude [*Stolzenburg et al.*, 2002].

The first and second upward positive leaders presented by *Yoshida et al.* [2010] were associated with unusually intense channel-base currents. During the time when VHF sources were located for the first leader, about 620  $\mu\text{s}$ , the channel-base current increased from about 3.3 kA to a peak of 6 kA, with 2 to 4 kA pulses occurring during this rise. During the time when VHF sources were located for the second leader, about 1.3 ms, the channel-base current increased from about 3.1 kA to about 18 kA, with six large current pulses occurring during this rise, the largest having a peak magnitude of 9.7 kA (above the steady current level). The currents during the development of the upward positive leaders in *Yoshida et al.* [2010] were significantly larger than the geometric mean and maximum of the average current reported by *Wang et al.* [1999a] (96 A and 1028 A, respectively) and *Miki et al.* [2005] (99.6 A and 316 A, respectively). Similarly, the largest current pulse peaks reported by *Yoshida et al.* [2010] were significantly larger than the maximum current pulse peaks reported by *Wang et al.* [1999a] (2046 A), *Miki et al.* [2005] (2179 A), and *Rakov et al.* [2003] (up to 5 kA).

The VHF sources associated with the first and second upward positive leader in *Yoshida et al.* [2010] ascended to altitudes of 2.4 km and 3.7 km, which are below the typical freezing level altitude of 4 km, and several kilometers below the altitude, 7 to 8 km, where the main negative

charge of thunderstorms are thought to be located in typical Florida summer thunderstorms [Koshak and Krider, 1989]. Yoshida et al. [2010] argued their results indicated that the storm in which the two flashes were triggered was not a typical convective storm, but more like a mesoscale convective system. The latter are known to have a complex structure, with as many as five stratified charge layers [Stolzenburg et al., 2002].

### **2.2.2 Altitude-Triggered Lightning**

Altitude-triggered lightning has been utilized less often than classical triggered lightning owing to a lower success rate and the lower chance of measuring channel base currents. Altitude-triggered lightning (or simply altitude triggers) involves placing a long metallic wire (essentially the same type of wire used in classical triggering) in the air that is not connected to ground, but instead is isolated electrically. This is typically accomplished by lifting the same type of triggering wire that is used in classical triggering, but with a gap between the bottom end of the upper wire and the top end of the grounded wire. The gap in the conducting wire can be tens to a few hundreds of meters in length. The upper wire can unspool to be several hundred meters in length. The grounded wire is typically a few tens of meters in length, and it increases the probability that the lightning will attach to the instrumented launcher so that channel-base currents can be measured. Altitude triggers sometimes occur when the grounded triggering wire unexpectedly breaks, as was the case for the altitude triggered lightning presented in this work.

Figure 2-4 illustrates the sequence of processes that occur during the initial stage of altitude-triggered lightning. Altitude triggers have an initial stage involving a bi-directional leader. An upward propagating positive leader initiates first from the upward tip of the upper wire. A few milliseconds after the initiation of the upward positive leader, a downward-propagating negative leader initiates from the bottom end of the upper wire. The downward negative leader develops stepwise in a manner that is similar to the stepped leaders that precede

nature first return strokes in CG flashes. As the negative leader approaches ground, an upward connecting leader forms. Once the negative leader and upward connecting leader attach, a return stroke is initiated. When the return stroke begins, the overall channel length is only about 1 km (from the ground to the top of the upward positive leader). Further, the return stroke propagation speed is two to three orders of magnitude faster than the speed of the upward positive leader. Thus, the return stroke catches up with the upward positive leader tip in about 10  $\mu$ s. This results in an intensification of the upward positive leader [Idone, 1992]. At this point, the triggered lightning develops with a similar sequence of steps as classical triggered lightning (as illustrated in Figure 2-3), including the wire explosion, its replacement with a plasma channel, an initial continuous current, and possibly leader/return stroke sequences.

There are many reports in the literature concerning altitude triggered flashes [e.g., Hubert, 1984; Rakov *et al.*, 1998; Saba *et al.*, 2005; Zhang *et al.*, 2009]. The review here will focus on observations pertaining to the downward negative stepped leader that develops in the bi-directional leader phase of the altitude trigger. The characteristics of the stepped leader in altitude triggers have been inferred from electric field waveforms measured near the triggered lightning, and streak photography. Laroche *et al.* [1988] described an altitude trigger in France with a triggering height of 670 m, and 200 m of dielectric thread. From electric field records, they concluded that the upward positive leader began 3 to 4 ms before the downward negative leader began. They reported that the bi-directional leader sequence occurred twice, with the second sequence occurring about 1 s after the first and leading to the full sequence of events described above. They inferred that the interstep time interval of the downward negative leader in both sequences was about 15  $\mu$ s.

*Laroche et al.* [1991] reported observations of an altitude trigger at the Kennedy Space Center, Florida during the summer of 1989. The wire was extended between 450 m and 610 m above ground when the flash began. The upper portion of the downward negative stepped leader was observed with U.V. streak photography developing into two branches with average step lengths of 3 m, and steps occurring every 18 to 19  $\mu\text{s}$ . The estimated initial speeds for the two branches were  $2.5 \times 10^5$  and  $3 \times 10^5 \text{ m s}^{-1}$ , and they both accelerated to speeds of  $3.1 \times 10^5$  and  $3.8 \times 10^5 \text{ m s}^{-1}$ , respectively. *Laroche et al.* [1991] observed, at 200 m from the channel, electric field steps due to the deposition of charge with each leader step, and at 600 m, smaller steps with more significant oscillations. From these observations, *Laroche et al.* [1991] concluded that, for electric field, the effect of the space charge deposition by each step is more important at 200 m, while at 600 m, the transient response of the bi-directional leader and wire is more important. *Laroche et al.* [1991] hypothesized that the reason for shorter negative leader step lengths in altitude triggers versus those in natural lightning results from the discharge being driven by the potential of the wire, and not the cloud charge.

*Lalande et al.* [1998] presented electric field, current, and streak photography observations of an altitude trigger in 1995 at Camp Blanding (the ICLRT). *Lalande et al.* [1998] observed that the downward negative stepped leader paused its development after eight steps for a time interval of about 800  $\mu\text{s}$ , even though the upward positive leader apparently continued to develop. The mean field change for these eight steps was  $15 \text{ V m}^{-1}$  (consistent with 170  $\mu\text{C}$  being deposited at a height of 450 m). When the stepped leader resumed its development, it stepped about once every 18.5  $\mu\text{s}$ , and the mean field variation of the steps was  $23.5 \text{ V m}^{-1}$  (consistent with 270  $\mu\text{C}$  being deposited at a height of 450 m). The streak photography showed that the negative leader step lengths were 3 to 5 m, the mean stepping period was 21  $\mu\text{s}$ , and the

stepped leader propagated with a longitudinal velocity of  $1.3 \times 10^5 \text{ m s}^{-1}$ . Finally, *Lalande et al.* [1998] inferred from electric field observations that the average charge-per-step was  $300 \mu\text{C}$ , and noted that in laboratory sparks, this value of charge is associated with negative leader steps having peak currents of about 600 A.

*Chen et al.* [2003] presented optical images from the A.L.P.S. array and electric field observations of five altitude triggers in Guangzhou, Southern China, during the summer of 1998. They found that the negative stepped leader onset occurs 3 to 8.3 ms after the positive leader onset. The negative stepped leaders apparently paused and resumed their development several times, and had step intervals ranging from 12 to  $30 \mu\text{s}$  that seemed to decrease as the leader developed closer to ground. *Chen et al.* [2003] always observed a few isolated electric field steps prior to the onset of the bi-directional leader, which they attributed to aborted positive leaders from the upper tip of the triggering wire (apparently similar to precursors in classical triggered lightning).

*Lu et al.* [2009] reported high-speed video and electric field observations for an altitude trigger in August of 2005 at Binzhou, Shandong Province, China. The upward positive leader propagated with an estimated 2-D speed of  $3.8$  to  $5.5 \times 10^4 \text{ m s}^{-1}$  from a height of 393 m to 452 m above ground. Three aborted downward negative stepped leaders were imaged over time intervals of about 1 ms. They first occurred about  $952 \mu\text{s}$  after the onset of the upward positive leader. The three aborted leaders propagated 37, 6, and 20 m. The ‘stable’ downward negative leader onset occurred about 4.1 ms after the onset of the upward positive leader, and apparently propagated to the upward connecting leader in 12 steps with an estimated 2-D speed of  $1.9 \times 10^5 \text{ m s}^{-1}$ . The time intervals between steps ranged from 5 to  $30 \mu\text{s}$ , and the mean time interval was  $15 \mu\text{s}$ . The mean step length was estimated to be about 3 m.

### 2.3 Corona Space Charge Layer at Ground

The ambient electric field of thunderstorms causes electrical discharge known as corona from various types of sharp objects located on the ground, often creating a space charge layer near ground. The usually upward-directed electric field due to negative cloud charges is reduced near ground by the presence of the positive corona space charge layer. A space charge layer (of either polarity) prevents the quasi-static (slowly varying over time scales of seconds to minutes) electric field at ground level from exceeding an absolute value of about 5 to 10 kV m<sup>-1</sup>, while the field above the layer can be up to an order of magnitude higher [e.g., *Standler and Winn*, 1979; *Chauzy and Raizonville*, 1982; *Soula and Chauzy*, 1991; *Willett et al.*, 1999]. When a significant space charge layer is present near ground, the relatively large and fast field change from a lightning flash typically causes a polarity reversal at ground but not at altitude, and the field recovery following a large and fast field change occurs more rapidly at ground than aloft [e.g., *Standler and Winn*, 1979; *Chauzy and Soula*, 1987; *Chauzy and Soula*, 1989]. Thus, inferences of, for example, aspects of charge transfer and continuing current from electric field measurements at ground may be compromised by the presence of a space charge layer. Additionally, when attempting to artificially initiate (trigger) lightning using the rocket-and-wire technique [*Rakov and Uman*, 2003], the electric field at ground is used as an often-inadequate proxy for the unknown triggering field at higher altitudes, and the variable field reduction of the space charge layer reduces the triggering efficiency. Although it would often be advantageous to measure the electric field above the space charge layer for the reasons given above, doing so presents logistical difficulties. Nevertheless, several researchers have measured the electric field at various heights, and from these measurements, inferred the vertical profile of the space charge density near ground.

There are many reports of a significant space charge layer existing near the ground below thunderclouds. Thunderstorm electric fields have been found to have higher magnitudes over water, where a lack of sharp objects minimizes space charge production by corona current. *Toland and Vonnegut* [1977] reported a maximum electric field intensity of  $130 \text{ kV m}^{-1}$  over water (a lake). *Chauzy and Soula* [1989] simultaneously measured the electric field on the shore of a lagoon and on a raft that was 100 m away from land, and found that the electric field magnitude over the water was generally higher than over land.

Several researchers have consistently reported measuring higher-magnitude electric fields above ground using field mills carried by balloon or rocket. In experiments at the Kennedy Space Center (KSC) in Florida and Langmuir Laboratory in New Mexico, *Standler and Winn* [1979] raised and lowered a field mill on a balloon between altitudes of 3 and 120 m altitude every few minutes to measure the electric field as a function of height while simultaneously measuring the ground-level electric field. They reported that when the ground level field exceeded  $3 \text{ kV m}^{-1}$  and  $5 \text{ kV m}^{-1}$  at KSC and Langmuir, respectively, the field aloft increased with altitude to a maximum of about  $20 \text{ kV m}^{-1}$ . They inferred a maximum charge density of  $0.8 \text{ nC m}^{-3}$  at a height between 30 and 50 m above ground, above which the charge density decreased. It is worth noting that *Standler and Winn* [1979] also reported measuring corona current flowing from “small evergreen trees” in New Mexico, and that the corona current level rapidly increased when the ground-level electric field exceeded  $5 \text{ kV m}^{-1}$ . The maximum corona current from a tree measured by *Standler and Winn* [1979] was 600 nA in an electric field of  $12 \text{ kV m}^{-1}$ .

In experiments in southwestern France, *Chauzy and Raizonville* [1982] reported five balloon-born electric field soundings with simultaneous ground-level field measurements

underneath thunderclouds. Three of the soundings were done with negative charge overhead and two with positive charge overhead. Their data showed that for both charge polarities overhead, the absolute value of electric field increased with altitude and became approximately constant at a height somewhere between 50 and 200 m above ground at levels between about 20 to 30 kV m<sup>-1</sup>, while at the same time the absolute value of ground-level electric field remained constant and never exceeded about 5 kV m<sup>-1</sup>. They inferred average space charge densities of 2 to 4 nC m<sup>-3</sup> and space-charge layer depths of about 100 to 200 m above ground when negative charge was overhead. When positive charge was overhead, they inferred a higher average space charge density of about -5 nC m<sup>-3</sup> in a more shallow space-charge layer that extended only up to a height of about 50 to 100 m above ground.

In experiments in two different locations in France and in different years, *Chauzy and Soula* [1987], simultaneously measuring the electric field at ground and at a height of 15 m above ground, found that the field aloft was up to 10 kV m<sup>-1</sup> greater than at ground level and an inferred charge density between about 3 and 6 nC m<sup>-3</sup>.

*Soula and Chauzy* [1991] simultaneously measured the electric field at ground and at four heights up to 803 m from an approaching storm at the KSC in Florida, during which there was no significant precipitation and four lightning flashes were triggered using the rocket-and-wire technique. The apparatus they used is described in *Chauzy et al.* [1991]. They found that ions created by corona at ground travel up to at least 600 m. They reported measuring a maximum electric field of 65 kV m<sup>-1</sup> at an altitude of 603 m, while the ground-level field measured simultaneously did not exceed 5 kV m<sup>-1</sup>. Their data indicated that the electric field became constant above 436 m. They inferred average space charge densities between the five electric-field measurement heights that ranged from about 0.2 to 1 nC m<sup>-3</sup>.

*Chauzy and Soula* [1999], using the ‘PICASSO’ model [e.g., *Qie et al.*, 1994] with measurements made in Southern France, at KSC [*Soula and Chauzy*, 1991], and at the Camp Blanding Army National Guard Base, Florida [*Uman et al.*, 1996], examined the time evolution of corona space charge up to a height of 1 km within a 10 km x 10 km area. *Chauzy and Soula* [1999] estimated that tens to a few hundreds of coulombs of corona space charge can be lifted to a height of 1 km via conduction or convection currents over periods of several tens of minutes, and thus the space charge may contribute to the development of the lower positive charge center in thunderclouds.

*Willett et al.* [1999] probed the vertical electric field up to an altitude of about 4 km at Camp Blanding using field mills carried by a rocket that was launched roughly five seconds prior to the launch of a separate wire-extending rocket in 15 attempts to trigger lightning. They presented for two of their flights (flights 6 and 13, their Figures 14 and 18) the electric field versus altitude soundings that showed that the electric field increased with altitude, an observation from which they inferred the presence of a space charge layer. In their flight 6 the ground-level electric field was about  $7 \text{ kV m}^{-1}$ , and it increased with height to about  $15 \text{ kV m}^{-1}$  at a height of about 60 m, above which the field stayed relatively constant. In flight 13 the ground-level electric field was about  $6 \text{ kV m}^{-1}$ , and it increased with height to about  $24 \text{ kV m}^{-1}$  at a height of about 500 m, above which the field stayed relatively constant. In both flights, the increasing electric field was attributed to space charge layers. For flight 13 they inferred an average space charge density of about  $0.3 \text{ nC m}^{-3}$  and noted that the charge density in the lower 60 m was probably three times this value. *Willett et al.* [1999] reported measuring a maximum electric field magnitude of  $38 \text{ kV m}^{-1}$  at altitudes between 3.2 and 3.7 km above ground.

## 2.4 The Stepping Mechanisms of Long Negative Laboratory Discharges and Their Relationship to Lightning

A significant portion of this work is based on observations of lightning leader propagation made with high-speed video cameras and time-correlated current and electric field measurements. Some of these observations show stepping mechanisms in negative polarity lightning leaders that appear similar to the stepping mechanisms of negative leaders in long laboratory sparks (Section 5.2). It is thus helpful to give the reader some background pertaining to long, negative leaders in laboratory sparks. There are relatively few reports in the literature focusing on the negative laboratory spark; most reports (of which there are many) focus exclusively on the simpler positive laboratory spark which requires a lower breakdown voltage and is more commonly encountered in high voltage engineering. However, much of the description of the long, negative leader is an extension of the description for its positive counterpart. For both polarities, the corona streamers and leader channels are similar; the two differ primarily in the extension mechanisms [Bazelyan and Raizer, 1998]. There are several key observational studies of the propagation of long, negative-polarity laboratory sparks in air that have aided in the understanding of the stepping mechanisms exhibited by such sparks [e.g., Gorin *et al.*, 1976; Les Renardières Group, 1981; Ortega *et al.*, 1994; Reess *et al.*, 1995; Bazelyan and Raizer, 1998; Gallimberti *et al.*, 2002]. These reports are reviewed below, with emphasis placed on the stepping mechanism (the space stem, pilot, and space leader)

The discharge begins with corona streamers [Loeb and Meek, 1941; Raether, 1964] that begin when a free electron, which can be produced by one of many processes (e.g., photoionization, radioactive decay, or cosmic rays), appears near the electrode within the volume (called the critical volume by Gallimberti [1979], and the ionization zone by Bazelyan and Raizer [1998]) where the convergent electric field is on the order of  $30 \text{ kV cm}^{-1}$  or more. The

field value at which breakdown occurs, or the inception field, generally depends on the electrode geometry, the gap distance, and the ambient air pressure [e.g., *Peek, 1929; Les Renardieres Group, 1972*]. Similarly, the inception voltage, defined as the voltage at which the first corona streamer burst appears, is somewhat random and depends on the voltage rise time and the electrode geometry [*Bazelyan et al., 1961; Les Renardieres Group, 1981*].

The initial free electron gains more energy from the electric field than it loses through interactions with air, so it accelerates away from the cathode, and generates additional electrons via impact ionization. These new electrons experience a similar acceleration and also generate new electrons, and so on, thereby creating electron avalanche breakdown. There is also electron emission from the cathode which occurs via impact or photo ionization, and a wide range of chemical reactions occur that influence the ion density. Corona streamers consist of thousands of such avalanches and extend to several tens of centimeters in length [e.g., *Les Renardieres Group, 1981; Reess et al., 1995*]. The mean charge injected into gaps by the first corona burst ranges from  $10^{-7}$  to  $10^{-6}$  C [e.g., *Les Renardieres Group, 1981; Ortega et al., 2005*]. The corona streamers push electrons from the vicinity of the electrode, and build up a positive space charge which produces a field reduction [e.g., *Trichel, 1938; Les Renardieres Group, 1981*]. Under the right conditions, the negative corona streamers can form in a pulsed manner (Trichel pulses) with a frequency on the order of tens to a hundred MHz [*Trichel, 1938; Reess et al., 1995*]. More detailed descriptions of the complex physics and chemistry of the corona streamers can be found in the literature [e.g., *Gallimberti, 1979; Les Renardieres Group, 1981; Wang and Kunhardt, 1990; Alexandrov and Bazelyan, 1996; Marrow and Lowke, 1997; Alexandrov and Bazelyan, 1999; Nudnova and Starikovskii, 2008; Winands et al., 2008; Nguyen et al., 2010*].

As long as the applied voltage is sufficiently high (the level depends on the gap geometry and air thermodynamics), the corona streamers will continue, causing the gas temperature to increase as a result of the Joule heating from the corona current. The next step in the formation of the leader is the development of one or more ‘stems’ (sometimes called space stems if they form unattached to an electrode). The physics of the space stem is not well-understood. *Reess et al.* [1995] performed an observational study of space stem formation in discharges in a 1.3 m point-to-plane gap, which is summarized in the following text. *Reess et al.* [1995] observed that the first space stems form in the vicinity of the cathode (where negative corona streamers previously formed) with the inception of retrograde positive streamers from luminous spots (spots that apparently have an excess of positive ions), and that the luminous spots often correspond to the branch points of the negative corona streamers. The retrograde positive streamers contact the cathode and bring forward the cathode’s potential, and supply the stem with electrons, allowing the formation of new negative streamers extending further into the gap. *Reess et al.* [1995] determined that about 300 nC of charge must be transferred to the stem before negative streamers can develop. Retrograde positive streamers grow from new space stems at branching points in the new negative streamers and travel back to the cathode (and through the previous space stem and positive streamers), in effect ‘moving’ the space stem further into the gap. This sequence occurs every few hundred nanoseconds [e.g., *Gorin et al.*, 1976; *Reess et al.*, 1995]. The space stem and its associated positive and negative streamers is sometimes called a ‘pilot’ [*Bacchiega et al.*, 1994]. *Les Renardieres Group* [1981], *Ortega et al.* [1994], and *Reess et al.* [1995] all report a similar ‘equivalent velocity’ for the space stem motion of  $1 \times 10^6 \text{ m s}^{-1}$ .

The corona streamer currents converge on the stem region (estimated to have a volume of about  $1 \text{ cm}^3$  by *Gorin et al.* [1976]) and increase the local thermal energy, producing significant

effects, including: (1) a temperature increase of the gas and plasma by Joule heating from about 300 K to 1500 K, (2) a hydrodynamic expansion and reduction in gas density, (3) an increase in the electron detachment of the negative ions due to the increase in temperature and reduced electric field, (4) a sharp increase the conductivity of the stem, and (5) an increase in the electric field at the stem tips. If the temperature in a stem reaches a critical temperature of about 1500 K, negative ions abruptly release their captured electrons. This causes a large and abrupt increase in the plasma conductivity, and the formation of a space leader.

The space leader appears as a thin luminous channel connecting corona regions to the high-voltage electrode. The leader cross-sectional area increases in time, and the longitudinal current is confined to a diameter between 0.5 mm and a 4 mm (the current diameter increases in time under by hydrodynamic expansion). *Ortega et al.* [1994], studying negative discharges in a 16.7-m gap, observed that the space stem became a space leader when it was typically between 1.4 to 2.2 m in front of the cathode or primary leader channel. It can be concluded that the space leader mechanism will not occur in gaps shorter than 1.4 m. The number of steps in *Ortega et al.*'s 16.7-m gap ranged from 4 to 7, which is higher than the number steps than was observed in 5 and 7 m gaps by *Les Renardières Group* [1981]. *Ortega et al.* [1994] reported estimates of the elongation speeds for the primary and space leader, and the propagation speed of the space stem, when the overall leader was less than 5 m in length. The speeds were apparently estimated from still photographs obtained with an image converter camera, but the rate at which the photographs were obtained is not stated. The primary leader elongated with an estimated mean speed in the range of  $1.3$  to  $2.8 \times 10^4$  m s<sup>-1</sup>. The estimated mean elongation speed was between  $3.2$  and  $4.9 \times 10^4$  m s<sup>-1</sup> for the cathode-directed end of the space leader (upper, positively charged end). The anode-directed end (bottom, negatively charged end) elongated with a slower mean speed

between  $1.2$  and  $2.9 \times 10^4 \text{ m s}^{-1}$ . When the positive end of the space leader merges with the cathode a wave carrying the higher cathode potential travels to the negative end of the space leader (forming a “step”), where it creates a relatively large corona streamer burst that contributes to production (heating and charging) of the following step.

*Ortega et al.* [1994] observed, with a shunt in the high-voltage electrode, that a current pulse with a peak current ranging from 100 to 600 A was associated with each leader step, although they noted that the peak current may have been restricted by the external circuit. The values of peak current did not appear to be related to the step number. A step formed by a single space leader will produce a narrow, unipolar current pulse. A step formed by two or more space leaders will produce a multi-peaked, unipolar pulse with a considerably longer width. In Figure 9 of *Ortega et al.* [1994], it appears that there is a current peak for each space leader that contributes to a step, although they did not explicitly state this. Between 200 and 400  $\mu\text{C}$  flowed from the high voltage electrode with each step, but it is not clear what fraction of the charge contributes to the new step (some may develop and be swept away by the high-electric fields in the gap). The charge per unit length for the first four steps was determined to range from 100 to 130  $\mu\text{C m}^{-1}$ .

*Ortega et al.* [1994] extended the work of *Les Renardières Group* [1981] in relating the potential of the space stem just before space leader inception,  $U_{SS}$ , to the voltage at the leader inception from the high voltage electrode,  $U_1$ . The value of  $U_{SS}$  was calculated using the following relation:

$$U_{SS} = U_p - E_{L-}L_- - E_{S+}L_{S+} \quad 2-1$$

where  $U_p$  is the peak high voltage electrode potential,  $L_-$  is the length of the negative (primary) leader,  $L_{S+}$  is the length of the positive corona streamers connecting the space stem to the

negative leader,  $E_{L-}$  is the electric field in the negative (primary) leader (determined from the graph in Figure 6.5.2 in *Les Renardières Group* [1981]), and  $E_{S+}$  is the electric field of the positive corona streamers (assumed to be  $500 \text{ kV m}^{-1}$ ). The values of  $U_1$  (the cathode potential at leader inception time) and  $U_{SS}$  increase with increasing distance between the high-voltage electrode or space stem and the ground plane (anode),  $D_{SS}$ , according to the following relation.

$$U_{SS} = 0.8(D_{SS} - 1.5)^{0.45} \quad 2-2$$

The similarity between  $U_1$  and  $U_{SS}$  is an indication that the leader inception from the high voltage electrode is preceded by the formation of a stem, as *Bacchiega et al.* [1994] observed. Equation 2-2 is probably only valid for gaps larger than 2 m, since the space leader apparently cannot form in much smaller gaps [*Ortega et al.*, 1994].

With knowledge of the space stem and space leader in hand, it is possible to describe schematically the spatial and temporal development of the long negative laboratory leader after the leader has started from the cathode, and before the final jump, as is done in Figure 2-5. The diagram in panel A of Figure 2-5 illustrates the “streamer zone” of a negative laboratory leader several microseconds after initiation from the high-voltage electrode, as first described by *Gorin et al.* [1976]: (1) primary leader channel that grows from the negative high-voltage electrode, (2) leader tip, (3) positive streamers (filamentary channels of low conductivity), (4) space stem, and (5) negative streamers emanating from the space stem. The streamer zone extends from the primary leader channel intermittently [e.g., *Reess et al.*, 1995]. Panel B of Figure 2-5 depicts negative leader development in time from left to right, as interpreted via streak photography, with electrode current shown below (Figure 2-5C). The negative electrode is at the top, and the leader develops downward toward a grounded plane. Numbers 1 through 5 correspond to the descriptions for Figure 2-5A. The primary leader tip extends quasi-continuously down curve 2

in Figure 2-5B, with the space stem moving along the negatively sloped dashed line labeled 4. The space stem eventually thermalizes and becomes a space leader (6) that develops bi-directionally. When the positive end (top) of the space leader merges with the negative leader tip (at 7), the higher potential of the leader channel is transferred to the negative end of the space leader (bottom), followed by a burst of negative corona (mobile, diffuse space charge) or corona streamers (filamentary channels) (8). At this point, current and luminosity waves travel up the leader channel, completing the leader step. The spark propagation continues in the corona created at 8 with the development of a new space stem that initiates the next leader step. Current pulses in the grounded electrode are associated with each step, shown in panel C of Figure 2-5.

In the long negative laboratory discharge, the negative leader connects to the ground plane (anode) via an upward positive connecting leader in the so-called final jump phase. According to *Les Renardieres Group* [1981], there are three different final jump mechanisms. In type A, the negative corona streamers reach the ground plane during the propagation of the space stem. The space step accelerates toward the anode, and upon reaching it, an upward positive connecting leader develops upward from the ground plane and connects to the established leader channel. In type B, after the downward negative corona streamers are in contact with the anode, a space leader develops between the primary downward negative leader and the upward positive connecting leader. In type B, the presence of the space leader alters the characteristics of the upward positive connecting leader. Finally, in type C, which is similar to type A, the burst of negative corona streamers following the connection of a space leader to the primary negative leader channel reaches the anode. An upward positive connecting leader develops toward the negative leader without the presence of a space stem (as was the case for type A). *Les Renardieres Group* [1981] observed, for negative discharges in a 7-m gap, that the upward

positive leader ranged between 0.7 to 3 m, or 10 to 45% of the gap distance. Based on the presence of channel loops, *Ortega et al.* [1994] inferred that the length of the upward positive connecting leaders were about 4 m, or about 24% of the gap length (16.7 m). *Les Renardieres Group* [1981] examine the variability in the upward positive connecting leader with gap distance, impulse shape, and overvoltage level.

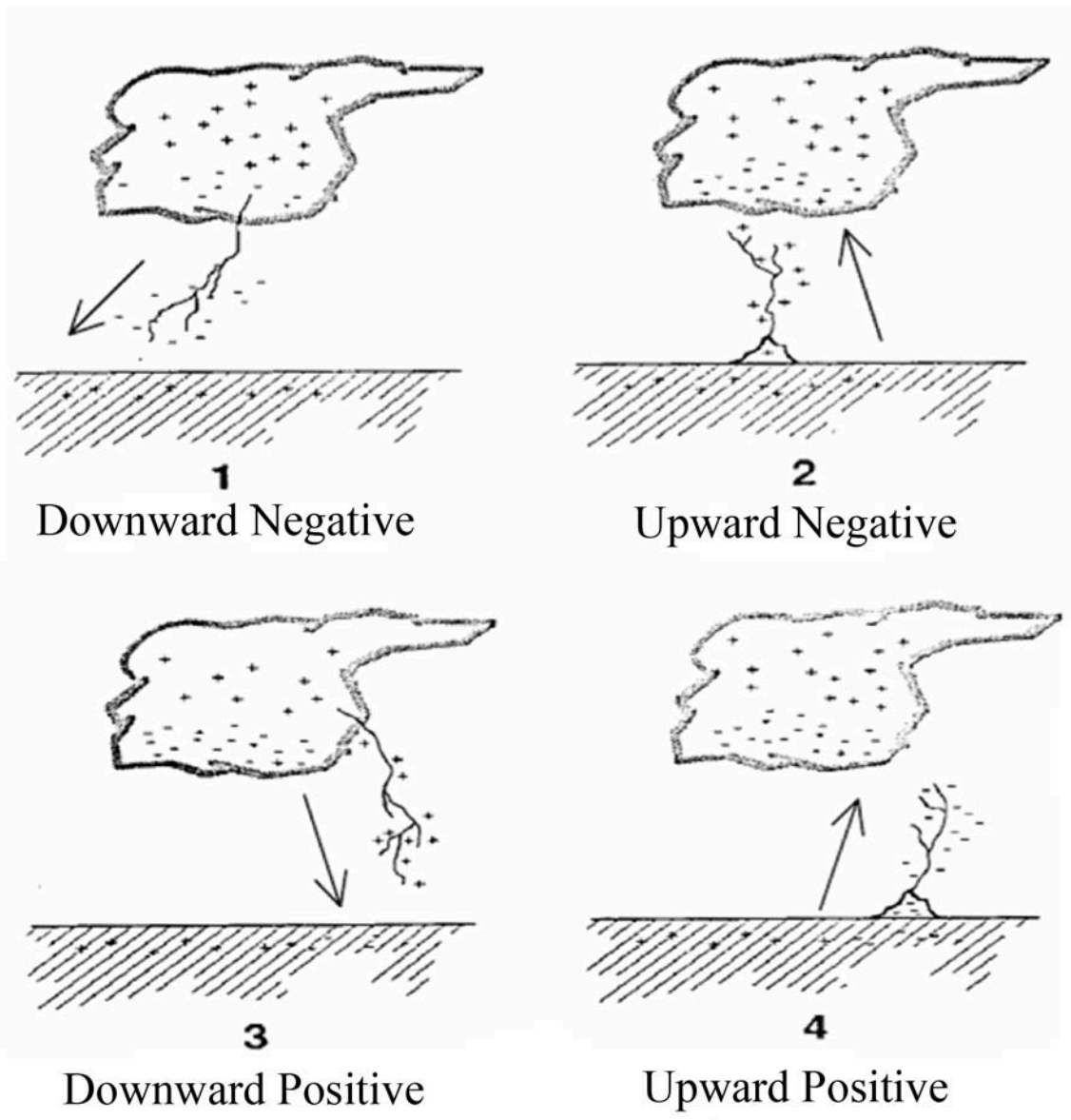


Figure 2-1. The four types of cloud to ground lightning, defined by the charge transfer to ground and direction of the leader. Adapted from *Rakov and Uman* [2003].

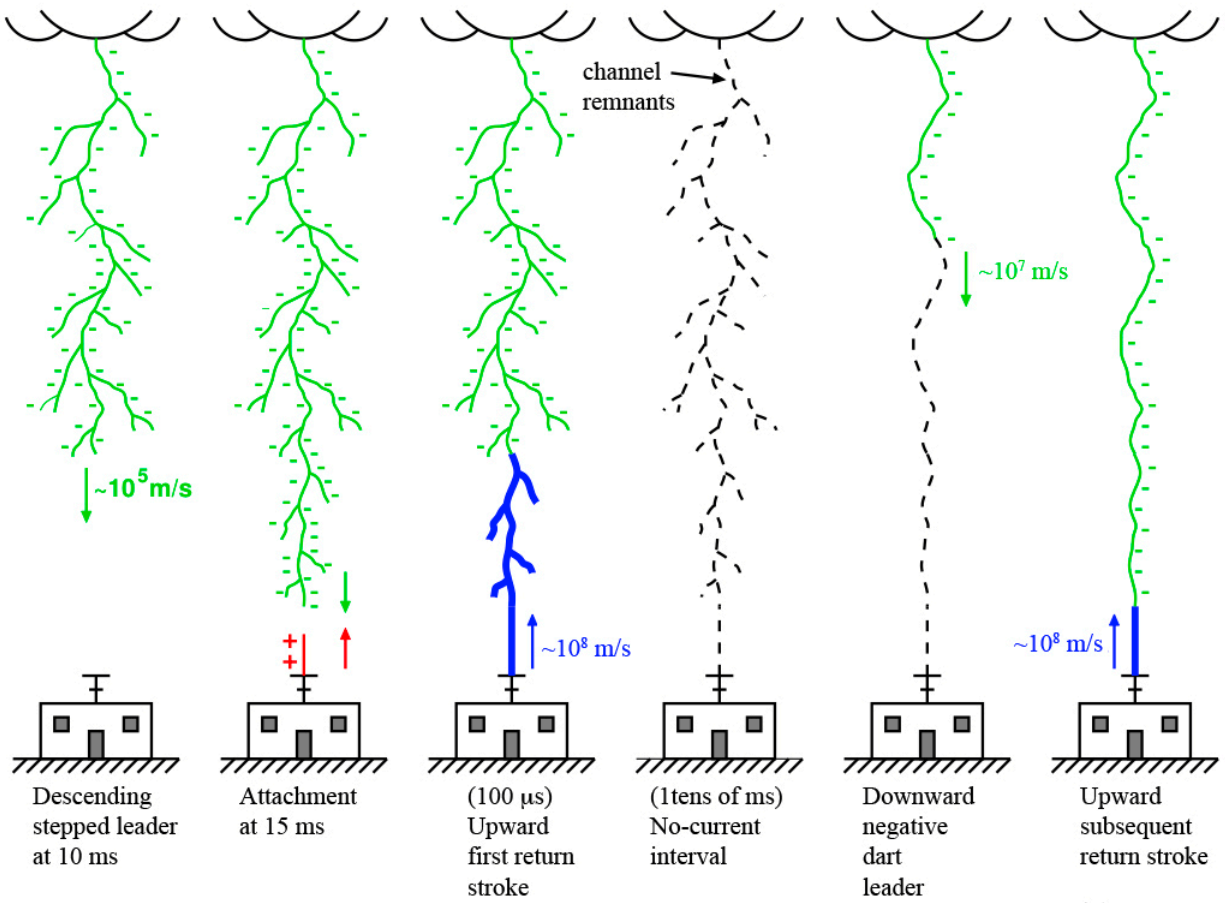


Figure 2-2. The sequence of events in a natural, downward negative cloud-to-ground lightning flash. Adapted from *Jerauld* [2007].

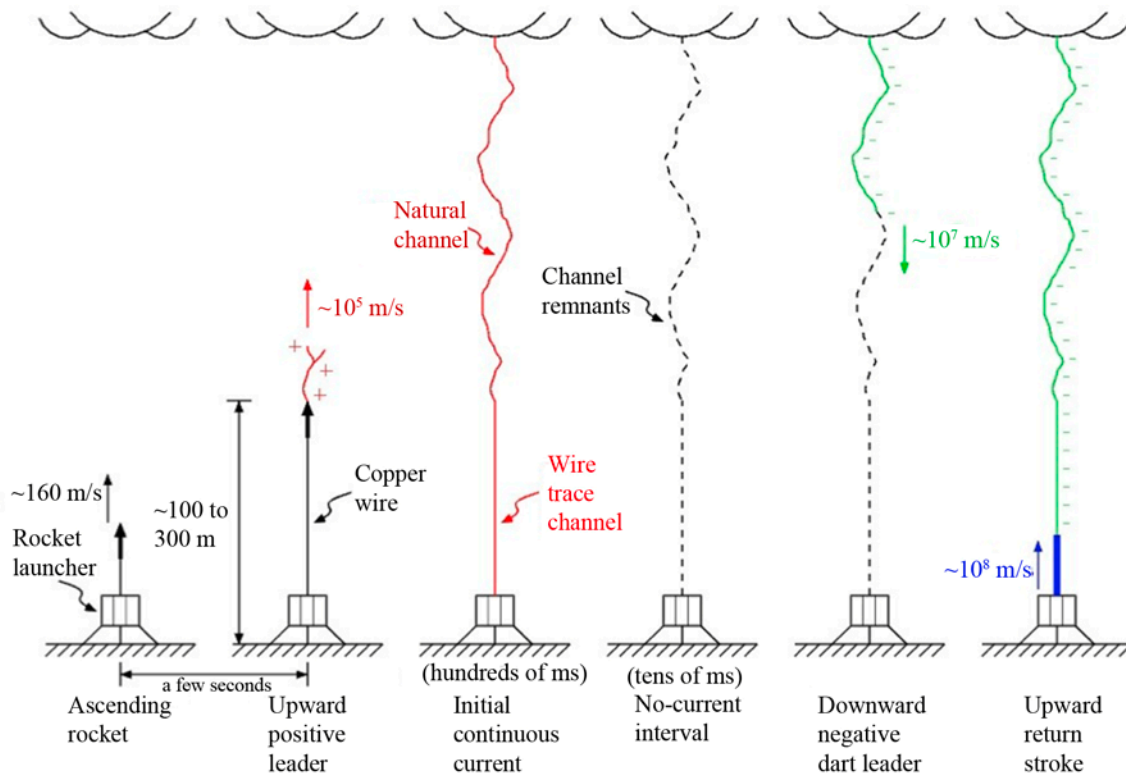


Figure 2-3. The sequence of events in a classical triggered lightning. Adapted from Rakov *et al.* [1998].

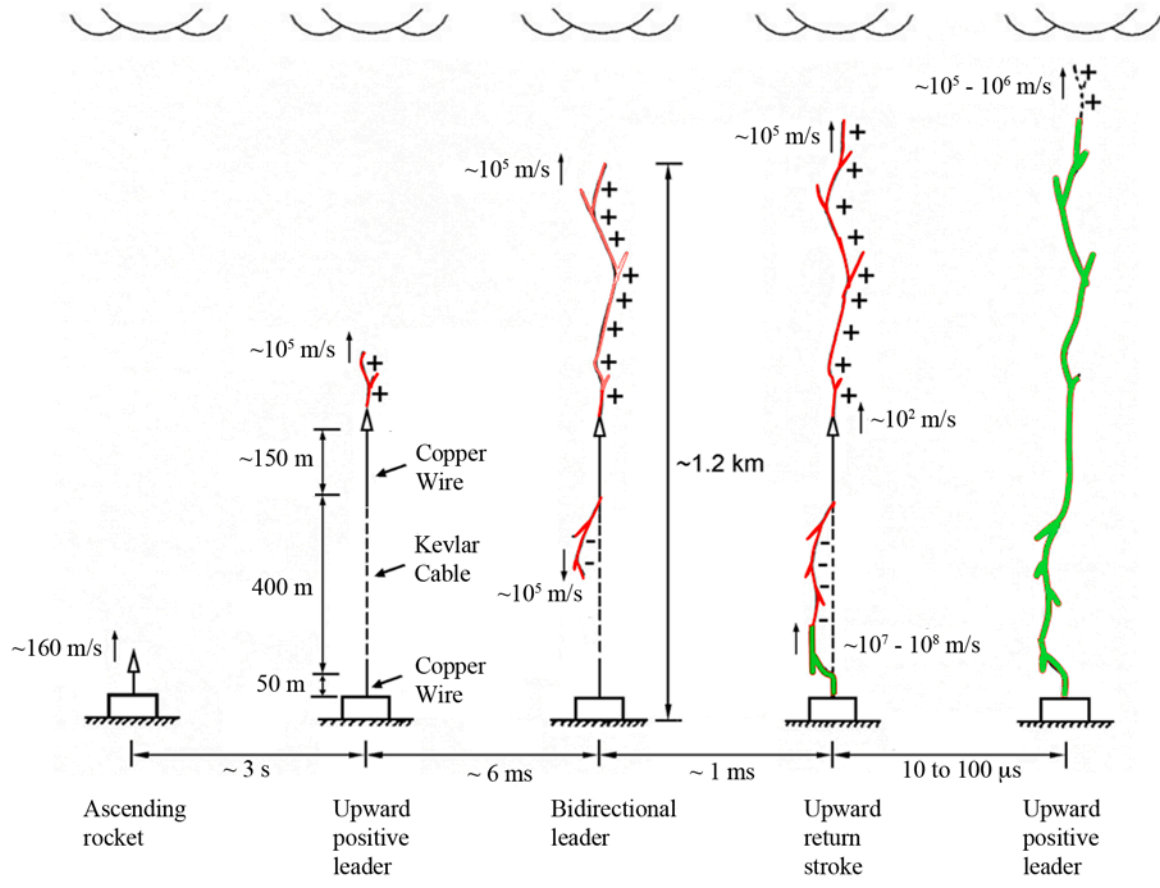


Figure 2-4. Sequence of events in altitude triggered lightning. Adapted from *Rakov et al.* [1998].

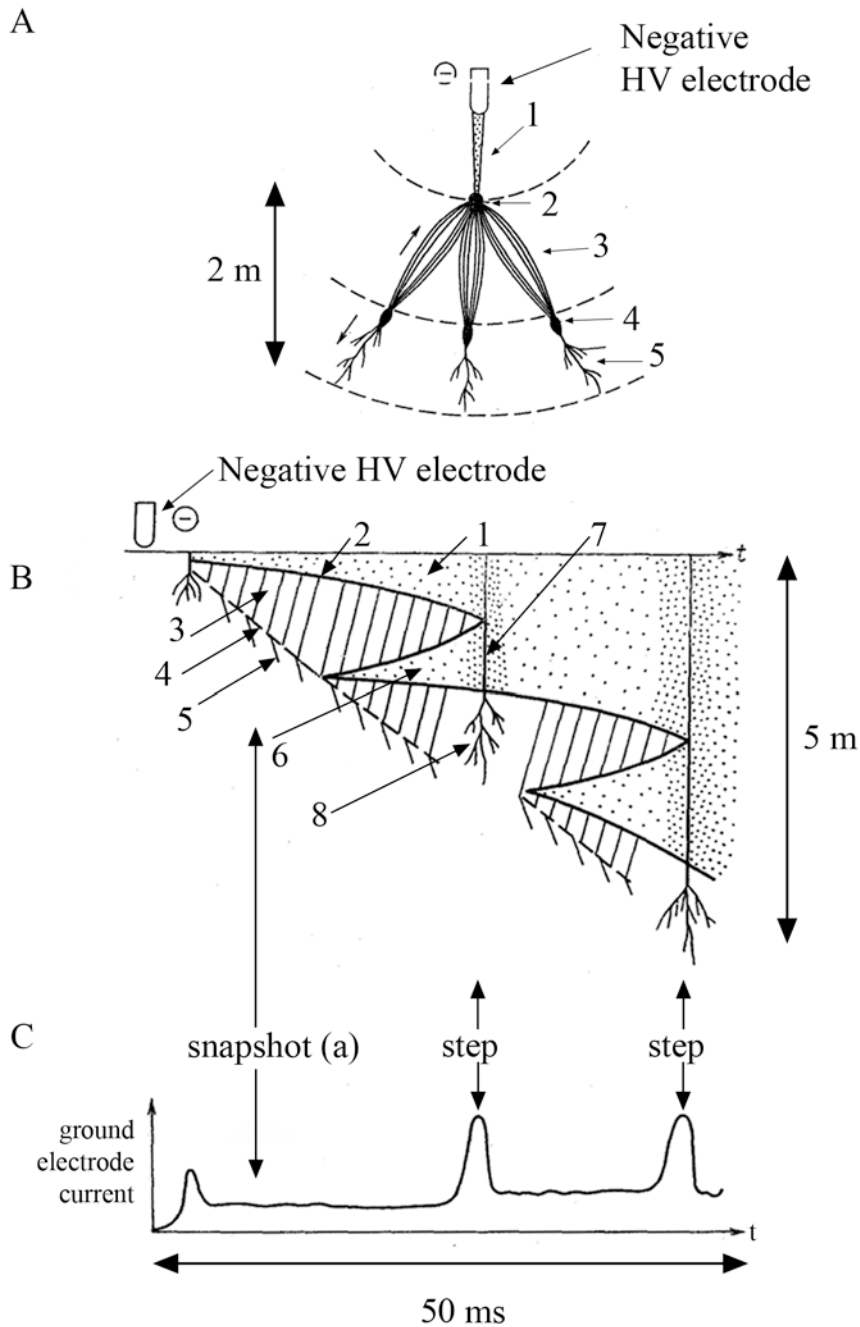


Figure 2-5. Schematics illustrating the stepped development of the negative leader. (A) Diagram (snapshot) showing the streamer zone structure ahead of a negative leader tip, (B) space-time diagram of negative leader development with time increasing from left to right over  $50 \mu\text{s}$ , (C) the corresponding current in the ground electrode . Diagrams are adapted from *Gorin et al.* [1976].

## CHAPTER 3 EXPERIMENT DESCRIPTION

The data and observations described herein were recorded at the International Center for Lightning Research and Testing (ICLRT), a facility that is located at the Camp Blanding National Guard base, about 5 miles east of Starke, FL. This work presents research on triggered lightning experiments performed at the International Center for Lightning Research and Testing (ICLRT). Beginning in 1993, many triggered lightning experiments have been performed at the ICLRT by many talented researchers from all around the world that have greatly advanced the understanding of lightning physics. The ICLRT facility is a state-of-the-art research facility which provides the means to study both natural and rocket-triggered lightning at ranges of a few meters to hundreds of meters including: measuring electric and magnetic fields [e.g., *Rakov et al.*, 2005; *Jerauld et al.*, 2008; *Howard et al.*, 2011], optical radiation [e.g., *Wang et al.*, 1999a; *Olsen et al.*, 2004; *Olsen et al.*, 2006; *Biagi et al.*, 2009; *Biagi et al.*, 2010; *Hill et al.*, 2011], high-energy radiation (x-rays) [e.g., *Dwyer et al.*, 2005; *Saleh et al.*, 2009; *Howard et al.*, 2008; *Howard et al.*, 2010], source-locations by VHF interferometry [e.g., *Yoshida et al.*, 2010], high-speed spectroscopy [e.g., *Walker et al.*, 2009; *Walker et al.*, 2010], for the case of rocket-triggered lightning, channel-base currents [e.g., *Wang et al.*, 1999b; *Rakov et al.*, 2003; *Schoene et al.*, 2009; *Schoene et al.*, 2010], and the effects of lightning currents in electrical power distribution lines [e.g., *Mata et al.*, 2000] and residential buildings [e.g., *Rakov et al.*, 2002; *Decarlo et al.*, 2008]. The research presented in this work was performed at the ICLRT during 2008 and 2009. During these two years, several new major experiments took place, requiring changes and additions to the existing instrumentation. Some of the key changes are briefly summarized below.

Before 2008, six identically configured electric field sensors were operated in order to measure field changes that are produced by return strokes with strike points occurring ‘on-site’; that is, within the confines of the physical area of the ICLRT facility at Camp Blanding. In 2008, the network of electric field sensors was altered for the Positive Lightning Experiment (PLE). The goal of the PLE was to measure the electric fields produced by positive cloud-to-ground (CG) lightning occurring at ranges from on-site to about 40 km. At these ranges, the positive CG processes of interest, namely the descending positive leader, return stroke, continuing current, and the overall charge transfer produce electric field changes with amplitudes varying up to five orders of magnitude, and time scales varying by up to seven orders of magnitude. Hence, multiple electric field sensors with different sensitivities and relaxation times were needed to measure properly the full range of possible values. The number of electric field sensors was increased from 6 to 10 in 2008. The sensitivities and relaxation times of the six existing sensors were changed, and the four new electric field sensors had higher sensitivities and longer relaxation times.

A new network of digital storage oscilloscopes (DSOs) was constructed for the PLE so that data from off-site positive CG lightning could be acquired without preventing the acquisition of data from on-site lightning by the Multiple-Station Network (MSE). The PLE DSO network had its own LabView control interface facilitating quick and easy operation of the common DSO functions (e.g., setting the trigger mode, loading setup panels, and saving data). During attempts to trigger lightning, the configuration of the PLE DSO network was changed to acquire long records, up to 5 s in duration, of channel-base currents, electric and magnetic fields, and a few x-ray measurements. The PLE DSO network recorded data for nearly all rocket launches, regardless of whether or not lightning was triggered (in the cases when lightning was not

triggered, transient currents in the triggering wire were still of interest). The PLE DSO network functioned as a backup data acquisition system for the rare instances when the MSE DSO network malfunctioned.

In addition to changing the electric field sensor configurations, the current sensor configurations were also altered in 2008, primarily for the ball lightning experiment [Hill *et al.*, 2010]. In the ball-lightning experiment, triggered lightning currents were made to flow through various materials with the goal of producing ball lightning. For this experiment, George Schnetzer and Mike Stapleton constructed a current intercepting wire system, which consisted of a rectangular wire located several meters over the top of the launch tower that was electrically connected to its own ground lead and ground rod located on a pole about 8 m to the west of the launch tower. The intercepting wire apparatus intercepted leader/return stroke sequences and provided them with a current path to ground that was physically and electrically separated from the initial stage current path to ground (which is guided past the intercepting wire by the triggering wire). Figure 3-1 shows an image of the launch tower with the current-interceptor installed. The intercepting ring may have encouraged the formation of upward positive connecting leaders, observations of which are analyzed below. The intercepting wire was removed on 21-October-2008, and was not used in 2009.

Digital high-speed video cameras were first used to observe triggered lightning at the ICLRT in 2008. A Phantom V7.0 high-speed video camera, located in the launch trailer, recorded 500 fps (frames-per-second) video of the ball lightning samples that were located on the launch tower (about 50 m away) as they were struck by lightning. The framing rate of the Phantom V7.0 was too slow to resolve any processes associated with lightning, although the camera provided evidence of ball lightning forming above steel plates [Hill *et al.*, 2010]. A

Phantom V7.3 and a Photron SA1.1 were operated from the office trailer (about 440 m from the tower), and they provided video of the lower several hundred meters of lightning channel at framing rates up to 20 kfps (kilo-frames-per-second), although they were generally operated at much slower framing rates, around 5 kfps. The V7.3 and SA1.1 yielded original lightning observations of upward and downward leaders and the attachment process [e.g., *Biagi et al.*, 2009]. In 2009, the high-speed video cameras were optimally configured, as discussed in Section 3.8, and recorded video of lightning at framing rates up to 300 kfps [e.g., *Biagi et al.*, 2010; *Hill et al.*, 2011].

The Multiple Station Experiment (MSE) operated throughout 2008 and 2009. Station 25 was added to the network in 2009. Station 25, located a few meters south of the launch trailer, had a  $dE/dt$  sensor and two new lanthanum bromide ( $\text{LaBr}_3$ ) x-ray sensors which could resolve x-rays occurring as often as tens of nanoseconds. In addition, 8 new plastic x-ray/muon detectors replaced the unshielded sodium iodide measurements at the 8 TOA stations. The MSE recorded data nominally from six of the ten electric field measurements, 47 x-ray sensors (including 8 plastic, 2  $\text{LaBr}_3$ , and 37 Sodium Iodide), two optical sensors, two magnetic field sensors at a single location in the cross-loop configuration, and up to six current measurements. A lengthy description of the MSE will be avoided here since only one  $dE/dt$  measurement and one x-ray measurement recorded by the MSE are presented in this work. However, a detailed description of the MSE can be found in the Ph. D. dissertations of Dr. Jason Jerauld and Dr. Joseph Howard [*Jerauld*, 2007; *Howard*, 2009].

### **3.1 Experiment Control**

The experiment at the ICLRT includes many field-deployed measurements located at various stations around the facility. The physical layout of the experiment stations and buildings are identified in the map presented in Figure 3-2. Table 3-1 gives the location of the sensors at

the various stations. Each station is numbered, and measurements at a given station share the station's number (e.g. E2 is the electric field sensor at Station 2). Each measurement is controlled by a device called a PIC controller (because it uses a PIC brand microprocessor) which communicates with a central control computer in the launch trailer via fiber optics. Analog data are also transmitted via fiber optic cables from the sensors to the launch trailer, where they are digitized using digital storage oscilloscopes.

### **3.1.1 PICs**

Field measurements are controlled by PIC controllers (hereafter called simply PIC) that are in communication with a central control computer in launch control (HAL) through fiber-optic link or RF link. The PICs provide the ability to (1) switch power to itself and other enclosed electronics, (2) apply attenuation to the sensor output before being input to the data transmission fiber-optic link, (3) probe the battery voltage and enclosure temperature, and (4) supply a calibration signal for the data fiber-optic links. The PICs are powered by 12-V batteries. The PIC input and output impedances are each 50  $\Omega$ . The data signal (coming from an antenna or electronics following an antenna) is fed through the PIC via BNC connectors, which can apply one or more of the following attenuations: -3, -6, -10, -14, and -20 dB. The PIC signal output is fed into a fiber-optic transmitter dedicated to transmitting the data stream to a fiber-optic receiver in the launch trailer. The PIC can block the signal from the sensor and output a calibration wave; either a  $1\text{-}V_{pp}$  or  $0.1\text{-}V_{pp}$  amplitude square wave with a frequency of 100 Hz. The calibration wave is used to determine the gain of the fiber-optic link.

For the experiments of 2008 and 2009, the 2001 and 2006 PIC models were used, and they are pictured in Figure 3-3 and Figure 3-4, respectively. The 2001 PIC and 2006 PIC connectivity is shown in schematically in Figures 3-5 and 3-6, respectively. Both provide power switching, attenuation, and calibration functionality described above. The 2006 PICs communicated with

the control computer via a single 62.5/125  $\mu\text{m}$  (core/cladding) glass fiber (called a control fiber to distinguish it from data fibers) for both received and transmitted commands, and could support two measurements (two separate data channels that could be configured differently with two correspondingly separate 12-V power output ports). The 2001 PIC only supports one data channel and one power output. To communicate with the control computer, the 2001 PICs were connected via two 1-mm diameter plastic fibers (one for receive and one for transmit) to either a 900 MHz radio frequency (RF) transceiver, or as a slave PIC to a 2006 PIC. The RF transceiver, also called an RF PIC, was powered by its own 12-V battery connected to a 10-W, voltage regulated solar panel recharging system. By 2008, the master-slave functionality of the 2006 PIC had eliminated the need for the RF PICs at nearly all stations. By 2009, only the still-photograph cameras were controlled through RF PICs, except for the occasional circumstance when a 2006 PIC would fail and need to be temporarily replaced by an RF PIC.

Each glass control fiber was connected to one of two 24-port fan-out boards in the launch trailer, which itself was connected to the control computer via RS-232. The control computer was also connected via RS-232 to a 900 MHz RF transceiver for communication with the RF PICs. Each PIC channel was assigned a 2-digit hex address for identification. PIC commands from the control computer were preceded by the appropriate hex address and sent to all PICs, but only the PIC configured with the matching address would respond. Similarly, a PIC's transmissions were preceded with its hex address to distinguish their communications from other PICs.

### **3.1.2 Fiber-Optic Links**

The Opticomm MMV-120C fiber-optic links utilize frequency modulation with a 70 MHz carrier frequency, and operate at a wavelength of 1310 nm. The links were originally designed for transmitting video signals, but the manufacturer agreed to make two modifications to better

suit them to lightning experimentation. First, the output and input resistances were modified from  $75\ \Omega$ , the industry standard for video links, to  $68\ \text{k}\Omega$ , the highest resistance that could be attained without compromising the functionality of the links. Second, the low-frequency cutoff was modified from 5 Hz to DC, giving the links a nominal bandwidth of DC to 30 MHz. The nominal output range is  $\pm 1\ \text{V}$ , and the links saturate at about  $\pm 1.2\ \text{V}$ . The links are specified as having a signal-to-noise ratio as about 67 dB, a value determined using the short-haul RS-250C standard in which the signal is low-pass filtered with a cut-off frequency of about 5 MHz. In practice, the true signal-to-noise ratio is a few dB lower, and it depends on the fiber length.

The Opticomm transmitters are powered by 12-V batteries (controlled by the PIC). The electrical signal is input via coaxial cable to a BNC port. The fiber output port is ST type. The Opticomm receivers in the launch trailer were placed in a rack-mounted power supply in groups of 16. Like the transmitter, the fiber port on the receiver is an ST type. The electric signal from each receiver is output from a BNC port to coaxial cable that is fed to one port of a BNC feed-through panel (with 32 ports, 2 rows of 16 columns) on the front of the rack, making it easily accessible inside the launch trailer.

The Opticomm links were connected with  $62.5/125\ \mu\text{m}$  (core/cladding) graded index multi-mode glass fibers with a nominal index of refraction of 1.483. Each fiber was covered, from cladding outward, by successive layers of plastic, Kevlar reinforcement, and additional plastic. Fibers were bundled in 6 or 8 strands on double-armored cables with a fiberglass strength member at the center. Typically, one fiber bundle ran to each station, with one fiber being used as a PIC control fiber.

The fiber-optic links gains can be tuned by two internal potentiometers (one for broad adjustments and one for fine adjustments). Thus, the link gain (which is ideally 1, or 0 dB) is

somewhat sensitive to temperature fluctuations, and the gains for different links are variable. It is important to know the link gains for measurements with absolute calibrations. Thus, prior to and following data acquisition sessions, each link was calibrated using the 100 Hz, 1-V<sub>pp</sub> square-wave calibration signal generated by the PIC.

### 3.1.3 Control Computers

The primary control computer, often referred to as HAL, was located in the launch trailer. HAL continuously operated LabView virtual instrument (VI) software that controlled nearly every instrument on site, as well as the digitizing scopes in the Multiple-Station Experiment (MSE). HAL displayed (and optionally recorded) the quasi-static electric field sensed by the NASA field mill. The main VI running on HAL is used to ‘arm the network’, which generally consisted of several steps, including: turning on the field instruments and MSE DSO (but not the PLE DSO, which ran separately from the MSE DSO) to calibration settings, instructing the DSO to record calibration shots for each instrument, and then putting the PICs and DSO into data acquisition mode, (a mode in which the DSA save data if lightning strikes on-site). HAL also ‘disarms the network’; that is, executes the above-stated steps in reverse order. The instruments and instructions for the PICs and DSO that HAL commanded were specified by a user in look-up tables, thus allowing for quick and easy arming for different experimental conditions. For example, when collecting data from off-site positive lightning in times when no on-site lightning is expected, HAL could turn on only the measurements connected to the PLE DSO, and not arm the MSE DSO.

Typically, the decision to arm/disarm the network was made by a human user. Alternatively, a user could enable HAL to arm/disarm the network automatically based on the quasi-static electric field, sensed by the NASA field mill. Generally, HAL automatically armed the network when the electric field exceeded a level of  $\pm 2 \text{ kV m}^{-1}$ , and disarmed the network

when the field remained below this level for 10 min. The automation provided by HAL allowed for the acquisition of data, at least from natural on-site lightning, without personnel manning the site. A secondary VI was used to monitor the PICs and their associated measurements, and perform troubleshooting and diagnostics. HAL's VIs were originally written by PhD student Rob Olsen III, although helpful modifications were made by PhD student Jonathon Hill to add flexibility to the arming/disarming criteria, and to provide a signal that could be used to trigger the DSO in the PLE experiment upon firing a rocket.

Since the PLE DSOs had a functionality that was different from the MSE DSO, they had their own control computer. The author-created VIs on the PLE control computer only controlled the DSO. The VIs allowed a user to quickly set the internal times (the Yokogawa scope times drifted a second every few minutes), save or discard data (after examination by the user), change the trigger state (auto, normal, single, off), and change data acquisition modes (for positive lightning or for triggered lightning). These configurations could be changed on individual DSOs, or all DSOs together. In addition, a user could use the PLE control computer to change the DSOs 'panels', or pre-determined configurations. Using panels to change the DSO configuration was useful when switching operational modes that would otherwise have required many DSO settings to be changed by hand. By using panels, a user could change multiple settings with one mouse click on the control computer, which is faster and less mistake prone than changing individual settings by hand on the external DSO interface.

#### **3.1.4 Rocket Launching Apparatus**

Figure 3-7 presents a close up view of the launch-tube apparatus, and Figure 3-8 presents a view of the bottom of a launch tube with rockets loaded and ready to launch. There are a total of twelve launch tubes, although typically only five were loaded. The Kevlar-coated, 0.2-mm diameter copper triggering wire was unspooled from the bottom of the rockets. Since classical

triggering was the desired outcome, the wires were electrically bonded to the launch tubes and grounding system (although in one instance a wire broke and led to an altitude trigger). The rocket's initial acceleration was high, so the wire was initially un-coiled by bungie that provided strain relief to prevent the wire from breaking. The rockets were 1-m long and 2-inch diameter fiberglass tubes with plastic stabilization fins and nose cone. A parachute was stored in the rocket body and was ejected a few seconds after launch to safely lower the rocket to ground. The rocket motors were ignited by a 9-V battery shorted across a squib wire placed inside the motor. The connection of the squib wire to the battery, and thus the rocket firing, was controlled by pneumatic relays that were pressurized via air tube feeding from a compressor in the NASA trailer. A battery-powered microcontroller was located on the launch tubes that opened the desired pneumatic relay upon receiving a command via fiber optic cable from the rocket launcher in the launch trailer. Thus, the rocket firing system was controlled solely by light and pressure signals, allowing the launch tower to be kept electrically isolated from the launch trailer for the safety of the personnel and electronics contained within, and discouraging the accidental launching of rockets by electrical pickup from nearby lightning.

There were several factors to consider when deciding to attempt triggering lightning. The electric field at ground should be high, indicating that there is sufficient cloud charge overhead. At the ICLRT, ground-level electric field values between 4 and 9 kV m<sup>-1</sup> (positive field pointing from ground to the cloud, indicating negative charge overhead) were considered to be indicative of sufficient over-head cloud charge, although the space charge layer near ground can make the ground-level field reading misleading (Section 7.1). In general, a higher success rate is achieved when attempts at triggering lightning were made during a thunderstorm's dissipating stage, when there was still sufficient cloud charge and electric field strength, but when the natural lightning

flash rate was low (about one flash every few tens of seconds). Wind and rain must also be taken into consideration, since high winds can cause a triggering rocket to veer off course horizontally, reducing the effective vertical speed and height that is achieved by the triggering wire. The presence of dense rain can prevent good photometric observations from being made because the lightning channel is obscured.

### **3.2 Waveform Digitization and Storage**

The models of Yokogawa and Lecroy digital storage oscilloscopes (DSO) used to digitize and store data at the ICLRT are summarized in Table 3-2. The Yokogawa DSO are used to digitize long, continuous records of the electric and magnetic fields, channel-base currents, optical luminosity, and x-rays at a relatively slow sample rate (10 MHz). The Lecroy DSOs have a higher bandwidth than the Yokogawa DSOs and digitize with a faster sampling rate (250 MHz) short records of the derivative electric fields, currents, and x-rays. The Lecroy DSOs have a memory segmentation feature, meaning that their acquisition memory can be partitioned and used by multiple triggers within a user-specified time window. This feature is particularly useful for recording lightning return strokes and not the interval between strokes, which may not be of interest.

#### **3.2.1 Yokogawa DL716**

The Yokogawa DL716 is a 16 channel DSO that was always operated at its maximum bandwidth of 4 MHz (-3 dB) and at its maximum sampling rate of 10 MHz. The DL716 can digitize up to 16 analog channels with 12-bit amplitude resolution. The DL716 has a record length of 16 mega-samples per channel, or a record length of 1.6 seconds when sampling at 10 MHz. The DL716 was operated with a  $\pm 1\text{V}$  amplitude range, or 200 mV/division. The input impedance for all channels was 1 M $\Omega$ . The DL716 is remotely controlled via IEEE488.2 (GPIB)

bus by Labview software. Data are offloaded via 10Base-T Ethernet using standard File Transfer Protocol (FTP) software.

### **3.2.2 Yokogawa DL750**

The Yokogawa DL750 is a 16 channel DSO that was always operated at its maximum bandwidth of 3 MHz (-3 dB) and at its maximum sampling rate of 10 MHz. The DL750 can digitize up to 16 analog channels with 12-bit amplitude resolution. The DL750 is specified as having 25 mega-samples per channel when using all 16 channels, but, for an unknown reason, it only recorded 20 mega-samples per channel, for a total record time of 2 s. The input impedance for all channels was 1 M $\Omega$ . One DL750 (in the positive lightning experiment network) was operated using only 11 channels, each having record length of 50 mega-samples, for a total record time of 5 s. The DL750 is remotely controlled via 100Base-T Ethernet using LabView software. Remote control was also possible over via GPIB. Data was download over 100Base-T Ethernet using standard FTP software.

As discovered by Dr. Joey Howard in early 2009 [Howard, 2009] the DL750 divides its amplitude range into 20 divisions, but only displays 10 of them. Since the voltage sensitivity is selected by adjusting the volts per division, the total amplitude range is normally twice that which is displayed on the DSO display. For example, when set to 200 mV/division, the DSO displayed  $\pm 1$  V ( $\pm 5$  divisions), but it actually recorded  $\pm 2$  V ( $\pm 10$  divisions). In such a case, half of the amplitude resolution of the DSO is wasted, since the nominal dynamic range of the fiber-optic transmitters was  $\pm 1$  V (and saturated at about  $\pm 1.2$  V). Further, for voltage levels outside of the nominal range of the FO link (1 to 1.2 V and -1 to -1.2 V), the FO links may not behave linearly. In February of 2009, the DL750 configurations were all changed to have 100 mV/division so that their full dynamic range was  $\pm 2$  V, and the ‘zoom’ of the vertical range was made x0.5 so that all 20 division would be displayed on the DSO screen. All data recorded

by DL750 before this change have half the expected vertical resolution, and waveform behavior outside a range of  $\pm 1$  V should be interpreted with caution.

### **3.2.3 LeCroy LT344 Waverunner**

The LT344 is a four channel DSO that samples with 8-bit amplitude resolution. The LT344 was operated with sampling rate of 250 MHz using its internal low-pass filter with a cutoff frequency of 25 MHz (-3 db). The LT344 has a maximum record length of 1 MB per channel when all four channels are used, for a total record time of 4 ms, but was operated in segmentation mode, with two 2-ms segments. The input impedance for each channel can be set to either 50  $\Omega$  or 1 M $\Omega$ . The full amplitude range was  $\pm 1$  V with 250 mV per division. The LT344 is controlled via 10Base-T Ethernet by Labview software, and data is downloaded on the same connection using LeCroy proprietary file transfer software.

### **3.2.4 LeCroy LT734 Waverunner 2**

The LeCroy LT374 Waverunner2, which is the successor to the LT344 Waverunner, is a DSO that samples with 8-bit resolution. The LT374 was operated with a sampling rate of 250 MHz using its internal low-pass filter with a cutoff frequency (-3 dB) of 20 MHz. The LT374 had a maximum record length of 4 MB, and the DSO was configured to record up to 8 segments, each having 2 ms duration. The full amplitude range was  $\pm 1$  V with 250 mV per division. The LT344 is controlled via 10Base-T Ethernet by Labview software, and data is downloaded on the same connection using LeCroy proprietary file transfer software.

### **3.2.5 Lecroy 44Xi**

The LeCroy 44Xi represents a major improvement from the older LT344 and LT374 models, especially in the ease of operation thanks to its responsive touch-screen controls. The 44Xi was operated in essentially the same manner as the older LeCroy DSOs: with a sample rate of 250 MHz using its internal low-pass filter with a cutoff frequency (-3 dB) of 20 MHz, and a

full amplitude range of  $\pm 1$  V with 250 mV per division. The 44Xi has a maximum record length of 12.5 MB per channel, and the DSO was configured to record up to 10 segments, each having a 5 ms duration. The 44Xi is controlled via 100Base-T Ethernet by Labview software, and data are downloaded on the same connection using LeCroy proprietary file transfer software.

### **3.2.6 MSE DSO Network**

All DSOs in the Multiple Station Experiment (MSE) were commanded by HAL via GPIB or Ethernet. The MSE DSO triggered in two circumstances: (1) when the output of the two optical sensors, one at the north-east corner of the site (NEO), and the other located at the south-west corner of the site (SWO) exceeded 100 mV for at least 1  $\mu$ s, or (2) when the triggered lightning channel-base current exceeded a level of  $\pm 6$  kA. The first circumstance occurs when natural lightning occurs on-site, and both circumstances typically occur during triggered lightning. The DSOs in the MSE included two Yokogawa DL716 for recording the output of x-ray sensors and one or two Yokogawa DL750 for recording electric fields, magnetic fields, current. All Yokogawas in the MSE shared at least one channel for synchronization. Time derivative electric field, x-ray incidence, and channel base currents were recorded on a combination of five Lecroy 44Xi, three Lecroy LT344, and one Lecroy LT3744, all operating with a sampling rate of 250 MHz (well above the Nyquist frequency) with the intent of finding source locations through time-of-arrival analysis [Howard *et al.*, 2008; Howard *et al.*, 2010; Howard, 2009]. More detail regarding the operation of the MSE DSO network can be found in the Ph. D. dissertations of Joey Howard and Jason Jerauld [Jerauld, 2007; Howard, 2009].

### **3.2.7 Positive Lightning Experiment DSO Network**

The PLE DSO network is comprised of three Yokogawa DL750 and a single LeCroy 44Xi. The LeCroy 44Xi is used mainly to triggering the DL750, as detailed below, and does not store data. Two of the DL750 (called scope 22 and scope 25) have identical measurements connected

in parallel to identical channels (e.g., both record E2 on channel 1), and were configured to digitize all 16 channels for a total time of 2 s at a sampling rate of 10 MHz. The third DL750 (called scope 30) utilizes only 11 of 16 available channels, but digitizes them for 5 s while still sampling at a rate of 10 MHz. The channel configurations for the PLE DSO are summarized in Table 3-3.

The PLE DSO network does not trigger with the MSE DSO, but instead triggers in one of two unique ways depending on its operational mode. The first operational mode (PLE mode) is designed to acquire data from off-site positive CG lightning, and the 44Xi is set to trigger on electric field change (ideally return-stroke field changes, sensed by E22 or E11), and also to output a TTL pulse that will trigger scope 22 and scope 25. The electric field record on the 44Xi can be quickly viewed (thanks to its responsive touch-screen interface) to determine if the data is worth saving. If it is, the control computer can command either scope 22 or scope 25 to save the data. The other scope can then be re-armed and acquire data. By using two identically configured DL750, the overall amount of downtime due to data offloading was reduced, thus allowing for more data acquisition. This design proved particularly valuable when recording data on positive CG lightning, which tend to occur only a few times within a time span of about 30 minutes or so at the end of storms.

The second operational mode (RTL mode) is used during triggered lightning experiments to acquire data for the entirety of the triggered lightning, including the wire ascent phase (which is of importance to this work). In contrast, the MSE typically triggers on return strokes, and does not acquire data from the wire ascent phase. When acquiring data on triggered lightning, the 44Xi served solely to provide a trigger signal for the three DL750: a 5 V, 1.8-s long square-pulse. The 44Xi itself was triggered by a TTL signal from HAL following a 1-s interval after a

pressing the launch button to fire a rocket (approximately 1 s elapses between pushing the button and rocket motor ignition), or by hand. Scope 30 and scope 22 trigger on the rising edge of the 44Xi trigger signal with no pre-trigger. Scope 25 was triggers on the falling edge of the 44Xi trigger signal, with 200 ms of pre-trigger. Thus, the measurements on scope 30 (mostly x-ray measurements) were digitized for 5 s, and the shared measurements (currents and fields) on scopes 22 and 25 were effectively digitized for 3.8 seconds, with 200 ms of overlap between allowing for straightforward synchronization of the two records.

### **3.3 Electric Field Mills**

A field mill is a device that has the capability to sense fields that do not vary in time (DC or static field), and electric fields that vary slowly over periods of seconds to minutes (quasi-static field change). Hereafter, the term quasi-static electric field will refer to the DC or slowly varying electric field as measured by the field mills. In 2008 and 2009, the quasi-static electric field at ground level was recorded at distances of 60 m and 350 m to the south-east and north-west of the launch tower, respectively, with tripod-mounted Campbell Scientific CS110 field mills in the inverted configuration (sensor is 2-m above and facing ground, as shown in Figure 3-9). The analog field mill data were digitized and transmitted via fiber optic cable to a data-storage PC in the launch trailer (the same PC that operated the Symmetricon GPS time card). The CS110 field mills use a reciprocating shutter, sample at 5 Hz, or every 200 ms (upper frequency response of about 2 Hz), and are specified by the manufacturer to have an amplitude accuracy of  $\pm 5\%$  of the reading. The amplitude resolution of the field mill measurements used here are limited to  $100 \text{ V m}^{-1}$ . The CS110 field mill data are not recorded with GPS timing, although an approximate time is supplied by the data-storage computer that is sufficiently accurate (within a few seconds) to distinguish between different lightning flashes. The sampling for the two field mills is not synchronous.

The ‘NASA’ field mill was located a few meters outside of launch control, and its reading was displayed, but generally not recorded, on the HAL control computer. The NASA mill had a rotating shutter, and sampled at 100 Hz (upper frequency response of about 50 Hz). The field changes that the NASA field mill reported were consistent with but generally lower than the field changes reported by the Campbell Scientific field mills. This difference is attributed to the NASA mill being shielded by the grounded catenary wire system that shields the launch trailer and NASA trailer. HAL could be configured to automatically arm experiments if the NASA field mill detected quasi-static electric fields exceeding a threshold value, typically  $\pm 2 \text{ kV m}^{-1}$ .

### **3.4 Broadband Electric Field and $dE/dt$**

#### **3.4.1 The Flat-Plate Antenna**

Broadband vertical-component electric fields are sensed at ground using flat-plate antennas, like those shown in Figure 3-10. The antenna consists of an electrically isolated circular plate that is mounted flush with the top face of a hollow aluminum housing. The circular plate has a radius of 22 cm, which is slightly smaller than the circular hole in the aluminum housing, so that the two are separated from each other by a 6-mm annular ring. The area of the circular plate is  $0.155 \text{ m}^2$ . The circular plate is mounted to the bottom face of the housing with nylon standoffs. The aluminum housing, which sits on the ground, is connected by a thick copper wire, or copper braid, to a 3-m ground rod. Wire mesh is attached to the outer edge of the top face of the housing (and to the ground rod) that extends several meters horizontally. The wire mesh serves to keep the circular flat plate, the top of the aluminum housing, and the Earth’s surface all flush with each other, and to increase the effective ground plane around the antenna, thereby leaving unenhanced the vertical electric field and minimizing horizontal field components that may exist due to the Earth’s relatively poor conductivity (measured to be  $2.5 \times 10^{-4} \text{ S m}^{-1}$  at the ICLRT [Rakov *et al.*, 1998]). A coaxial cable on the inside of the housing

has its center conductor on one end connected to the circular plate, and the other end is connected to the internal side of a BNC bulk-head feed through on the side of the housing so that the outer conductor of the coaxial cable is at the housing potential (which is ideally ground potential). The antenna output voltage is fed from the external port of the antenna-housing BNC feed-through to a similar BNC feed-through on a Hoffman box via 3-m of coaxial cable inside copper shield braid. The Hoffman box itself is placed in a pit that is next to the antenna and about a half a meter deep, and the pit is covered by reflective insulation (tuff-R) and the wire mesh that is attached to the antenna for protection from extreme temperatures from direct sunlight and electromagnetic interference. In addition to the standard control and communications electronics, the Hoffman box contains the sensor load impedance. The type of load impedance used depends on how the antenna is to be operated.

The operation of the flat plate antenna can be understood from its Norton or Thevenin equivalent circuit. We begin by assuming that the flat-plate antenna, surrounding ground mesh, and surrounding Earth are all perfect conductors. The boundary condition for the normal component of electric field on a perfectly conducting surface can be expressed by

$$\epsilon \vec{E} \cdot \hat{n} = \rho_s \quad 3-1$$

where  $\epsilon$  is the permittivity of the dielectric medium with units  $F m^{-1}$ ,  $\vec{E}$  is the electric field vector with units  $V m^{-1}$ , and  $\rho_s$  is the surface charge with units  $C m^{-2}$ . We are concerned with electric fields in air where the permittivity is essentially that of free space ( $\epsilon = \epsilon_0 = 8.85 \times 10^{-12} F m^{-1}$ ), and the normal component of the electric field at ground is  $E_z$ , so Equation 3-1 becomes Equation 3-2.

$$\epsilon_0 E_z = \rho_s \quad 3-2$$

The surface charge density  $\rho_s$  is the total charge on the circular plate,  $Q_{\text{plate}}$ , divided by the plate area,  $A_{\text{plate}}$ , so Equation 3-2 can be expressed as Equation 3-3.

$$Q_{\text{plate}} = \epsilon_0 A_{\text{plate}} E_z \quad 3-3$$

Equation 3-3 assumes that the smallest signal wavelength of  $E_z$  is much greater than the diameter of the flat plate, a condition that is satisfied for the signals of interest.

The Norton equivalent short-circuit current,  $i_{\text{sc}}(t)$ , is equal to the time-derivative of Equation 3-3

$$i_{\text{sc}}(t) = \frac{d}{dt}[Q_{\text{plate}}] = \epsilon_0 A_{\text{plate}} \frac{dE_z}{dt}. \quad 3-4$$

Thus, the flat-plate antenna can be viewed as a current source with a magnitude that is proportional to the incident time-varying electric field. The Norton equivalent current provides the basis for an equivalent circuit that is best analyzed in the frequency domain. Using the Fourier transform and the knowledge that differentiation with respect to time corresponds to multiplication by  $j\omega$  in the frequency domain, we find that the time-domain expression for the equivalent current, Equation 3-4, can be transformed into a frequency-domain expression given by Equation 3-5.

$$I(\omega) = \epsilon_0 A_{\text{plate}} j\omega E_z(\omega) \quad 3-5$$

The quantities  $I(\omega)$  and  $E_z(\omega)$  are the Norton equivalent current and normal-component electric field in the frequency domain, respectively, and are functions of angular frequency  $\omega$  and not time  $t$ . Figure 3-11 shows the frequency domain equivalent circuit for the flat-plate-antenna sensor, where the current  $I(\omega)$  is defined by Equation 3-5,  $Z_s$  is the source (antenna) impedance and  $Z_L$  is the load impedance, which will depend on the application.

The antenna's output voltage signal in the frequency-domain,  $V_{\text{out}}(\omega)$ , is simply the voltage across the parallel elements of the equivalent circuit shown in Figure 3-11, given by

$$V_{\text{out}}(\omega) = I(\omega)Z_{\text{Total}} = I(\omega)(Z_s \parallel Z_L) = \epsilon_0 A_{\text{plate}} j\omega E_z(\omega) \left( \frac{Z_s Z_L}{Z_s + Z_L} \right) \quad 3-6$$

The voltage output of the flat-plate antenna depends on its surface area  $A_{\text{plate}}$ , source impedance, and load impedance. For example, as noted in *Howard* [2009], if the quantity  $Z_s Z_L / (Z_s + Z_L)$  is real and equal to unity, then  $V_{\text{out}}(\omega)$  is simply  $j\omega E_z(\omega)$  scaled by the frequency-independent gain  $\epsilon_0 A_{\text{plate}}$ . If  $Z_s Z_L / (Z_s + Z_L)$  is imaginary and  $1/(j\omega)$ , then  $V_{\text{out}}(\omega)$  is simply  $E_z(\omega)$  scaled by the frequency-independent gain  $\epsilon_0 A_{\text{plate}}$ .

The source impedance is dominated by the antenna capacitance, which has been measured to be about 80 pF for the typical flat-plate antenna used at the ICLRT, allowing us to ignore the antenna's inductive impedance and resistance. As noted in *Jerauld* [2007], the impedance of the wire that connects the antenna to the load can be neglected. Thus, the source impedance is given by

$$Z_s = \frac{1}{j\omega C_{\text{ant}}} \quad 3-7$$

where  $C_{\text{ant}}$  is the antenna capacitance.

As mentioned above, the load impedance is specified by the application. For  $V_{\text{out}}(\omega)$  to be proportional to the electric field, a capacitive  $Z_L$  is required. In practice, the load impedance for an electric field sensor is a resistor placed in parallel with a capacitor, where the resistor serves to discharge the capacitor so that the output voltage decays to zero with a time constant  $RC_{\text{int}}$ . For  $V_{\text{out}}(\omega)$  to be proportional to the time-derivative electric field, a resistor is used for  $Z_L$ .

When the load is a resistor and capacitor in parallel, the load impedance is given by

$$Z_L = \frac{1}{j\omega C_{int}} \parallel R = \frac{\frac{R}{j\omega C_{int}}}{R + \frac{1}{j\omega C_{int}}} = \frac{1}{1 + j\omega RC_{int}} \quad 3-8$$

where  $C_{int}$  is the so-called integrating capacitance. All elements of the source and load impedances are in parallel, so the total capacitive impedance is  $1/j\omega(C_{ant}+C_{int})$ . Thus, the total impedance of the equivalent circuit,  $Z_S \parallel Z_L$ , is given by

$$Z_{Total} = \frac{1}{j\omega(C_{int} + C_{ant})} \parallel R = \frac{1}{1 + j\omega R(C_{int} + C_{ant})}. \quad 3-9$$

Inserting Equation 3-9 into Equation 3-6 yields

$$V_{out}(\omega) = \varepsilon_0 A_{plate} j\omega E_z(\omega) \left( \frac{1}{1 + j\omega R(C_{int} + C_{ant})} \right) \quad 3-10$$

In the electric field configuration,  $C_{ant}$  is on the order of microfarads, so  $C_{ant} \gg C_{int}$ , and the output voltage can be approximated by

$$V_{out,E}(\omega) = \varepsilon_0 A_{plate} j\omega \left( \frac{1}{1 + j\omega RC_{int}} \right) E_z(\omega) \quad 3-11$$

After division by  $j\omega RC_{int}$ , Equation 3-11 becomes

$$V_{out,E}(\omega) = \frac{\varepsilon_0 A_{plate}}{C_{int}} \left( \frac{1}{1 + \frac{1}{j\omega RC_{int}}} \right) E_z(\omega). \quad 3-12$$

The expression in the parenthesis on the right-hand side of Equation 3-12 is the form of a single pole high-pass filter with a cutoff frequency

$$\omega_0 = \frac{1}{RC_{int}} \quad 3-13$$

For signals with  $\omega \gg \omega_0$ , the output voltage of the electric field sensor is

$$V_{\text{out,E}}(\omega) = \frac{\epsilon_0 A_{\text{plate}}}{C_{\text{int}}} E_z(\omega). \quad 3-14$$

Equation 3-14 is expressed in the time domain by

$$V_{\text{out,E}}(t) = \frac{\epsilon_0 A_{\text{plate}}}{C_{\text{int}}} E_z(t) \quad 3-15$$

Thus, the electric field sensitivity depends on both the flat-plate area and the value of the integrating capacitance, and the low-frequency roll-off,  $f_0$ , depends on the values of  $R$  and  $C_{\text{int}}$ .

The high-frequency response is limited by the digitizer.

In the time domain, the low-frequency roll-off introduces an exponential decay-time  $\tau$  to a step function input, given by

$$\tau = \frac{1}{\omega_0} = RC_{\text{int}}. \quad 3-16$$

If the electric field output were a unit step function (equal to 1 at  $t = 0$ ), the output would decay to  $e^{-1}$  ( $\sim 0.37$ ) after a time  $\tau$ . Thus, Equation 3-15 is valid only for measurement on times scales much less than  $\tau$ .

In practice, the product  $RC_{\text{int}}$  can be made sufficiently large such that  $f_0$  is on the order of a few hertz or less, making  $\tau$  of the order of seconds, much longer than lightning processes, with the possible exception of very long continuing current. The value of  $R$  is typically on the order of megaohms, and the value of  $C_{\text{int}}$  is typically on the order of a microfarad or hundreds of nanofarads. However, there is an inherent trade-off between the sensor sensitivity and low-frequency roll-off: while increasing  $C_{\text{int}}$  lowers the value of  $f_0$ , it also lowers the sensitivity. This trade-off is one reason that several electric field sensors were used, each having different sensitivities and values of  $f_0$  (the other being the limited dynamic range of the sensor).

As mentioned above, the flat-plate antenna operates as a time-derivative electric field sensor if a resistive load is used. In this case,  $C_{\text{int}}$  is set to zero in Equation 3-10, yielding

$$V_{\text{out,dE/dt}}(\omega) = \varepsilon_0 A_{\text{plate}} R \left( \frac{1}{1 + j\omega RC_{\text{ant}}} \right) j\omega E_z(\omega). \quad 3-17$$

The expression in the parenthesis of the right-hand side of Equation 3-17 is the form of a single-pole low-pass filter with a high-frequency cutoff point of

$$\omega_0 = \frac{1}{RC_{\text{ant}}}. \quad 3-18$$

At the ICLRT, the load resistance is  $50 \Omega$  for all dE/dt sensors, and if  $C_{\text{ant}} = 80 \text{ pF}$ , then  $f_0 = \omega_0/2\pi \cong 40 \text{ MHz}$ , well above the highest recorded frequency of  $25 \text{ MHz}$ . Thus, for the dE/dt measurements at the ICLRT, it is always true that  $\omega \ll \omega_0$ , in which case Equation 3-17 becomes

$$V_{\text{out,dE/dt}}(\omega) = \varepsilon_0 A_{\text{plate}} R j\omega E_z(\omega). \quad 3-19$$

Equation 3-19 is expressed in the time domain by

$$V_{\text{out,dE/dt}}(t) = \varepsilon_0 A_{\text{plate}} R \frac{dE_z}{dt} \quad 3-20$$

### 3.4.2 Electric Field Sensor

A schematic of the connections inside the Hoffman box for the electric field sensor is shown in Figure 3-12. The antenna output voltage is fed from the Hoffman-box BNC feed-through to an ‘RC’ box via coaxial cable. The RC box is connected directly to a BNC port on the amplifier, and the amplifier output is fed to the PIC input via coaxial cable. The PIC output is fed to the Opticomm fiber-optic transmitter, which sends the data to the Launch trailer via  $62.5/125 \mu\text{m}$  fiber.

The RC box (a small Pomona box), shown in Figure 3-13, contains a printed-circuit board (PCB) on which the load capacitors (integrating capacitors) and load resistors are surface mounted and connected in parallel. In practice, many parallel capacitors were used to reduce the inductance. Using surface-mount devices as opposed to wire-lead devices reduced lead inductance. Placing the antenna load in its own box provides interchangeability: The antenna load can be quickly changed simply by swapping the RC box, without having to perform soldering or changing the amplifier circuit.

Beginning in spring of 2008, new amplifiers with an updated design were used in the electric field sensors that could simultaneously provide higher gain and increased bandwidth than the previously used amplifier (described in detail in *Jerauld* [2007]). A circuit schematic is shown in Figure 3-14, and a picture of a constructed amplifier in a Pomona box is shown in Figure 3-15. The amplifier is based on the OPA657 op-amp operating in the non-inverting mode. There are two circuits shown in Figure 3-14: the top is the ‘rail-splitter’ circuitry and power switch (relay), and the bottom is the amplifier. The negative and positive bias power pins on the amplifier are connected to the negative (0 V) and positive (+12 V) terminals of a battery. The rail-splitter, which is simply a voltage divider (two 100-k $\Omega$  resistors in series) and voltage follower, creates a stable, 6-V reference for the amplifier, so that the amplifier bias is actually  $\pm 6$  V. If the same battery were used to power the PIC and Opticomm, the amplifier voltage would be 6 V above the common ground potential of the PIC and Opticomm, which is outside the Opticomm input voltage range ( $\pm 1.25$  V). Therefore, it was necessary to power the amplifier with its own battery, and this power was relay-controlled by the PIC power. Each amplifier was built with the same specification, and had a similar gain, with  $G_{\text{amp}} \cong 42$  (32 dB), with the exception of the amplifier for E2, which had a gain of 240 (48 dB). This allowed amplifiers to

be swapped without significantly changing sensitivity. In the case that the gain was too high, PIC attenuation,  $G_{pic}$  could be used to lower the overall signal gain. Equation 3-21 gives the complete equation relating the output voltage of the electric field sensor to the incident electric field, taking into account the potential gain of the amplifier, attenuation provided by the PIC, and fiber-optic link scaling factor (determined from the calibration signals).

$$V_{out,E}(t) = \frac{\epsilon_0 A_{plate}}{C_{int}} G_{amp} G_{PIC} G_{link} E_z(t) \quad 3-21$$

One way to increase the sensitivity of electric field sensors is to increase the surface area of the electrode exposed to the ambient field. Before the new amplifiers with increased gain were available, the surface of the E6 and E22 antennas were increased to provide additional gain. The E6 antenna was similar to the flat-plate design described above, but the circular sensing plate had a 61-cm radius and an area of 1.2 m<sup>2</sup> (as opposed to 22-cm radius and 0.155 m<sup>2</sup> area). The E22 antenna was a not a circular plate in an aluminum housing, but instead was a square sheet of fine metallic screen supported by a rigid PVC structure. The square E22 antenna was 1.08 m on a side, and had an area of 1.17 m<sup>2</sup>. The E22 antenna is held several cm above ground, providing field enhancement, and the metallic screen edges have many needle-like points. However, it is possible to calibrate the sensitivity of E22 to an antenna with a known calibration.

As can be seen in Table 3-4, which summarizes the configurations of the ten electric field sensors, there were different sensitivity and relaxation times. As mentioned above, this was done in an attempt to measure the full range of field changes produced by positive CG lightning. The electric field sensors with a combination of high sensitivity and relaxation times (in particular E4, E5, E6, E9, E11, E22, E23) saturate upon exposure to rain because the rain is charged. The E2 sensor had the highest sensitivity and a relaxation time of 10 ms; it also saturated when exposed to rain.

On 7-July-2008, thin plastic domes (trash can lids, about 1-mm thick) were placed over some of the flat-plate antennas, as shown in Figure 3-16, to shield them from rain and prevent saturation. The lids were secured to the edge of the aluminum housing by UV-resistant zip-ties. The larger E6 and E22 antennas were covered with corrugated plastic roofing material. Although the plastic covers solve the saturation issue, it is likely that they also distort the electric field above the sensor, and thus alter the amplitude calibration of the sensors. To estimate the effect of the plastic covers on the amplitude calibration, two flat-plate antennas with similar loads and amplifier gains were placed about 2 feet from each other at station 23; one had a plastic dome, one did not. The intent was to compare their respective readings. However, this station suffered constant flooding, and no reliable data were acquired with which to make the comparison.

As detailed in Section 7.3.3, the field change readings from E2 (with a plastic dome) were compared to the expected field changes from precursors. This comparison indicates that the plastic dome over the E2 antenna may have enhanced the field strength by 29% at the sensor. It should be assumed that the same enhancement occurs for the other flat-plate antennas that are similarly covered by a plastic dome.

### **3.4.3 dE/dt Sensor**

A schematic view of the connections inside the Hoffman box for the dE/dt sensor is shown in Figure 3-17. The antenna output voltage is fed from the Hoffman-box BNC feed-through directly to the PIC input, which applies -6 dB attenuation. The PIC output is fed to a 50- $\Omega$  terminator on the Opticomm input, which sends the data to the Launch trailer via 62.5/125  $\mu\text{m}$  fiber. Thus, the load impedance for the dE/dt antennas is 50  $\Omega$ . Equation 3-22 gives a complete equation relating the output voltage of the dE/dt sensor taking into account the PIC attenuation

$G_{\text{PIC}}$ , and fiber-optic link scaling factor  $G_{\text{link}}$  (calculated from the calibration signals discussed in Section 4.2.1).

$$V_{\text{out,dE/dt}}(t) = \epsilon_0 A_{\text{plate}} R G_{\text{PIC}} G_{\text{link}} \frac{dE_z}{dt} \quad 3-22$$

With  $G_{\text{PIC}} = 0.5$  (-6 dB),  $R = 50 \Omega$ , and assuming  $G_{\text{link}} = 1$ , the nominal cal factor for the dE/dt sensors is  $29.2 \text{ kV m}^{-1} \mu\text{s}^{-1} \text{ V}^{-1}$ , so a single volt corresponds to a dE/dt value of  $29.2 \text{ kV m}^{-1}$ .

### 3.5 Channel-Base Currents

The channel-base currents are measured using non-inductive resistors (shunts) and Pearson coils (current transformers). The lightning current is fed to a Hoffman box, either by copper braid wires or by connecting the box itself to the launch tubes. The current flows from the box to a shunt that is bolted to the external surface of the box, as shown in Figure 3-18. After passing through the shunt, the current flows from a lug that is outside of the box to a copper braid wire that is connected to a ground rod. Most of the shunt's heat-dissipating mass and its voltage (BNC) output are located in the box. The voltage output from the shunt is fed either directly to a PIC, or first to amplification electronics, and then to a PIC, depending on the application. The PIC voltage output is fed via coaxial cable to an Opticomm transmitter, which sends the signal to the launch trailer via fiber optic cable.

Ideally, the current is confined to the external surface of the Hoffman box and shunt, and the electromagnetic fields inside the box are zero. However, the Hoffman box has a non-zero resistance and inductance, and a non-zero time-varying voltage difference exists between any two points on the box's inner surface. To reduce noise from electromagnetic interference, the amplification electronics, PIC, Opticomm transmitter, and battery are all contained inside of another sealed metallic 'electronics' box that provides extra electromagnetic shielding. The electronics box is electrically isolated from the Hoffman box by mounting it to Plexiglass with

nylon hardware, and the Plexiglass itself is attached to the Hoffman box. The electrical isolation prevents the formation of ground loops and the resulting distortion of the current signal. The voltage signal from the shunt enters the secondary box through a BNC bulkhead feed-through.

In the instances when a Pearson coil is used, it is clamped around the current-carrying copper braid wire outside of the Hoffman box containing the shunt. The voltage output from the coil is fed into a Hoffman box (that is different from the box containing the shunt) through a BNC bulkhead feed-through to a PIC terminated in  $50\ \Omega$ . The PIC voltage output is fed via coaxial cable to an Opticomm transmitter, which sends the signal to the launch trailer via fiber optic cable.

In 2008, IS currents and RS currents were separated through the use of a rectangular intercepting wire placed several meters above the launch tubes. The intercepting wire and the launch tube assembly, shown in Figure 3-1, are connected by different ground leads to different ground rods that were separated by a distance about 8 m. The locations at which the IS and RS currents are measured are identified in Figure 3-1. For each current, there are two shunt measurement at different amplitude scales, and a single Pearson coil measurement. The configurations of the six current measurements in 2008 are summarized in Table 3-5. Note that the measurements of the IS are called the 'ICC' measurements (for initial continuous current, the process of most interest in 2008). A diagram is given in Figure 3-19 that illustrates schematically the ICC and RS current measurement configurations in 2008, which are essentially identical to each other.

The ICC shunt, a T&M Research R-7000-10, has a constant resistance of  $1\ \text{m}\Omega$  for frequencies ranging from DC to 8 MHz. The ICC shunt's voltage is measured on two scales by applying its output in parallel to the inputs of two PICs; one applies -33 dB attenuation, and the

other applies -13 dB attenuation. The measurement with more attenuation is called the ‘ICC-high current’ measurement because it is designed to measure larger currents, in this case from about 1.4 kA to 28 kA. The measurement with less attenuation is called the ‘ICC-low current’ measurement because it was designed to measure current amplitudes that are a factor of 10 less than those measured by the high current measurement, in this case 140 A to 2.8 kA. The ICC-low measurement was a custom built, model 6801 Pearson coil current transformer, with a linear frequency response from 8 Hz to 5 MHz, with a transimpedance of  $1.2 \times 10^{-2} \text{ V A}^{-1}$ ; it measured currents ranging from about 5 to 110 A.

The RS current transformer was also a model 6801 Pearson coil, but it had a transimpedance of  $1.3 \times 10^{-2} \text{ V A}^{-1}$ , and it measured currents ranging from about 6 to 115 A. The RS shunt was a T&M Research R-5600-8 with a constant resistance of 1.4 m $\Omega$  for frequencies ranging from DC to 12 MHz. Like the IS shunt measurements, the RS shunt had a high-current and low-current measurement. The RS-high current measurement was attenuated by -23 dB; it measured currents ranging from about 3.2 kA to 65 kA. The RS-low current measurement was attenuated by -3 dB; it measured currents ranging from 320 A to 6.5 kA.

The tower current measurement setup was changed prior to the 2009 triggering season. The intercepting wire was not used, so the only current measurements were attached directly below the launch tube assembly. The large, aging Hoffman box containing the old RS shunt and electronics was replaced by a larger, custom-made stainless steel box. There was room for up to five separate electronics boxes in the new custom box, which is shown in Figure 3-20 (with only 4 electronics boxes, 1 of which was not used, and NASA-operated digitizing equipment not discussed here). The configurations of the current measurements operated in 2009 are summarized in Table 3-6, and illustrated schematically in Figure 3-21.

The ICC shunt (R-7000-10) from 2008 was bolted to the center of the custom box in a similar manner to what was done in the old Hoffman box. The shunt voltage was fed to three different measurements: (1) the II-high, (2) the II-low, and (3) the II-VLS (very low shunt). The II-high measurement had -36 dB attenuation; it measured currents ranging from about 3 kA to 63 kA. The II-low measurement had -16 dB attenuation; it measured currents ranging from about 300 A to 6.3 kA. The II-VLS had no attenuation, but instead was amplified by a factor of 46.5 (33 dB). The amplifier circuit was the same as the amplifier used with the electric field sensors (pictured in Figure 3-15). An easily replaceable protection circuit, which included a current limiting resistor and zener-diode voltage clamp to limit the input voltage to around 5 V, was placed in front of the amplifier front end. The II-VLS measured currents ranging from about 1 A to 21 A.

The RS Pearson coil that was used in 2008 was used to measure mid-range currents until 14-Jul-2009. In an effort to keep the ground lead as straight as possible, a mount was built for the Pearson coil so it could be placed directly under the shunt lug, as shown in Figures 3-7 and 3-20. The II-VLP (very low Pearson) measurement was attenuated by -3 dB; it measured currents ranging from about 6 to 115 A.

## **3.6 High-Speed Video Cameras**

### **3.6.1 Photron SA1.1**

The Photron SA1.1, shown in Figures 3-22 and 3-23, detects light with a 1024 x 1024 pixel CMOS sensor. The dimension of each square pixel is 20  $\mu\text{m}$  x 20  $\mu\text{m}$ . The Photron was operated from the office trailer with one of three lenses with different focal lengths: 50 mm, 24 mm, and 20 mm, yielding spatial resolutions of 0.18, 0.37, and 0.44 meters per pixel, respectively, at a range of 440 m, the approximate distance between the camera and the launch tower. The lens aperture was typically set as low as possible, up to  $f/2$ , to maximize the amount

of light collected by the sensor. Using the full pixel count (~1.04 megapixel), the Photron could record up to 5.4 kfps. However, the Photron was typically operated at much faster framing rates, up to 300 kfps, although with lower pixel resolution. The Photron acquired data on a continuous loop buffer, so it could record 100% pre-trigger. The manufacturer specifications indicate that the Photron can operate with a shutter speed of  $(\text{frame rate})^{-1}$ , meaning all light incident on the sensor during a frame time is integrated. However, it is likely that the camera has a few hundred nanoseconds of dead time during each frame. The Photron digitizes grayscale with 12-bit amplitude resolution. The Photron has 32 GB of internal memory, which can be divided into 64 memory segments, and the total duration of video that could be recorded depended on the framing rate and pixel count. During a triggering session, the Photron memory was divided into a number of segments equal to the number of rockets expected to be launched. The Photron was synchronized with IRIG-B GPS time code. The Photron was controlled by computer via 100Base-T Ethernet connection, and the same connection was used to offload each frame as individual lossless 16-bit image files (the 'raw' format). The Photron could be triggered by hand (using a short-circuit switch) or by the trigger pulse generated by the MSE trigger system, which was sent from the launch trailer to the office trailer via Opticom fiber optic link. The Photron is not absolutely calibrated, so radiometric measurements were not possible.

In 2008, two Photron SA1.1, called the UF Photron (owned by the University of Florida) and OU Photron (owned by the University of Oklahoma, and operated in collaboration with Professor William Beasley), were operated from the office trailer, about 440 m from the launch tower. The OU Photron was only available for two storm sessions (17-September-2008 and 10-October-2009). It imaged the lower several hundred meters of lightning channel with a relatively slow framing rate (5.4 kfps), allowing the UF Photron to be operated at a faster

framing rate (up to 100 kfps). Before the OU Photron was made available, the UF Photron was only operated at a framing speed up to 50 kfps. The OU and UF Photron configurations for different storm sessions in 2008 are given in Table 3-7 and Table 3-8, respectively.

In early 2009, it was discovered that the Photron operates at faster frame rates for horizontal rectangular pixel areas than vertical rectangular pixel areas. For example, with a pixel area of 64 x 128 (vertical x horizontal), the Photron will operate as fast as 300 kfps, but with a pixel area of 128 x 64, the Photron will only operate up to 108 kfps. Before the 2009 triggering experiments, a custom tripod mount was built, shown in Figures 3-22 and 3-23, in which the Photron could rest on its side so that the higher framing rate could be utilized. The horizontal images were rotated in post processing. In 2009, the Photron framing rate was increased incrementally (and the pixel resolution was correspondingly decreased) with each storm session, up to 300 kfps. For faster framing rates, the pixel resolution becomes too small to be of use. The UF Photron configurations for different storm sessions in 2009 are given in Table 3-9.

From 7-July-2009 to 18-August-2009, the OU Photron was returned to the ICLRT. It was placed in the launch trailer (a distance of about 50 m from the launch tower) to image the lightning with increased spatial resolution; this camera was equipped with a 14-mm focal length lens, which provided a spatial resolution of about 8 cm. Even with the relatively wide-angle lens, the close proximity of the SA1.1 to the launch tower restricted its view of the triggered lightning to the lower 40 m or so of channel with a maximum framing rate of 75 kfps. Unfortunately, a computer virus corrupted most of the data acquired by this camera, rendering it unusable.

It was discovered in August of 2009 that the Photron records a few frames less than the expected number of frames per second. Further, the number of frames per second varies by

1 frame. For example, when the Photron is set operate at a framing rate of 300 kfps, it will actually record  $299992 \pm 1$  fps; that is, 299992 frames will be recorded for one second, and for the next second, the number of frames recorded may be 299993. Fortunately, this makes virtually no difference in the frame times, since the  $1/299992 \text{ s} \cong 3.3334 \text{ } \mu\text{s}$  and  $1/300000 \text{ s} \cong 3.3333 \text{ } \mu\text{s}$ . Only a few framing rates were tested to determine the actual number of frames that were recorded, and these are summarized in Table 3-10. Note that the deviation from the true framing rate increases with increasing framing rates.

The Photron does not give correct time stamps. Although the GPS time stamp for the trigger frame is accurate, the time stamps assigned to successive frames (in either time direction) are progressively inaccurate. For example, if the Photron is operated at 300 kfps (actually about 299992 fps) for 1 second with no pre-trigger, the time of the first frame will be accurate, but the time reported for of the last frame will be  $30 \text{ } \mu\text{s}$  less than 1 second. Thus, when analyzing Photron data, it is important to calculate the frame times independently, and not rely on the time stamps reported by the Photron.

### **3.6.2 Phantom V7.1**

The Phantom V7.1, shown in Figures 3-22 and 3-23, detects light with a 800 x 600 pixel CMOS sensor. The dimension of each square pixel is  $22 \text{ } \mu\text{m} \times 22 \text{ } \mu\text{m}$ . The Phantom was operated at framing rates between 5 kfps and 12 kfps. The Phantom acquired data on a continuous loop buffer, so it could record 100% pre-trigger. There is a small amount of dead time associated with each frame, around several  $\mu\text{s}$  (depending on the framing rate), an interval that is of little consequence since the frame times are between  $100 \text{ } \mu\text{s}$  and  $200 \text{ } \mu\text{s}$ . The Phantom digitized grayscale with 14-bit amplitude resolution. The Phantom was computer controlled via 100Base-T Ethernet connection using 'Phantom Camera Control' software. The Phantom had 8 GB of internal memory, and videos were offloaded via Ethernet to the control computer as

'cine' files, a proprietary format, after which individual frames were saved for analysis and presentation purposes. The Phantom did not suffer the timing inaccuracies and variable framing rate exhibited by the Photron. The Phantom was nearly always triggered by hand, although it could be triggered by the trigger pulse from the MSE trigger system.

The Phantom was only used in 2009, and it was used in place of the OU Photron to image the lower several hundred meters of lightning channel with a relatively slow framing rate. The Phantom viewed in the direction of the launch tower from the office trailer (440 m away) through the same window as the Photron. The Phantom was equipped either with a 24-mm or 20-mm focal length lens to give a spatial resolution of 0.40 and 0.48 m/pixel, respectively. The lens aperture setting depended on the background light conditions, but in general it was set as low as possible without saturating the camera, typically  $f/8$ . Like the Photron, the Phantom operated faster for horizontal windows than vertical windows, so it was mounted on its side. A list of the Phantom configurations utilized in 2009, including pixel resolutions, lens settings, spatial resolutions, and framing rates, are given in Table 3-11.

Table 3-1. Sensor locations at the ICLRT.

Designation	Easting (m)	Northing (m)	Elevation (m)	Latitude	Longitude	Distance to Tower <sup>b</sup> (m)
Origin <sup>a</sup>	0.0	0.0	0.0	29.93899065	82.03648403	607.7
DE-1	137.1	499.6	3.0	29.94346957	82.03495231	318.1
T-1F	141.0	488.8	3.3	29.94337157	82.03491468	311.7
T-1U	138.2	489.2	3.7	29.94337560	82.03494311	314.5
E-2	424.4	570.2	3.8	29.94405042	82.03196110	156.3
T-2	427.5	580.4	4.7	29.94414255	82.03192649	166.1
DE-3	373.5	569.2	3.6	29.94405142	82.03248851	169.4
T-3F	370.9	575.0	3.5	29.94410482	82.03251415	175.8
T-3U	370.9	577.7	3.7	29.94412902	82.03251305	178.2
DE-4	680.8	493.8	4.7	29.94331163	82.02932329	249.6
E-4	683.6	492.5	4.7	29.94329927	82.02929405	251.9
T4-F	691.3	484.1	5.1	29.94322224	82.02921654	256.9
T4-U	692.2	486.6	5.4	29.94324471	82.02920611	258.5
DE-5	375.2	479.5	4.3	29.94324182	82.03249149	94.1
E-5	377.9	478.9	4.2	29.94323644	82.03246331	91.8
T5-F	382.0	468.7	4.4	29.94314365	82.03242317	81.8
T5-U	379.3	468.7	4.7	29.94314415	82.03245086	83.9
E-6	101.8	310.5	2.3	29.94177175	82.03535988	357.6
T-6	104.9	301.4	3.0	29.94168893	82.03533024	357.5
T7-F	392.6	255.2	4.3	29.94121552	82.03236144	168.0
T7-U	389.5	254.6	4.4	29.94121138	82.03239285	169.4
DE-7	393.1	244.7	3.5	29.94112083	82.03235826	177.8
DE-8	570.3	286.1	4.9	29.94146024	82.03051350	180.6
T8-F	578.5	280.3	4.7	29.94140589	82.03043067	190.5
T8-U	576.0	279.0	5.2	29.94139507	82.03045638	189.7
DE-9	134.9	97.3	5.7	29.93984149	82.03506485	443.2
E-9	134.3	98.0	5.7	29.93984859	82.03507150	443.1
T-9F	133.8	104.9	6.0	29.93991034	82.03507496	438.6
T-9U	131.0	104.5	6.2	29.93990750	82.03510425	440.9
E-10	695.6	203.2	5.5	29.94068782	82.02923471	329.1

a) The southeast corner of the office trailer. b) With respect to T20, which is located on the launcher platform.

Table 3-1. Continued.

Designation	Easting (m)	Northing (m)	Elevation (m)	Latitude	Longitude	Distance to Tower (m)
T-10	695.7	194.1	6.3	29.94060558	82.02923595	335.1
E-11	165.9	262.5	2.1	29.94132629	82.03470770	317.1
DE-11	168.2	260.7	2.1	29.94130938	82.03468380	315.9
T-11F	173.4	252.6	2.3	29.94123483	82.03463147	315.5
T-11U	175.8	254.1	2.7	29.94124776	82.03460687	312.7
T-12	284.4	288.5	3.8	29.94153706	82.03347429	203.6
T-13	463.8	324.2	5.6	29.94182414	82.03160836	93.1
T-14	506.7	447.4	6.1	29.94292722	82.03113612	70.7
T-15	507.9	547.1	4.5	29.94382576	82.03110204	146.7
T-16	261.4	496.3	3.7	29.94341599	82.03366567	199.7
DE-17	481.3	413.1	5.9	29.94262269	82.03140659	37.6
T-17	481.3	403.6	6.5	29.94253666	82.03140909	39.2
E-18	715.3	596.2	6.6	29.94422813	82.02894235	326.3
T-18	712.4	605.3	7.6	29.94431092	82.02897026	329.1
T-19	15.7	229.4	2.3	29.94105632	82.03626989	466.7
T-20	443.8	415.1	18.9	29.94264819	82.03179454	0.0
T-21	569.1	439.1	4.4	29.94283991	82.03049198	127.5
B-22	581.7	604.0	5.1	29.94432498	82.03032401	233.9
E-22	585.5	600.7	5.2	29.94429451	82.03028540	233.5
T-22	575.6	601.4	5.5	29.94430271	82.03038783	228.2
E-23	233.2	562.1	2.6	29.94401517	82.03394324	256.9
T-23	233.2	554.5	3.3	29.94394629	82.03394446	252.5
B-24	311.9	421.7	3.4	29.94273356	82.03315952	132.1
T-24	306.8	423.2	3.9	29.94274804	82.03321169	137.3
DE-25	445.6	454.5	5.0	29.94300302	82.03176734	39.4
T-25	456.2	458.7	5.7	29.94303903	82.03165698	45.3
Campbell OT	153.7	578.5	3.3	29.94417846	82.03476245	333.0
Campbell LC	508.9	424.9	5.5	29.94272413	82.03111869	65.8

Table 3-2. Makes, models, and salient specifications of the DSO used at the ICLRT.

Make	Model	Quantity	Bit Depth	Number of Channels	Sample Rate Used (MHz)	Bandwidth (MHz)	Record Length (MS/ch)
Yokogawa	DL716	2	12	16	10	4	16
Yokogawa	DL750	5	12	16	10	3	25
Lecroy	LT344L	6	8	4	250	25	1
Lecroy	LT374L	2	8	4	250	20	4
Lecroy	44Xi	4	8	4	250	20	12.5

Table 3-3. PLE DSO channel assignment.

Channel	Scope 22/25 <sup>a</sup>	Scope 30 <sup>b</sup>	Scope 27 <sup>c</sup>
1	E2	E22	E11
2	E4	T2U	E22
3	E5	T5U	-
4	E6	T12U	-
5	E6	T13U	-
6	E10	T14U	-
7	E11	T15U	-
8	E18	-	-
9	E22	T25U	-
10	E23	T20U	-
11	B24NS	T24U	-
12	B24EW	-	-
13	B22NS	II-VLS	-
14	B22EW	-	-
15	II-LO	-	-
16	II-VLS	-	-

a) Scope 22 and Scope 25 had the same channel assignments. b) Scope 30 only utilized 11 channels. c) Scope 27 is a LeCroy 44Xi with only 4 channels: only channels 1 and 2 were used.

Table 3-4. Electric field sensor configuration.

Sensor	Flat-plate area (m <sup>2</sup> )	Load resistance (Ω)	Load capacitance (F)	Relaxation time (s)	Amplifier gain	Nominal cal factor (kV m <sup>-1</sup> / V)
E2	0.155	5.0 x 10 <sup>5</sup>	2.20 x 10 <sup>-8</sup>	0.011	240	0.0668
E4	0.155	2.1 x 10 <sup>6</sup>	2.19 x 10 <sup>-6</sup>	4.60	41.9	38.1
E5	0.155	2.1 x 10 <sup>6</sup>	2.22 x 10 <sup>-6</sup>	4.67	41.9	38.6
E6	1.166	2.0 x 10 <sup>4</sup>	4.54 x 10 <sup>-7</sup>	0.009	41.8	0.588
E9	0.155	4.3 x 10 <sup>6</sup>	9.34 x 10 <sup>-7</sup>	4.02	42.5	16.0
E10	0.155	2.1 x 10 <sup>6</sup>	2.08 x 10 <sup>-6</sup>	4.33	41.9	36.2
E11	0.155	4.8 x 10 <sup>5</sup>	9.20 x 10 <sup>-8</sup>	0.0092	51.1	1.3
E18	0.155	4.8 x 10 <sup>6</sup>	9.09 x 10 <sup>-7</sup>	4.32	42.0	15.8
E22	1.166	2.0 x 10 <sup>4</sup>	4.39 x 10 <sup>-7</sup>	0.0088	42.1	1.0
E23	0.155	4.3 x 10 <sup>6</sup>	1.02 x 10 <sup>-6</sup>	4.38	41.1	18.1

Table 3-5. 2008 channel-base current measurements configurations.

Measurement	Sensing device	Nominal transimpedance (V A <sup>-1</sup> )	PIC attenuation	Nominal cal factor (kA V <sup>-1</sup> )
ICC-high	R-7000-10	0.001	0.0224 (-33 dB)	28.3
ICC-low	R-7000-10	0.001	0.224 (-13 dB)	2.83
ICC-VL	Pearson Coil model 6801	0.001	0.707 (-3 dB)	0.108
RS-high	R-5600-8	0.00125	0.0707 (-23 dB)	64.7
RS-low	R-5600-8	0.00125	0.707 (-3 dB)	6.47
RS-UL	Pearson Coil model 6801	0.025	0.707 (-3 dB)	0.113

Table 3-6. 2009 channel-base current measurements.

Measurement	Sensing device	Nominal transimpedance (V A <sup>-1</sup> )	PIC attenuation	Amplifier gain	Nominal cal factor (kA V <sup>-1</sup> )
II-high	R-7000-10	0.001	0.0158 (-36 dB)	0.0	63.0
II-low	R-7000-10	0.001	0.158 (-16 dB)	0.0	6.3
II-VLS	R-7000-10	0.001	0.0	46.5 (33 dB)	0.022
II-VLP	Pearson Coil model 6801	0.025	-0.707 (-3 dB)	0.0	0.108

Table 3-7. OU Photron configurations in 2008.

Date	Frame rate (kfps) <sup>a</sup>	Pixel area, vertical x horizontal	Lens focal length (mm)	Lens aperture	Spatial view, vertical x horizontal <sup>b</sup>	Spatial resolution (m per pixel) <sup>b</sup>	(Frame rate) <sup>-1</sup> (μs)
17-September	5.4	1,024 x 1,024	24	unknown	376 x 376 <sup>c</sup>	0.37	185
9-October <sup>d</sup>	5.4	1,024 x 1,024	24	unknown	376 x 376 <sup>c</sup>	0.37	185

a) Nominal frame rate. b) At a distance of 440 m from the camera sensor. c) The camera viewing out of south-facing window; much of the image was blocked by office trailer wall. d) These settings were used for the second and third trigger on this date (UF08-20 and UF08-21).

Table 3-8. UF Photron configurations in 2008.

Date	Frame rate (kfps) <sup>a</sup>	Pixel area, vertical x horizontal	Lens focal length (mm)	Lens aperture	Spatial view, vertical x horizontal (m) <sup>b</sup>	Spatial resolution (m per pixel) <sup>b</sup>	(Frame rate) <sup>-1</sup> (μs)
30-June	10	960 x 448	50	unknown	166 x 78	0.18	100
12-July	20	640 x 256	50	unknown	113 x 45	0.18	50
10-September	5.4	1,024 x 1,024	24	unknown	376 x 376 <sup>c</sup>	0.37	185
11-September	50	320 x 128	50	unknown	56 x 23	0.18	20
17-September	50	320 x 128	50	unknown	56 x 23	0.18	20
9-October <sup>d</sup>	100	96 x 128	50	unknown	17 x 23	0.18	10
9-October <sup>e</sup>	67.5	192 x 128	50	unknown	35 x 23	0.18	148

a) Nominal frame rate. b) At a distance of 440 m from the camera sensor. c) The camera viewing out of south-facing window; much of the image was blocked by office trailer wall. d) Settings for the second trigger of on this date (UF08-20). e) Settings for the third trigger of on this date (UF08-21).

Table 3-9. UF Photron configurations in 2009.

Date	Frame rate (kfps) <sup>a</sup>	Pixel area, vertical x horizontal	Lens focal length (mm)	Lens aperture	Spatial view, vertical x horizontal (m) <sup>b</sup>	Spatial resolution (m per pixel) <sup>b</sup>	(Frame rate) <sup>-1</sup> (μs)
19-February	50	320 x 128	24	f/4	56 x 23	0.18	20.0
26-May	108	320 x 128	24	f/2.8	118 x 47	0.37	9.26
27-May	108	320 x 128	24	f/2.8	118 x 47	0.37	9.26
04-June	135	320 x 96	24	f/2.8	118 x 35	0.37	7.41
18-June	180	320 x 64	24	f/2.8	118 x 23	0.37	5.56
29-June	240	320 x 48	20	f/2.8	141 x 21	0.44	4.16
30-June	300	320 x 32	20	f/2.8	141 x 14	0.44	3.34
07-July	180	320 x 64	20	f/2.8	141 x 28	0.44	5.56

a) Nominal frame rate. b) At a distance of 440 m from the camera sensor.

Table 3-10. Photron framing rates, specified and actual.

Specified framing rate (fps)	Actual framing rate (fps)
675,000	674,981 $\pm$ 1
500,000	499,986 $\pm$ 1
450,000	449,988 $\pm$ 1
300,000	299,992 $\pm$ 1
250,000	249,993 $\pm$ 1

Table 3-11. Phantom configurations 2009

Date	Frame rate (kfps)	Pixel area, vertical x horizontal	Lens focal length (mm)	Lens aperture	Spatial view, vertical x horizontal (m) <sup>a</sup>	Spatial resolution (m per pixel) <sup>a</sup>	(Frame rate) <sup>-1</sup> (μs)	Exposure time (μs)
19-February	6.4	800 x 600	24	f/4	322 x 242	0.40	156.25	154.25
29-March	5	800 x 600	24	f/11	322 x 242	0.40	200.00	149.5 <sup>b</sup>
26-May	5	800 x 304	24	f/11	322 x 123	0.40	200.00	190.0
27-May	10	800 x 208	24	f/11	322 x 84	0.40	100.00	98.0
04-June	10	800 x 208	24	f/8	322 x 84	0.40	100.00	98.0
18-June	10	800 x 200	24	f/4	322 x 81	0.40	100.00	98.0
29-June	8	800 x 200	24	f/8	322 x 81	0.40	125.00	120.0
30-June	8	800 x 200	24	f/8	322 x 81	0.40	125.00	120.0
07-July	8	800 x 200	20	f/8	387 x 97	0.48	125.00	123.0
14-July	6.4	800 x 200	20	f/8	387 x 97	0.48	156.25	150.0
18-July	6.4	800 x 200	20	f/8	387 x 97	0.48	156.25	150.0
18-August	6.4	800 x 200	20	f/8	387 x 97	0.48	156.25	150.0

a) At a distance of 440 m from the camera sensor. b) This exposure time was set manually.

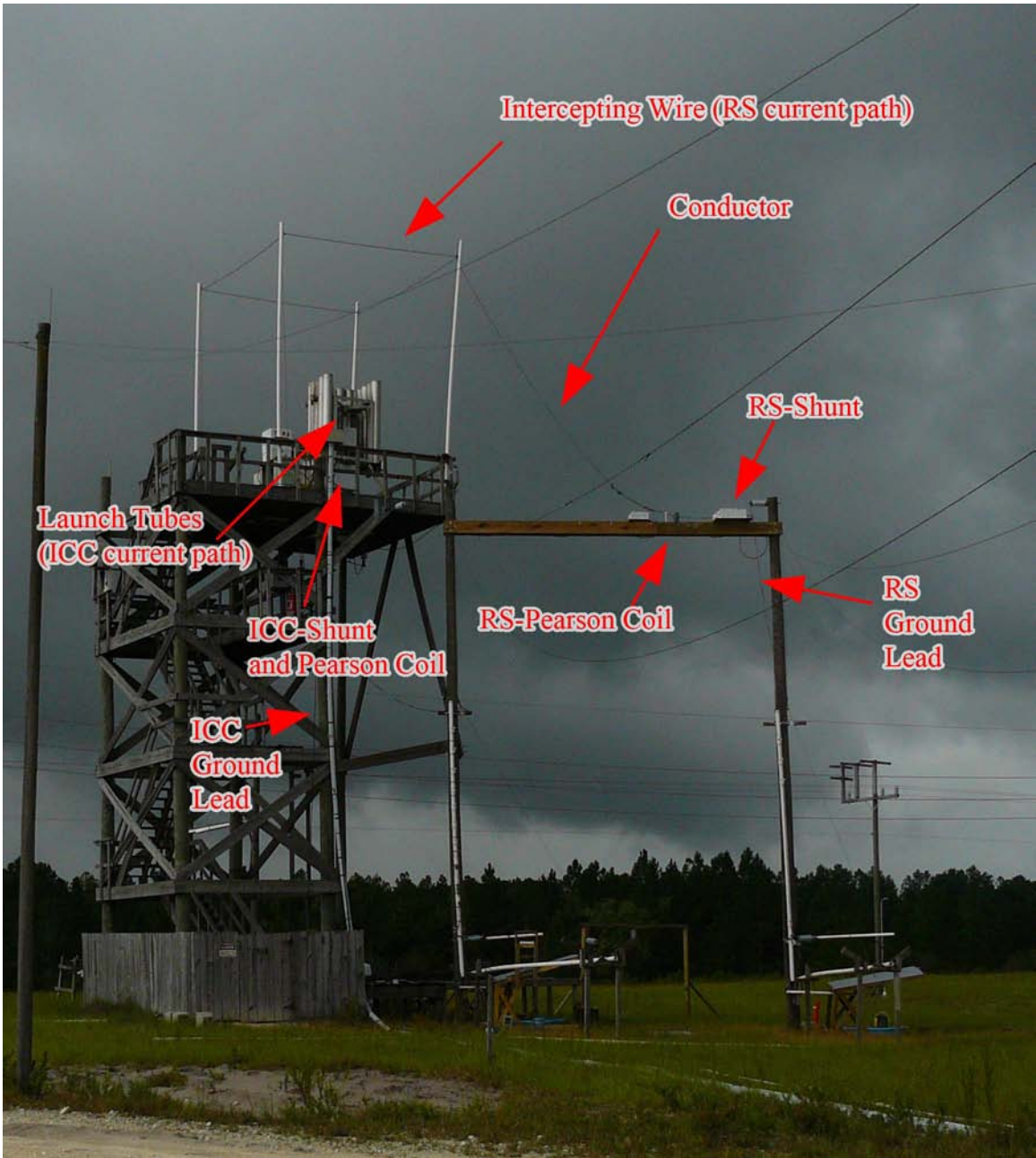


Figure 3-1. The launch tower with the current interceptor installed. Photograph taken by Dustin Hill.

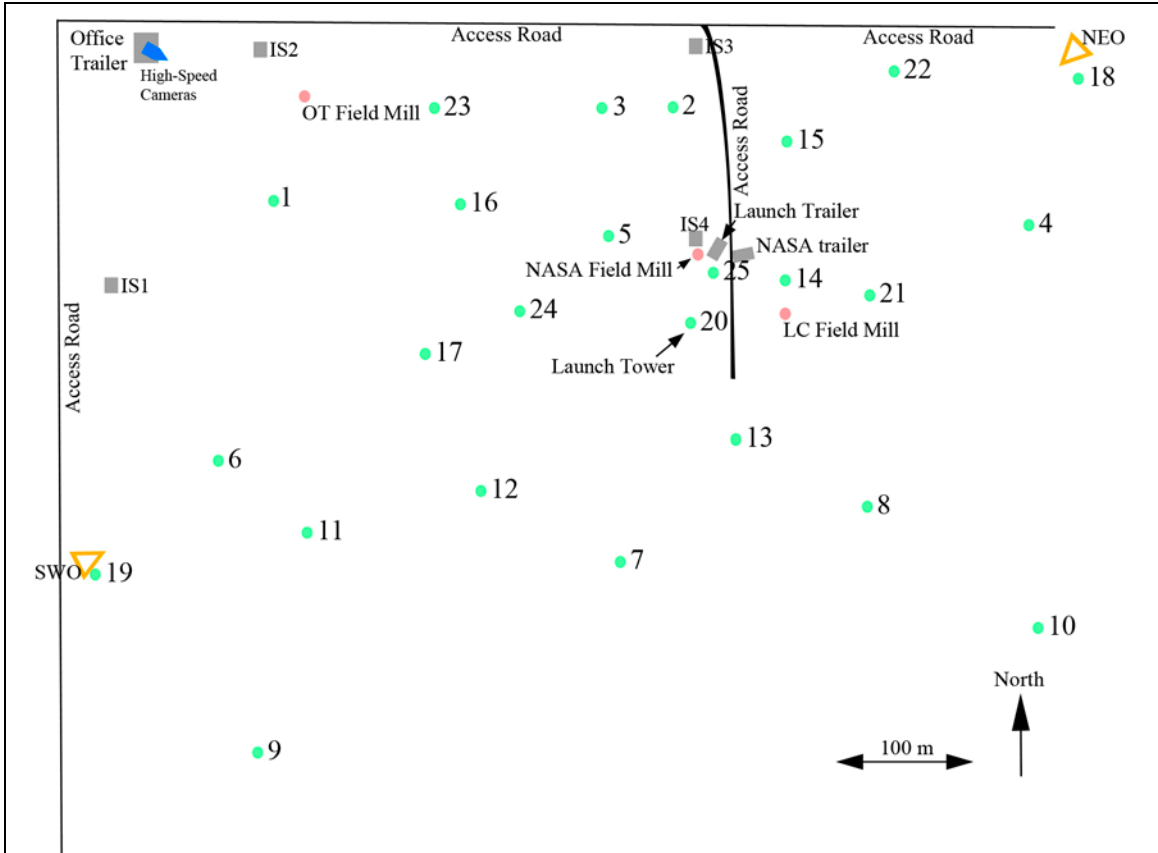


Figure 3-2. The layout of stations and buildings at the ICLRT.

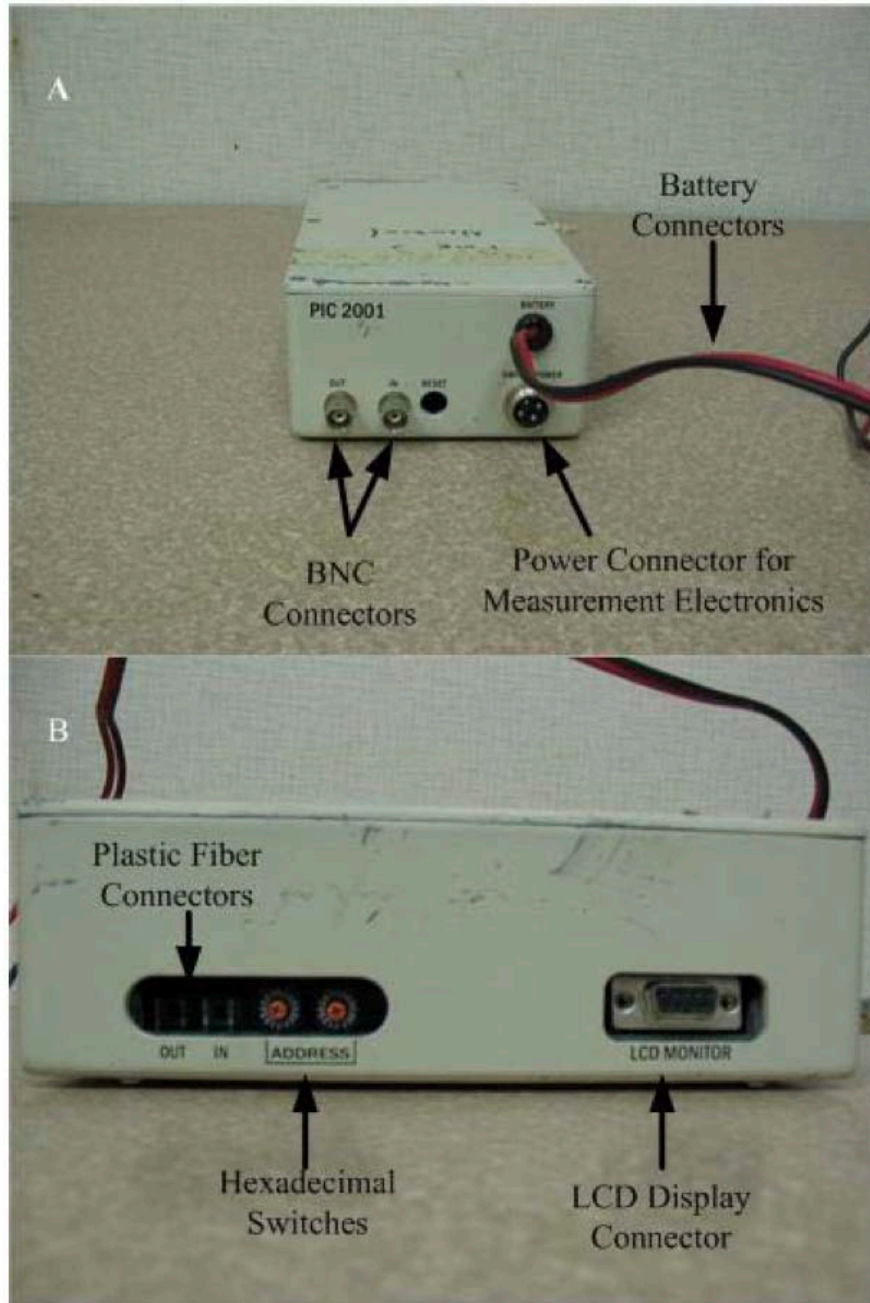


Figure 3-3. The 2001 PIC controller. A) Front view. B) Side view. Adapted from *Howard* [2009].

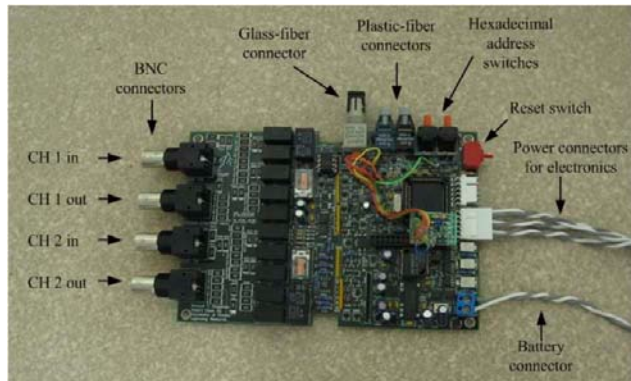


Figure 3-4. The 2006 PIC controller. Adapted from *Howard* [2009].

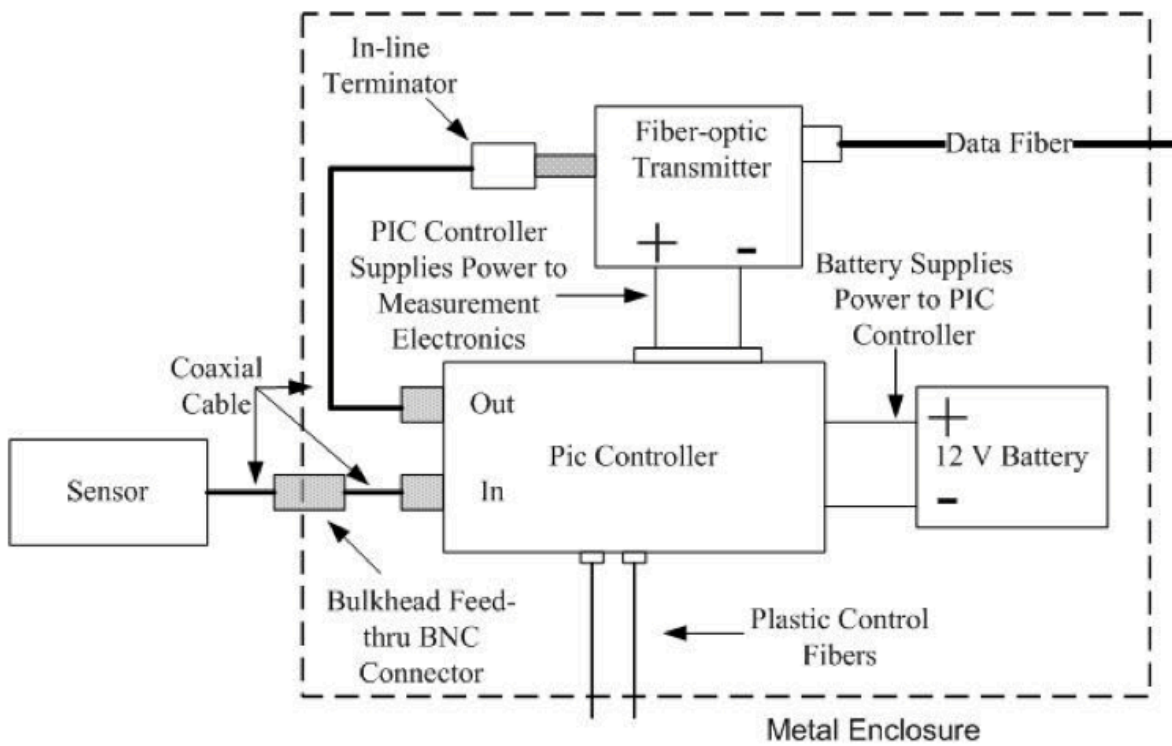


Figure 3-5. Schematic of the typical 2001 PIC installation. Adapted from *Howard* [2009].

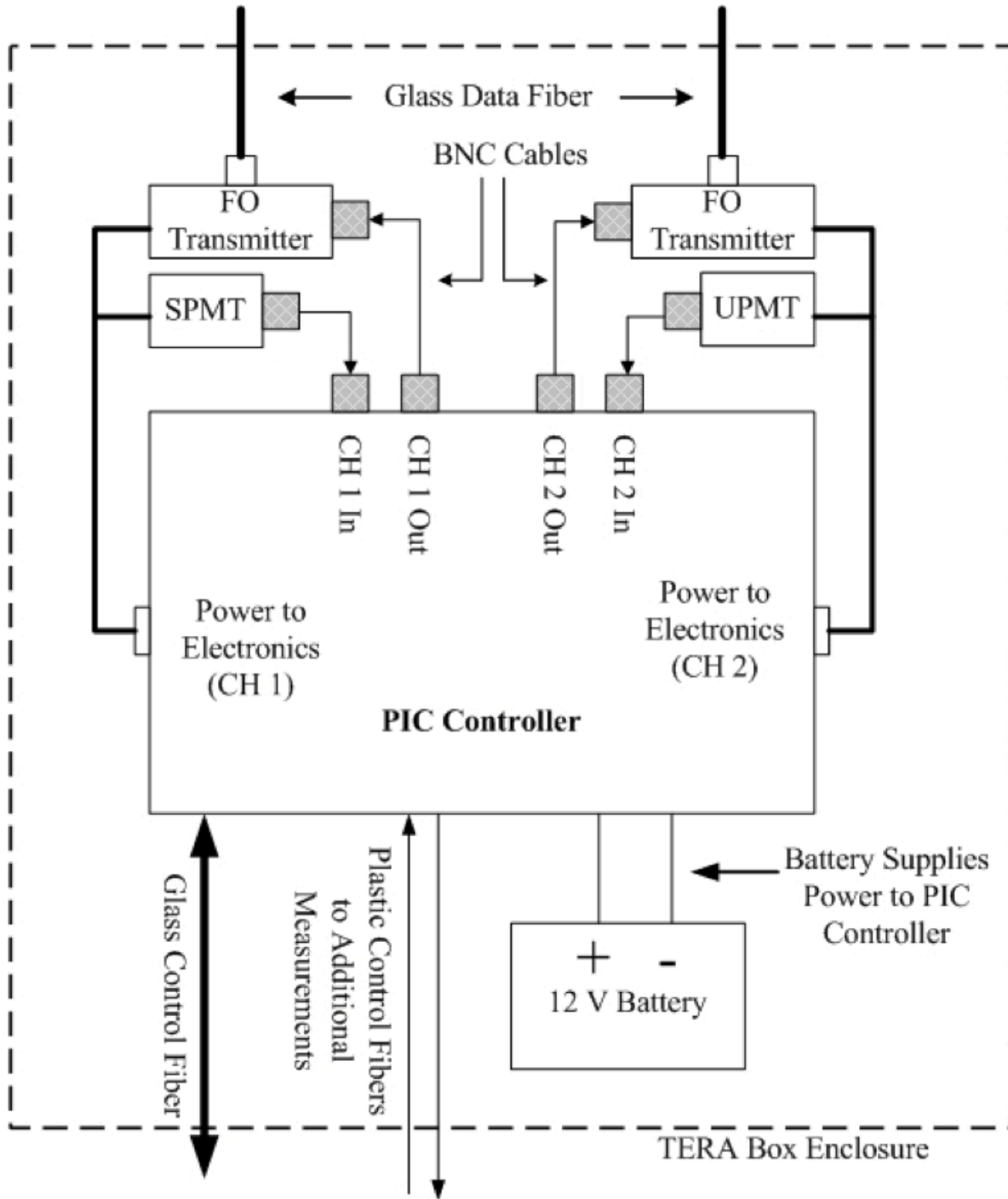


Figure 3-6. Schematic of a typical 2006 PIC installation. Adapted from Howard [2009].

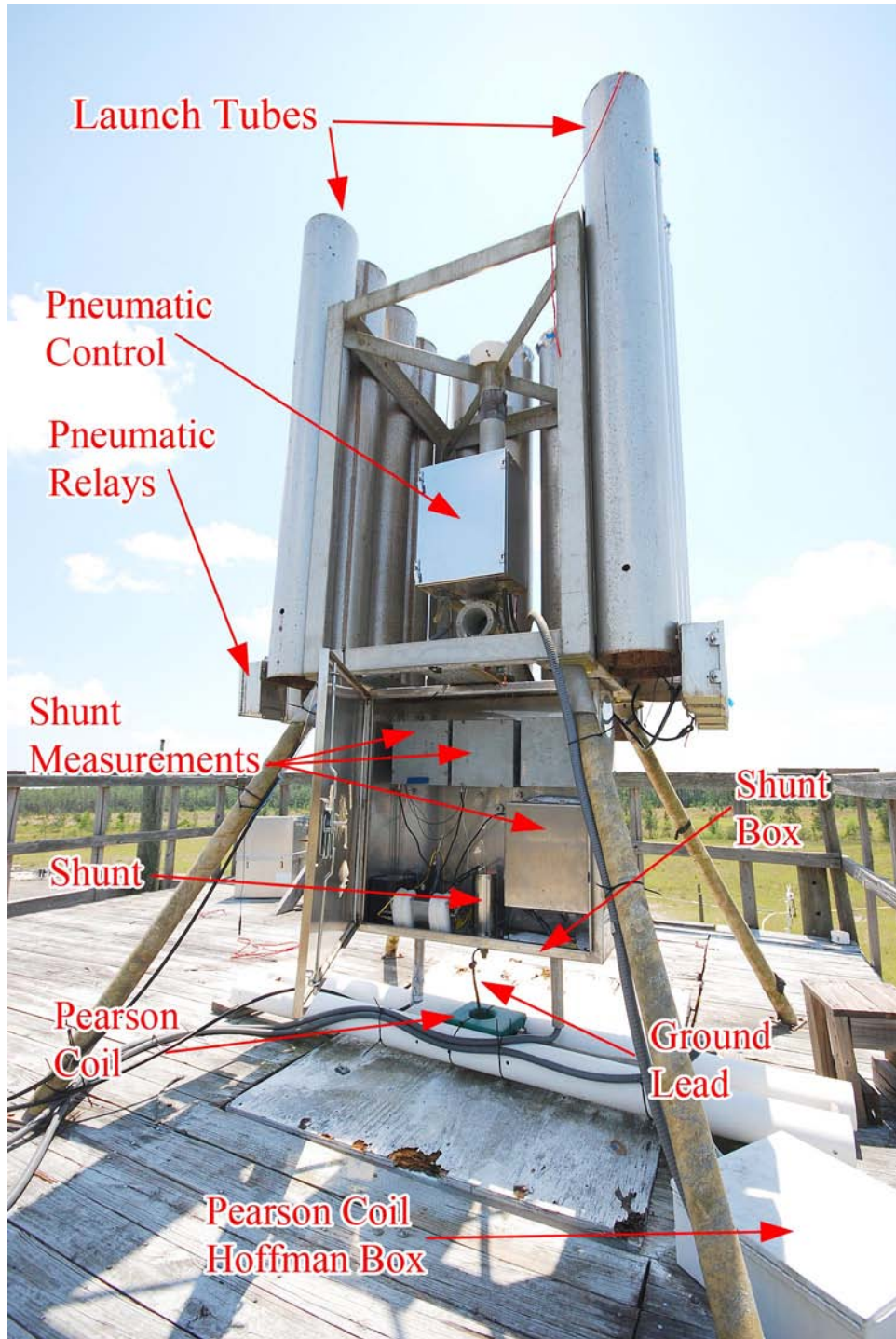


Figure 3-7. The launch tube apparatus. Photograph taken by Dustin Hill.

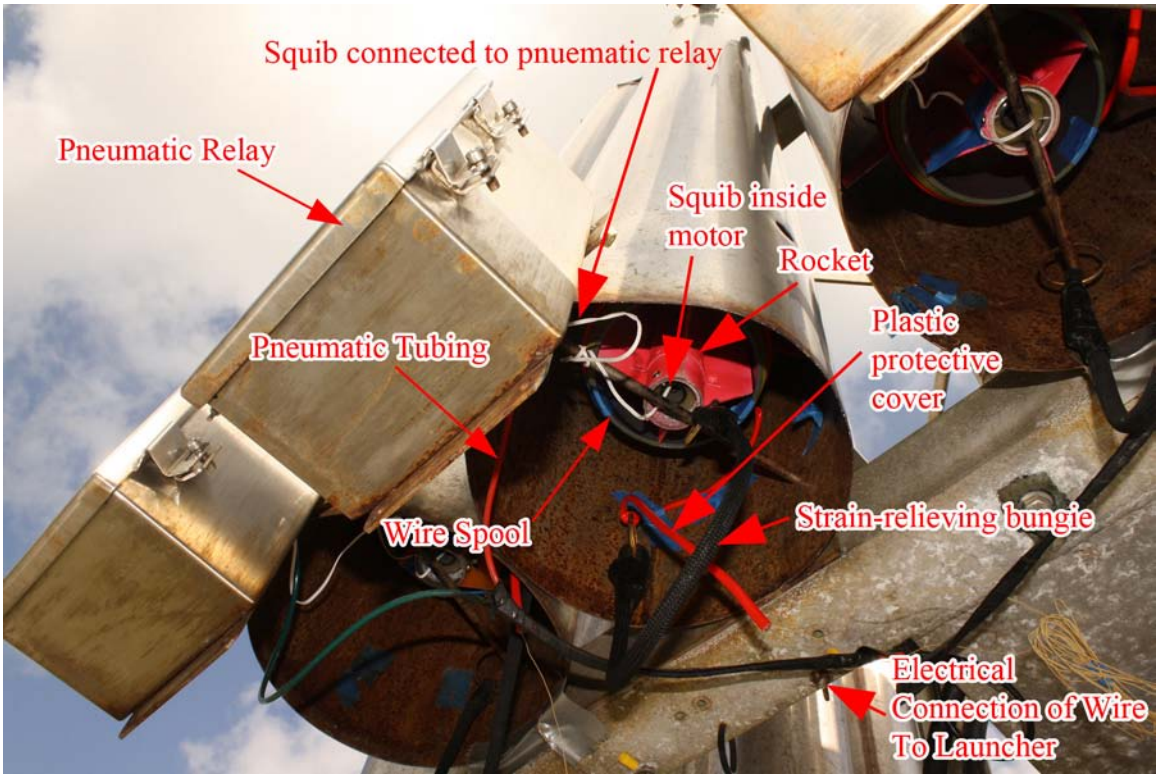


Figure 3-8. The bottom of the launch tubes showing a loaded rocket installation.

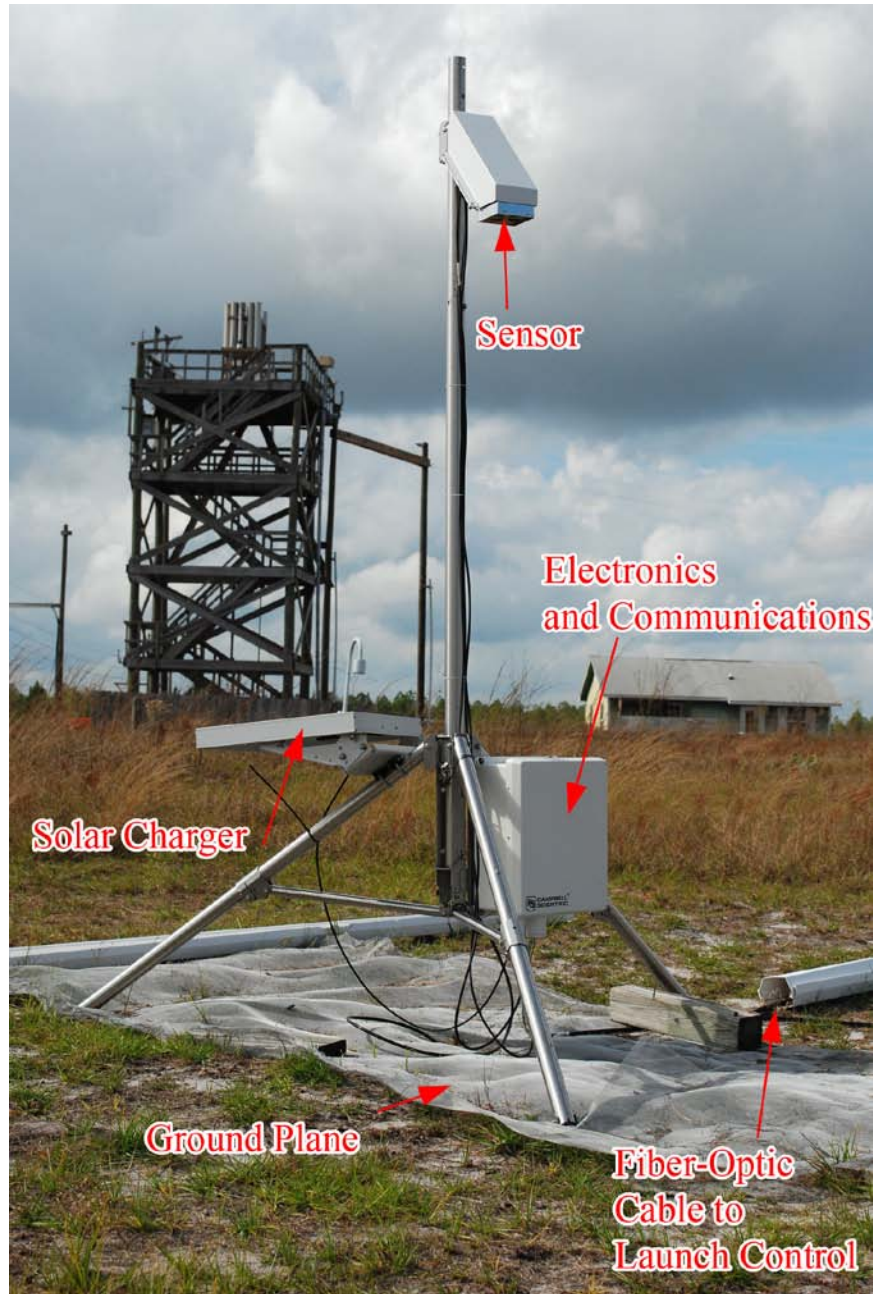


Figure 3-9. A Campbell Scientific field mill installation (LC field mill). The launch tower is visible in the background about 60 m away. Photograph taken by Dustin Hill.

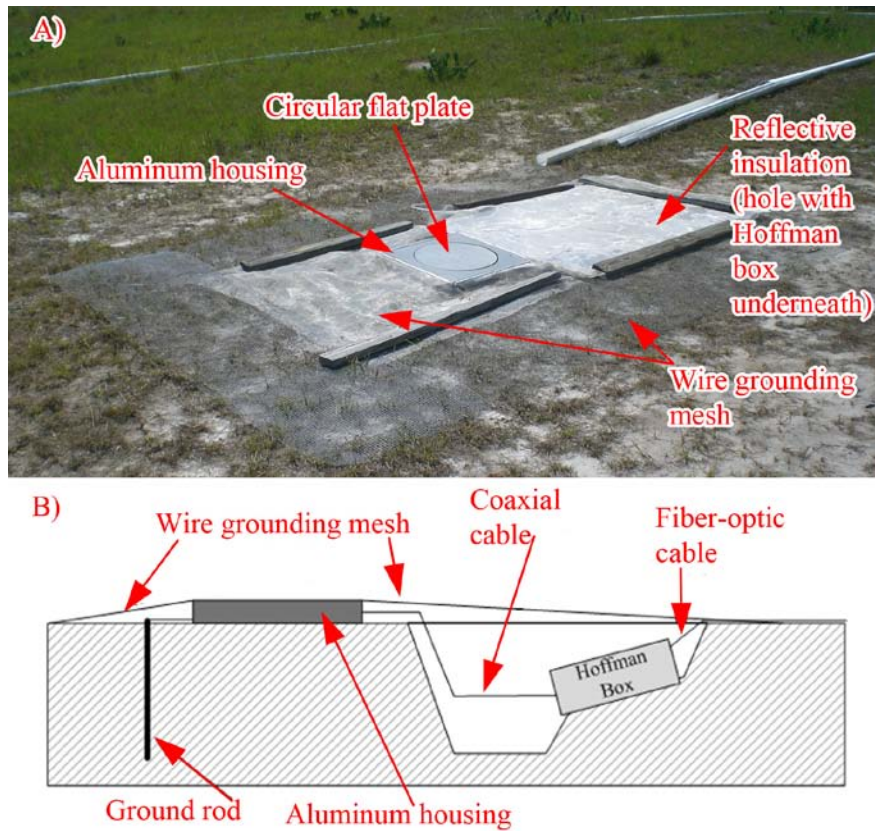


Figure 3-10. A field deployed flat-plate antenna sensor. A) Picture showing the typical flat plate antenna installation. B) Diagram showing the side view of the installation, including the Hoffman box underground.

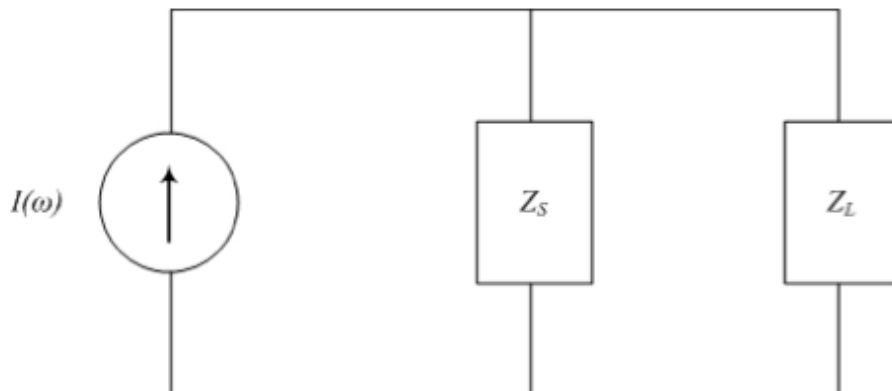


Figure 3-11. The frequency-domain Norton equivalent circuit for the flat-plate antenna.

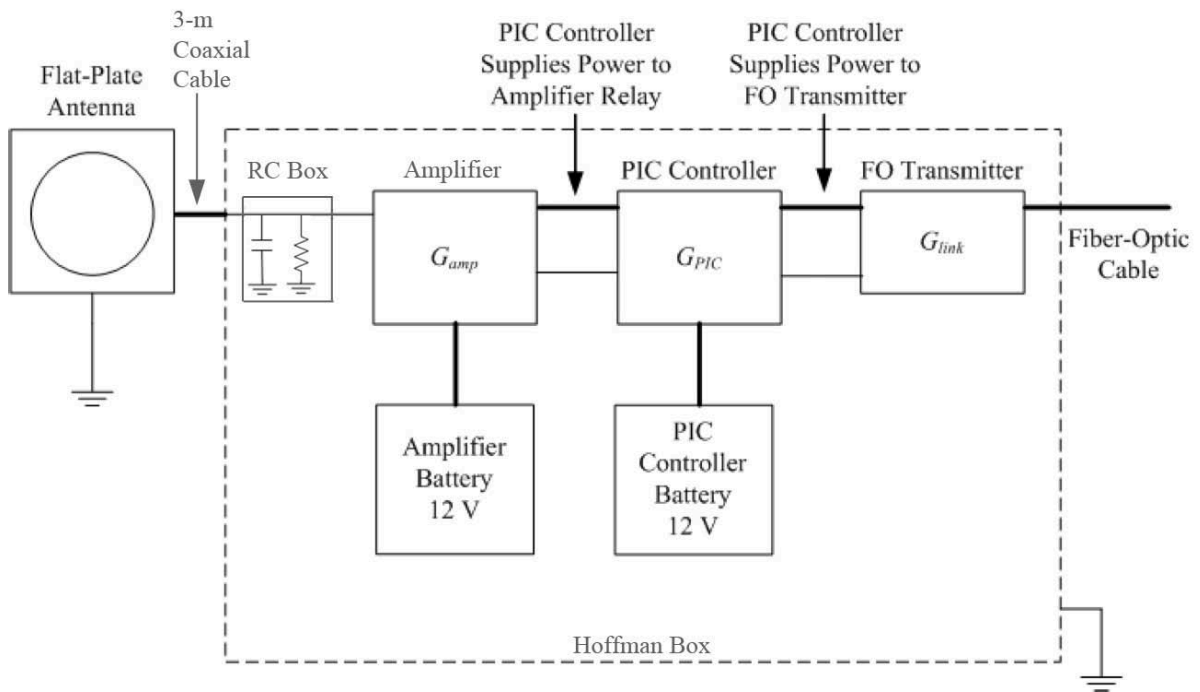


Figure 3-12. Schematic of an electric field sensor configuration.

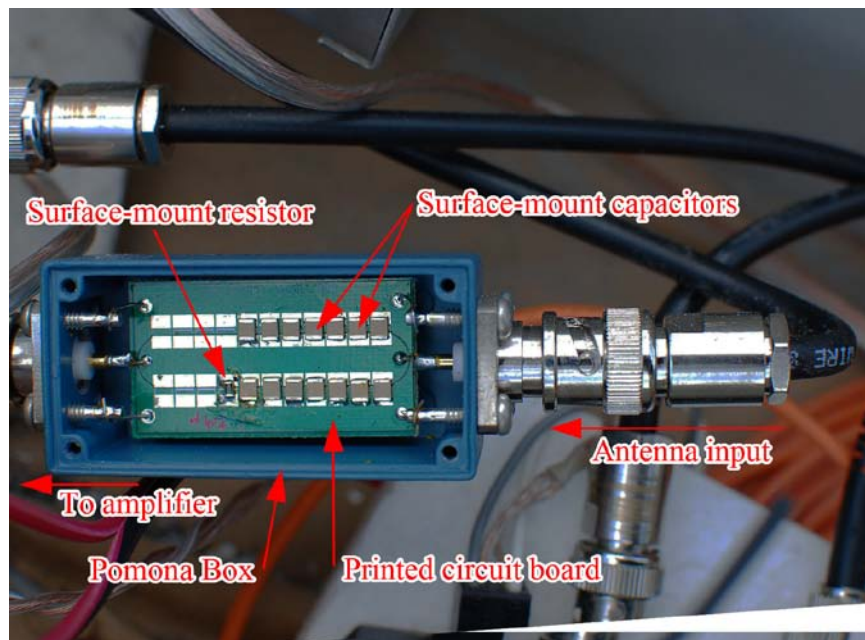


Figure 3-13. Picture of an RC box. Photograph taken by Dustin Hill

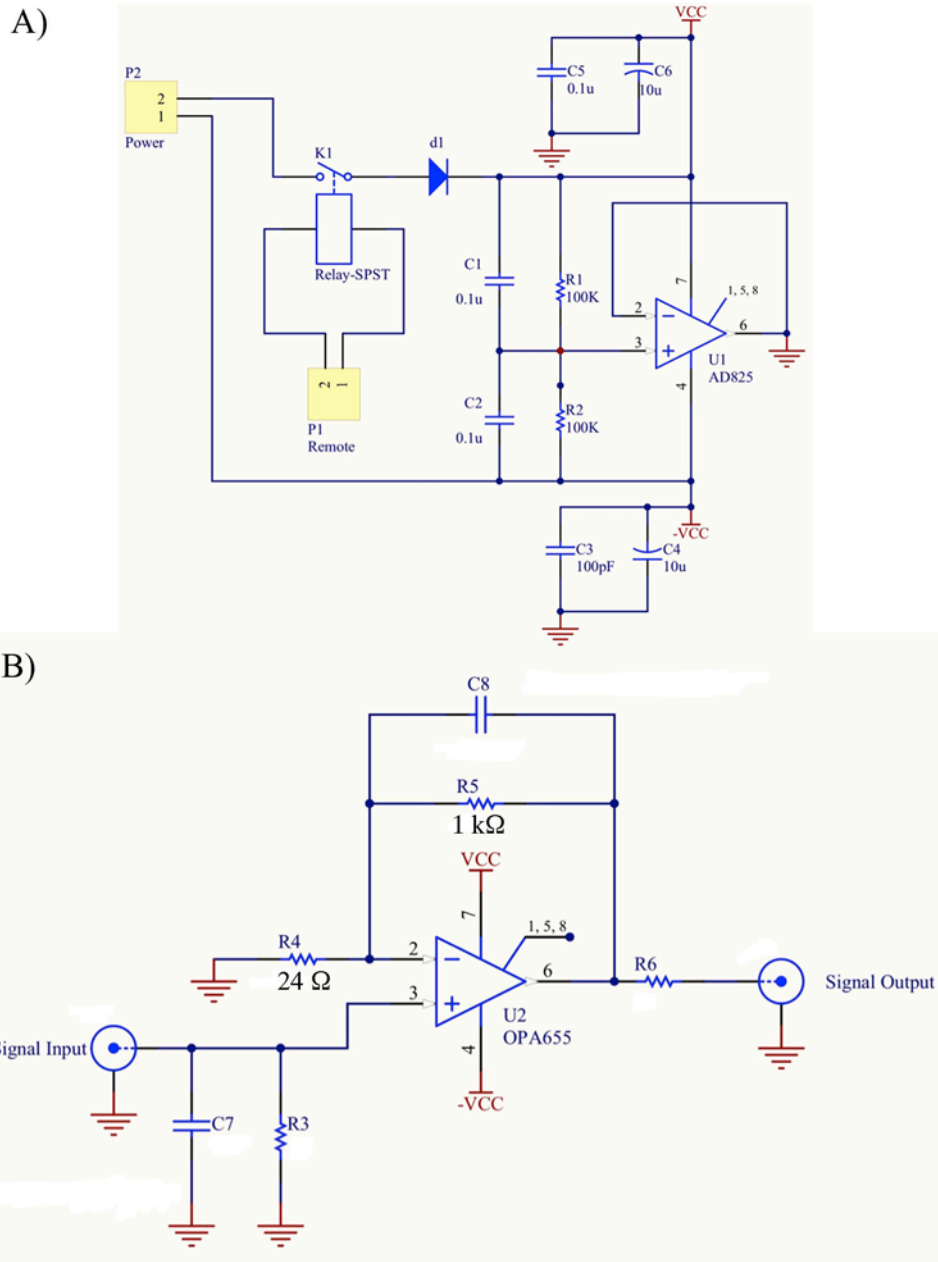


Figure 3-14. Circuitry of the amplifier used in the electric field and II-VLS current sensors. A) The rail-spitter circuit, and B) the non-inverting amplifier. Note that typical circuit element values are shown for, and that in the non-inverting circuit, C7, R3, C8, and R6 are not used (they were included in the design but ended up not being needed). The gain of the amplifier is  $(1+R5/R4)$ , which. If  $R5 = 1\text{ k}\Omega$  and  $R4 = 24\ \Omega$ , then the amplifier gain is about 42.6 (32.6 dB).

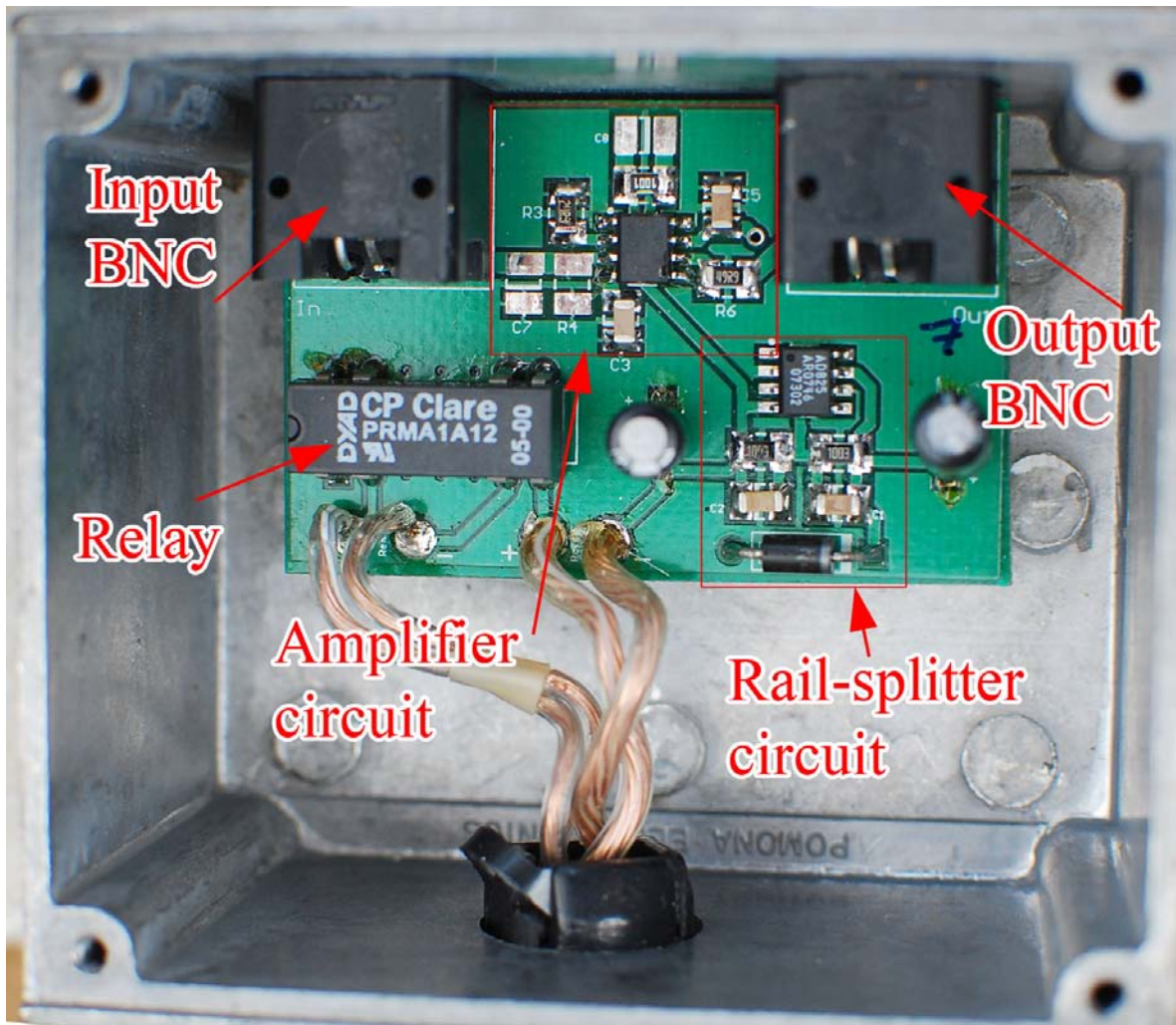


Figure 3-15. Amplifier circuit board mounted inside a Pomona box. Photograph taken by Dustin Hill.



Figure 3-16. Flat-plate antenna covered with a plastic dome.

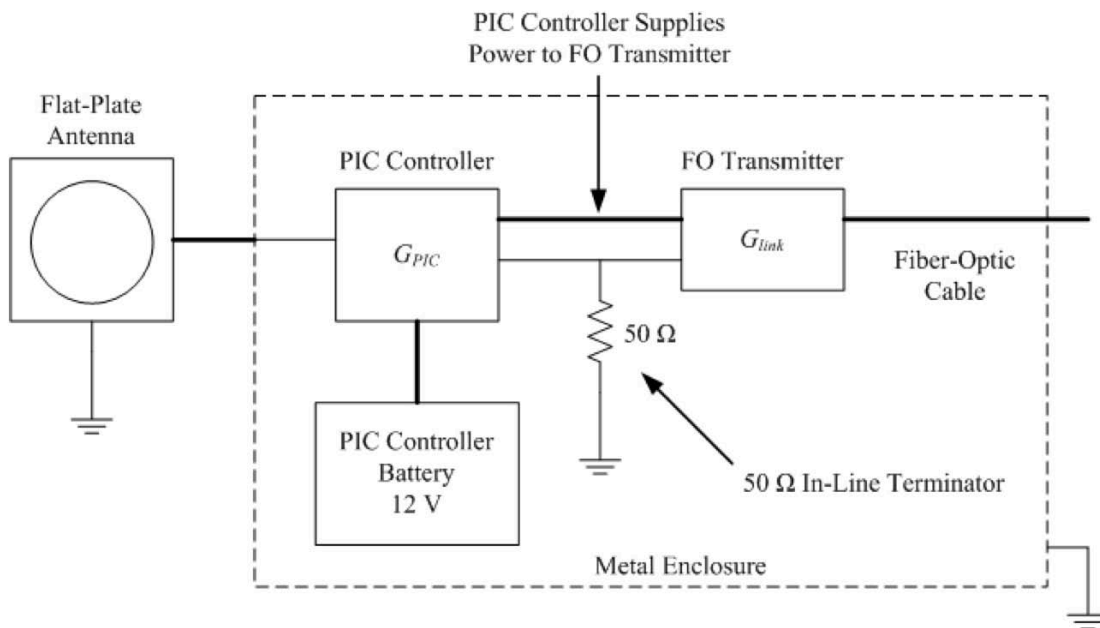


Figure 3-17. Schematic of the dE/dt measurement configuration. Taken from Howard [2009].

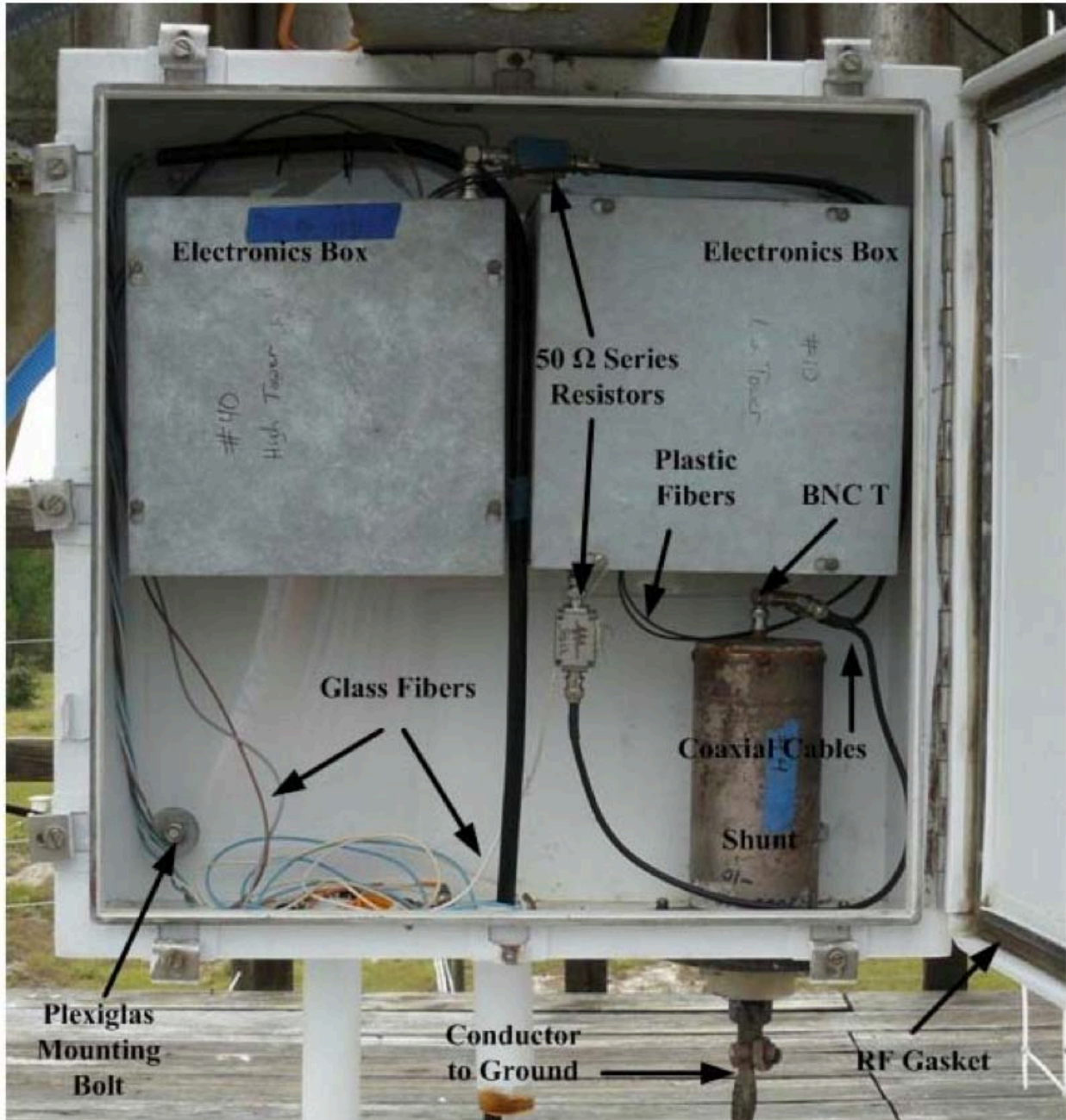


Figure 3-18. Inside the 2008 shunt box. The shunt is mounted to the box. The lightning current travels through the box, through the shunt, and down the conductor to ground. Adapted from *Howard* [2009].

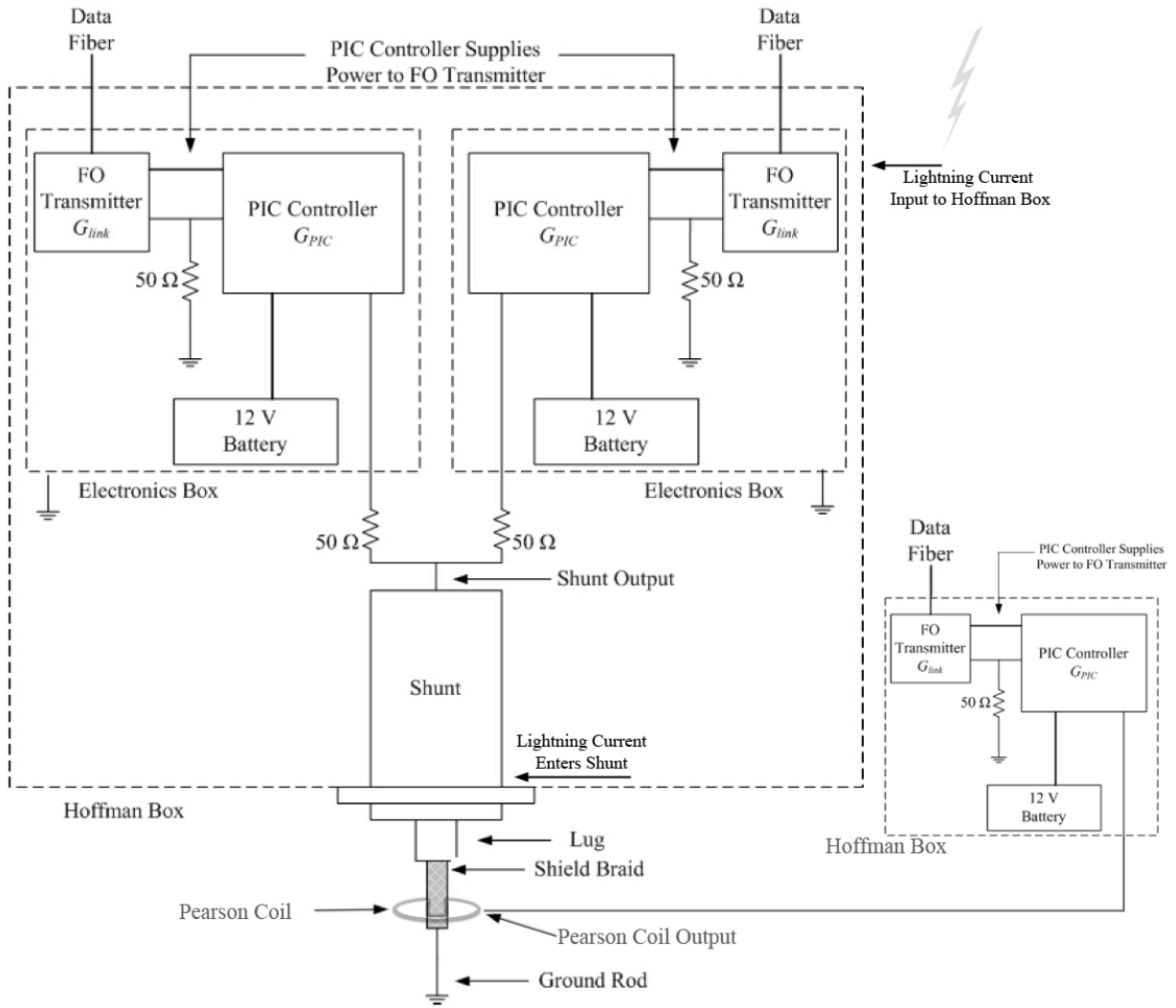


Figure 3-19. Current schematic for the 2008 current setup. This schematic applies for both the RS-path current measurement and the ICC-path current measurement. Lightning current travels through the Hoffman box into the shunt, and then to ground.



Figure 3-20. The 2009 tower current measurement configuration. Note the NASA experiment is not discussed here. Photography taken by Dustin Hill.

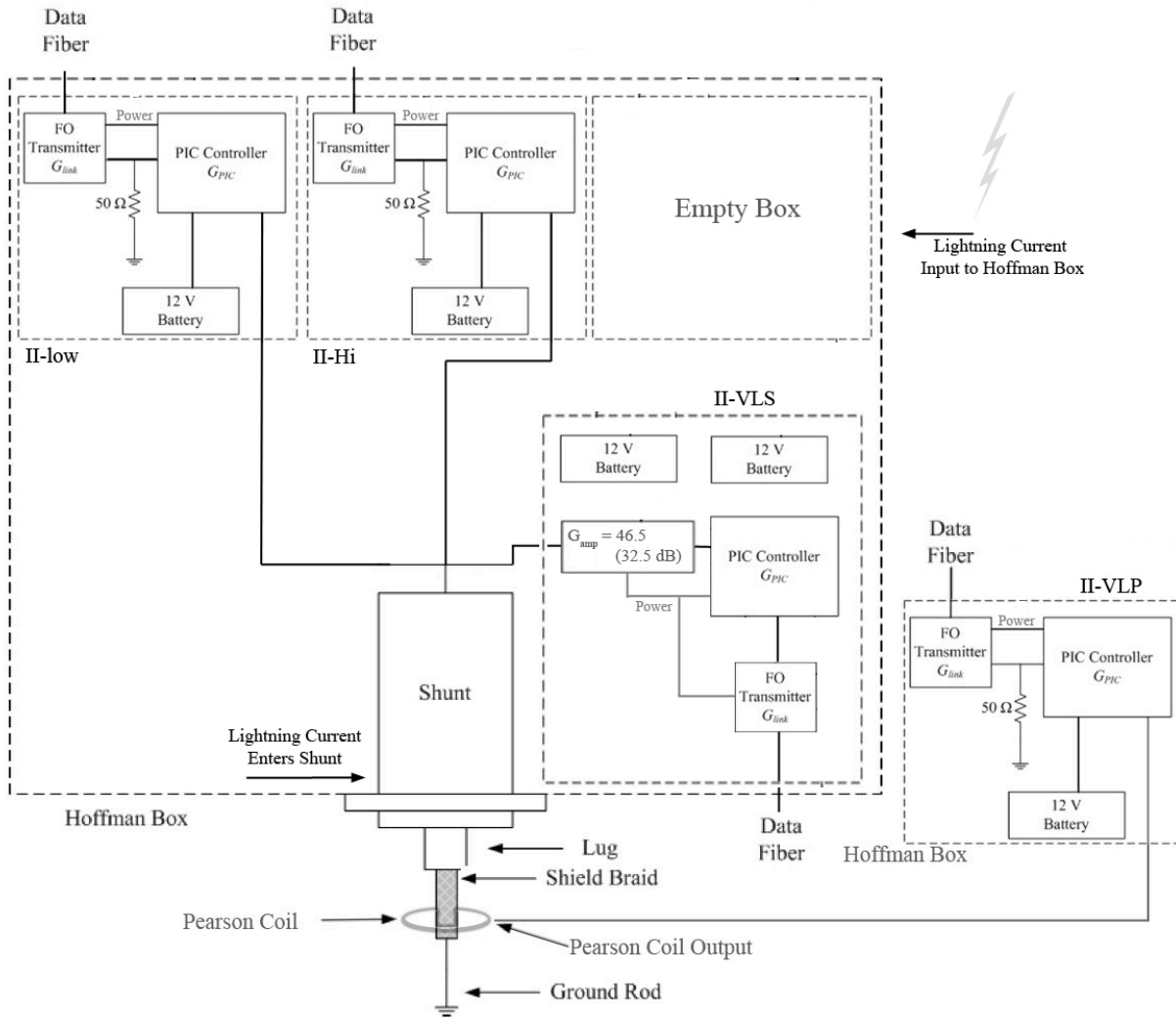


Figure 3-21. Schematic of the 2009 tower current configuration. Lightning current travels through the Hoffman box into the shunt, and then to ground.



Figure 3-22. The high-speed video cameras setup in the office trailer.



Figure 3-23. The Phantom V7.2 and the Photron SA1.1.

## CHAPTER 4 DATA

### 4.1 Summary of Collected Data

The data presented in this work were collected from triggered lightning flashes in 2008, 2009, and from a single flash (consisting of only an initial stage) that was triggered in September of 2010. In 2008, a total of 21 rockets were launched, which resulted in 11 triggered flashes (52% success rate). Of these 11 triggers, 7 had at least one return stroke, and the total number of return strokes was 36. The other four triggers consisted of only the initial stage. In 2009, a total of 43 rockets were launched, which resulted in 26 triggered flashes (60% success rate). Of the 26 triggers, 18 had at least one return stroke, and the total number of return strokes was 75. The other 8 triggers consisted of only the initial stage. Data from one triggered lightning in the 2010 season was used (in Chapter 7). Table 4-1 summarizes the triggered lightning statistics for 2008 and 2009. Table 4-2 summarizes for each triggered lightning in 2008 the dates, trigger times, number of return strokes, the ground-level quasi-static electric field magnitude at launch, and the type of high-speed video acquired. Tables 4-3 and 4-4 summarize the same information for each triggered lightning flash in 2009 and 2010. Tables 4-5 and 4-6 summarize the times and peak currents for each triggered return stroke in 2008 and 2009, respectively. Rocket-triggered flashes have been historically labeled with the nomenclature UFYY-FF, where UF indicates a rocket-triggered lightning, YY is the year, and FF identifies the shot attempt (rocket launch number) for that year; this convention is used in this work.

### 4.2 Data Processing

The binary files recorded by the Yokogawa and Lecroy digital storage oscilloscopes (DSOs), and the RAW format images files stored by the high-speed video cameras were read using MATLAB scripts. Additional scripts were written to create data displays, such as graphs

and image sequences. In general, a unique script was written for each graph or image sequence, although they had many common interchangeable algorithms. Some image processing, namely contrast enhancement and image-intensity inversion, was performed using Adobe Photoshop.

#### 4.2.1 Waveform Data

In order to use the waveform data (e.g., electric fields and current waveforms) for analysis and modeling purposes, it was necessary to: (1) apply the nominal calibration scaling factor,  $G_{\text{nom}}$ , to convert from digitizer volts to physical units (such as A for current), (2) adjust for the fiber optic link gain,  $G_{\text{link}}$ , and (3) remove artificial offset introduced by the fiber-optic link and/or DSOs,  $V_{\text{offset}}$ . The resulting of this process, described by

$$P = G_{\text{nom}} G_{\text{link}} (V_{\text{scope}} - V_{\text{offset}}) \quad 4-1$$

with  $V_{\text{scope}}$  being the voltage level digitized by the DSO, and  $P$  being the calibrated data in physical units. The value of  $G_{\text{link}}$  is determined from the 100 Hz, 1 V<sub>pp</sub> square wave signal recorded before and after a data recording session, as discussed in Section 3.2.3. The value of  $V_{\text{offset}}$ , when applicable, was typically determined by taking the average of at least 1000 sample points from an interval in which the true physical signal is believed to be zero, often at the beginning of a record. The value of  $G_{\text{link}}$  was determined by the following:

$$G_{\text{link}} = \frac{V_{\text{cal-expected}}}{0.5(V_{\text{cal-pre}} + V_{\text{cal-post}})} \quad 4-2$$

where  $V_{\text{cal-expected}}$  is the expected amplitude of the calibration signal (1 V) and  $V_{\text{cal-pre}}$  and  $V_{\text{cal-post}}$  are the actual amplitudes of the calibration signals recorded before and after a storm session, respectively. The values of  $V_{\text{cal-pre}}$  and  $V_{\text{cal-post}}$  were nearly always within a few tens of millivolts of each other. Note that in instances when only one calibration signal was recorded, its voltage

value was used for both  $V_{\text{cal-pre}}$  and  $V_{\text{cal-post}}$  in Equation 4-2. In cases when the calibration signal was not recorded,  $G_{\text{link}}$  was assumed to be the expected value.

#### **4.2.2 Image Data**

The image analysis performed in this work was essentially visual, and not numerical (such as using edge finding algorithms). Visual analysis is subject to interpretation, and it is important to do analysis using good-quality displays. Images will appear to the eye with more contrast on a liquid-crystal display (LCD) monitor than a cathode ray tube (CRT) monitor. Further, LCD monitors using in-plane switching (IPS) or pattern vertical alignment (PVA) technologies have far better contrast than an LCD using twisted nematic (TN) technology. Indeed, some features that are visible on an IPS or PVA display might not be evident on a TN display, even with contrast enhancement. Ambient background light can reduce the effect contrast of a computer display, so it is best to do computer image analysis in a dark room. All of the image analysis was performed on the raw images on an S-PVA (super pattern vertical alignment) LCD monitor, (Dell-2408WFP) with a maximum contrast ratio of 3000:1, typically in a darkened, windowless room.

Paper or photo hardcopies of images will clearly be influenced by the type of printer and paper that is used. In this work, and in the associated publications, the reproductions of high-speed video images were typically enlarged and contrast enhanced for improved visualization. In addition, the images were typically cropped horizontally to show only the region containing the lightning channel. All resolutions given throughout this work are vertical x horizontal. When making enlargements, an effort was made to use the same integer multiple in the vertical and horizontal direction, thereby retaining the resolution aspect ratio. For example, to double the size of an image (enlarge by 200%), the number of pixels in the horizontal and vertical direction were increased by a factor of two. Nearest neighbor interpolation (NNI) was used to determine

new pixel intensity values, which does a good job of preserving edges, and does not alter the intensity information. For example, In the case of 200% enlargement, 1 pixel becomes a 2 x 2 area of 4 pixels with the same intensity as the original pixel. NNI does not use any potentially distortion-introducing anti-aliasing filters which can distort the image. However, the high-speed video images and image sequences were often arbitrarily resized so that the horizontal dimension fit the page width, thus maximizing the image size and increasing the visibility of the luminous phenomena of interest. Any resized image displayed in a figure was compared with the raw image to ensure that the display faithfully represented the data in the raw image.

Unfortunately, there were some mistakes made when saving the high-speed video data. First, some of the Photron data were saved in 'RAW' file format, which, for the Photron, only supported 8-bit amplitude resolution, even though the data were recorded with 12-bit amplitude resolution. The Photron data must be saved using a special file format, designated 'RAWW', in order to preserve the 12-bit amplitude resolution. In the 'RAWW' file format, each 12-bit sample (corresponding to 1 pixel from 1 frame) were written to 2 bytes, with either the first or last four bits being set to zero. Second, the Photron software (PV3.2) allows the user to alter the intensity contrast, brightness and gamma, and features an option to save the data with these alterations, or without them. Before this save option was discovered, some Photron data were erroneously saved with altered intensity settings. The events for which these data-saving errors were made are noted in Tables 4-2 and 4-3.

Table 4-1. Summary of triggering in 2008 and 2009.

Description	2008	2009
Number of rockets launched	21	43
Total number of triggered lightning flashes	11	26
Number of flashes with initial stage only	4	8
Number of flashes with return strokes	7	18
Total number of return strokes	36	75

Table 4-2. Summary of data acquired in 2008.

Flash ID	Date (mm/dd/yy)	Time	Number of Strokes	E at launch (kV m <sup>-1</sup> ) <sup>a</sup>	UF Photron Data	OU Photron Data
UF08-02	06/10/08	19:32:16	5	N/A	No	No
UF08-04	06/29/08	21:36:29	IS-only	5.2	No	No
UF08-08	06/30/08	18:41:24	5	5.7	Yes <sup>b</sup>	No
UF08-11	07/12/08	17:52:49	3	5.9	Yes	No
UF08-12	07/23/08	18:40:21	IS-only	5.8	No	No
UF08-13	07/27/08	20:22:21	IS-only	6.2	No	No
UF08-17	09/11/08	20:36:56	IS-only	5.3	Yes	No
UF08-18	09/17/08	22:04:15	9	6.3	Yes <sup>b</sup>	Yes
UF08-19	10/09/08	18:11:39	3	5.4	No	No
UF08-20	10/09/08	18:24:15	9	5.3	Yes	Yes
UF08-21	10/09/08	19:17:48	2	5.2	Yes <sup>b</sup>	Yes

a) Ground-level electric field 60 m from the launch tower (physics sign convention). b) Data saved with altered intensity values.

Table 4-3. Summary of data acquired in 2009.

Flash ID	Date (mm/dd/yy)	Time	Number of Strokes	E at launch (kV m <sup>-1</sup> ) <sup>a</sup>	UF Photron Data	Phantom data
UF09-01	02/19/09	12:40:53	IS-only	4.5	No	Yes
UF09-04	02/19/09	13:04:05	IS-only	4.6	Yes	Yes
UF09-06	03/28/09	01:56:06	5	6.0	No	No
UF09-11	05/26/09	20:13:25	3	5.7	Yes <sup>b</sup>	Yes
UF09-12	05/26/09	20:31:21	1	5.1	Yes <sup>b</sup>	No
UF09-13	05/27/09	20:19:37	9	6.0	Yes <sup>b</sup>	Yes <sup>c</sup>
UF09-15	06/04/09	20:20:09	IS-only	6.0	No	Yes
UF09-17	06/04/09	20:37:13	5	6.0	Yes <sup>c</sup>	Yes
UF09-20	06/18/09	16:35:03	4	7.4	Yes	Yes
UF09-21	06/18/09	16:44:42	IS-only	3.2	No	Yes
UF09-22	06/18/09	16:58:11	8	5.6	Yes <sup>c</sup>	Yes
UF09-25	06/29/09	21:09:17	5	5.9	Yes	No
UF09-26	06/29/09	21:18:32	5	5.5	Yes	Yes
UF09-27	06/29/09	21:31:18	7	4.9	Yes	Yes
UF09-29	06/30/09	13:49:17	5	8.5	Yes	Yes
UF09-30	06/30/09	14:01:04	1	7.2	Yes	Yes
UF09-31	06/30/09	14:12:14	5	8.1	Yes	Yes
UF09-32	07/07/09	15:12:54	1	6.5	Yes	Yes
UF09-34	07/09/09	17:15:34	4	5.6	No	No
UF09-35	07/14/09	21:07:58	IS-only	6.4	No	Yes
UF09-37	07/14/09	21:21:21	IS-only	6.6	No	Yes
UF09-38	07/14/09	21:25:15	1	6.7	No	No
UF09-40	07/18/09	15:25:01	IS-only	5.2	No	Yes
UF09-41	08/18/09	16:22:25	IS-only	6.4	No	No
UF09-42	08/18/09	16:24:42	1	7.6	No	Yes
UF09-43	08/18/09	16:30:09	5	7.3	No	No

a) Ground-level electric field 60 m from the launch tower (physics sign convection). b) Data save with 8-bit resolution. c) Data saved with altered intensity values.

Table 4-4. Summary of the triggered lightning flash from 2010.

Flash ID	Date (mm/dd/yy)	GPS time	E at launch (kV m <sup>-1</sup> ) <sup>a</sup>
UF10-25	09/27/10	18:34:20.558752	5.1

a) Ground-level electric field 60 m from the launch tower (physics sign convention).

Table 4-5. Summary of return stroke times and peak currents in 2008. Instances when return-stroke peak currents were not available are marked with N/A.

Flash ID	Date (mm/dd/yy)	Hour	Minute	Second	Stroke	Peak Current (kA)
UF08-02	06/10/08	19	32	16.546405	1	18.7
		19	32	16.677830	2	8.0
		19	32	16.708177	3	22.0
		19	32	16.818693	4	14.0
		19	32	16.828135	5	4.3
UF08-08	06/30/08	18	41	28.958560	1	23.5
		18	41	29.013714	2	13.3
		18	41	29.078171	3	10.8
		18	41	29.204311	4	13.4
		18	41	29.293099	5	11.4
UF08-11	07/12/08	17	52	49.133847	1	17.7
		17	52	49.161172	2	10.7
		17	52	49.188131	3	11.7
UF08-18	09/17/08	22	4	17.637823	1	11.1
		22	4	17.661084	2	8.5
		22	4	17.695004	3	20.5
		22	4	17.757405	4	15.6
		22	4	17.810386	5	N/A
		22	4	17.895307	6	7.3
		22	4	17.909987	7	N/A
		22	4	18.079641	8	N/A
		22	4	18.094242	9	N/A
UF08-19	10/09/08	18	11	42.973488	1	16.0
		18	11	43.032189	2	15.0
		18	11	43.208505	3	19.0
UF08-20	10/09/08	18	24	18.355067	1	8.1
		18	24	18.361326	2	4.7
		18	24	18.387358	3	9.1
		18	24	18.393885	4	5.3
		18	24	18.440662	5	12.4
		18	24	18.534700	6	11.2
		18	24	18.610483	7	11.8
		18	24	18.703408	8	6.2
		18	24	18.837247	9	13.4
UF08-21	10/09/08	19	17	51.975022	1	8.6
		19	17	52.060087	2	18.0

Table 4-6. Summary of return stroke times and peak currents in 2009. Instances when GPS times or return-stroke peak currents were not available are marked with N/A.

Flash ID	Date (mm/dd/yy)	Hour	Minute	Second	Stroke	Peak Current (kA)
UF09-06	03/28/09	N/A	N/A	N/A	1	16.8
		N/A	N/A	N/A	2	7.6
		N/A	N/A	N/A	3	11.9
		N/A	N/A	N/A	4	6.0
		N/A	N/A	N/A	5	8.9
UF09-11	05/26/09	20	13	28.061461	1	N/A
		20	13	28.087430	2	N/A
		20	13	28.219430	3	N/A
UF09-12	05/26/09	20	31	23.496924	1	34.5
UF09-13	05/27/09	20	19	37.082304	1	N/A
		20	19	37.084693	2	N/A
		20	19	37.091822	3	N/A
		20	19	37.094276	4	N/A
		20	19	37.097406	5	N/A
		20	19	37.098878	6	N/A
		20	19	37.457390	7	N/A
		20	19	37.498066	8	N/A
		20	19	37.569844	9	N/A
UF09-17	06/04/09	20	37	13.416051	1	22.8
		20	37	13.562980	2	21.0
		20	37	13.571341	3	4.9
		20	37	13.583893	4	21.9
		20	37	13.650808	5	44.8
UF09-20	06/18/09	16	34	3.119539	1	14.4
		16	34	3.215808	2	20.0
		16	34	3.266208	3	14.6
		16	34	3.357608	4	7.9
UF09-22	06/18/09	16	58	10.997707	1	15.5
		16	58	11.027656	2	11.6
		16	58	11.153341	3	9.4
		16	58	11.161657	4	8.9
		16	58	11.225880	5	10.7
		16	58	11.229780	6	3.1
		16	58	11.398570	7	2.9
		16	58	11.419171	8	10.8
UF09-25	06/29/09	21	9	17.612277	1	15.7
		21	9	17.778748	2	9.1
		21	9	18.232577	3	16.3
		21	9	18.280832	4	18.8
		21	9	18.641641	5	31.6

Table 4-6 Continued.

Flash ID	Date (mm/dd/yy)	Hour	Minute	Second	Stroke	Peak Current (kA)
UF09-25	06/29/09	21	9	17.612277	1	15.7
		21	9	17.778748	2	9.1
		21	9	18.232577	3	16.3
		21	9	18.280832	4	18.8
		21	9	18.641641	5	31.6
UF09-26	06/29/09	21	18	36.306798	1	26.6
		21	18	36.327519	2	11.4
		21	18	36.605640	3	11.6
		21	18	36.716802	4	23.2
		21	18	36.786340	5	13.7
UF09-27	06/29/09	17	31	23.005941	1	8.4
		17	31	23.049751	2	15.4
		17	31	23.080486	3	11.8
		17	31	23.097855	4	10.1
		17	31	23.111993	5	5.6
		17	31	23.230472	6	15.6
		17	31	23.320614	7	28.3
UF09-29	06/30/09	13	49	17.096270	1	10.5
		13	49	17.253414	2	11.5
		13	49	17.281337	3	11.4
		13	49	17.427614	4	15.6
		13	49	17.487826	5	18.9
UF09-30	6/30/09	14	1	4.391149	1	30.6
UF09-31	6/30/09	14	12	24.486065	1	6.4
		14	12	24.510480	2	13.6
		14	12	24.568247	3	11.1
		14	12	24.583725	4	6.4
		14	12	24.596714	5	7.5
UF09-32	07/07/09	15	12	57.261135	1	19.5
UF09-34	07/09/09	17	15	40.445418	1	11.5
		17	15	40.457757	2	6.3
		17	15	40.752652	3	15.2
		17	15	40.842385	4	16.4
UF09-38	07/14/09	21	25	18.526361	1	28.0
UF09-42	08/19/13	16	24	41.585945	1	14.7
UF09-43	08/19/13	16	30	12.252596	1	24.9
		16	30	12.309397	2	9.5
		16	30	12.432971	3	9.5
		16	30	12.500518	4	9.6
		16	30	N/A	5	N/A

CHAPTER 5  
OBSERVATIONS OF LIGHTNING LEADERS WITH HIGH-SPEED VIDEO AND  
CORRELATED CHANNEL-BASE CURRENT, REMOTE ELECTRIC FIELDS, AND X-RAY  
EMISSION

Streak photography on film has historically been the most common method of obtaining time and space resolved optical measurements, both for rocket-and-wire triggered and natural lightning [e.g., *Schonland*, 1956; *Berger and Volgensager*, 1966; *Orville and Idone*, 1982; *Jordan et al.*, 1992; *Rakov et al.*, 2003; *Olsen et al.*, 2006]. The use of photodiode arrays has offered an alternate method of obtaining high-speed optical measurements [e.g., *Yokoyama et al.*, 1990; *Wang et al.*, 1999a, 1999b, 1999c; *Olsen et al.*, 2004; *Lu et al.*, 2008], generally exhibiting an order of magnitude faster time-resolution than streak photography, but with poorer spatial resolution and more ambiguity in the data interpretation. High-speed digital video photography is a relatively new technology that provides optical data with both relatively high time and spatial resolution [e.g., *Ballarotti et al.*, 2005; *Qie and Kong*, 2007; *Saba et al.*, 2008; *Zhang et al.*, 2009; *Kong et al.*, 2009; *Warner et al.* 2011]..

In this chapter, original observations of lightning leaders with high-speed video observations along with correlated channel-base current, remote electric fields, and x-ray emissions are presented. The major findings of the work presented in this chapter include: (1) Observations showing that negative lightning leaders do in fact develop through stepping mechanisms that are very similar, if not identical to, laboratory long spark leaders. (2) An upward positive leader was observed with high-speed video and correlated wire-base current developing in a stepped manner from a triggering wire. (3) Positive upward connecting leaders (in triggered lightning) have been imaged for the first time with high-speed video cameras, including eight strokes in a single flash. One image was recorded just prior to the attachment process, when the streamer zone of the downward negative leader was close to or in contact with

the positive upward connecting leader. Much of the content in this section has been published by the author in two journal articles [*Biagi et al.*, 2009; *Biagi et al.*, 2010] and, at the time of writing this dissertation, some of the other material is being prepared for publication. In this chapter, a positive electric field at ground corresponds to the electric field vector pointing downward (atmospheric sign convention), and positive current and positive electric field change at ground correspond to the removal of negative charge from or the deposition of positive charge in the atmosphere.

### **5.1 Observations of a Stepped Upward Positive Leader Initiating Triggered Lightning**

The upward positive leader that initiated the triggered flash UF09-30 began its development when the wire tip height was about 123 m. As a result, the lower 12 m of the upward positive leader was imaged by the Photron camera that was operating at 300 kfps (3.3  $\mu$ s per frame). In addition, the lower 200 m or so of upward positive leader was imaged by the Phantom camera operating at 8 kfps (120  $\mu$ s per frame). Example images from the Phantom and Photron are shown in Figure 5-1A and Figure 5-1B, respectively. The Photron camera was slightly tilted with respect to the Phantom, and its field of view is identified in Figure 5-1A as a darker region. As is evident in Figure 5-1, the Photron viewed mostly triggering wire. The upward positive leader developed only in the upper right region of the Photron image. The Photron recorded a total of 60 images in 200  $\mu$ s before the upward positive leader propagated out of the camera's field of view. The upper right, 13 m x 5 m region viewing of the upward positive leader in these 60 images are arranged in a sequence of three rows in Figure 5-2, increasing in time from left to right and from top to bottom. The leader channel lengths after each new step are displayed in Figure 5-2, and given in Table 5-1. The wire-base current recorded by the II-VLS measurement is also shown in Figure 5-2 (with a time scale that is aligned with the high-speed video frames). The II-VLS measurement saturated at about  $\pm 21$  A.

However, most of the current pulses were resolved by the II-Lo current measurement, which is shown in Figure 5-3 on approximately the same time scale as the current plots in Figure 5-2. The steps in Figures 5-2 and 5-3, and Table 5-1, are identified by lower-case letters near the respective current pulses.

Several interesting observations can be made from the data presented in Figures 5-2 and 5-3 and the measurements summarized in Table 5-1. The upward positive leader developed to about 11 m in length in 8 distinct steps (steps a through h), with step lengths that ranged from 0.8 m to 2.2 m with a mean value of 1.5 m. The channel diameter for the first step appears to illuminate two pixels, or a width of up to 0.88 m. It is difficult to resolve the channel diameter in successive steps, but it appears to never exceed two pixels. However, the channel appears to have lower luminosity on each side extending out 1 pixel, or about 0.44 m. This luminosity may be camera blooming, or evidence of a corona sheath. The leader extended upward with an overall speed of  $5.5 \times 10^4 \text{ m s}^{-1}$  in its first 11 m of development, and by the time the leader exited the Phantom field of view at an altitude of about 310 m, the leader development speed had increased to  $2.1 \times 10^5 \text{ m s}^{-1}$ . Steps e, f, g, and h developed in two high-speed video frames. In the first frames for Steps f, g, and h, isolated luminosity appears first at the top of previously formed channel segment (with no separation between the two), followed by a re-illumination of the previously established channel in the following frame, indicating that a current wave was generated at the leader tip that travels down the channel. The bottom end of the newly formed steps was always at the upper end of the previously established leader. The interstep time interval (determined from the time between current pulses) ranged from 16.6 to 30.4  $\mu\text{s}$  with a mean value of 21.1  $\mu\text{s}$ .

It is evident in Figures 5-2 and 5-3 that a single current pulse is detected at the wire base for each step observed in the high-speed video images. The incident current pulse that is injected into the leader and wire by each step is likely unipolar with a full width on the order of several microseconds, as is shown in the modeling detailed in Section 6.4 of this work for similar current pulses produced by precursors (precursors are usually leader channels that stop developing after a few meters). Owing to transmission-line effects, what is measured at the wire base is a single current pulse exhibiting more or less damped-oscillatory behavior. The first peak of the damped-oscillatory signature that is measured at the wire base is the superposition of the current pulse that was generated at the wire tip after having traveled down the wire, and a reflected current pulse of the same polarity from the approximately short-circuit termination at the ground rod. During the time when the first current pulse is flowing through the wire base, there are several sequences of current pulse reflections from the ground and wire tip, and a polarity reversal occurs with each wire-tip reflection. These reflected current pulses superimpose with the original unipolar pulse, yielding the oscillatory behavior. The magnitude of successive reflected current pulses are increasingly smaller due to energy losses associated with the wire, and absorption by the leader and ground.

With the exception of Steps d and e, the current pulses detected at the wire base become smoother and less oscillatory as the leader grows in length. It is reasonable to assume that the electrical characteristics of the triggering wire did not change in the 200  $\mu$ s during which the steps occurred, nor does the wire length or the grounding impedance. Under these assumptions, the change in the current pulses detected at ground can be attributed to the upward developing leader channel increasingly attenuating successive current pulse reflections.

The measured peak currents for Steps a through j, determined from the II-Lo current record shown in Figure 5-3, are given in Table 5-1, and they ranged from 17 to 153 A with an arithmetic mean of 59 A. As discussed above, and shown via the modeling in Section 6.4, the current peak at the wire base is most likely not the same as the peak of the incident current due to transmission-line effects. The incident current peaks can be estimated by scaling the measured wire-base current peaks to account for the propagation losses in the wire and the current reflection from ground using Equation 6-16. Using the values determined in the analysis of Section 6.4.3,  $\alpha = 8.2 \times 10^{-4} \text{ Np m}^{-1}$ ,  $\Gamma_G = 0.9$ , and a wire length of 123 m, Equation 6-16 predicts that the currents should be scaled by a factor  $G = 0.58$ . The scaled peak current amplitudes are given in Table 5-1, and they ranged from 10 to 89 A with an arithmetic mean of 34 A.

The apparent charges associated with Steps a, b, d, e, f and g were estimated by computing the time integral of the current signature in the II-Lo measurement from the beginning of the current pulse to the time when the reflections drop below the noise floor. The charge for Step i was computed from the II-VLS measurement. The charge cannot be computed for Steps c, h, and i because their signal to noise ratio is too low. The unscaled current is used for this computation, and it is assumed that, by the end of the damped oscillatory signature, a charge is lowered to ground that is equal to the charge deposited by the new leader step (but of opposite polarity). This computation is similar to what is done for precursors in Section 6.3.2. The charges for the current pulses associated with the ten steps in Figure 5-2 and 5-3 are given in Table 5-1, and ranged from 22 to 107  $\mu\text{C}$  with an arithmetic mean of 64  $\mu\text{C}$ . The ratio of the step charges to the step lengths ranged from 26 to 110  $\mu\text{C m}^{-1}$  with an arithmetic mean of 51  $\mu\text{C m}^{-1}$ .

## 5.2 Observations of Leader Stepping Mechanisms

### 5.2.1 Dart Stepped Leaders in Classical Triggered Lightning

**UF08-18.** There were two downward negative dart-stepped leaders in two different triggered lightning flashes for which the streamer zone (as defined in Section 2.4) ahead of the leader tip and stepping mechanisms were particularly well resolved. The first was the eighth return stroke of flash UF08-18, which is presented in *Biagi et al.* [2009]. This stroke occurred about 444 ms after the first stroke, 170 ms after the fourth stroke and 830 ms after the triggering wire exploded during the initial stage of the flash. Two 20- $\mu$ s frames of the dart-stepped leader were imaged by the Photron preceding this stroke. True value and intensity-inverted value images for both frames (not subtracted) are shown in Figure 5-4, along with 100  $\mu$ s of current (RS-VL) and electric field (E6) data (in Panel E) with time zero corresponding to return stroke 8. The corresponding pulses in electric field and current seen in 5-4E confirm that the leader in fact developed through steps. Note that the second frame in Figure 5-4 (shown as panel C and D) is also shown in Figure 5-18. As seen in Figure 5-4, a 7 m long streamer zone is visible at the top of the second frame before return stroke 8 (panels A and B). In the next frame, the downward leader extended about 25 m into the frame. If the leader is just above the image two frames before the return stroke, the leader traveled 25 m in two frames (20-40  $\mu$ s), and hence its speed was between  $1.25 \times 10^6 - 2.5 \times 10^6 \text{ m s}^{-1}$ . The downward leader observed one frame prior to the return stroke in Figure 5-4 has several short branches along its path that emanate corona streamers up to 5 m long. An upward connecting leader that is 16 m long is also visible (and discussed further in Section 5.4). The downward and upward connecting leaders are about 15 m apart in the frame, and there is a low level of luminosity connecting them (that was not remnant channel luminosity from return stroke 7), apparently indicating that the downward streamer zone has reached the upward connecting leader. In the frame prior to the eighth return stroke of

UF08-18 (panels C and D of Figure 5-4), a luminous segment about 2 m in length that is brighter than the surrounding streamer zone is apparent, with its lowest point being about 4 m below the downward leader. It is thought this is a space stem or space leader that helped initiate the next step of the downward stepped leader (*Biagi et al.* [2009] termed it a space stem). As is noted in Section 2.4.2, the positive, cathode-directed end of the space leader (the upper end) develops with a speed about three times greater than that of the negative, anode-directed end (the bottom end) [e.g., *Les Renardieres Group*, 1981; *Ortega et al.*, 1994]. Thus, if the upper end developed 3 m upward before connecting to the primary leader, then the lower end likely developed downward an addition 1 m. Based on these rough calculations, the space leader is thought to have extended the channel by 5 or 6 m, and it probably was not involved with the attachment to the upward positive connecting leader.

**UF09-25.** The second dart-stepped leader in a triggered lightning flash with well-resolved stepping mechanisms preceded return stroke 5 of UF09-25. This stroke occurred about 1.029 s after the first stroke, 361 ms after the fourth stroke and 1.560 s after the triggering wire exploded during the initial stage of the flash. The long time interval between the wire destruction and the fifth stroke makes it unlikely that significant copper residue from the destroyed triggering wire was present along the leader path. Figure 5-5 shows a sequence of the ten high-speed video frames depicting the leader descending from 150 m to 11 m above ground level, with time increasing from left to right in 4.17  $\mu$ s intervals. The frames span about 21 m horizontally, and have heights labeled in 10 m increments. In the first nine frames the leader descended from 150 m to 47 m with an average speed that was between  $2.7 \times 10^6$  and  $3.4 \times 10^6$  m s<sup>-1</sup>, depending on when the leader first reached 150 m and 46 m during the integration times of Frames 1 and 9, respectively. The leader speed may have increased in the lower 45 m of development during the

integration of Frames 9 and 10, either because the leader accelerated (an actual increase), or because an upward positive connecting leader intercepted the downward leader (an apparent increase), although there is no optical evidence of the latter having occurred. The large increase in luminosity in the lower 40 m seen in Frame 10 is from the beginning stage of the upward-propagating return-stroke current wave. Frame 11 (not shown here) was completely saturated by return stroke luminosity.

The features of most interest in Figure 5-5 are the luminous segments of channel (identified by white arrows and labeled with lower-case letters) that are separate from and below the primary leader channel. The sections of the frames just below the leader tip are shown expanded by a factor of 4 and contrast-enhanced in Figure 5-6. Table 5-2 gives the distances between the lower tip of the primary channel and the lower tip of the segment, and the length of the segments. The luminous segments ahead of the leader tip in Frames 4 (segment d), 5 (segment g), 7 (segments h and i), and 8 (segment j) had a luminance about equal to that of the leader channel; these are thought to be space leaders. When they were imaged, the lengths of the space leaders ranged from 1 to 4 m, and their lower tips were between 4 and 12 m below the primary channel. The other luminous segments in Frames 1, 2, 3, 4 (segments a, b, c, and e), 5 (segment f) and 8 (segment k) were less well defined and significantly less luminous than the leader channel, although still more luminous than the surrounding corona streamers; these are thought to be space stems. When they were imaged, the lengths of the space stems ranged from 1 to 2 m, and their lower tips were between 2 and 8 m below the primary leader channel. Lower-luminosity corona and forked corona streamers are present in the vicinity of the leader tip that apparently did not develop in a direction greater than 60 degrees from vertical, best seen in the expanded and contrast-enhanced image 2 in Figure 5-6.

Figure 5-7 shows the deposited x-ray energy (A), time-derivative electric field (B), and launch tower current (C) during the time when the ten high-speed video frames were recorded (frame intervals are shown at the top of the figure,  $\pm 4.17 \mu\text{s}$ ). Positive  $dE/dt$  and current correspond to negative charge moving downward or positive charge moving upward. The return stroke began just after time zero. There were 10 distinct pulses in the  $dE/dt$  record that were likely produced by leader steps, and there was a “leader burst” [Howard *et al.*, 2010; Murray *et al.*, 2005] about  $1 \mu\text{s}$  before the return stroke began. In each of the 10  $dE/dt$  pulses, there were one to three secondary peaks following and/or preceding the largest peak. Corresponding current pulses were measured between the launch tubes and ground before the current sensor electronics saturated (at about  $-10 \mu\text{s}$ ), and each had one to two peaks with timing that matched that of the peaks in  $dE/dt$ . A low-amplitude, steady-state current apparently began to flow after the pulse at  $-30 \mu\text{s}$ , most likely due to corona emission from the tower since there was no optical evidence of an upward positive connecting leader. Corresponding x-ray pulses were recorded for five of the  $dE/dt$  and current pulses, although the timing of the secondary x-ray peaks did not always match that of the  $dE/dt$  peaks. For example, the inset plots in Figure 5-7 show on a  $2\text{-}\mu\text{s}$  time scale a pulse in x-ray,  $dE/dt$ , and current that occurred at  $-17 \mu\text{s}$ . The  $dE/dt$  pulse had one primary and two secondary peaks, the current had two corresponding peaks, and there was only one x-ray peak.

### 5.2.2 Downward Negative Stepped Leader in Altitude Triggered Lightning

**UF09-13.** Event UF09-13 was an attempt at classical triggering lightning that resulted in an altitude trigger after the wire broke during the rocket ascent. The wire extension began when the electric field magnitude at ground was about  $-6 \text{ kV m}^{-1}$ . The triggered lightning included 9 leader/return stroke sequences. Figure 5-8 shows a picture of the lightning channel from a high-definition (HD, 1080i resolution) camera operating at framing rate of 30 fps (33 ms per

frame). The HD image shows the lower portion of the exploded triggering wire with its bottom at a height around 133 m. The downward-negative stepped leader developed from the bottom of the triggering wire and developed towards the launch trailer (about 50 m to the north of the launch tower). The lightning struck one of the lightning rods connected to the catenary wires that protect the launch trailer from a strike. The white box in Figure 5-8 shows the approximate view of the Photron camera (the Photron was about 10 m south of the HD camera). Unfortunately, the upward positive leader was not imaged because the upper end of the triggering wire was above the field of view of the cameras.

The Photron, operating at a framing rate of 108 kfps, recorded about 586  $\mu\text{s}$  of the downward leader development below a height of about 123 m in 63 frames, (9.3  $\mu\text{s}$  per frame), and these frames are shown in Figure 5-9. Images 2 through 63 shown in Figure 5-9 have the background luminosity subtracted; each image is the recorded image minus the luminosity that was recorded in image 0 (not shown). In effect, what is shown is the change in the luminosity from Image 0. The images in Figure 5-9 have also been intensity-inverted and contrast enhanced for improved visualization. The tower can be seen in the lower right corner of Images 1 and 64. The leader develops from the upper right corner downward and to the left in a step-wise manner. A leader branch apparently extends outside of the Photron's FOV in Image 18 at a height of about 106 m. The primary leader channel (the channel that connected to ground) extends outside of the Photron's FOV during Image 38 at a height of about 69 m. The leader develops outside of the Photron's FOV during the time when Images 39 through 49 were recorded. In Image 50, the tip of a leader branch barely enters the Photron's FOV at a height of about 48. In Image 56, another leader branch develops into the Photron's FOV at a height of about 32 m. This branch

develops an additional 10 m or so in length, and then apparently ceases. The return stroke occurs in image 64, producing heavy blooming. No branches were observed in the HD video.

The features of most interest in Figure 5-9 are found at the leader tip in Images: 7 through 11, 33, 34, 36, 37, and 56 through 59. Expanded views of the leader tip in these images are given in Figures 5-10, 5-11, and 5-12 (enlarged by a factor of 4). Secondary segments of luminosity that are believed to be space stems or space leaders are identified by lower-case letters. Table 5-3 gives the distances between the lower tip of the primary channel and the lower tip of the segment, and the length of the segments. Note that all length and distance measurements are made assuming that the luminosity is a distance of 440 m from the camera. The length measurements would change by up to 12% if the luminosity were 50 m farther or closer than 440 m. Moreover, there can be significant errors in the length measurements if the luminosity had significant development towards or away from the camera (i.e. perpendicular to the camera sensor plane). In the following descriptions, the primary leader channel, or just primary channel, will refer to any portion the main channel that connects to ground, including branches.

Figure 5-10 shows expanded views of the leader tip in Images 7 through 11. In Image 7, it is clear that a space leader has formed that is about 3 m in length, with the farthest tip being about 4 m from the primary channel. The space leader in Image 7 apparently failed to connect to the primary leader channel since no luminosity is evident in the following image. In Image 8, a space stem has formed that is about 1 m in length, with the farthest tip being about 3 m from the primary leader channel. Connecting corona streamers are evident between the space stem and primary channel. In Image 9, the primary leader extends in length to about the position of the space stem in Image 8, and fan-shaped corona streamers are emanating from the leader tip.

Another space stem forms in image 10 that is also about 1 m in length, with the farthest tip being about 5 m from the primary channel. Again, connecting corona streamers are evident between the space stem and primary channel. The space stem in Image 10 has a higher luminosity than that in Image 8, making it more distinct. In Image 11, the primary leader extends in length to about the position of the space stem in Image 10, and corona streamers are emanating from the leader tip.

Figure 5-11 gives a view of the leader tip in Images 33 through 37 that is enlarged by a factor of 4. In Image 33, a space stem has formed that is about 1 m in length, with the farthest tip being about 4 m from the primary channel. In Image 35, corona streamers can be seen emanating from the left leader tip; in Image 36, a space leader has formed in these corona streamers that is about 2 m in length, with the farthest tip being about 4 m from the primary channel. Connecting streamers are evident between the space leader and the primary channel. In Image 37, the primary channel has extended into the region where the space leader formed in Image 36.

Figure 5-12 gives a view of the leader branch in Images 56 through 59 that is enlarged by a factor of 4. In Image 56, the leader branch enters the Photron's FOV from the left side, and corona streamers emanating from the leader tip are evident. In Image 57, two space stems have formed apparently simultaneously and in parallel. Both of these space stems are about 2 m in length, and their farthest tips are about 5 m from the primary channel. Connecting streamers are evident between the space stems and the leader channel. In Image 58, the leader channel has extended to the spot where space stem 'g' formed, and it has corona streamers emanating from its tip. In Image 59, a space leader formed in the vicinity of space stem 'f'. This space leader is about 6 m in length, and its farthest tip is about 8 m from the primary channel. Like the space

leader in image 7 (Figure 5-10), the space leader in image 59 apparently never connected to the primary leader channel.

The  $dE/dt$  record from dE-5 (about 94 m west of the tower) during the time when the stepped leader was imaged is presented in Figure 5-13. About 36 distinct  $dE/dt$  pulses were detected by dE-5. The time between the pulses ranged from 3.6 to 26.6  $\mu\text{s}$ , and the mean time between pulses was 12.9  $\mu\text{s}$ . These times are similar to the inter-step time intervals reported by others for negative stepped leaders in altitude triggered lightning [Laroche *et al.*, 1988; Laroche *et al.*, 1991; Lalande *et al.*, 1998; Chen *et al.*, 2003; Lu *et al.*, 2009]. Moreover, the mean interstep time interval determined from the dE-5 record is greater than the frame times of the high-speed camera, confirming that it was possible for the camera to resolve individual steps and their associated processes. Some of the pulses occurring close in time were likely associated with the same step, as was reported by Howard *et al.* [2010]. The large  $dE/dt$  pulse at time zero was produced by the return stroke that occurred when the leader attached to ground. Note that the return stroke was not a typical return stroke since, as described in Section 2.2.2, the height of the upper end of the channel was limited to the height attained by the upward positive leader.

### 5.3 Upward Positive Connecting Leaders

Of the 36 return strokes triggered in 2008, 19 were imaged in high-speed video. Upward positive connecting leaders were observed preceding 12 of these 19 return strokes (63%), in three different flashes: return strokes 1 and 2 of UF8-08 (shown in Figures 5-14 and 5-15, respectively), return strokes 2 and 3 of UF08-11 (shown in Figures 5-16 and 5-17, respectively), and return strokes 1 through 8 in UF08-18 (shown in Figure 5-18, and panels C and D of Figure 5-4 show the upward positive connecting leader for the eight stroke). Of the 75 return strokes triggered in 2009, a total of 64 were imaged in high-speed video. Upward positive connecting leaders were observed preceding only 3 of these 64 return strokes (4.7%), each in a different

flash: return stroke 9 of UF09-13 (shown in Figure 5-19), return stroke 2 of UF09-17 (shown in Figure 5-20), and the return stroke 7 of UF09-27 (shown in Figure 5-21). As noted in Section 3.6, the tower current configuration was different in the two years; a grounded rectangular intercepting wire was placed several meters above the launch tubes in 2008, but not in 2009.

Table 5-4 summarizes the lengths of the upward positive connecting leaders and the estimated attachment height assuming that the upward and downward leaders propagated with the same speed (so that they met in the middle of the gap between them). As can be seen in Figures 5-14 through 5-21 and Table 5-4, the lengths of the upward positive connecting leaders in the high-speed video images vary from 5 m to 74 m, with a mean length of 23 m. The estimated attachment heights for the leaders were essentially the same for return strokes within the same flash: about 96 and 98 m for the two strokes in UF08-08, about 52 m for the two strokes in UF08-11, and between 41 and 44 m for six (of eight) of the strokes of UF08-18. The estimated attachment heights for strokes 6 and 8 of flash UF08-18 were similar and lower than the attachment heights of the other six strokes, about 34 and 36 m, respectively. Interestingly, strokes 6 and 8 of UF08-18 are believed to have been preceded by dart-stepped leaders. The leader channels were significantly less luminous for strokes 2 and 7 than for the other strokes of UF08-18, possibly because only streamers were imaged, or alternatively, because less charge was deposited along the leader channel resulting in less current and thus less luminosity [*Idone and Orville*, 1985]. For all 15 return strokes for which an upward positive connecting leader was observed, the estimated attachment heights varied from 24 to 98 m with a mean of 50 m. Unfortunately, no upward positive connecting leader was imaged in two consecutive frames, so it is impossible to estimate their development speed.

Of the 15 downward negative leaders imaged with upward positive connecting leaders, 11 are inferred to be dart leaders because (1) they produced smooth electric field changes without pulse activity, (2) they produced no appreciable current (or current pulses) in the launching apparatus, and (3) no clear streamer zones, corona streamers or stepping processes were evident in the high-speed video images. The downward negative leaders for return strokes 5, 6 and 8 of UF08-18 (Figure 5-18) and return stroke 2 of UF09-17 (Figure 5-20) are inferred to be dart-stepped leaders because there were pronounced pulses in electric field and corresponding current pulses were detected in the launching apparatus. The current pulses observed for these leaders were likely the response of the rocket-launching apparatus and the grounding conductor acting as an electric-field derivative ( $dE/dt$ ) antenna located directly beneath the approaching downward-propagating leader, while the electric field pulses were radiated from the downward steps. In this view, there is no evidence that the upward connecting leaders were stepped. Alternatively, the current pulses detected in the launching apparatus may in fact be due to the upward connecting leader stepping, but only when, and in response to, corresponding downward leader stepping.

The observations for the dart-stepped leader preceding return stroke 5 of UF09-25 (Figure 5-5) supports the view that the current pulses are due to the downward leader and not an upward connecting leader that is stepped. For this leader, pronounced current pulses were detected in the launching apparatus during the 30  $\mu$ s interval leading to the return stroke. However, as seen in Figure 5-5, no upward positive connecting leader was imaged in any of the nine 4.2- $\mu$ s high-speed video frames recorded during the time when the current pulses were detected. Considering that streamers emanating from the downward leader were detected by the camera, one might expect that if an upward positive connecting leader were present, it would also be detected. In

this view, it can be concluded for the case of the fifth return stroke of UF09-25 that the current pulses must have been induced by the downward negative leader steps.

#### 5.4 Discussion

The upward positive leader discussed in Section 5.2 developed in a stepwise manner. As noted in Section 2.2.1.2, other researchers, using streak photography, have similarly observed upward positive leaders in triggered lightning developing intermittently [e.g., *Laroche et al.*, 1988; *Idone*, 1992; *Rakov et al.*, 2003; *Idone* in *Rakov and Uman*, 2003]. Intermittent development of positive leaders has also been observed in upward negative lightning from tall buildings and towers [e.g., *McEchron*, 1939; *Berger and Vogelsanger*, 1966; *Berger and Vogelsanger*, 1969], in downward positive lightning [e.g., *Wang et al.*, 2011], and in long laboratory sparks [e.g., *Gorin et al.*, 1976; *Les Renardieres Group*, 1977; *Gallimberti*, 1979; *Domens et al.*, 1991; *Bazelyan and Raizer*, 1998; *Bazelyan and Raizer*, 2000; *Gu et al.*, 2010]. The high-speed video images presented in Figure 5-2 are the first images from a framing camera of a positive leader clearly stepping and as it first develops from a triggering wire with wire-base current pulses precisely correlated with each step. The luminosity waves that appear to propagate downward from the leader tip are consistent with similar observations by *Idone* [1992] and *Rakov et al.* [2003]. The currents determined for each leader step, both measured and scaled (on average 59 and 34 A, respectively), are consistent with other reports of first current pulses associated with the upward positive leader at low altitudes [*Laroche et al.*, 1988; *Lalande et al.*, 1998; *Willett et al.*, 1999; *Biagi et al.*, 2009], but are up to two orders of magnitude less than the peak currents (on average 1.6 kA) reported for individual steps in an upward positive leader at higher altitudes (probably somewhere around 300 to 500 m) by *Rakov et al.* [2003]. The individual steps of the upward positive leader examined by *Rakov et al.* [2003] transferred on

average 31 mC of charge, which is significantly (a thousand times) more than the average charge per step, 64  $\mu\text{C}$ , for the upward positive leader in UF09-30.

The measured charges for the upward positive leader steps in UF09-30 are consistent with charge measurements of long positive laboratory sparks which range from about 35 to 50  $\mu\text{C m}^{-1}$  [e.g., *Les Renardieres Group*, 1972; *Les Renardieres Group*, 1974; *Les Renardieres Group*, 1977; *Domens et al.*, 1991]. *Domens et al.* [1991], who studied the 3-D development and charges of positive leaders in a 16.7-m spark gap, determined that 50  $\mu\text{C}$  of charge flowed through the high voltage electrode for each meter of leader growth. For the upward positive leader of UF09-30, the charge per unit length was computed for each step by dividing the total charge per step by the step's length. The computed charge per unit length ranged from 26 to 110  $\mu\text{C m}^{-1}$  with an arithmetic mean of 51  $\mu\text{C m}^{-1}$ , which is essentially the same value determined for the long laboratory spark by *Domens et al.* [1991].

The upward positive leader developed from the wire tip at a height of about 123 m with a speed of  $5.5 \times 10^4 \text{ m s}^{-1}$ , and its speed had increased to  $2.1 \times 10^5 \text{ m s}^{-1}$  when it reached a height of 310 m. The speed at 310 m is consistent with what has been reported by *Idone* in Ch.7 of *Rakov and Uman* [2003] and *Laroche et al.* [1988] for leaders at altitudes around 1 km. It is worth noting that *Yoshida et al.* [2010], who presented a detailed description of the same upward positive leader as it developed to higher altitudes using 3-D interferometric images, reported that the leader developed from 1.5 to 3.7 km with a three-dimensional speed of  $3.3 \times 10^6 \text{ m s}^{-1}$ . The lengths of the leader's first steps between heights of 123 and 134 m (0.8 to 2.2 m), were smaller than those measured by *Laroche et al.* [1988] (14 m) for a leader at a height of about 1 km. The mean interstep time intervals for the upward positive leader in UF09-30 was about 21  $\mu\text{s}$ , which is consistent with the average interstep time interval reported by *Laroche et al.* [1988] of 20  $\mu\text{s}$ ,

but less than the average interstep time of 50  $\mu\text{s}$  that *Rakov et al.* [2003] inferred from current and electric field records for an upward positive leader at a height of 300 to 500 m. The apparent diameter of the upward positive leader (0.88 m) is likely the diameter of the leader's corona sheath, whereas the longitudinal current is confined to a small core several millimeters in diameter, as is observed for long positive polarity laboratory leaders [e.g., *Gorin et al.*, 1976; *Gallimberti*, 1979]

The luminous segments of secondary channel depicted in Figures 5-4 through 5-6 and 5-9 through 5-12, that were below and separated from the primary leader channel, have spatial dimensions that are similar to or slightly larger than the space stems and space leaders observed in long laboratory sparks. The lengths of the observed space leaders ranged from 2 to 6 m, and their farthest tips were between 4 and 12 m from the primary channel. *Ortega et al.* [1994] reported that space leaders in a 16.7 m spark gap develop a distance of 1.4 to 2.2 m ahead of leader channels and extend the leader channel by 1 to 5 m. *Les Renardières Group* [1981] reported similarly that space leaders in 5 m and 7 m gaps develop 1 m to 2.5 m ahead of leader channels and extend the leader channel by about 1 m.

*Les Renardières Group* [1981] observed multiple simultaneous space leaders in long laboratory sparks, with the number of space leaders that develop simultaneously increasing with increasing voltage rise times. *Ortega et al.* [1994] reported the simultaneous development of "several" space leaders from different space stems, in series (co-linear) or parallel (side-by-side), and noted that a space stem may develop into a space leader only if an additional space stem develops further ahead of the leader channel. *Ortega et al.* [1994] reported that current pulses from laboratory leader steps exhibited two distinct peaks when they formed with two space leaders. Space stems and space leaders were observed forming in series and in parallel ahead of

the leaders in UF09-13 and UF09-25. For UF09-13, two space stems were observed to have existed in parallel, or side by side, in Frame 57 (best seen in Figure 5-12). For UF09-25, it is evident in Frame 7 of Figure 5-5 and Figure 5-6 that two well-defined segments of luminosity appear in series ahead of the leader channel that were about as luminous as the leader channel, suggesting that they were probably space leaders. Additionally, there were two segments of luminosity ahead of the leader in Frames 4, 5, and 8. In Frames 4 and 8, it appears that there is a space stem ahead of a space leader, and in Frame 5, it appears that there is a space leader ahead of a space stem. The observations of space stems and space leaders forming in series and in parallel are consistent with the observations of laboratory sparks noted in above.

*Howard et al.* [2010], using a  $dE/dt$  time-of-arrival network to locate sources of natural and triggered lightning steps with an accuracy on the order of meters, reported that the location of subsidiary peaks in a single overall leader-step  $dE/dt$  pulse were grouped within a few tens of meters, indicating that the causative leader step was formed through a complex series of breakdowns. This hypothesis is supported by the observations presented in Section 5.3. For the dart-stepped leader preceding return stroke 5 of UF09-25, all of the  $dE/dt$  pulses that were measured during the time when the leader was imaged had one to three secondary peaks, and the corresponding current pulses (the current system was likely acting in part as a  $dE/dt$  antenna) had similar peaks (Figure 5-7). Many of the  $dE/dt$  pulses recorded during the time when the downward negative leader developed to ground in the altitude trigger, UF09-13, also had secondary peaks (Figure 5-13).

If there were 10 steps observed for the dart stepped leader in UF09-25 (Figures 5-5 and 5-6), as the  $dE/dt$  record indicates (Figure 5-7), then the average step length was about 11 m, which is close to the 5 to 10 m reported by *Orville and Idone* [1982] for steps of dart-stepped

leaders in triggered lightning. *Schonland* [1956] reported that leader step lengths in natural dart-stepped leaders near ground were on average 12.7 m, and *Idone and Orville* [1984] reported step lengths of 10 to 30 m. The average downward speeds for the dart-stepped leaders in UF09-13 (Figure 5-5) and UF09-25 were between  $1.25 \times 10^6$  and  $2.5 \times 10^6$  m s<sup>-1</sup>, and  $2.7 \times 10^6$  and  $3.4 \times 10^6$  m s<sup>-1</sup>, respectively. These values are consistent with the observed range of speeds, between  $2 \times 10^6$  m s<sup>-1</sup> and  $8 \times 10^6$  m s<sup>-1</sup>, reported for dart-stepped leaders in previous studies [*Schonland*, 1956; *Orville and Idone*, 1982; *Wang et al.*, 1999b]. Although it appears likely that the steps in the dart-stepped leader discussed here developed through mechanisms similar to those in long laboratory sparks, it is not clear that such mechanisms operate on the longer spatial scales usually reported for stepped leaders in natural lightning, between 10 and 200 m [*Schonland*, 1956; *Berger and Vogelsanger*, 1966; *Chen et al.*, 1999]. The longer leader steps observed by others may be produced through multiple space leaders developing in series and nearly simultaneously. Alternatively, as noted by *Hill et al.* [2011], it is possible that observed steps with lengths up to 200 m are in fact observations of upward propagating luminosity waves that were produced by steps of short lengths.

The time coincident x-ray, dE/dt, and current pulses, along with the optical observation of step formation support the well-established fact that x-ray emissions are produced during the leader phase of lightning and are associated with the leader steps [e.g., *Dwyer et al.*, 2004; *Dwyer et al.*, 2005b; *Howard et al.*, 2008]. The high electric fields of corona streamer tips that develop from leaders are presently thought to produce cold runaway electrons that cause x-ray emission via bremsstrahlung radiation [*Dwyer*, 2004; *Moss et al.*, 2006]. X-ray emission has also been observed in laboratory sparks smaller than 2 m, but apparently only in association with corona streamer development [*Dwyer et al.*, 2005a; *Rahman et al.*, 2008; *Dwyer et al.*, 2008].

The streamer zone of negative laboratory leaders can be several meters in length, and in gaps shorter than 2 meters the streamer zone connects to ground without the development of space leaders [Gorin *et al.*, 1976; Ortega *et al.*, 1994; Reess *et al.*, 1995]. A detailed study of laboratory spark leaders that develop step-wise via the space leader mechanism (gaps greater than 2 m length and with long voltage rise times) using microsecond or sub-microsecond high-speed video and synchronized x-ray measurements might help to clarify when and where x rays are produced in lightning and long laboratory spark leaders.

The high-speed video images presented in Figure 5-14 through 5-21 represent the first photographic observations of upward positive connecting leaders in lightning. The image presented in Figure 5-4 (and Figure 5-18) showing the upward positive connecting leader and downward negative dart stepped leader preceding return stroke 8 of UF08-18 is the only known image in which the streamer zone of the downward negative leader is in contact with the upward positive leader in lightning. It is curious that so many upward connecting leaders were observed in 2008 while so few were observed in 2009. In 2008, upward positive connecting leaders were observed for 12 of the 19 (63%) return strokes imaged by high-speed cameras, whereas in 2009, only upward positive leaders were observed for only 3 of the 64 (4.7%) return strokes imaged by high-speed cameras. Two theories are presented to explain this disparity. First, the rectangular intercepting wire placed above the launch tower only in 2008 (not in 2009) may have enhanced the local electric field in such a way as to encourage the development. The second theory involves how the camera framing speed relates to its sensitivity. The Photron was generally operated at higher framing rates in 2009 than in 2008. Since the time-per-frame decreases with increasing framing speed, the amount of light that is integrated in each frame may also decrease, rendering faint objects undetectable. Wang *et al.* [1999a], using the ALPS photodiode array,

reported that the luminosity of one upward connecting discharge was an order of magnitude lower than that of the downward negative leader. However, it seems unlikely that upward positive connecting leaders would be completely undetectable when the following is considered: (1) corona and corona streamers are evident in many of the downward negative leaders, even those imaged at a framing speed of 300 kfps, and (2) upward positive leader steps developing from the triggering wire were imaged for flash UF09-30 (Figure 5-2) that were of low luminosity. Thus, the author favors the first theory.

Table 5-1. Salient information for the stepped upward positive leader of UF09-30.

Step	Step length (m)	Total leader length (m)	Interstep time interval ( $\mu\text{s}$ )	Measured peak current (A)	Scaled peak current (A) <sup>a</sup>	Step charge ( $\mu\text{C}$ )	Ratio of step charge to step length ( $\mu\text{C m}^{-1}$ )
a	1.8	1.8	n/a	123	71	47	26
b	0.8	2.6	21.4	37	21	22	28
c	0.9	3.5	21.7	25	14	n/a <sup>c</sup>	n/a <sup>c</sup>
d	2.2	5.7	30.4	153	89	107	49
e	1.8	7.5	18.6	122	71	99	55
f	0.4	7.9	17	32	19	44	110
g	2.1	10	20.5	41	24	70	33
h	1.8	11.8	19.0	17	10	n/a	n/a <sup>c</sup>
i	n/a <sup>b</sup>	n/a	16.6	23	14	60 <sup>d</sup>	n/a <sup>c</sup>
j	n/a	n/a	24.9	20	12	n/a	n/a <sup>c</sup>
arithmetic mean	1.5	n/a	21.2	59	34	64	51

a) The measured peak current is scaled to take account of reflections at ground and attenuation along the wire (using Equation 6-16 in Section 6.4.3). b) The leader was developing outside of the camera's field of view for Steps i and j. c) Only the first peak of these current pulses was resolved, the rest of the pulse was below the noise floor so the charge could not be determined. d) The charge for Step i was determined from the II-VLS shunt measurement (the others were determined from the II-Lo measurement).

Table 5-2. Lengths and distances for the space stems and space leaders observed in event UF09-25.

Segment (type) <sup>a</sup>	Mechanism <sup>a</sup>	Distance between the lower tip of the primary channel and the lower tip of the segment (m)	Segment length (m)
a	ss	4	1
b	ss	7	1
c	ss	2	1
d	sl	4	2
e	ss	8	2
f	ss	2	1
g	sl	12	2
h	sl	7	4
i	sl	12	4
j	sl	4	2
k	ss	8	1
arithmetic mean		6.4	1.9

a) The mechanism thought to have been observed, either space stem (ss) and space leader (sl).

Table 5-3. Lengths and distances for the space stems and space leaders observed in event UF09-13.

Segment	Mechanism <sup>a</sup>	Distance between the lower tip of the primary channel and the lower tip of the segment (m)	Segment length (m)
a	sl	4	3
b	ss	3	1
c	ss	5	1
d	ss	4	1
e	sl	4	2
f	ss	5	2
g	ss	5	2
h	sl	8	6

a) The mechanism thought to have been observed, either space stem (ss) and space leader (sl).

Table 5-4. Upward positive connecting leader lengths.

Flash ID	Stroke	Length (m)	Estimated attachment height (m) <sup>a</sup>
UF08-08	1	35	96
	2	74	98
UF08-11	2	16	52
	3	5	52
UF08-18	1	9	43
	2	16	43
	3	10	42
	4	22	43
	5	13	41
	6	15	34
	7	12	44
	8	16	36
UF09-13	9	64	64
UF09-17	2	10	24
UF09-27	7	22	37
Arithmetic		23	50
Mean			

a) Note that the upward connecting leaders initiated from the top of the intercepting wire (17 m above ground level) in 2008, and the launch tubes (14 m above ground level) in 2009.

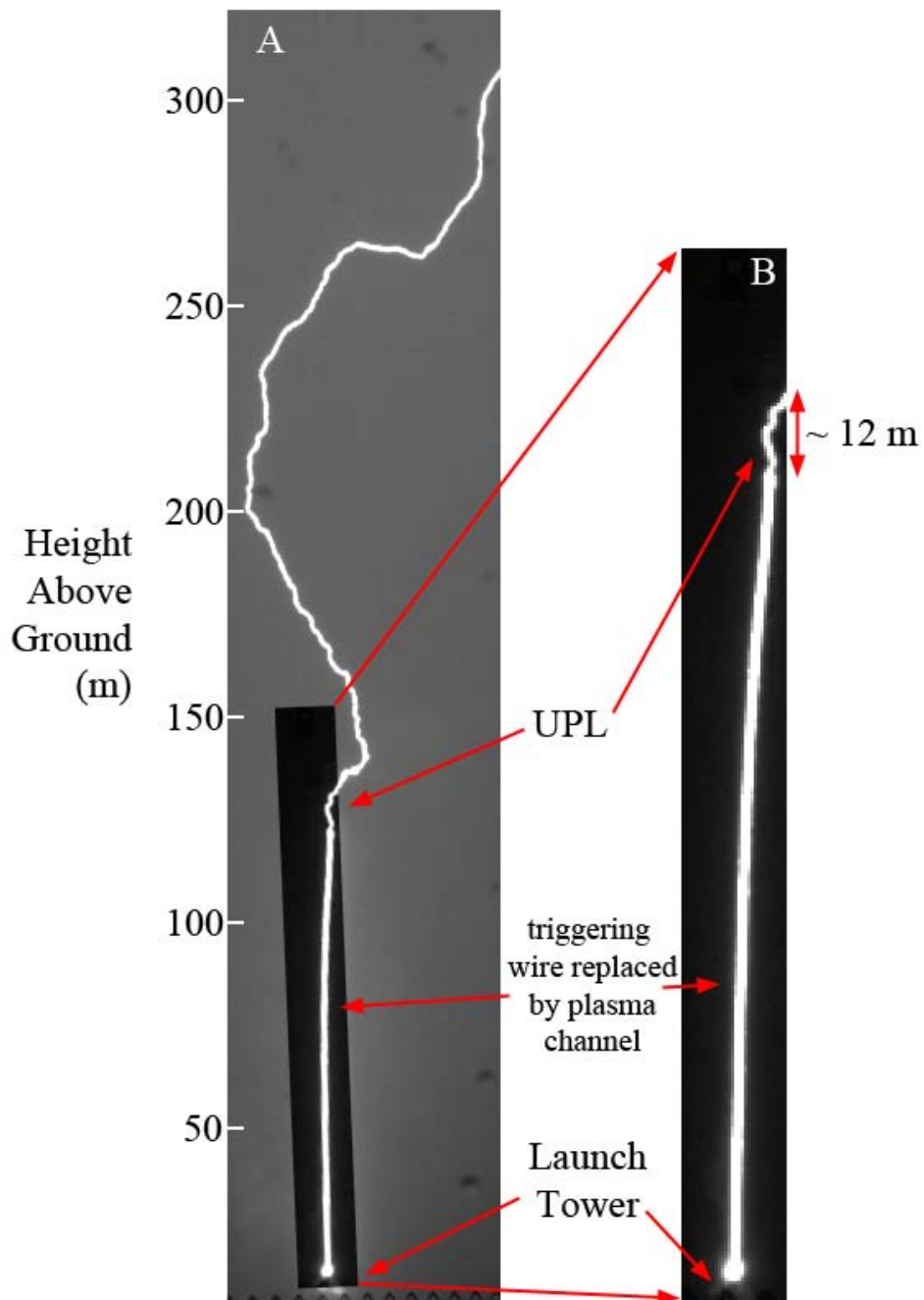


Figure 5-1. High-speed video images of the channel during the initial stage of UF09-30. A) Image recorded by the Phantom camera at 8 kfps (120  $\mu$ s per frame) showing the destroyed triggering wire that has been replaced by a plasma channel and the upward positive leader (UPL) channel. The darker region of the image identifies the Photron field of view. B) Image recorded by the Photron camera at 300 kfps (3.3  $\mu$ s per frame) showing the plasma channel that replaced the destroyed triggering wire and about 12 m of the upward positive leader channel.

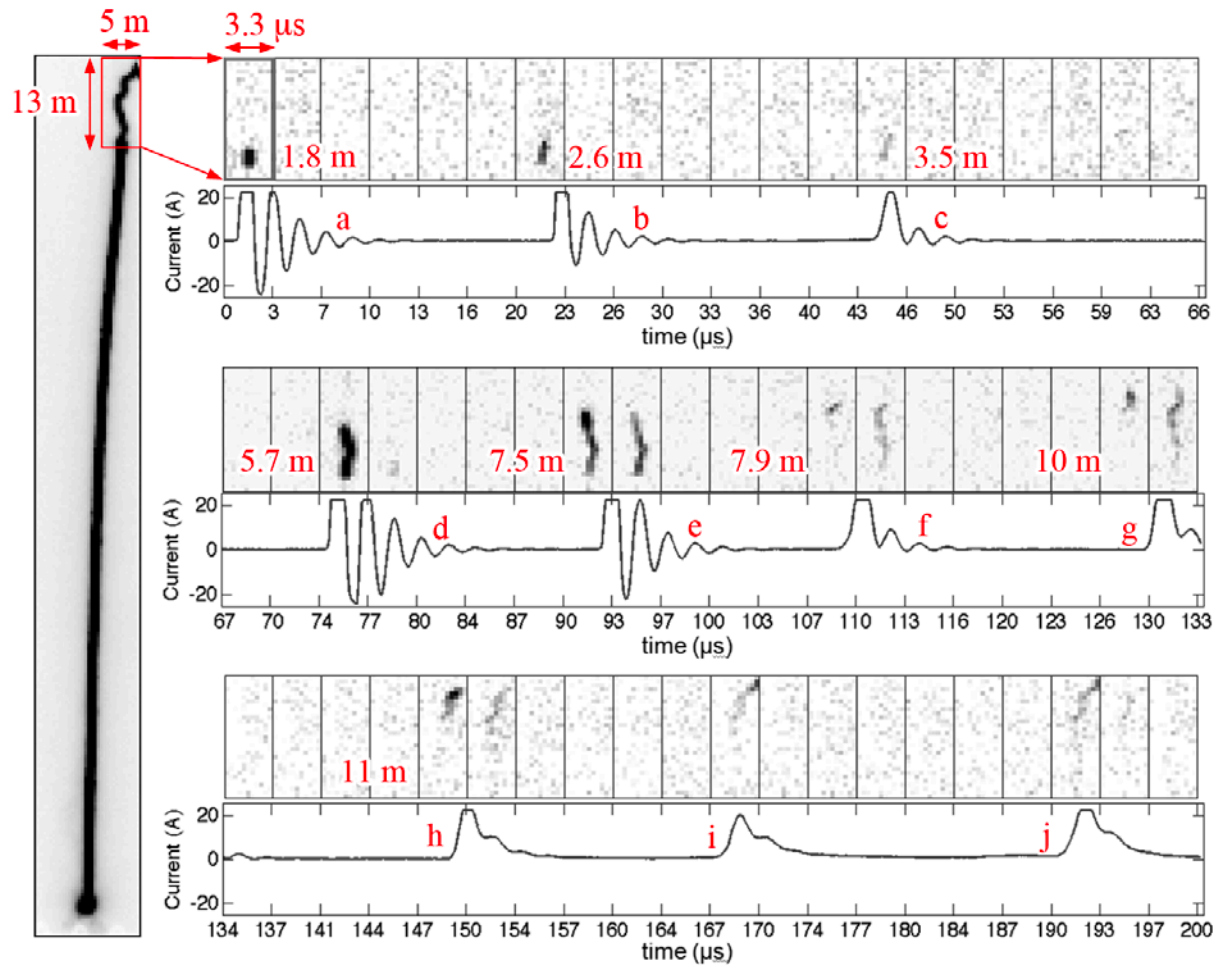


Figure 5-2. The sequence of 60 Photron images containing the UPL for UF09-30, along with the synchronized wire-base current. The part of the Photron image containing lightning channel is shown on the left for reference. All of the images are intensity inverted and contrast enhanced. Each image in the sequence views about 13 x 5 m of space, and is an integration of luminosity over a time of 3.3  $\mu$ s. The numbers next to the leader channel is the total length of the leader channel at each step. The current measurement from the II-VLS sensor saturated at about 21 A (also shown in the panel B of Figure 5-3).

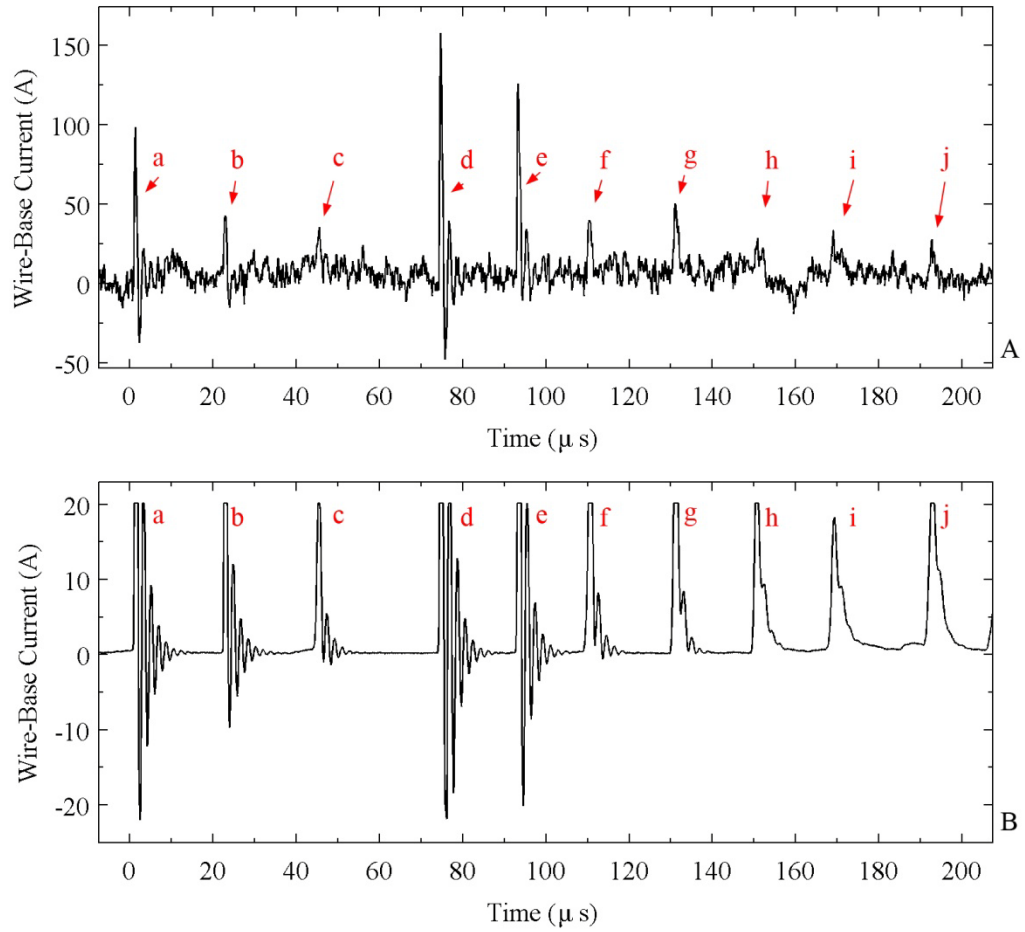


Figure 5-3. The wire-base current associated with the ten upward positive leader steps in UF09-30 that were imaged with high-speed video. A) The II-Lo measurement. B) The II-VLS measurement (also shown in Figure 5-2).

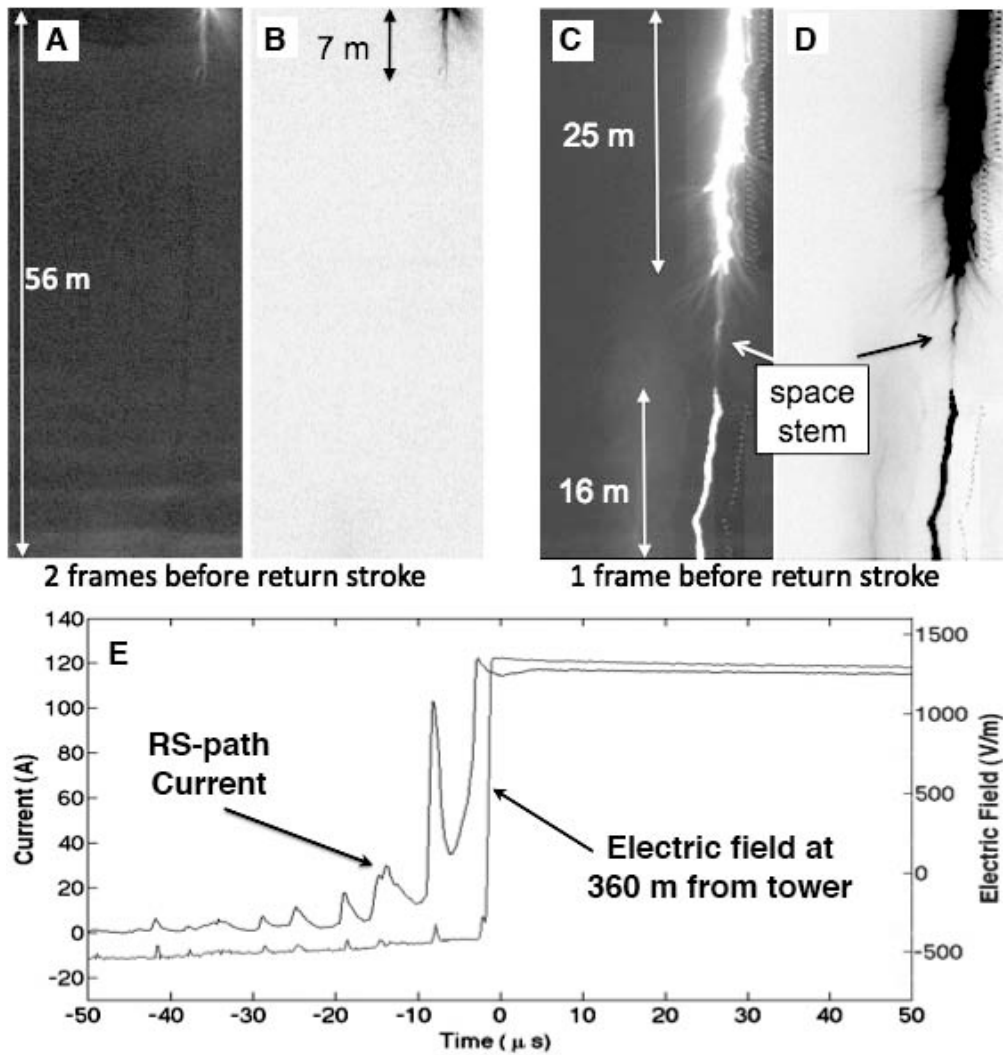


Figure 5-4. High-speed video images, and correlated electric field and current pulses for the dart-stepped leader preceding return stroke 8 of UF08-18. The current (RS-VL) and electric field both (E6) saturated before the return stroke. In images C and D, 'zipper-like' luminosity is evident to the right of the channel that is camera artifact.

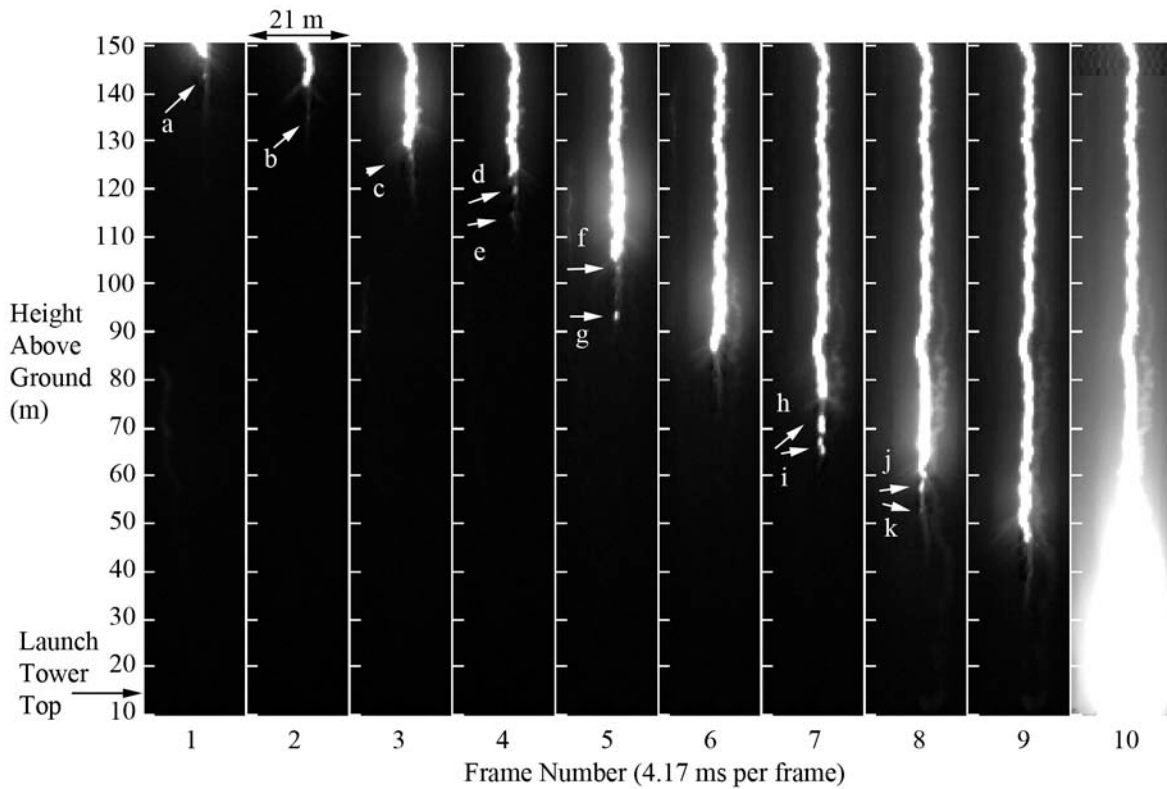


Figure 5-5. Ten high-speed video frames depicting the leader for the fifth stroke of UF09-25 developing from 150 m height to ground during a time of 41.7  $\mu$ s. The frames were recorded at a framing rate of 240 kfps (4.17  $\mu$ s per frame). The top of the launch tower (the top of the launch tubes) is 14 m above ground. The luminous segments that formed separately from and below the downward-extending leader channel are pointed to by white arrow and identified by white, lower-case letters (some of them may be too faint to be seen in this reproduction, but are readily identifiable in the data and in the reproductions in Figure 5-6). The return stroke began during frame 10.

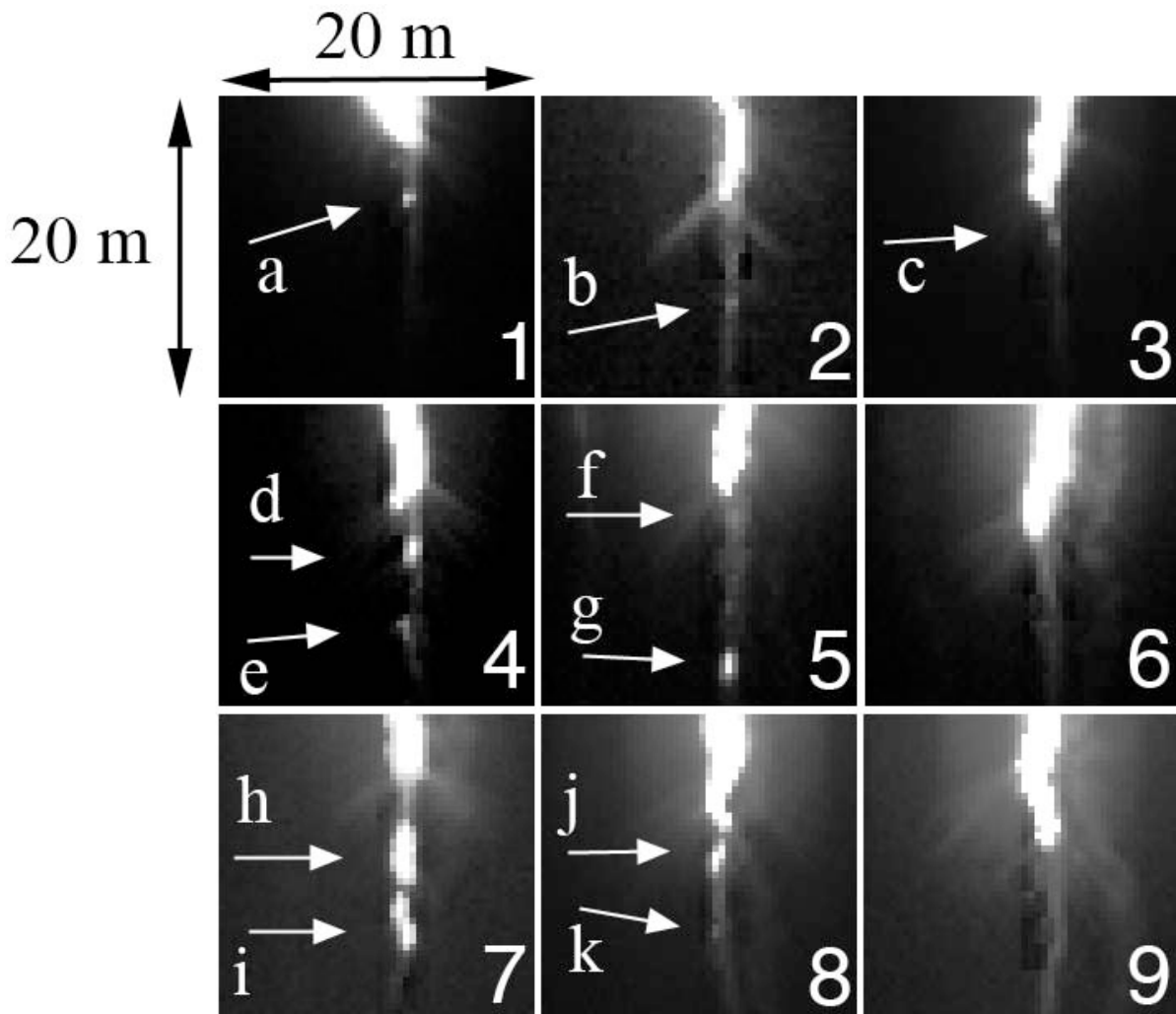


Figure 5-6. Expanded and contrast-enhanced reproductions of the bottom of the downward-extending leader channel seen in the first nine frames in Figure 5-5. Each image shows about 20 m x 20 m. The white arrows and white lower-case letters correspond to those in Figure 5-5, and point to the luminous segments of interest.

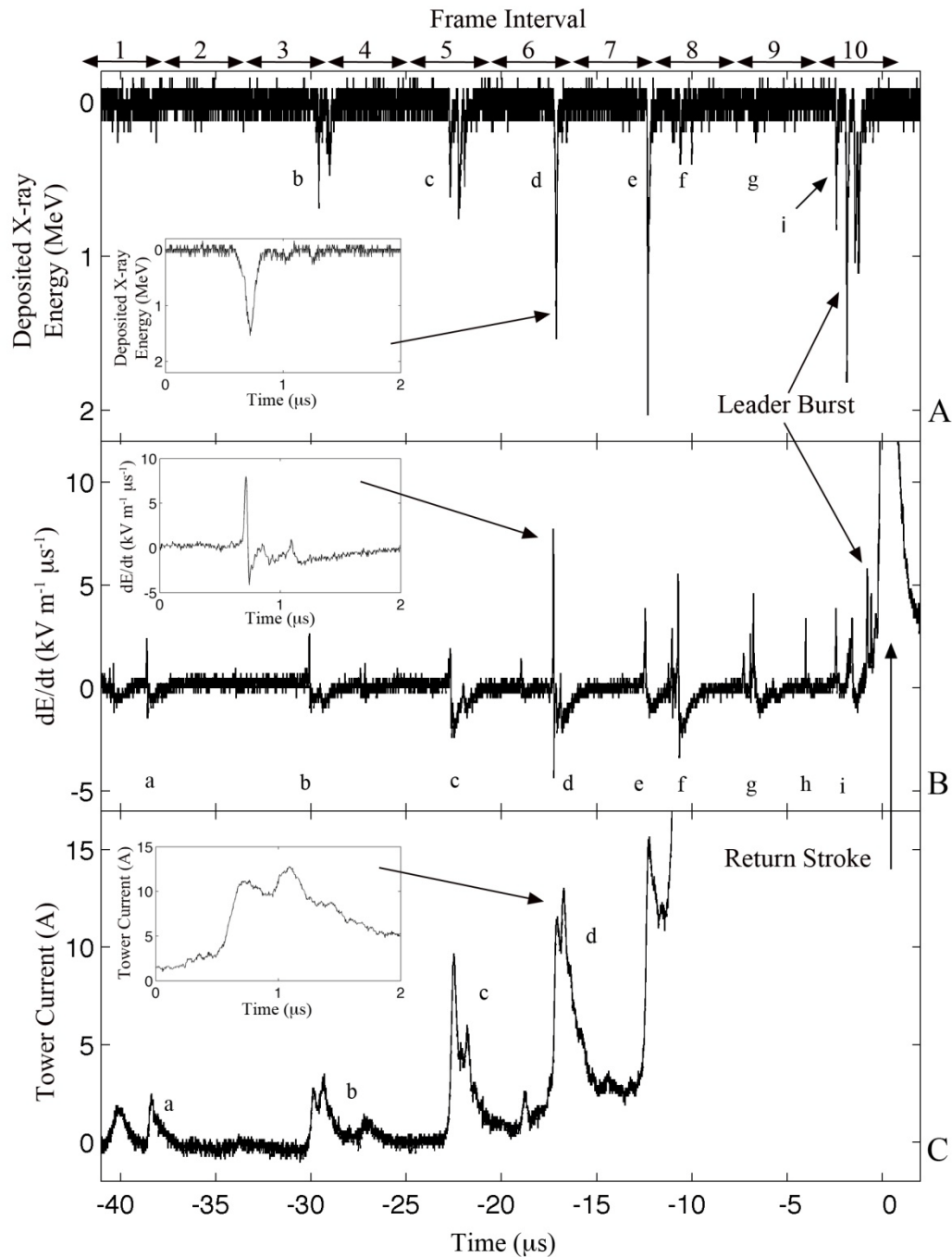


Figure 5-7. The x-ray emission,  $dE/dt$ , and tower current that were recorded during the time when the 10 images shown in Figures 5-5 and 5-6 were recorded. Frame intervals shown at top. The return stroke began at time zero. The inset plots show the pulses that occurred at  $-17 \mu\text{s}$  on a  $2\text{-}\mu\text{s}$  timescale. Note that the lower-case letters that are shown here to make clear which pulses are correlated do not represent the lower-case letters used in Figures 5-6 and 5-7.

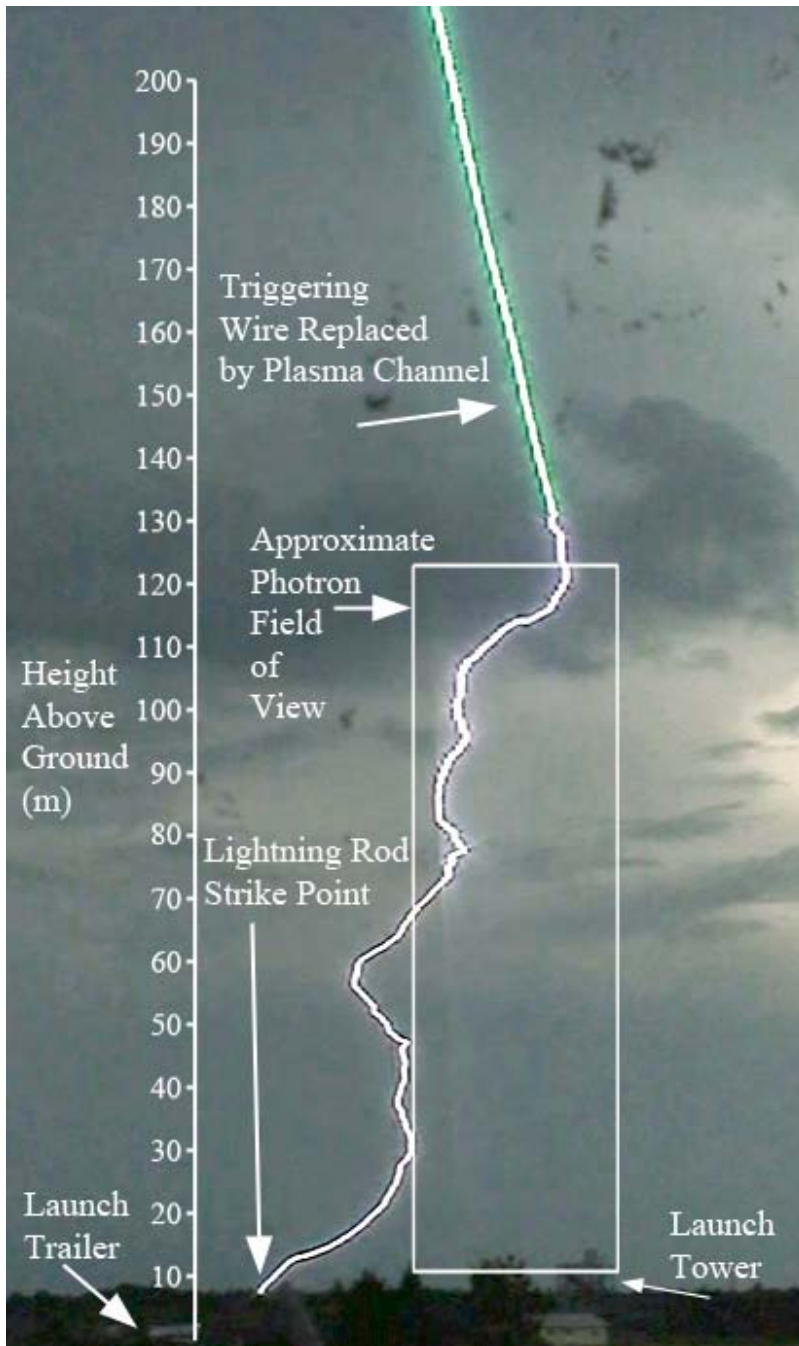


Figure 5-8. An image of the lower 200 m of channel for UF09-13 recorded by the HD camera. The straight green segment is the remnant of the exploded triggering wire that has been replaced by a plasma channel. The channel below was forged by negative downward stepped leader. The lightning struck a lightning rod on the system of protective catenary wires over the launch trailer. The white box shows the approximate Photron FOV.

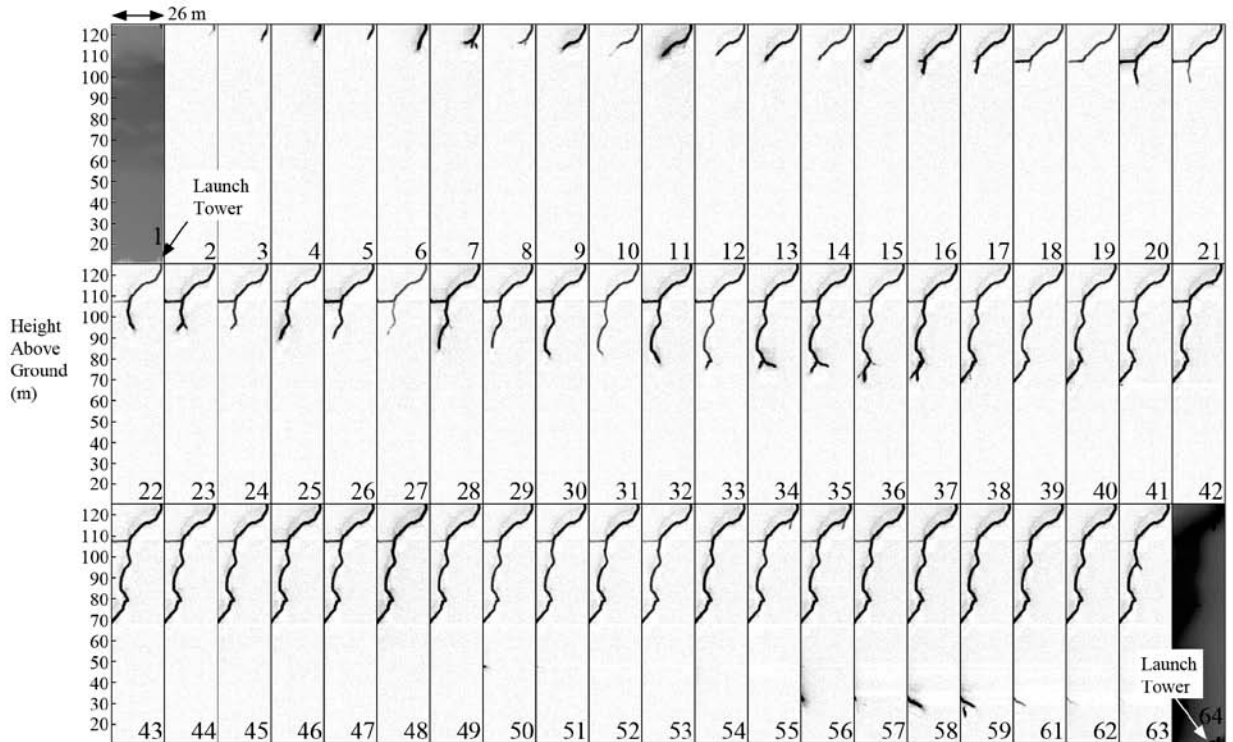


Figure 5-9. A sequence of 64 images recorded at 108 kfps ( $9.3 \mu\text{s}$  per image) showing the first downward negative stepped leader in UF09-13. There are three rows of 21 images, each showing heights spanning from about 12 to 125 m above ground, and each about 26-m horizontally. Each row of images has the heights marked on the left. Images 2 through 64 have had the background luminosity removed by subtracting image 0 (not shown). The light gray 'shadow' channel above the real channel (most visible in images 16 and 17) is camera artifact.

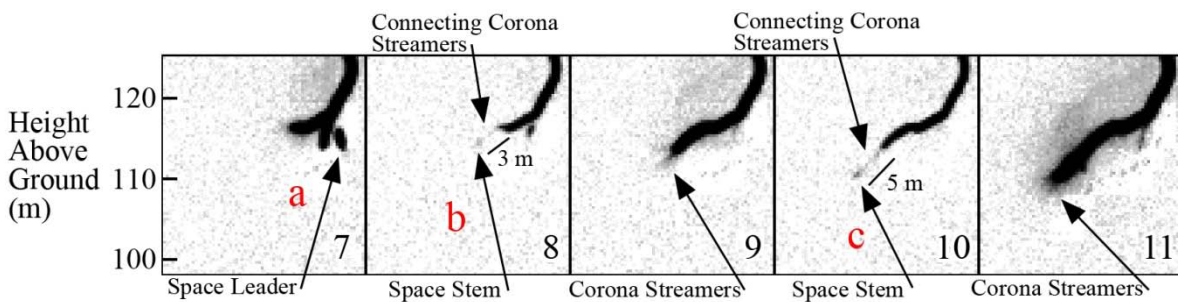


Figure 5-10. The leader tip seen in Images 7 through 11 from Figure 5-9 enlarged by a factor of 4. Black arrows point to features of interest, and red, lower-case letters identify space stems and space leaders. A space leader is evident in Image 7. Space stems are evident in Images 8 and 10. Small black lines identify the measurements of the approximate distances between the lower tip of the space stem and the lower tip of the primary leader.

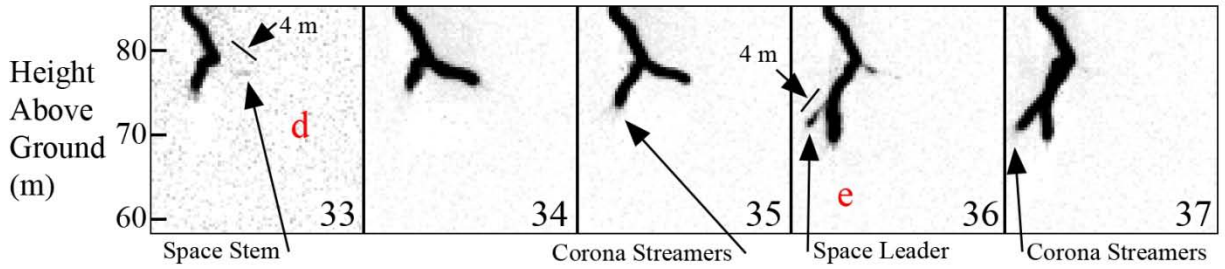


Figure 5-11. The leader tip seen in images 33 through 37 from Figure 5-9 enlarged by a factor of 4. Black arrows point to features of interest, and red lower-case letters identify a space stem and space leader that are evident in images 33 and 36, respectively. Small black lines identify the measurements of the distances between their lower tips and the corresponding leader channel.

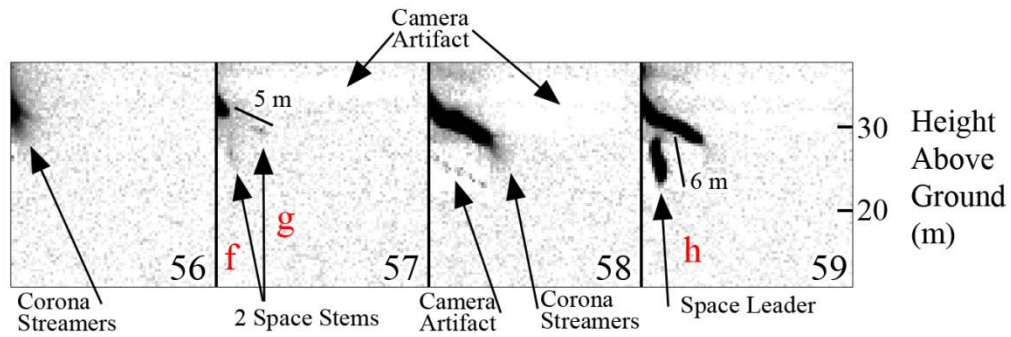


Figure 5-12. The tip of a leader branch seen in images 56 through 59 from Figure 5-9 enlarged by a factor of 4. Black arrows point to features of interest, and red lower-case letters identify space stems and space leaders. Note that the height scale is displayed on the right. Two space stems are evident in image 57, with the lower tips being about 4 m from the leader tip (indicated by thin black line). A space leader is evident in image 59 that is about 5 m in length.

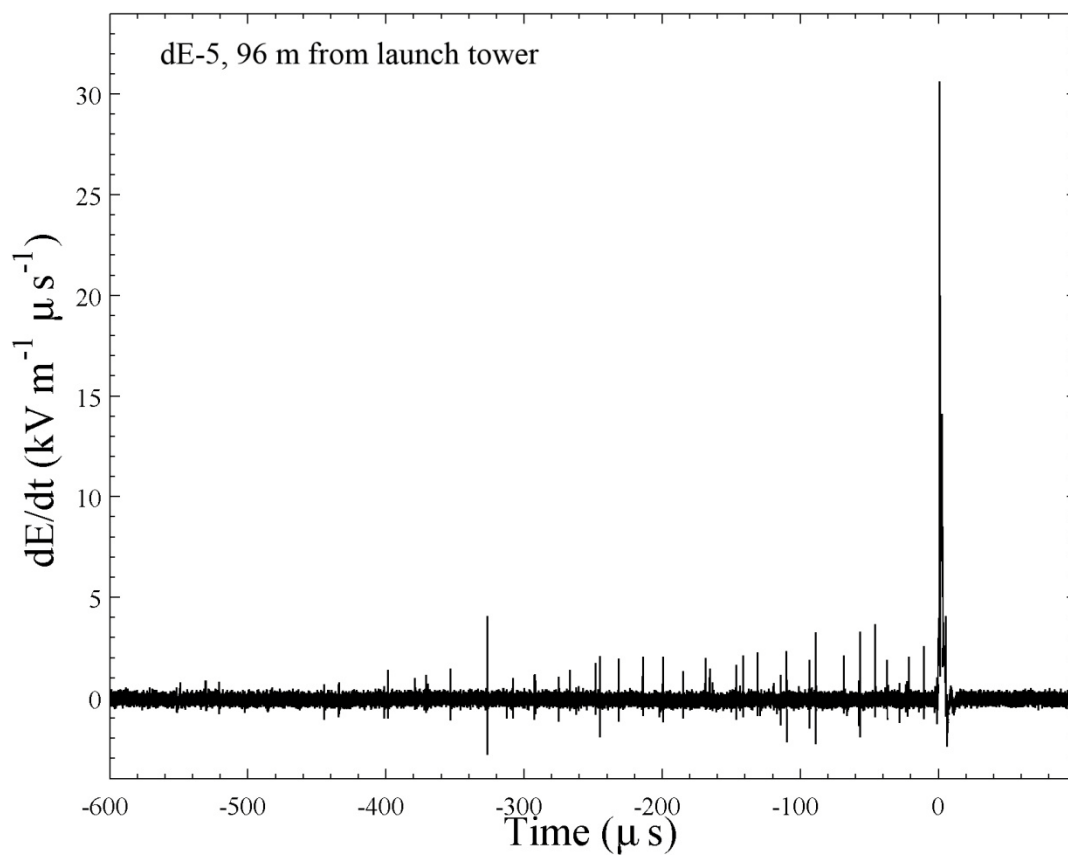


Figure 5-13. The  $dE/dt$  record from dE-5 during the time when the downward negative stepped leader in UF09-13 was imaged. The return stroke occurred at about time zero.

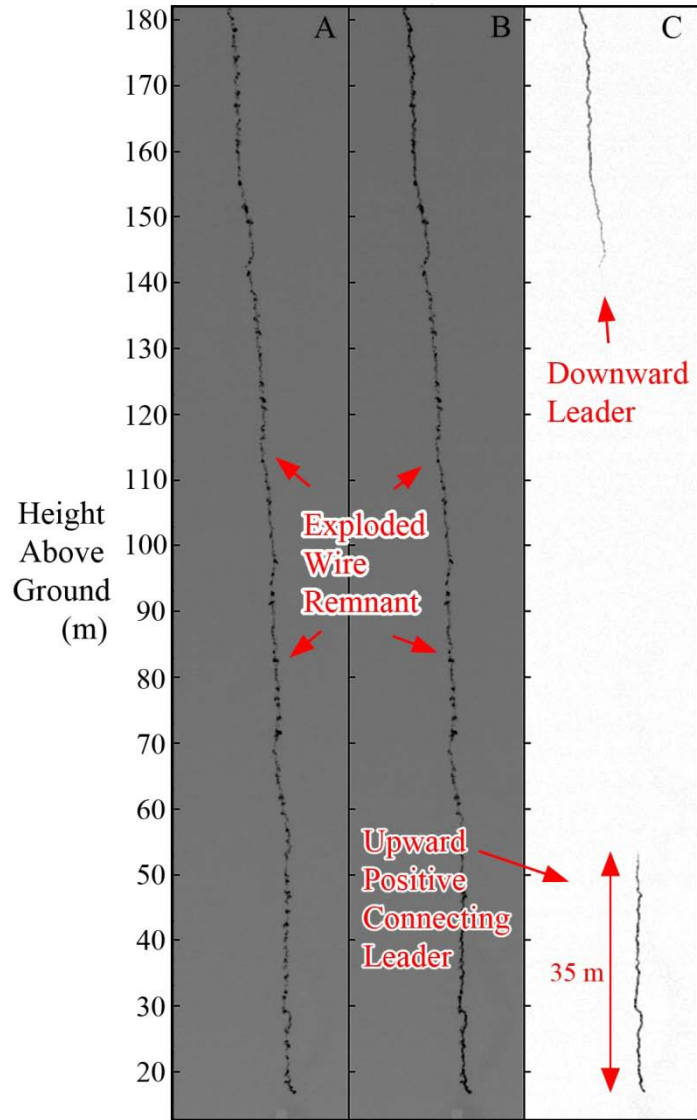


Figure 5-14. High-speed video images of the leader preceding return stroke 1 of UF08-08. The 320 x 48 pixel images were recorded by the UF Photron at a framing rate of 10 kfps (100  $\mu$ s per image). Image C is obtained by subtracting the luminosity in A from the luminosity in B. All images are intensity inverted and contrast enhanced.

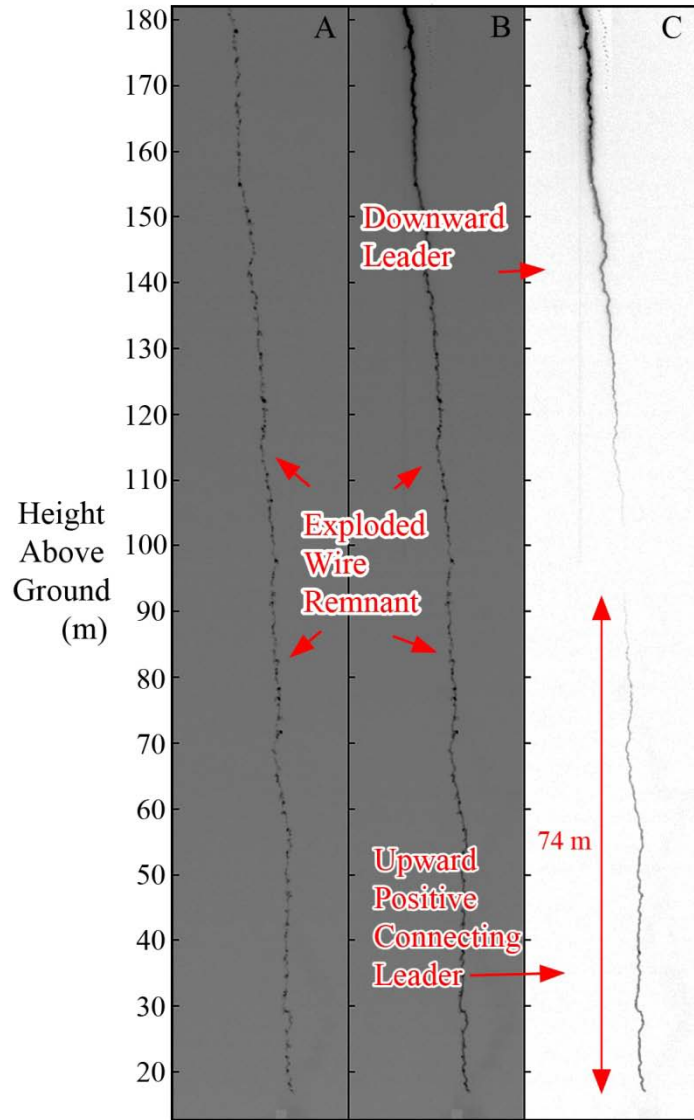


Figure 5-15. High-speed video images of the leader preceding return stroke 2 of UF08-08. The 320 x 48 pixel images were recorded by the UF Photron at a framing rate of 10 kfps (100  $\mu$ s per image). Image C is obtained by subtracting the luminosity in A from the luminosity in B. All images are intensity inverted and contrast enhanced.

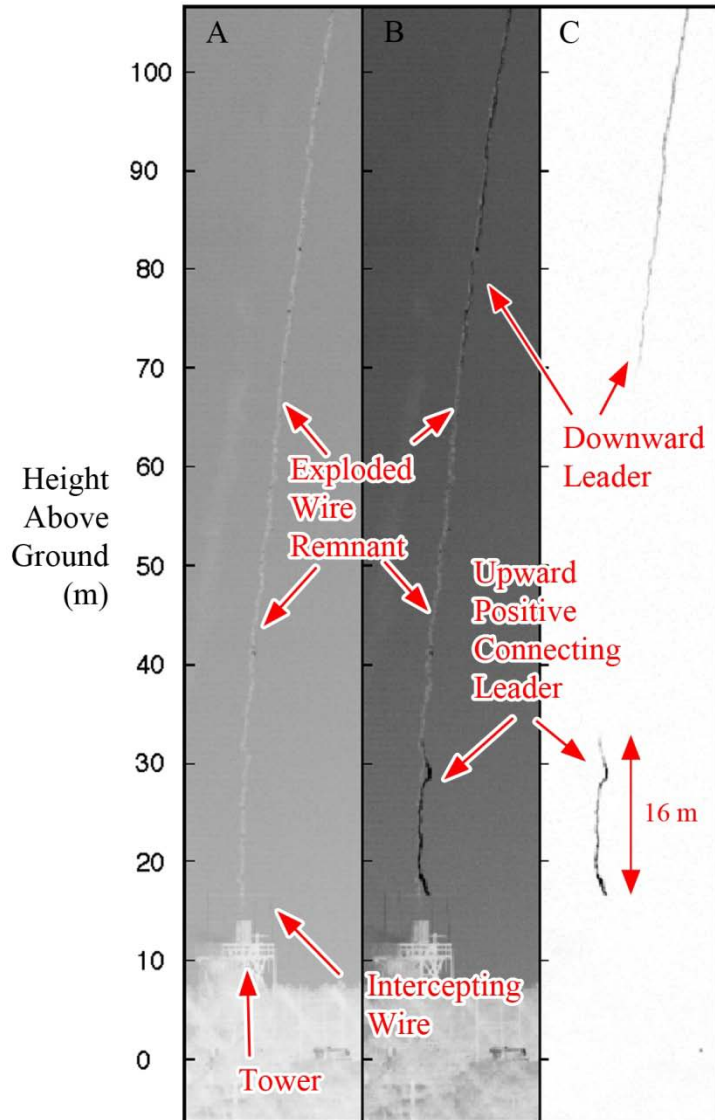


Figure 5-16. High-speed video images of the leader preceding return stroke 2 of UF08-11. The 640 x 101 pixel images were recorded by the UF Photron at a framing rate of 20 kfps (50  $\mu$ s per image). Image C is obtained by subtracting the luminosity in A from the luminosity in B. All images are intensity inverted and contrast enhanced.

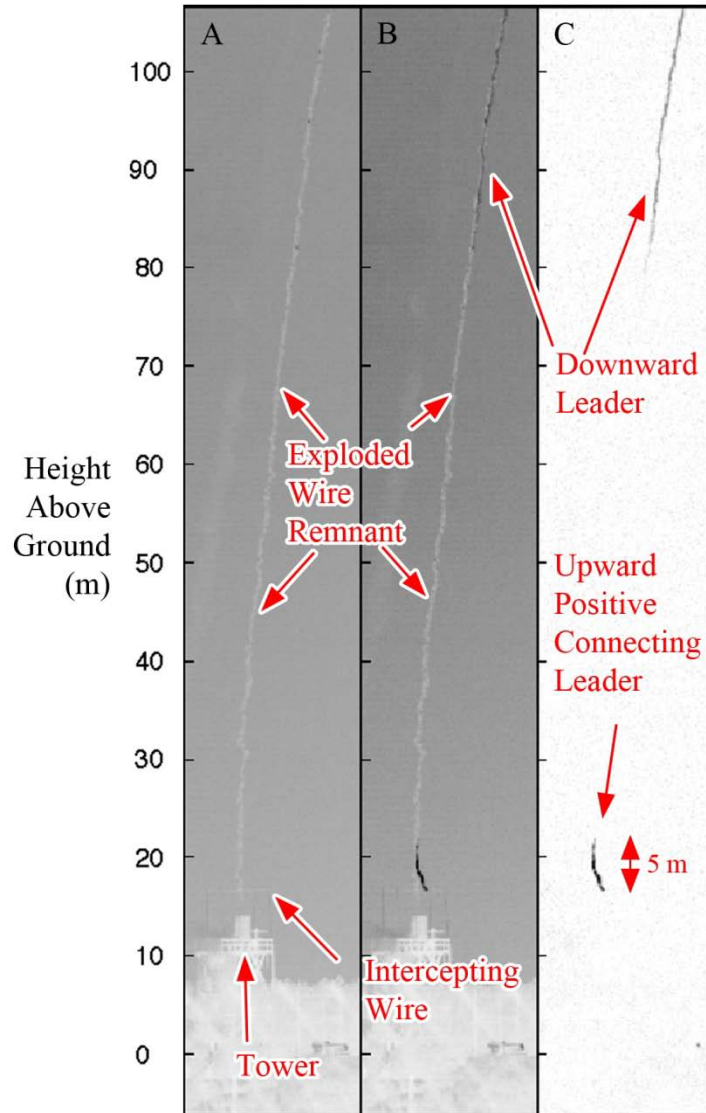


Figure 5-17. High-speed video images of the leader preceding return stroke 3 of UF08-11. The 640 x 101 pixel images were recorded by the UF Photron at a framing rate of 20 kfps (50  $\mu$ s per image). Image C is obtained by subtracting the luminosity in A from the luminosity in B. All images are intensity inverted and contrast enhanced.

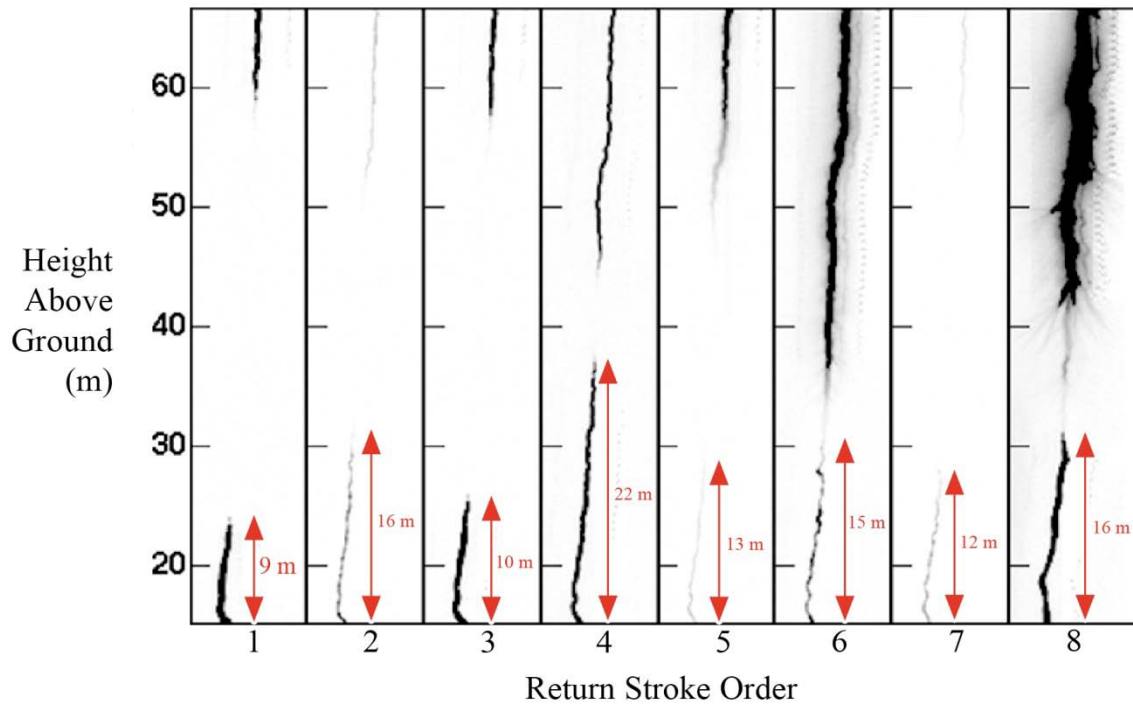


Figure 5-18. High-speed video images of the leader preceding return strokes 1 through 8 of UF08-18. The 320 x 60 pixel images were recorded by the UF Photron at a framing rate of 50 kfps (20  $\mu$ s per image). Each image is obtained by subtracting the two frames prior to the corresponding return stroke leaving primarily the leader luminosity. All images are intensity inverted. Return stroke 8 is also shown in Figure 5-4. In some of the images, ‘zipper-like’ luminosity is evident to the right of the channel that is camera artifact.

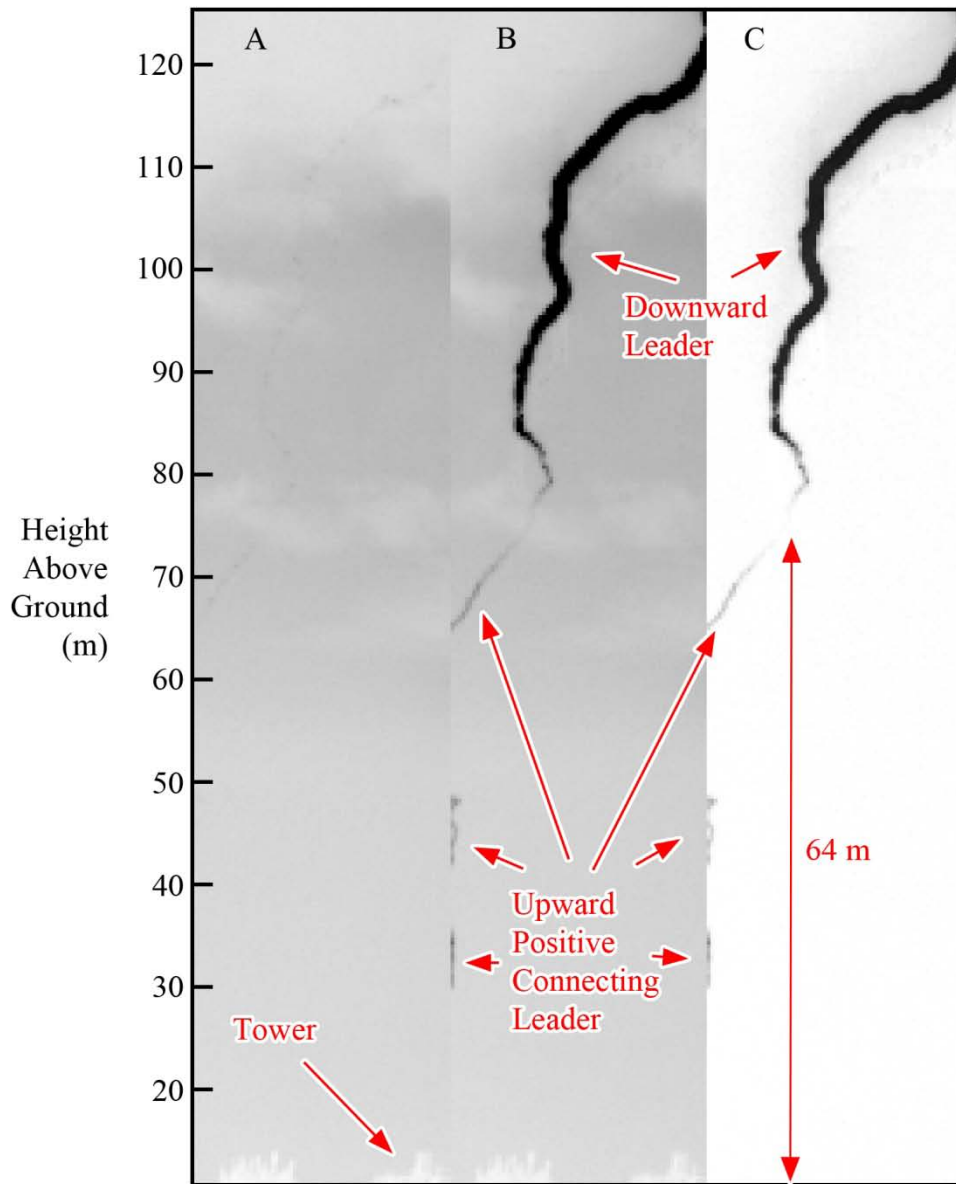


Figure 5-19. High-speed video images of the leader preceding return stroke 9 of UF09-13. The 320 x 70 pixel images were recorded by the UF Photron at a framing rate of 108 kfps (9.3  $\mu$ s per image). Image C is obtained by subtracting the luminosity in A from the luminosity in B. All images are intensity inverted.

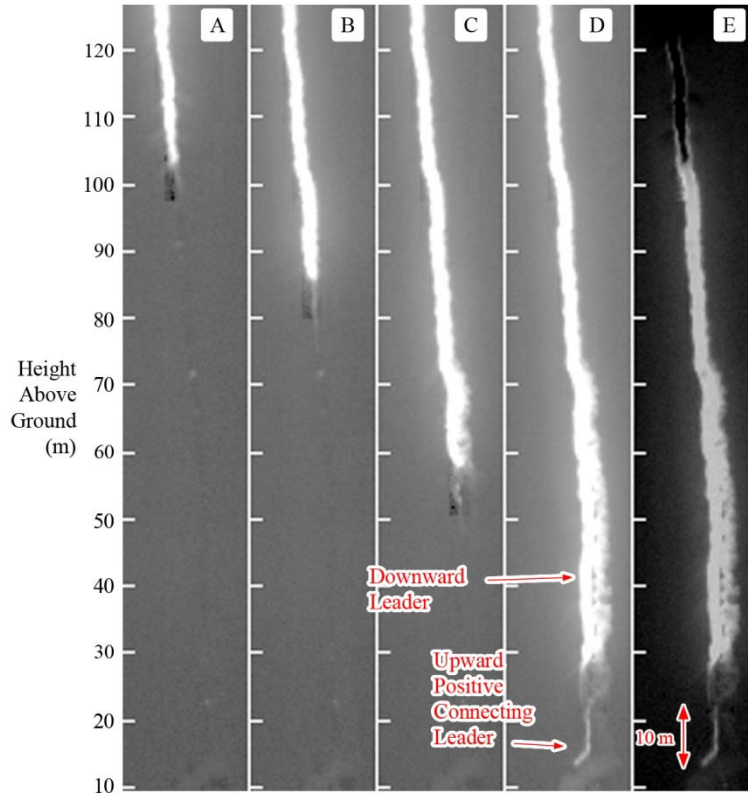


Figure 5-20. High-speed video images of the leader preceding return stroke 2 of UF09-17. The 320 x 96 pixel images were recorded by the UF photron at a framing rate of 135 kfps (7.41  $\mu$ s per image). Image E is obtained by subtracting the luminosity in A from the luminosity in D. All images are normal intensity (not inverted). The darker, rectangular region below the leader tip is a camera artifact.

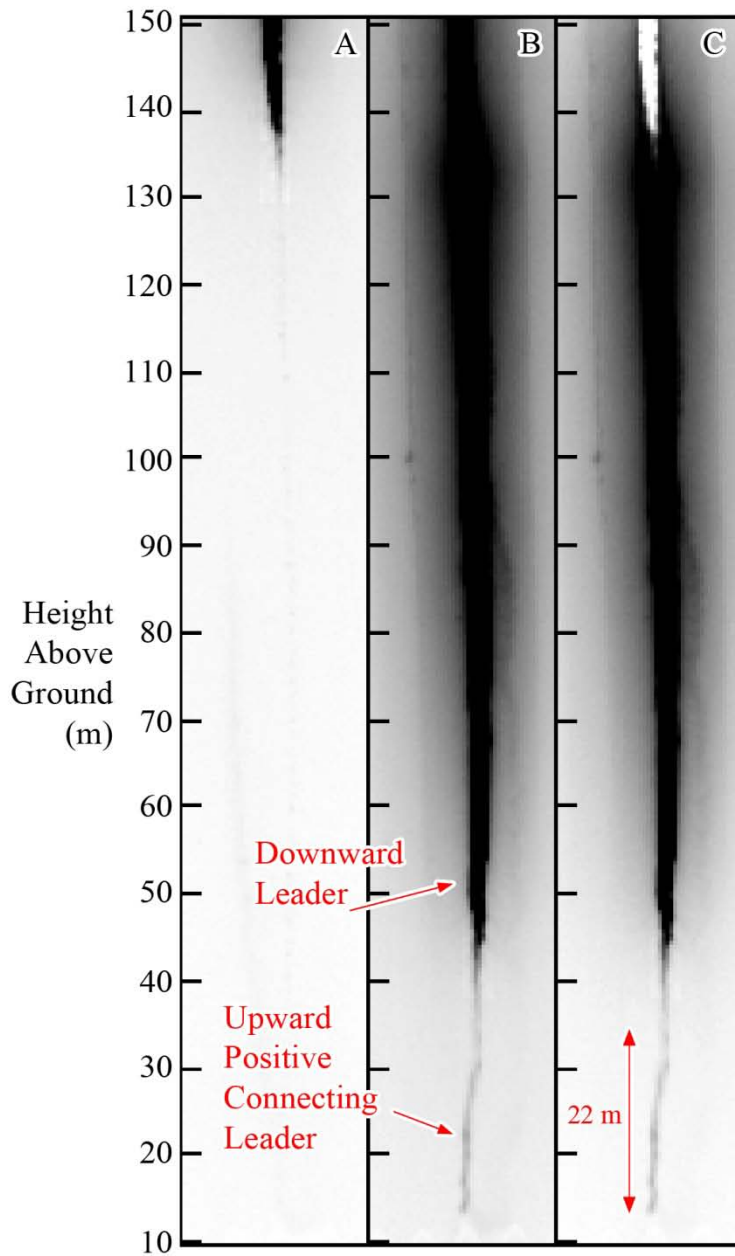


Figure 5-21. High-speed video images of the leader preceding stroke seven of UF09-27. The 320 x 48 pixel images were recorded by the UF photron at a framing rate of 240 kfps (4.2  $\mu$ s per image). Image C is obtained by subtracting the luminosity in A from the luminosity in B. All images are intensity inverted and contrast enhanced.

## CHAPTER 6

### TRANSIENT CURRENT PULSES IN ROCKET-EXTENDED WIRES USED TO TRIGGER LIGHTNING

In rocket-and-wire triggered lightning, transient current pulses in the triggering wires are observed at ground before the development of a sustained upward positive leader from the wire tip. The current pulses are caused by electrical breakdown at the tip of wire where the electric field is significantly enhanced. The triggering wire behaves like a transmission line with the precursor-pulse round-trip propagation time on the wire being greater than the pulse width. Current-pulse reflections are produced at the ground and at the wire tip. As a result, the current signature from a single precursor observed at ground is a sequence of pulses of alternating polarity and decreasing in amplitude during some tens of microseconds.

The electrical breakdown that produces the current pulses preceding the inception of a sustained upward positive leader were first termed “precursors” by *Willett et al.* [1999]. The relatively little information in the literature regarding precursors has been summarized in Section 2.2.1.1. In this chapter, new observations and measurements of precursor luminosity, currents, and remote electric fields will be presented. Then, wire-base precursor current measurements are analyzed to estimate current-pulse propagation speeds on the triggering wire and the current-pulse attenuation due to propagation losses and reflections at both ends of the triggering wire. Finally, a transmission line model is presented and used to predict wire-base current signatures, and make inferences regarding the electrical characteristics of the triggering wire, and the ground termination. In this chapter, a positive electric field at ground corresponds to the electric field vector pointing upward (physics sign convention). Positive current and negative electric field change at ground correspond to the removal of negative charge from or the deposition of positive charge in the atmosphere.

## **6.1 Data and Observations**

The luminosity, wire-base current, and electric field signatures for 410 precursors in 15 wire launches have been examined. In this section, the luminosity that was often observed at the wire tips in association with the precursors is described. Then, examples are presented of the wire-base current and electric field signatures of precursors from two separate wire launches. Finally, a description is given of the variability in precursor behavior that was observed.

### **6.1.1 Luminosity Associated with Precursor Current Pulses**

Of the 410 precursor current signatures examined, 339 (83%) were correlated with observations of luminosity at the wire tip in high-speed video recordings that varied from a meter or so of dim, diffuse glow that often appeared fan-shaped, to distinct leader channels of several meters length. In seven cases, leader channel extended from the wire tip in two consecutive high-speed video frames (or a time of a few hundred microseconds) to a maximum length from 3 to 8 m. Each observation of leader channel corresponded to ‘bursts’ of precursors (2 to 7 precursors occurring in rapid succession within tens of microseconds of each other) indicating that the aborted leaders developed stepwise. The type of luminosity that was observed, or lack thereof, certainly depended on the general visibility conditions (e.g., background light, rain) as well as the camera frame rate and lens aperture.

### **6.1.2 Precursor Current and Electric Field Signatures**

Figure 6-1 presents an example of the wire-base current for a precursor observed when the wire-top height was 339 m, for which the current pulse width was clearly shorter than the round-trip propagation time (the time between successive peaks). As a result, the current pulses produced by successive reflections at the wire base and wire tip are easily distinguishable, and measuring the amplitudes and timing of the precursor signature features is straightforward. The

first pulse (and peak  $i_1^{\text{peak}}$ ) of the damped-oscillatory signature measured at the wire base is the superposition of the current pulse that was generated at the wire tip, after having traveled down the wire, and a reflected current pulse of the same polarity from the approximately short-circuit termination at the ground rod. The reflected current pulse propagates up the wire to the wire tip, where it encounters approximately open-circuit conditions, and an opposite-polarity (negative) current pulse reflection is produced that travels down the wire to ground. The second peak of the damped-oscillatory signature measured at the wire base is the superposition of the negative current pulse and another ground-reflected current pulse (that is also of negative polarity). This sequence of reflections repeats, with the current polarity reversing with each wire-tip reflection, explaining the oscillatory nature of the wire-base measurement. Energy losses associated with the wire (resistance, radiation, and corona leakage current) and imperfect reflections at the wire tip and at the ground attenuate the current, and hence damp the oscillatory current-pulse signature observed at ground. The shape of each successive pulse appears increasingly distorted, or ‘smoothed’, indicating that there is some frequency dependence in the process.

Figure 6-2 presents the current and electric field signatures for a precursor that occurred at a wire-top height of 168 m (about half that of the precursor shown in Figure 6-1). Note that the individual pulses for the precursor signature of Figure 6-2 are not well-separated in time. A low-level, steady current flows for about 40  $\mu\text{s}$  and reaches a level of about 1 A before the much larger damped-oscillatory signature begins. A slow ramp in the electric field begins with the steady current flow, and ends when the damped-oscillatory signature begins. These features were observed in 126 (31%) of the 410 precursors analyzed. It is certainly possible that these features always occur but are sometimes below the noise floor of the measurements (a current level of about 1 A and a field change of about 1  $\text{V m}^{-1}$ ) and thus are undetectable.

The precursor signatures presented in Figures 6-1 and 6-2 are relatively simple in shape. The majority of the precursor signatures analyzed displayed more complexity in the pulse structure, such as two or more peaks (like the third current pulse in Figure 6-3C), non-monotonic rising and falling edges, and/or irregular oscillations, indicating a more complex electrical breakdown at the wire tip. The current pulses in most precursor signatures overlapped; that is, they were not clearly separated in time. In addition, since the pulse structure is more distorted with each successive reflection cycle, distinguishing features, such as two peaks, are often lost, typically by the fourth pulse. Precursors tended to occur in bursts more frequently with increasing wire-top height. There was no obvious relationship between the height at which the precursors occurred and the precursor features, such as low-level steady current or pulse shape.

Figure 6-3 shows how the precursor signatures change as the triggering wire extends with three examples of precursor signatures in wire-base current and electric field from wire launch UF09-11 (the 11<sup>th</sup> launch of 2009) at the beginning (26.20435 s), in the middle (26.77435 s) and just before the UPL (27.59095 s) when the wire-top heights were 31 m, 90 m, and 200 m, respectively (the full record for Launch UF09-11 is shown in Figure 6-4). As the wire-top height increased, the number of current reflections increased, and the pulses increased in width. Note that for the precursor that occurred when the wire top height was 200 m, the initial current-pulse has a multi-peak structure that is lost by the fourth pulse.

### **6.1.3 Precursor Rates**

Precursors occur at different rates in different wire extension. As an example, data are presented for two launches within a time of about 18 minutes in which precursors occurred at significantly different rates, even though the wires were extended upward beneath the same thunderstorm at similar extension rates, and initiated sustained upward positive leaders at about the same heights. As can be seen in Figure 6-4, precursors in launch UF09-11 occurred quasi-

periodically (with a periodicity that was regular, but with slightly different times from precursor to precursor) throughout the wire ascent, generally every several hundred microseconds to a few milliseconds. Based on the total time during which precursors occurred in launch UF09-11 (about 1.4 s), somewhere between 5,000 and 10,000 individual precursors occurred during the wire ascent. In the second wire launch (UF09-12), shown in Figure 6-5, precursors occurred quasi-periodically only during a 250-ms interval for wire-top heights from about 30 m to 60 m, followed by a 380-ms interval with no measurable current in the wire, and then a 680-ms interval in which 41 precursors without obvious periodicity.

In Figure 6-4, the precursor current pulses began at about 26.1 s, when the wire tip was at a height of about 30 m AGL. Note that the pulses in electric field before time 26.1 s were not produced by current in the wire. Between times 26.1 and 26.3 s, the current pulses occur sporadically and are unipolar, while the corresponding electric field pulses are bipolar. The pulses begin occurring quasi-periodically just after time 26.3 s. Figure 6-6 presents a 300-ms expanded view of pulses from 26.35 s to 26.65 s showing that the amplitude envelope of the current pulses exhibits somewhat periodic variations, and that the current pulses occur less frequently when the pulse amplitudes are larger, a general feature of all the launches. After time 26.8 s in Figure 6-4, the amplitude envelope of the current pulses varies with more distinct periodicity. At time 26.9 s, current pulses and pulse-bursts begin occurring, somewhat randomly, with magnitudes many times that of the pulses occurring quasi-periodically.

#### **6.1.4 Negative-Polarity Precursors**

In one launch (UF09-01), made when the ground-level electric field was  $-4.5 \text{ kV m}^{-1}$  indicating that predominately positive charge was overhead, observations were made of negative-polarity precursor signatures in current and electric field occurring quasi-periodically every several hundred microseconds in a manner similar to those from UF09-11 (Section 6.2.3).

These negative-polarity precursor signatures are presented in Figure 6-7. Launch UF09-01 was not recorded in video, so there was no measurement of the wire-top height versus time or observations of luminosity corresponding to the precursors. However, based on the time when the rocket was launched and the modeled trajectory in Section 7.3.1, it is estimated that the precursor signatures presented in Figure 6-7 occurred when the wire-top height was somewhere between 75 and 125 m. The observed negative-polarity precursors do not appear much different in rate and shape from positive-polarity precursors. The negative-polarity precursors occurred at a rate of about one every 1 ms, and generally had peak currents of several amperes and electric field changes of a few volts per meter.

## **6.2 Analysis**

This section contains analysis of measured precursor current signatures. First, the current-pulse propagation speed along the wire is measured. Then, information is developed from which the apparent attenuation of the current pulses due to propagation losses and imperfect current reflections with each round trip on the wire can be estimated and compared to the model predictions in Section 6.4.3. Finally, the charges in the first current-pulse and in the entire precursor current signature, as measured at the wire base, are compared.

### **6.2.1 Propagation Speed**

The current-pulse propagation speed on the triggering wire is measured from wire-base current measurements by dividing the wire-top height by one-half of the average of the times between the successive peaks (round-trip propagation times) for the first six peaks. For most precursors, the peak-to-peak times were equal within 200 ns, or 2 sample points. There were 271 precursor signatures with single-peaked pulses that were not saturated and hence suitable for current-pulse propagation speed measurement. The speeds of the current-pulses for these precursors are plotted versus wire height in Figure 6-8. There is uncertainty of at least 200 ns

(one sample point time for each peak-time measurement) in the round-trip propagation time that introduces a margin of error in the calculated current-pulse speed (shown as blue bars in Figure 6-8) that depends on the wire-top height (the longer the wire length, the longer the peak-to-peak time is, and thus the 200 ns timing uncertainty becomes less of a factor). The current-pulse propagation speed is roughly between  $2.7 \times 10^8$  and  $2.8 \times 10^8$  m s<sup>-1</sup> (disregarding the 200-ns uncertainty) for wire-top heights from 80 m to 200 m. The speed decreases for larger wire-top heights, to as low as about  $2.3 \times 10^8$  m s<sup>-1</sup>, or about 20% lower, for a wire-top height of 340 m. The measured speeds of three specific precursors used in the modeling (Section 6.4) are identified in Figure 6-8 by red circles. None of the six wires studied here exhibited a tilt angle of more than a few degrees or had a significant curvature. It is estimated that the wire tops did not deviate horizontally from the launch tower more than 10 m.

### 6.2.2 Precursor Charge and Current

The precursor signature in Figure 6-1 is one of 19 signatures of the 410 analyzed in which the starting point of the successive pulses were clearly distinguishable so that pulse amplitudes could be measured accurately. For these 19 precursor signatures, which occurred at wire-tip heights between 135 m and 340 m, the peak amplitudes of the first four current pulses,  $i_n^{\text{peak}}$  where  $n = 1, 2, \dots, 4$  (as identified in Figure 6-1), were measured. Figure 6-9 is a scatter plot of the computed ratios  $i_2^{\text{peak}} / i_1^{\text{peak}}$ ,  $i_3^{\text{peak}} / i_2^{\text{peak}}$ , and  $i_4^{\text{peak}} / i_3^{\text{peak}}$  versus wire-top height for the 19 precursors signatures. The ratios were roughly normally distributed from 0.45 to 0.75, and the arithmetic mean of all the ratios was 0.60 with standard deviation of 0.08. There was no apparent relationship between ratios of current peaks and wire-top height.

There was a clear relationship between the charge in the first current-pulse,  $Q_1$ , and the total charge delivered to ground by the end of the entire precursor current signature,  $Q_{\text{Total}}$ .

These charges were determined by computing the time integral of the current from the beginning of the precursor signature to: (a) the beginning of the second pulse for  $Q_1$ , and (b) the point when the current attenuates below the measurement noise floor for  $Q_{\text{Total}}$ . The charges  $Q_1$  and  $Q_{\text{Total}}$  were computed for 15 of the 19 precursor signatures analyzed in Figure 6-9 in which there was little to no overlap of pulses, so that the charge of the first current pulse could be accurately determined. Figure 6-10 is a scatter plot of  $Q_1$  versus  $Q_{\text{Total}}$  for these 15 precursors. There is linear relationship between the two, with a correlation coefficient of 0.99. Neglecting the non-zero intercept, the ratio  $Q_1/Q_{\text{Total}}$  is 1.64. Figure 6-10 also shows the charges  $Q_1$  and  $Q_{\text{Total}}$  that were computed for the model-predicted current signatures for precursors 2 and 3 (sSection 6.4). Precursor 1 was not used for the calculation because its pulses overlapped, making it impossible to determine accurately the charge in the first pulse.

### **6.3 Modeling**

In this section, three representative precursor current signatures (referred to as precursors 1, 2 and 3) are modeled. These three precursors occurred on the same triggering wire (UF09-37) when the wire top was at heights of 205 m, 307 m, and 339 m, respectively. First, a description is given of the assumed model input incident current waveforms, which are inferred from the wire-base measurements. Next, a description is given of the distributed (transmission line) circuits and the characteristic electrical parameters used to model the precursor current propagation on the triggering wire, ground lead, and ground rod, as illustrated in Figure 6-12, summarized in Table 6-1, and discussed in Section 6.4.2. Finally, in Section 6.4.3 the model predictions are presented and compared to the measurements.

#### **6.3.1 Model Input**

Panels A, B and C of Figure 6-11 present the model input incident current pulses for precursors 1, 2 and 3, respectively. The shape of the incident current pulse is assumed to be

identical to the shape of the measured precursor from time zero to the time when the second pulse begins. In each precursor modeled here, a power-law relation is fit to the smooth current decay from the first pulse peak time to the time when the second pulse begins. The input current from the time when the second pulse begins to a time 25  $\mu\text{s}$  after the pulse begins is an extrapolation of the power-law relation, and the last point of the input current is set equal to zero. The first pulse of the precursor signature measured at ground is the superposition of the incident wave and a reflected wave at ground, and as a result is larger in amplitude (almost twice) than the current pulse arriving at ground (and could be potentially different from the input pulse in shape, which is assumed to not be the case) which itself is attenuated from its initial value by propagating down the wire. Thus, the assumed input current pulses were reduced in amplitude by multiplying the entire input waveforms by scaling factors. The scaling factors, given in Figure 6-11 and Table 6-1, were found through trial and error by running the model and checking the match between the model-predicted first-pulse amplitude and the measured first-pulse amplitude.

### **6.3.2 Model Description**

The transmission line model [e.g., *Sadiku*, 1994, Ch 11], shown in Figure 6-12, consists of three interconnected sections representing the triggering wire (top), the ground-lead (middle), and the ground rod (bottom). Each is considered to be a straight, vertical, and uniform transmission line with different parameters. The transmission-line sections shown in Figure 6-12 are implemented in Pspice using the lumped-element lossy transmission line model (TLUMP128) [*Roychowdhury and Pederson*, 1991; *Roychowdhury et al.*, 1994]. The Pspice model predictions for propagation on the triggering wire were verified in several cases by multiplying the discrete Fourier transform of the input signal with the propagation constant (Equation 6-2) in the frequency domain, and then taking the inverse discrete Fourier transform of

the result. The result of the frequency domain multiplication yielded results that were identical to the time-domain convolution performed by the Pspice model. The Pspice software provided a straightforward way to connect the three transmission lines so as to be able to model the complex reflections at the transmission line connections (triggering wire to ground lead, and ground lead to ground rod). The incident precursor current pulse (at the top of the circuit in Figure 6-12) is input to the circuit using an ideal current source, making the current reflection coefficient at the wire tip -1. Note that the actual current measurement is made and the presented model output is calculated at the top of the ground lead, which is located at the bottom of the triggering wire. Nevertheless, the model predicts essentially the same current waveform at the bottom of the ground lead as at the top of the ground lead, but slightly delayed in time (by about 40 ns).

The complex sinusoidal current  $I(z)e^{j\omega t}$  on the transmission-lines used to represent the triggering wire, ground lead, and ground rod, with  $\omega = 2\pi f$ ,  $f$  the frequency in Hertz, and  $j = \sqrt{-1}$ , is described by the single frequency time-harmonic, wave equation in the frequency (or phasor) domain [Sadiku 1994]:

$$\frac{\partial^2 I(z)}{\partial z^2} = \gamma^2 I(z) \quad 6-1$$

where  $z$  is the propagation distance, and  $\gamma$  is the propagation constant, defined in terms of the distributed-circuit parameters as

$$\gamma = \alpha + j\beta = \sqrt{(R + j\omega L)(G + j\omega C)} \quad 6-2$$

where  $R$ ,  $L$ ,  $G$  and  $C$  are the series resistance, series inductance, shunt conductance, and shunt capacitance, respectively, all per-unit-length. In Equation 6-2,  $\alpha$  is the attenuation constant and  $\beta$  is the phase constant, given by:

$$\alpha = \text{Re}\{\gamma\} = \left\{ \left[ \text{RG} - \omega^2 \text{LC} + \sqrt{(\text{RG} - \omega^2 \text{LC})^2 + \omega^2 (\text{LG} + \text{RC})^2} \right] / 2 \right\}^{1/2} \quad [\text{Np m}^{-1}] \quad 6-3$$

$$\beta = \text{Im}\{\gamma\} = \left\{ \left[ \omega^2 \text{LC} - \text{RG} + \sqrt{(\text{RG} - \omega^2 \text{LC})^2 + \omega^2 (\text{LG} + \text{RC})^2} \right] / 2 \right\}^{1/2} \quad [\text{radian m}^{-1}] \quad 6-4$$

The attenuation constant unit ‘Np’ is a Neper, the commonly used dimensionless unit of attenuation. The transmission line characteristic impedance, the ratio of the voltage to the current for a wave traveling in the +z direction, is given by:

$$Z = \frac{\sqrt{\text{R} + j\omega\text{L}}}{\sqrt{\text{G} + j\omega\text{C}}} \quad [\Omega] \quad 6-5$$

The time-domain solution to Equation 6-1 for a wave propagating in the +z direction is:

$$I(z, t) = \text{Re}\{I_0 e^{-\gamma z} e^{j\omega t}\} = I_0 e^{-\alpha z} \cos(\omega t - \beta z) \quad [\text{A}] \quad 6-6$$

where ‘Re’ means the real part, and  $I_0$  is the current amplitude at  $z = 0$  (assumed to be real). The current wave propagation speed (phase velocity) predicted by Equation 6-1 is:

$$v_p = \frac{\omega}{\beta} \quad [\text{m s}^{-1}] \quad 6-7$$

The following is a description of how the values of transmission-line parameters for the triggering wire, ground lead, and ground rod were determined. The triggering wire has characteristic per-unit-length values of: series resistance  $R_{\text{TW}}$  due to the finite conductivity of the copper, series inductance  $L_{\text{TW}}$  due to the magnetic flux around the wire per unit current in the wire, and shunt capacitance  $C_{\text{TW}}$  due to the charge on and around the wire (in a corona sheath) per unit voltage. For the vertical wire above ground transmission line, one can visualize the return path (the second conductor required for any transmission line) as being the wire’s image below ground. Such a transmission line is necessarily non-uniform, particularly near ground, with the per-unit-length values of shunt capacitance and series inductance varying with height

[e.g., *Baba and Rakov, 2003; Theethayi and Cooray, 2005; Baba and Rakov, 2005; Visacro and De Conti, 2005*]. However, as a simplifying approximation, it is assumed here that all transmission line parameters are constant with height and independent of frequency, some aspects of these assumptions being discussed later in this section and in Section 6.4.3. The DC value of per unit length resistance of the 0.2-mm diameter triggering wire,  $R_{TW}$ , was measured to be  $0.5 \Omega \text{ m}^{-1}$ . The measured series resistance of the triggering wire was found via the model to be insufficient to attenuate the current pulses to the extent observed in the measured precursor signatures. Additional current attenuation was provided in the model by using an effective shunt conductance per unit length  $G_{TW}$  (associated with radial leakage current). It is important to note that the  $G_{TW}$  does not represent the true physical configuration since, in reality, transverse conduction current exists only within the corona sheath, but not in the space between the outer boundary of the corona sheath and ground. The value of  $G_{TW}$  (constant with height) was chosen in the model so that the model-predicted precursor signature amplitude attenuation matched that of the measurement. Thus, the shunt conductance should be viewed as a means to apply additional attenuation to the current pulse as it propagates on the transmission line. The inductance per unit length  $L_{TW}$  is calculated using the relation given for a vertical conductor above ground by [e.g., *Bazelyan et al., 1978; Rakov, 1998*]:

$$L = \frac{\mu_0}{2\pi} \ln\left(\frac{2h}{r}\right) \quad [\text{H m}^{-1}] \quad 6-8$$

where  $h$  is the height above ground,  $r$  is the conductor radius, and  $\mu_0$  is the permeability of free space. Equation 6-8 describes  $L_{TW}$  as a weak function of height that varies little over the heights of interest. The value used in the modeling is  $L_{TW} = 3.0 \mu\text{H m}^{-1}$ , which is the value yielded by Equation 6-8 for a 0.2-mm diameter wire for intermediate heights around 150 m.

If the current pulses propagate on the triggering wire with low losses ( $R \ll \omega L$  and  $G \ll \omega C$ ), as will be shown in Section 6.4.3 to be the case for the primary frequencies present in the pulses, the attenuation and phase constants described in Equations 6-3 and 6-4 can be approximated as:

$$\alpha = \frac{1}{2} \left( R_{TW} \sqrt{\frac{C_{TW}}{L_{TW}}} + G_{TW} \sqrt{\frac{L_{TW}}{C_{TW}}} \right) \quad [\text{Np m}^{-1}] \quad 6-9$$

$$\beta = \omega \sqrt{L_{TW} C_{TW}} \left[ 1 + \frac{1}{8} \left( \frac{G_{TW}}{\omega C_{TW}} - \frac{R_{TW}}{\omega L_{TW}} \right)^2 \right] \quad [\text{radians m}^{-1}] \quad 6-10$$

If the squared term in the brackets of Equation 6-10 is assumed to be zero, which is a good approximation in the low loss case, then Equation 6-7 becomes:

$$v_p = \frac{1}{\sqrt{L_{TW} C_{TW}}} \quad [\text{m s}^{-1}] \quad 6-11$$

where  $v_p$  is the current propagation speed along the wire, and  $L_{TW}$  is the per-unit-length inductance of the wire given by Equation 6-8. The values of capacitance per unit length,  $C_{TW}$ , that are used in the modeling are inferred from Equation 6-11 and the measured current propagation speeds from Section 6.3.1. The inferred values of  $C_{TW}$  are larger than the values expected from the relation given by *Bazelyan et al.* [1978] for a vertical conductor of radius  $r$  at a height  $h$  above ground:

$$C = \frac{2\pi\epsilon_0}{\ln(2h/r)} \quad [\text{F m}^{-1}] \quad 6-12$$

where  $\epsilon_0$  is the permittivity of free space. As expected, using the values of  $L$  and  $C$  given by equations 6-8 and 6-12 in place of  $L_{TW}$  and  $C_{TW}$  in Equation 6-11 yields a propagation speed  $v_p = c$ . The  $C_{TW}$  is often viewed as being given by Equation 6-12, but for a value of radius that is larger than the conductor (wire) radius and equal to that of the corona sheath [e.g., *Bazelyan et*

*al.*, 1978; *Kodali et al.*, 2005]. The value of  $L_{TW}$  computed from Equation 6-8 is unchanged by radial expansion of charge since the inductance depends on the longitudinal current, which flows solely in the wire [*Rakov*, 2007]. The corona sheath and the lower-than-light current-pulse propagation speed are discussed further in Section 6.5.

The ground lead that connects the bottom of the triggering wire to the ground rod has per-unit-length values of series resistance  $R_{GL}$ , series inductance  $L_{GL}$ , and shunt capacitance  $C_{GL}$ . The ground lead (2.5-cm wide copper braid) has a measured series resistance per unit length  $R_{GL}$  of  $1 \text{ m}\Omega \text{ m}^{-1}$ . The shape of the copper braid was somewhere between flat and cylindrical, but as a simplifying approximation it is assumed to be uniformly cylindrical with an effective radius of 1.25 cm. Under this assumption, it is expected that the electric field on the ground lead surface (which is estimated to be on the order of  $10^5 \text{ V m}^{-1}$  in Section 6.5) is below the level necessary for corona inception. The ground lead shunt conductance is assumed to be zero, and the current propagation speed on the ground lead wire is assumed to be equal to the speed of light. The per-unit-length values of series inductance and shunt capacitance for the ground lead, determined from Equations 6-8 and 6-12 using  $h = 11 \text{ m}$  (the upper height of the ground lead) and an effective radius of  $r = 1.25 \times 10^{-2} \text{ m}$ , are  $L_{GL} = 1.5 \text{ }\mu\text{H m}^{-1}$ , and  $C_{GL} = 7.4 \text{ pF m}^{-1}$ , respectively.

The buried ground rod is modeled in two different ways: as a lumped resistor of  $20\text{-}\Omega$ , and as a 25-m long buried transmission line with series resistance  $R_{GR}$ , series inductance  $L_{GR}$ , shunt capacitance  $C_{GR}$ , and shunt conductance  $G_{GR}$ . The value of series resistance  $R_{GR}$  is DC resistance for a 16-mm diameter steel rod, approximately  $8 \text{ m}\Omega \text{ m}^{-1}$ . The values of  $L_{GR}$ ,  $C_{GR}$ , and  $G_{GR}$  are adapted from a model used in *Mata et al.* [2000] for similar ground rods at the ICLRT. The shunt conductance is the inverse of the low-frequency, low-magnitude current resistance between the ground rod and the reference ground (surrounding soil), which has been

measured to be  $20 \Omega$  [Crawford *et al.*, 2001]. To determine the shunt conductance per unit length, the total measured resistance was first converted to a parallel resistance per unit length via multiplication by 25, yielding  $500 \Omega$ , and then taking the inverse, yielding  $G_{GR} = 2 \text{ mS m}^{-1}$ . The total values of C and L of the ground rod are determined using the following relations from Mata *et al.* [2000]:

$$C = \frac{\epsilon_r l}{18 \ln(4l/d)} \times 10^{-9} \quad \text{[F]} \quad 6-13$$

$$L = 2l \ln\left(\frac{4l}{d}\right) \times 10^{-7} \quad \text{[H]} \quad 6-14$$

where  $l$  is the length of the ground rod (25 m),  $\epsilon_r$  is the relative permittivity of the soil (assumed to be 10), and  $d$  is the diameter of the ground rod (16 mm). The total values of C and L for the grounding rod according to Equations 6-13 and 6-14 were 1.6 nF and 44  $\mu\text{H}$ , respectively. The total values of C and L were converted into per-unit-length values via division by 25, or the number of 1-m segments for the ground rod, yielding values of  $L_{GR} = 1.8 \mu\text{H m}^{-1}$  and  $C_{GR} = 64 \text{ pF m}^{-1}$ .

### 6.3.3 Model Predictions

Table 6-1 summarizes the parameters of the triggering-wire transmission line that yielded the model predictions used to fit the measurements, the scaling factor needed to match the first-pulse amplitude of the model output and measurements, the wire-top heights at which the precursors occurred, and the measured current propagation speeds on the triggering wire (Section 6.3.1). Figure 6-13 presents the three measured precursor signatures and the corresponding model predictions for the case that the grounding system is represented by a lumped resistor and for the case that the grounding system is represented by a 25-m transmission line. Each of the three rows of Figure 6-13 shows a different precursor on a 25- $\mu\text{s}$  time scale on the left, and an

expanded view from 4  $\mu\text{s}$  to 9  $\mu\text{s}$  on the right. Overall, the model predictions matched better the measurements when the grounding system was represented by a 25-m transmission line than when the grounding system was represented by a lumped resistor: (1) the model-predicted current-pulse peaks occurred later in time, and matched better the times when the measured current pulse peaks occurred, (2) the model-predicted current-pulse shapes were ‘smoother’, and matched better the shapes of the measured current pulses, and (3) the model-predicted current pulse amplitudes matched better the measured current pulse amplitudes. For either grounding system, the model predicts that all the precursor charge eventually leaves the bottom of the triggering wire by the end of the 25- $\mu\text{s}$  model run.

As evident from Figure 6-8, the measured current-pulse propagation speeds were lower for precursors occurring at greater wire-top heights. This observation was reproduced in the modeling by using greater triggering-wire capacitance per unit length for longer wire. As can be seen in Table 6-1, the measured current propagation speed for precursors 1 and 2 was  $2.6 \times 10^8 \text{ m s}^{-1}$ , and according to Equation 6-11, the capacitance per unit length of the triggering wire,  $C_{\text{TW}}$ , for these precursors 1 and 2 was  $4.9 \text{ pF m}^{-1}$ . The measured current propagation speed for Precursor 3 was  $2.5 \times 10^8 \text{ m s}^{-1}$ , or about 4% slower than the speed for Precursors 1 and 2, and according to Equation 6-11, the value of  $C_{\text{TW}}$  was  $5.3 \text{ pF m}^{-1}$ , or about 8% higher than the value of  $C_{\text{TW}}$  for precursors 1 and 2. For precursor 2, there is timing mismatch between the model-predicted current pulse peaks and the measured current pulse peaks, most notably in Figure 6-13 for the seventh current pulse at 16  $\mu\text{s}$ , possibly indicating that the value of  $C_{\text{TW}}$  used for precursor 2,  $4.9 \text{ pF m}^{-1}$ , was too low. Using a  $C_{\text{TW}}$  value of  $5.1 \text{ pF m}^{-1}$  in the model yields a signature with current-pulse reflection timing that matches better that of the measured current-pulse reflections.

The values of  $R_{TW}$ ,  $L_{TW}$ ,  $G_{TW}$ , and  $C_{TW}$  for the triggering wire that yielded the best model predictions satisfy the low-loss conditions for frequency content  $f \gg R_{TW}/2\pi L_{TW} \cong 30$  kHz and  $f \gg G_{TW}/2\pi C_{TW} \cong 40$  kHz, so Equations 6-9 and 6-10 are good approximations for the main portion of the pulse since a transient pulse having a full width of 3  $\mu$ s, like that of the input current pulses, approximately corresponds to a primary sinusoidal wave in the Fourier spectrum having a period of 6  $\mu$ s, or a frequency of about 170 kHz, above the low-loss frequencies noted above. Clearly, however, the input current pulses contain low-frequency components that do not satisfy the low-loss criterion, and a DC component to which the transmission line theory does not apply. Low-loss restrictions were not used in the model solutions presented in Figure 6-13 (or Figure 6-14 discussed below). The calculations above indicate that the primary current-pulse frequency content is sufficiently high to propagate on the triggering wire in the low-loss mode, which justifies the calculation of  $C_{TW}$  from the propagation speed using Equation 6-11 for lossless transmission lines (in Section 6.4.2).

Further justification that the current pulses propagate on the triggering wire in the low-loss mode can be found by comparing the exact attenuation constant given by Equation 6-3, to the low-loss attenuation constant, given by Equation 6-9, using the characteristic values found via modeling. The attenuation constant for propagation on the triggering wire yielded by Equation 6-3 is  $8.2 \times 10^{-4}$  Np  $m^{-1}$  for frequencies less than about 10 kHz, and for greater frequencies, the attenuation constant increases by less than 1% at the highest measured frequency of 3 MHz. The attenuation constant is essentially identical for the three values of  $C_{TW}$  in Table 6-1. The low-loss approximation for the attenuation constant yielded by Equation 6-9, which is frequency independent, is the same,  $8.2 \times 10^{-4}$  Np  $m^{-1}$ . The attenuation constant value of  $8.2 \times 10^{-4}$  Np  $m^{-1}$  for the triggering wire was determined by comparing the model current-pulse peak amplitudes

after the current pulses have traversed 25% and 75% of the triggering-wire length. The pulse peak decreases by 8% for 100 m of propagation on the triggering wire.

The characteristic impedance of the triggering wire,  $Z_{TW}$ , yielded by Equation 6-5 using the characteristic values found via modeling, is about 600  $\Omega$  for frequencies below about 10 kHz, increases for higher frequencies, and becomes constant at about 800  $\Omega$  for frequencies higher than 200 kHz. The characteristic impedance of the ground rod,  $Z_{GR}$ , is 2  $\Omega$  for frequencies below 100 Hz, and increases to about 120  $\Omega$  at a frequency of 3 MHz. If the presence of the ground lead between the triggering wire and ground rod has a negligible effect on the current entering the grounding system transmission line, as the model predicts, then the current reflection coefficient at the bottom of the triggering wire (as though it were connected directly to the 25-m transmission line grounding impedance) is given by:

$$\Gamma_{TW-GR} = \frac{Z_{TW} - Z_{GR}}{Z_{TW} + Z_{GR}} \quad 6-15$$

According to Equation 6-15, the current reflection coefficient is slightly less than 1 at frequencies below 10 kHz, and it decreases with increasing frequencies to a value just below 0.8 at a frequency of 3 MHz. The current reflection coefficient at the bottom of the triggering wire can be inferred by taking the ratio of the peak amplitude of the first upward, ground-reflected current pulse to the peak amplitude of the first downward current pulse. These two pulses overlap near the bottom of the triggering wire, so the peak amplitudes were measured in the model at the mid-point of the triggering wire, and then adjusted appropriately to account for the expected attenuation after propagating a distance equal to half the triggering-wire length by multiplication with  $\exp(-\alpha \cdot \text{wirelength}/2)$ . Doing this for precursors 1, 2 and 3 yielded an inferred current reflection coefficient at ground of about 0.9, which is in the range of values calculated using Equation 6-15.

The ratio of the input incident current-pulse amplitude and the first current-pulse amplitude measured at the wire base (the scaling factor described in Section 6.4.1) increased with increasing wire-top height. For precursors 1, 2 and 3, the amplitude scaling factors determined by trial and error were 0.62, 0.68, and 0.72, respectively. If the current reflection coefficient at the bottom of the triggering wire of length  $l$  is  $\Gamma_G$  and the attenuation constant is  $\alpha$ , then the scaling factors that were used for precursors 1, 2 and 3 can be approximated by Equation 6-16.

$$G = \left[ (1 + \Gamma_G) \exp(-\alpha l) \right]^{-1} \quad 6-16$$

For  $\alpha = 8.2 \times 10^{-4} \text{ Np m}^{-1}$  and  $\Gamma_G = 0.9$ , Equation 6-16 yields scaling factors of 0.62, 0.67, and 0.69 for precursors 1, 2 and 3, respectively.

The analysis of Section 6.3.2 was performed on precursors 2 and 3 (precursor 1 did not meet the criterion for inclusion in the analysis because the successive pulses overlapped and the starting points of successive pulses were not distinguishable). The modeled peak current amplitude ratios ( $i_2^{\text{peak}}/i_1^{\text{peak}}$ ,  $i_3^{\text{peak}}/i_2^{\text{peak}}$ ,  $i_4^{\text{peak}}/i_3^{\text{peak}}$ ) are similar to those in Figure 6-9, ranging from 0.51 to 0.74 with an arithmetic mean of 0.62. The charges  $Q_1$  and  $Q_{\text{Total}}$  from the modeled and measured current signatures for precursors 2 and 3 were similar (Figure 6-10). The ratios of  $Q_1/Q_{\text{Total}}$  for the model-predicted signatures 2 and 3 were 1.63 and 1.47, similar to the ratios for the measured signatures, 1.62 and 1.47. The similarities in the measured and modeled signatures for precursors 1 and 2 discussed above demonstrates the validity of the model.

## 6.4 Discussion

There is a good match between the model-predicted and measured precursor current signatures for all three representative precursors. The precursor current signatures from the distributed circuit model match better the measured precursor signatures when the grounding system is represented by a 25-m transmission line, rather than a lumped resistor. The apparent

frequency dependence of the ground-rod characteristic impedance may be compensating for neglected frequency dependence elsewhere in the model, such as the tendency for high-frequency currents to flow closer to the conductor surface, thereby lowering the cross-sectional area through which the current flows and increasing the effective resistance, known as the skin effect [Sadiku 1994, Ch. 10]. For the copper triggering wire, the skin depth (the conductor depth at which the current density is about a factor  $e^{-1}$  smaller than at the conductor surface) is equal to the wire radius (0.1 mm) at a signal frequency of about 425 kHz. As noted in Section 6.4.3, the current-pulse frequency content is mostly greater than 170 kHz, so the true value of  $R_{TW}$  is expected to be higher than the measured DC value, but only up to a factor of 1.6 higher at 3 MHz (the low-pass filter 3-dB point cutoff frequency of the digitizer). If the model value of  $R_{TW}$  were made higher, then the additional current pulse attenuation provided by the non-zero value of  $G_{TW}$  might not be necessary for the modeled pulse amplitudes to match the measured ones.

As noted in Section 6.4.2, in the transmission-line representation for the vertical wire above ground, the shunt capacitance and series inductance, and hence the characteristic impedance must vary with height. A non-uniform transmission-line model may reproduce better some of the observed current-pulse attenuation and shape change (dispersion) due to the distributed reflections that are expected when the characteristic impedance varies in the longitudinal direction [Baba and Rakov, 2005]. However, it is likely that a non-zero series resistance would still be necessary to reproduce the observed current pulse attenuation.

Figure 6-14 presents model predictions for precursor 3 when the value of either  $R_{TW}$  or  $G_{TW}$  is varied by factors of 0, 1, 2, 5 and 10, to illustrate the range of behavior that might be expected if triggering wires of different dc resistance were used, or if the value of  $G_{RW}$  were different. The top plots show, on different time scales, five model predictions for five values of

$R_{TW}$ : 0, 0.5, 1, 2.5 and  $5 \Omega \text{ m}^{-1}$ , with  $L_{TW}$ ,  $C_{TW}$  and  $G_{TW}$  being equal to the values used for the model predictions in Figure 6-13. The bottom two plots show, on different time scales, five model predictions for five values of  $G_{TW}$ : 0, 1.3, 2.6, 6.5 and  $13 \mu\text{S m}^{-1}$ , with  $L_{TW}$ ,  $C_{TW}$  and  $G_{TW}$  equal to the values used for the model predictions in Figure 6-13. In all cases the grounding system is modeled as a 25-m transmission line. Note that the measurements are not shown in the plots of Figure 6-14. It is evident from Figure 6-14 that changing either  $R_{TW}$  or  $G_{TW}$  changes the amplitudes of the model-predicted current pulses, but does not noticeably change the current pulse shapes, or the times at which they occur. If the value of either  $R_{TW}$  or  $G_{TW}$  is a factor of 5 higher than the value used to obtain the model predictions in Figure 6-13, then the current is attenuated to essentially zero by the third reflection. If the value of either  $R_{TW}$  or  $G_{TW}$  is higher by a factor of 10, then the current is attenuated to essentially zero by the first reflection. If the value of either  $R_{TW}$  or  $G_{TW}$  is zero, then the reflections continue past the time of 25- $\mu\text{s}$  to which the model calculations were made. The model predictions presented in Figure 6-14 show that the current propagation speed is not appreciably changed for the different values of  $R_{TW}$  or  $G_{TW}$  that produce reasonable current attenuation, or for the case that  $R_{TW}$  and  $G_{TW}$  were zero, and the observed current attenuation is a result of some other factor, such as charge deposition to an extending plasma channel at the wire tip (as suggested for the stepped upward positive leader discussed in Section 5.5).

The waveform measurements (and necessarily the modeling results because  $C_{TW}$  is chosen to give the measured speed) show that the current propagation speed on the triggering wire is less than the speed of light, and that the current propagation speed decreases with increasing wire-top height. A current propagation speed less than the speed of light on a vertical conductor can be viewed as a result of the increased capacitance per unit length, as per Equation 6-12, due to the

existence of a ‘corona sheath’ that increases the effective charge radius [Rakov, 2007]. As discussed in Chapter 7 of this work, a corona sheath surrounding the wire is likely created via radial corona streamers initiated by the enhanced radial electric field on the thin-wire surface. The modeling results of Chapter 7 (Section 7.5) predict a substantial corona sheath extending out to about 5 meters that, in the time necessary to extend a grounded triggering wire to a height of 285 m, builds up to several millicoulombs of charge with the line charge density on the order of tens of  $\mu\text{C m}^{-1}$  that increases with height. The prediction of a corona sheath around the grounded triggering wire in Chapter 5 is supported by the results presented here, namely that the current propagation speed is less than the speed of light.

In the following, the radial electric field strength on the wire surface due to the precursor charge on the wire is inferred, and the issue of corona charge surrounding the wire due to the precursor’s radial electric field is discussed. The line charge density on the wire from the precursor current,  $\rho$ , can be estimated by dividing the precursor current by the current propagation speed. The charge density for a single current peak of 50 A traveling at a speed of  $2.6 \times 10^8 \text{ m s}^{-1}$  is on the order of  $200 \text{ nC m}^{-1}$ , much smaller than the charge per unit length of tens of  $\mu\text{C m}^{-1}$  induced by the quasi-static ambient field. However, according to Gauss’s law for the radial electric field  $E_r$  from a line charge  $\rho$  [e.g., Sadiku 1994, Ch. 4]:

$$E_r = \frac{\rho}{2\pi\epsilon_0 r} \quad 6-17$$

a line charge density of  $200 \text{ nC m}^{-1}$  can produce an electric field of  $36 \text{ MV m}^{-1}$  at the triggering wire surface, well above the threshold for corona discharge. It takes a time of about 400 ns for the current to propagate 100 m at a speed of  $2.6 \times 10^8 \text{ m s}^{-1}$ . During a single wire traversal, the intense radial electric fields on the wire surface from the precursor charge exist for about  $1 \mu\text{s}$  (for a 300-m wire-top height). If the radial corona streamers propagate at a speed of  $0.1 \text{ m } \mu\text{s}^{-1}$

[Cooray, 1993], there is little time for space charge development from precursor current electric fields. Further, whatever space charge is created, it is mitigated by the oscillating current polarity, that is, charge is deposited along the wire when the current pulse is of negative polarity, and charge is removed when the current pulse is of positive polarity. Nevertheless, there will be some deposited corona charge around the wire, with some, if not most, of it flowing back into the grounded wire. The argument above is supported by the circuit model which predicts that essentially all of the charge input at the top of the triggering wire leaves the bottom of the triggering wire by the end of the 25- $\mu$ s model run. In the model, the charge deposited on the transmission line capacitors by the decrease (attenuation) in peak current with distance in propagation flows off those capacitors to ground within the 25  $\mu$ s duration of the model run. If all of the precursor charge is brought to ground, it is reasonable that precursor charge can be inferred from nearby static electric field change using a point-charge at the wire-tip approximation, as is done in Chapter 7 (Section 7.3.3). According to Equation 6-17 the electric field on the surface of the ground lead, with an assumed effective radius of 1.25 cm, will be about  $3 \times 10^5 \text{ V m}^{-1}$ , so the assumption that the shunt conductance per unit length for the ground lead  $G_{GL}$  is zero is a reasonable one.

The following text contains some speculation regarding the observed variability in the number and rates of precursors in different wire extensions and the periodicity of their peak amplitude envelope. The observed variability in the number of precursors may indicate that wires extend through different vertical profiles of space charge density, and thus different profiles of electric field. The periodicity exhibited in the amplitude envelope of the precursor pulses in UF09-11 may be a result of the wire tip traveling through layers of periodically increasing and decreasing electric fields. Alternatively, the variability in rates of precursor

occurrence may instead be due to different vertical profiles of humidity. It is well known that positive-polarity corona processes in laboratory spark gaps require a higher electric field strength in air with high humidity than in air with lower humidity [e.g., *Griffiths and Phelps*, 1976; *Gallimberti*, 1977].

Table 6-1. Precursor information, triggering-wire transmission-line parameters corresponding to the model-predicted precursor signatures that best match the measured precursor signatures, and the amplitude scaling factor of the input current pulse.

Precursor	GPS time	Wire-top height (m) <sup>a</sup>	R <sub>TW</sub> (Ω m <sup>-1</sup> )	L <sub>TW</sub> (μH m <sup>-1</sup> )	G <sub>TW</sub> (μS m <sup>-1</sup> )	C <sub>TW</sub> (pF m <sup>-1</sup> )	Measured Speed (m s <sup>-1</sup> ) <sup>†</sup>	Amplitude Scaling Factor
1	21:21:24.089508	205	0.5	3.0	1.3	4.9	2.6 x 10 <sup>8</sup>	0.62
2	21:21:25.351162	307	0.5	3.0	1.3	4.9	2.6 x 10 <sup>8</sup>	0.68
3	21:21:25.940685	339	0.5	3.0	1.3	5.3	2.5 x 10 <sup>8</sup>	0.74

a) The wire length is this value minus 11 m

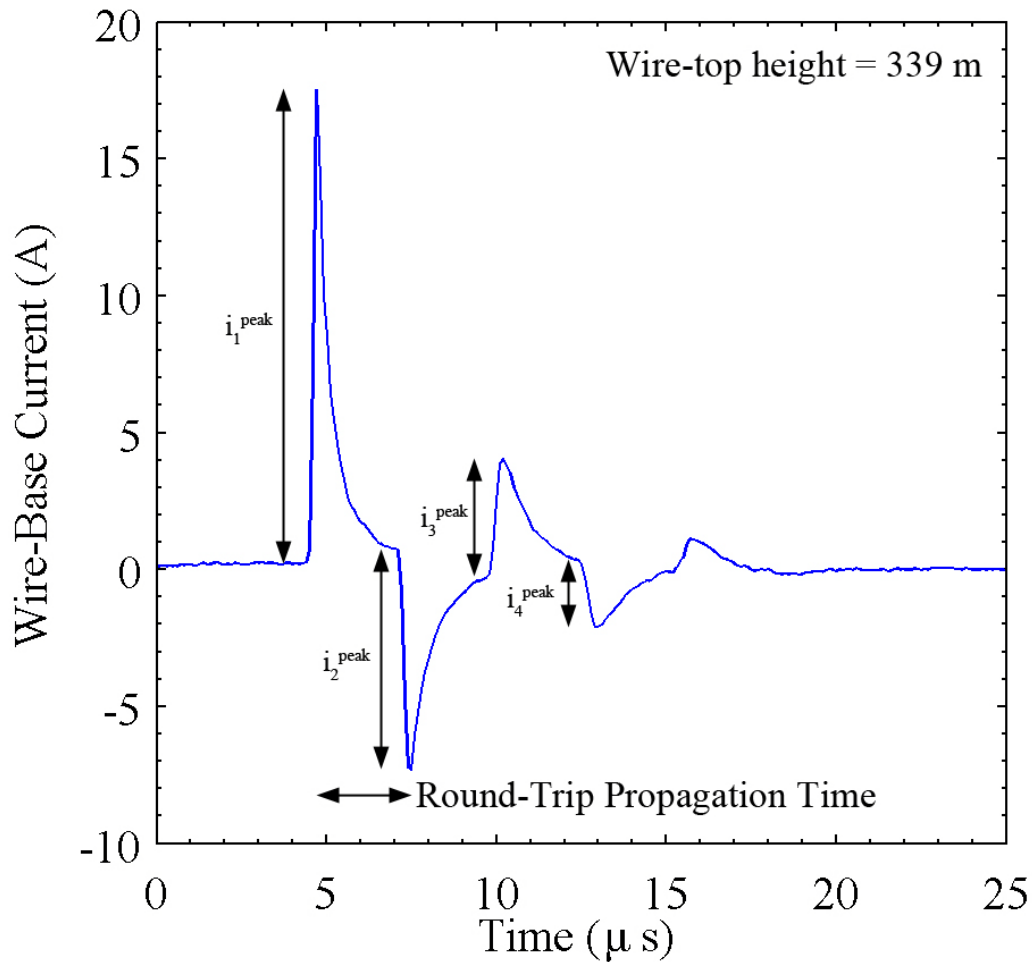


Figure 6-1. Current signature of a precursor in which the first current pulse, and subsequent current pulses resulting from reflections from the wire base and wire top, are clearly separated in time and easily distinguishable. Peak amplitude measurements that are used in the analysis of Section 6.3.2 are identified along with the round-trip propagation time (peak-to-peak time). This is precursor 3 that is modeled in Section 6.4.

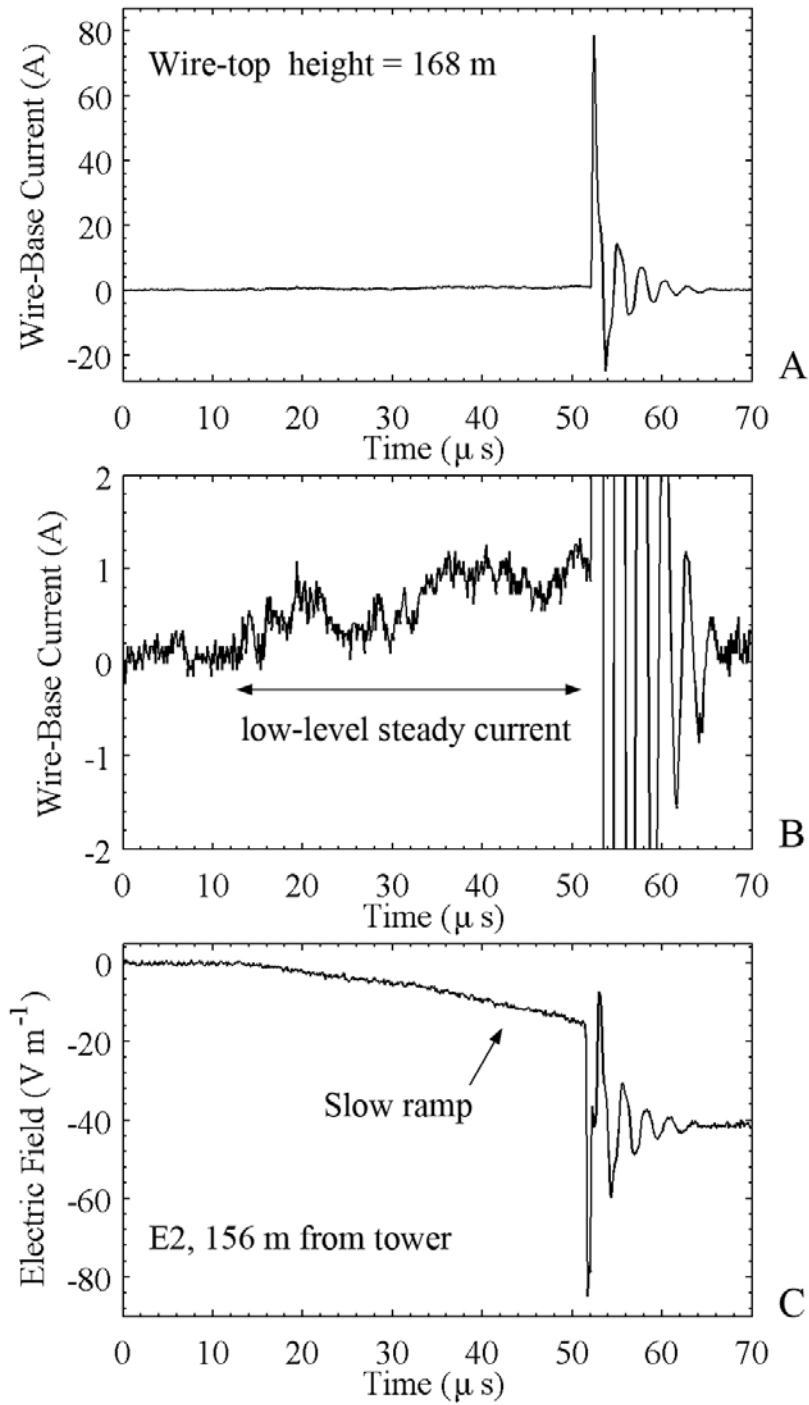


Figure 6-2. Current and electric field signatures produced by a precursor that exhibited an initial low-level, steady current, and corresponding electric field ramp. A) wire-base current shown on full-scale, B) wire-base current shown at  $\pm 2$  A scale, and C) electric field.

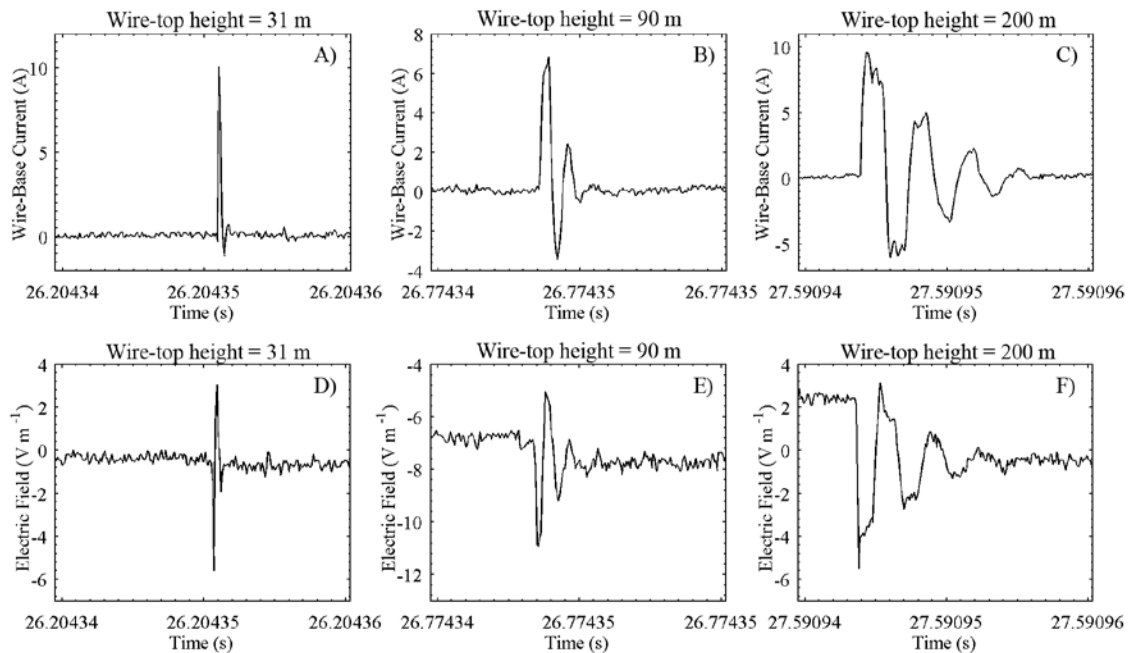


Figure 6-3. The wire-base current, and respective electric field measured by E2 at 156 m for three precursor signatures from event UF09-11. Each column shows the current in the top panel and the electric field in the bottom panel. Each plot is  $20 \mu s$  full scale. The wire-top heights were about 31 m, 90 m, and 200 m for the left, middle, and right panels, respectively. As the wire-top height increased the number of current reflections increased, and the pulses increased in width.

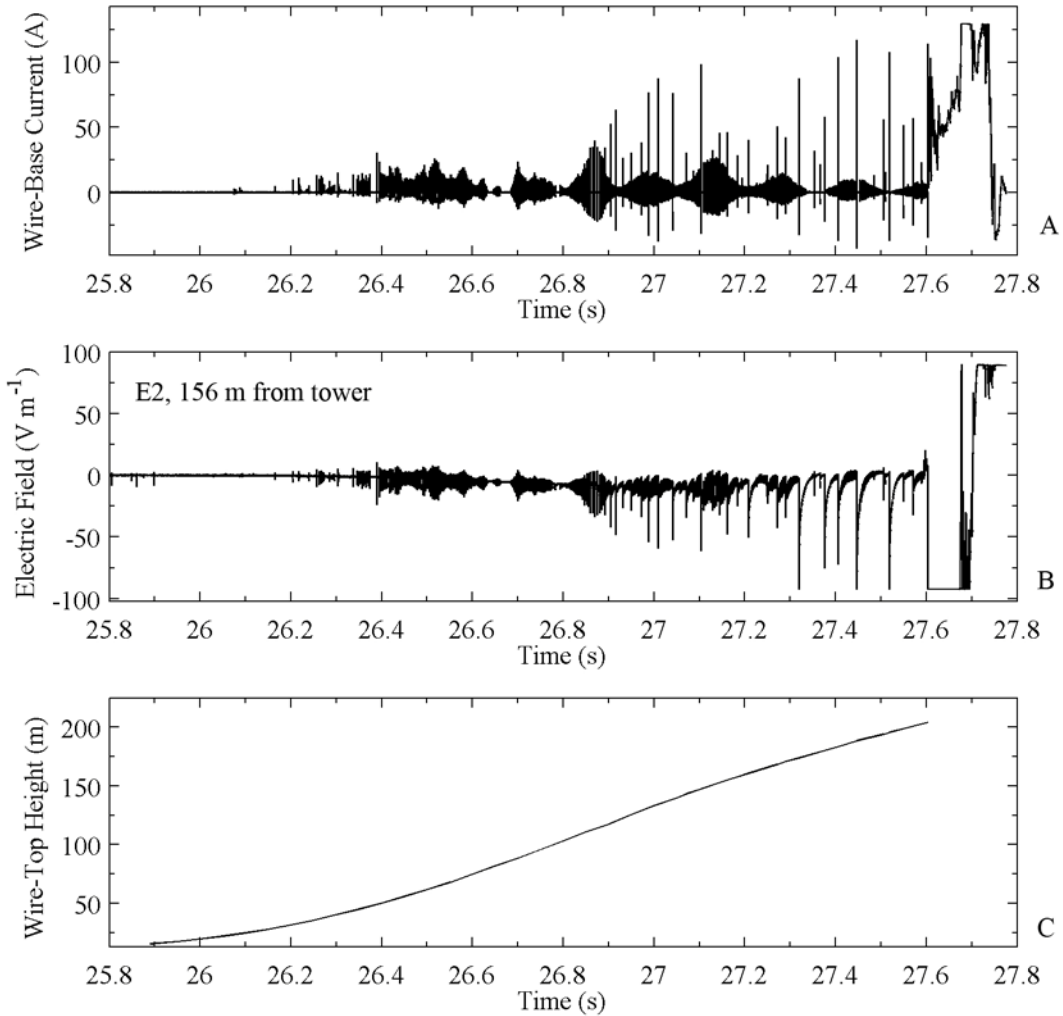


Figure 6-4. The wire-base current, and respective electric field measured by E2 at 156 m for three precursor signatures for wire launch UF09-11 on a 2 s time scale. The wire-base current and electric field measurements saturate at about 125 A and  $\pm 85 V m^{-1}$ , respectively. The sustained upward positive leader began at time 27.604 seconds when the wire-tip height was about 234 m. The solid 'envelope' in the current record that varies with a period around 200 ms is composed of thousands of individual pulses that are not resolvable on this time scale, some of which are shown in Figure 6-6.

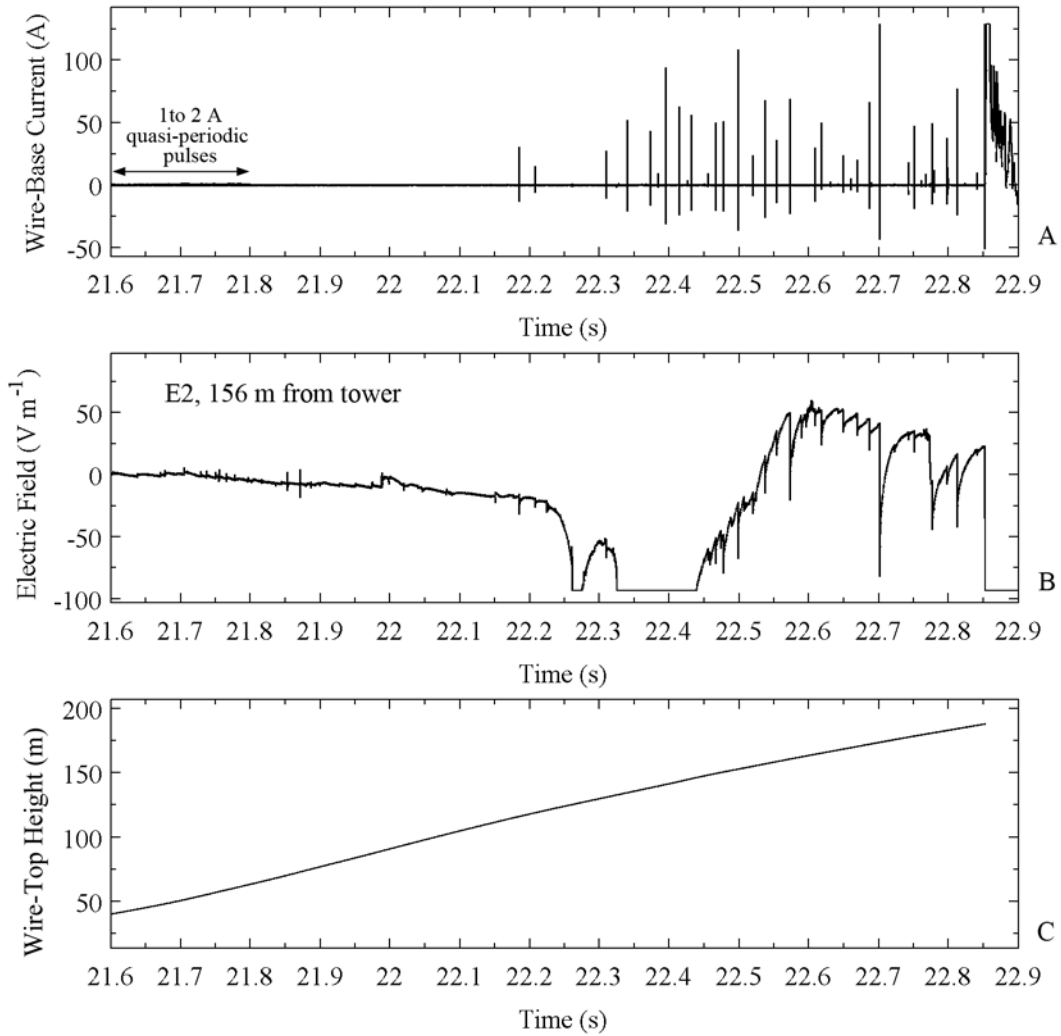


Figure 6-5. The wire-base current, and respective electric field measured by E2 at 156 m for UF09-12 on a 1.3-s time scale. The wire-base current and electric field records began when the wire tip was at a height of about 40 m, and they saturate at about 125 A and  $-85 V m^{-1}$ , respectively. The sustained upward positive leader began at about 22.85 s when the wire-tip height was about 190 m. Note that much of the recorded electric field change from time 21.6 s to 22.4 s is due to separate and unrelated lightning process (signatures corresponding to distant preliminary breakdown and cloud discharges are evident when the field record is examined on an expanded time scale).

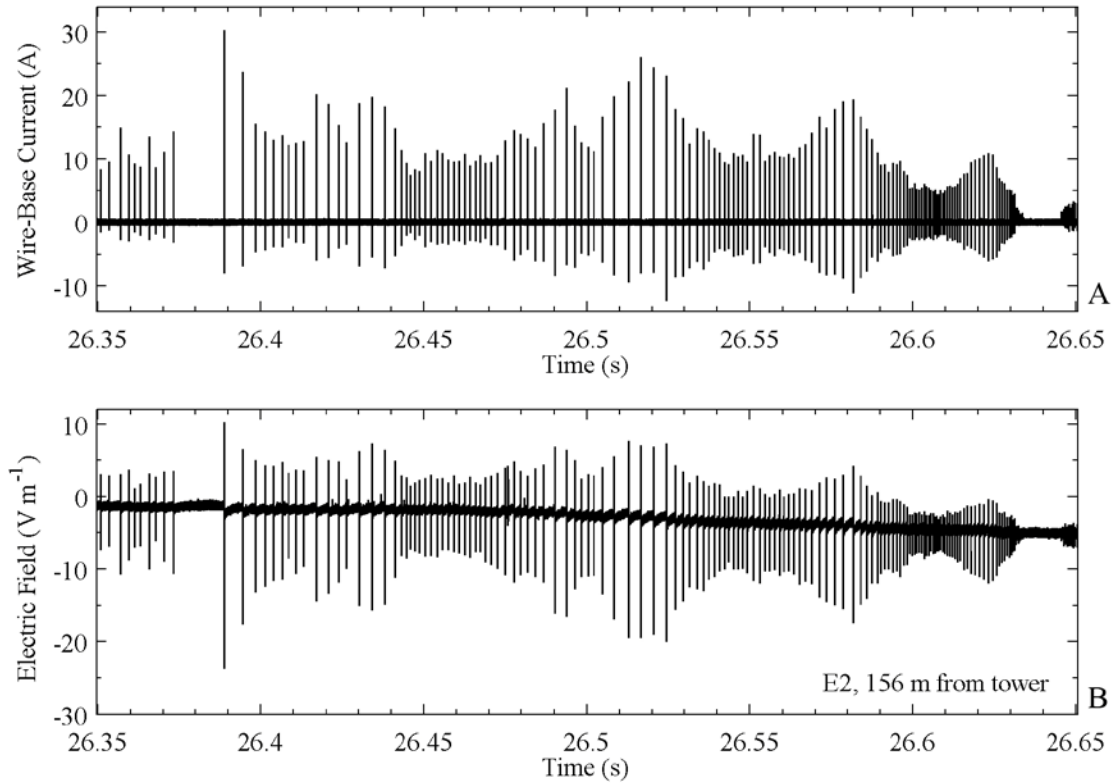


Figure 6-6. An expanded view of the wire-base current and electric field of the precursors in UF09-11 viewed at 300 ms full scale. (A) The wire-base current. (B) The electric field from E2 at 156 m. Pulses generally occur less frequently (the interpulse time is greater) when the pulse amplitudes are larger.

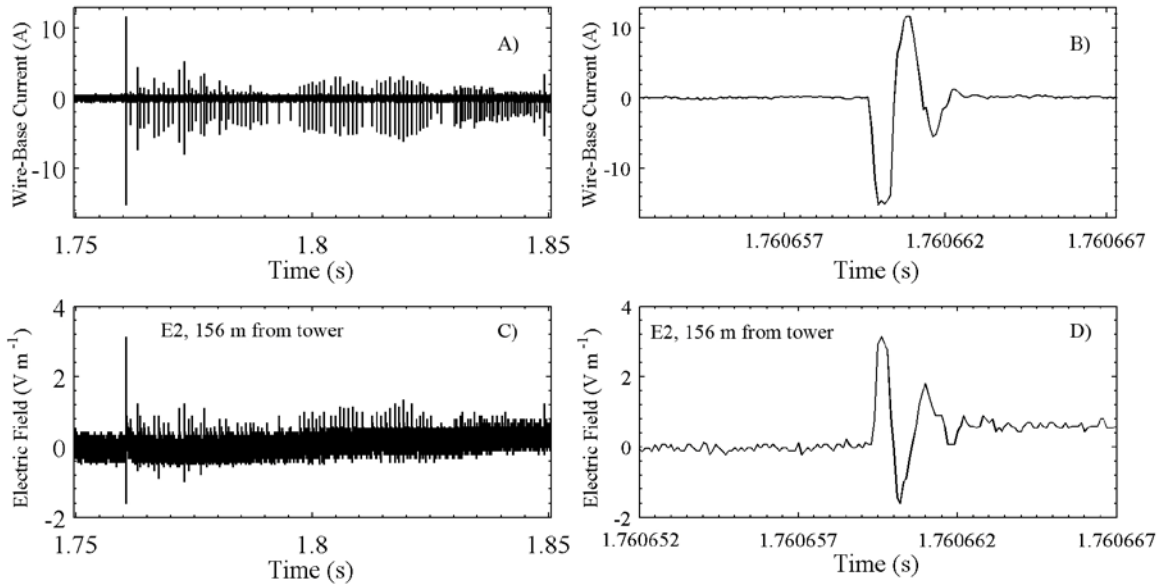


Figure 6-7. Wire-base current and electric field signatures of negative-polarity precursors during wire launch UF09-01. The wire-base currents are shown in the top plots (A and B), and the remote electric fields are shown in the bottom plots (C and D). The left plots show the precursors on a 100-ms time scale. The right plots shows, on a 15- $\mu$ s time scale, the largest precursor signature that occurred at time 1.76066 s. It is estimated that these precursor signatures occurred when the wire-top height was somewhere between 75 and 125 m (Section 6.2.4).

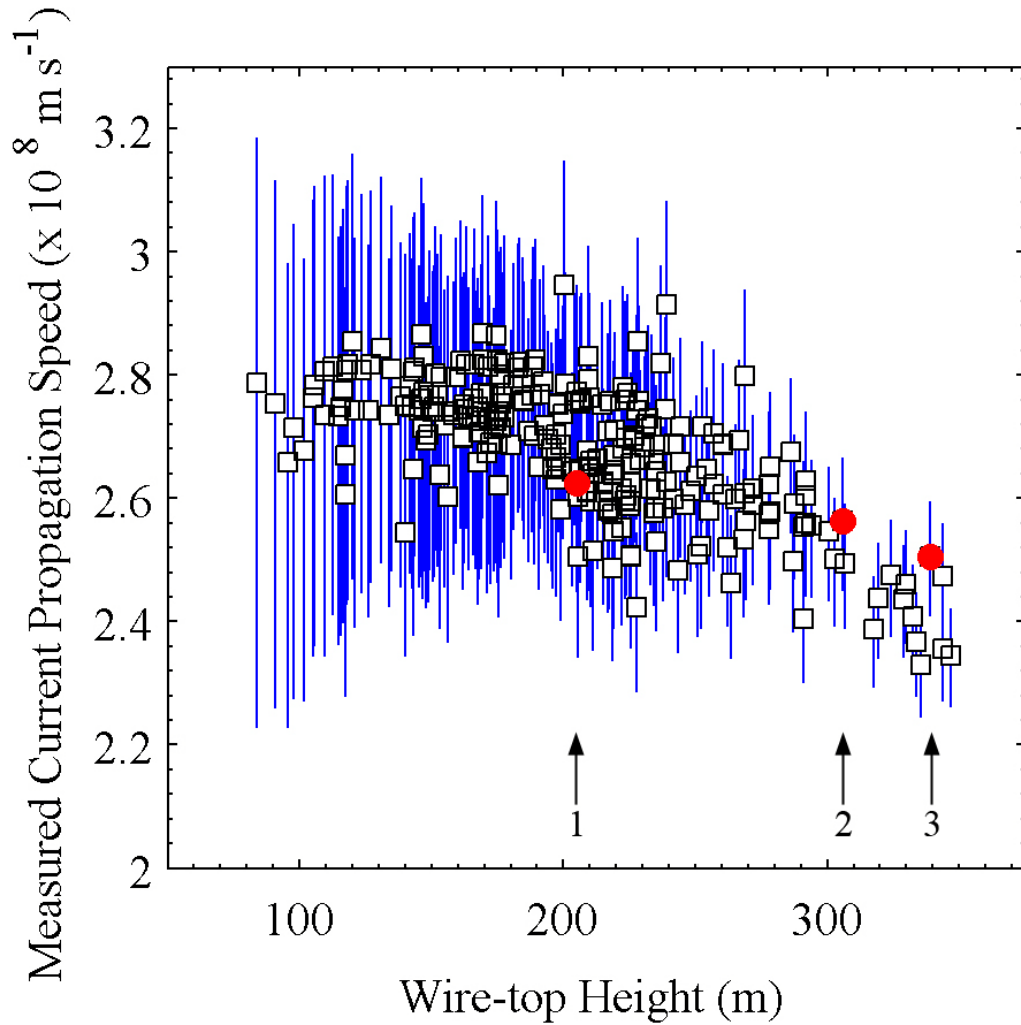


Figure 6-8. A scatter plot showing the measured current propagation speeds (the ratio of wire-top height to one-half of the average peak-to-peak times) versus wire-top heights for 271 precursors. The blue vertical lines show the margins of error that result from the peak-time measurements having a timing uncertainty of 200 ns ( $\pm 100$  ns). The data points for precursors 1, 2 and 3 that are modeled in Section 6.4 are plotted as red circles, and pointed to by black arrows numbered 1, 2 and 3. Note that the vertical scale starts at  $2 \times 10^8$  m s<sup>-1</sup> and that many data points overlay.

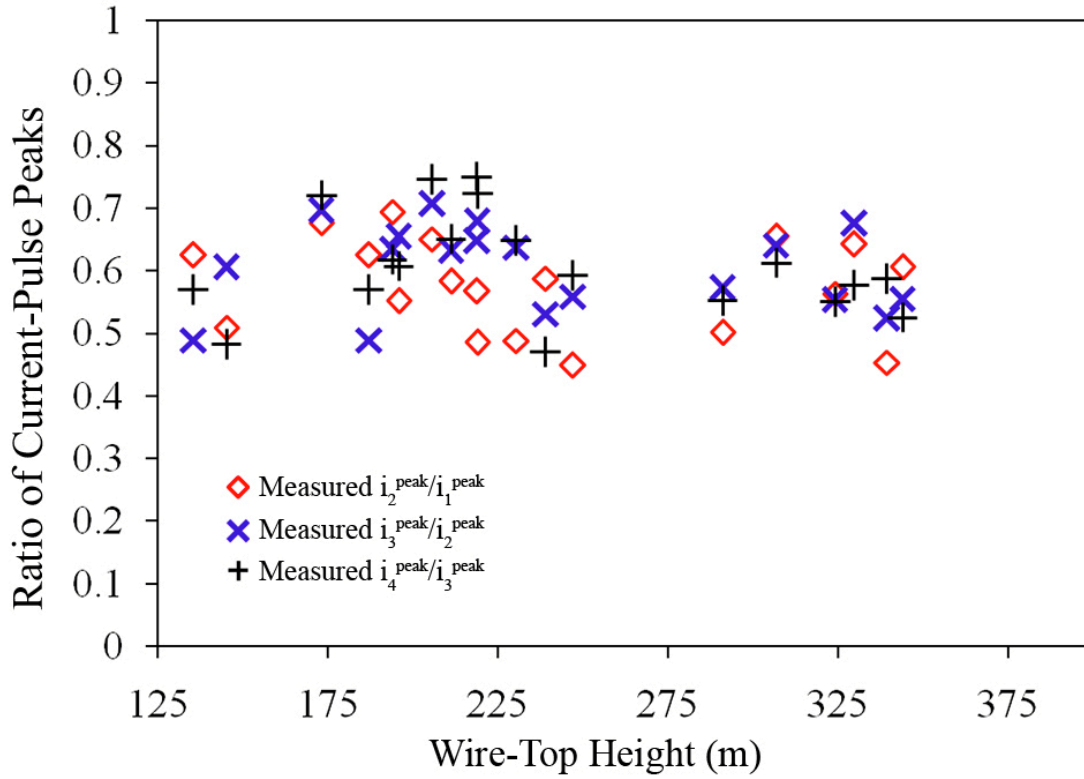


Figure 6-9. A scatter plot of the current-peak ratios. Red diamonds, blue 'x', and black 'plus' marks show the values  $i_2^{\text{peak}}/i_1^{\text{peak}}$ ,  $i_3^{\text{peak}}/i_2^{\text{peak}}$ ,  $i_4^{\text{peak}}/i_3^{\text{peak}}$  for 19 measured precursor current signatures (Section 6.3.2).

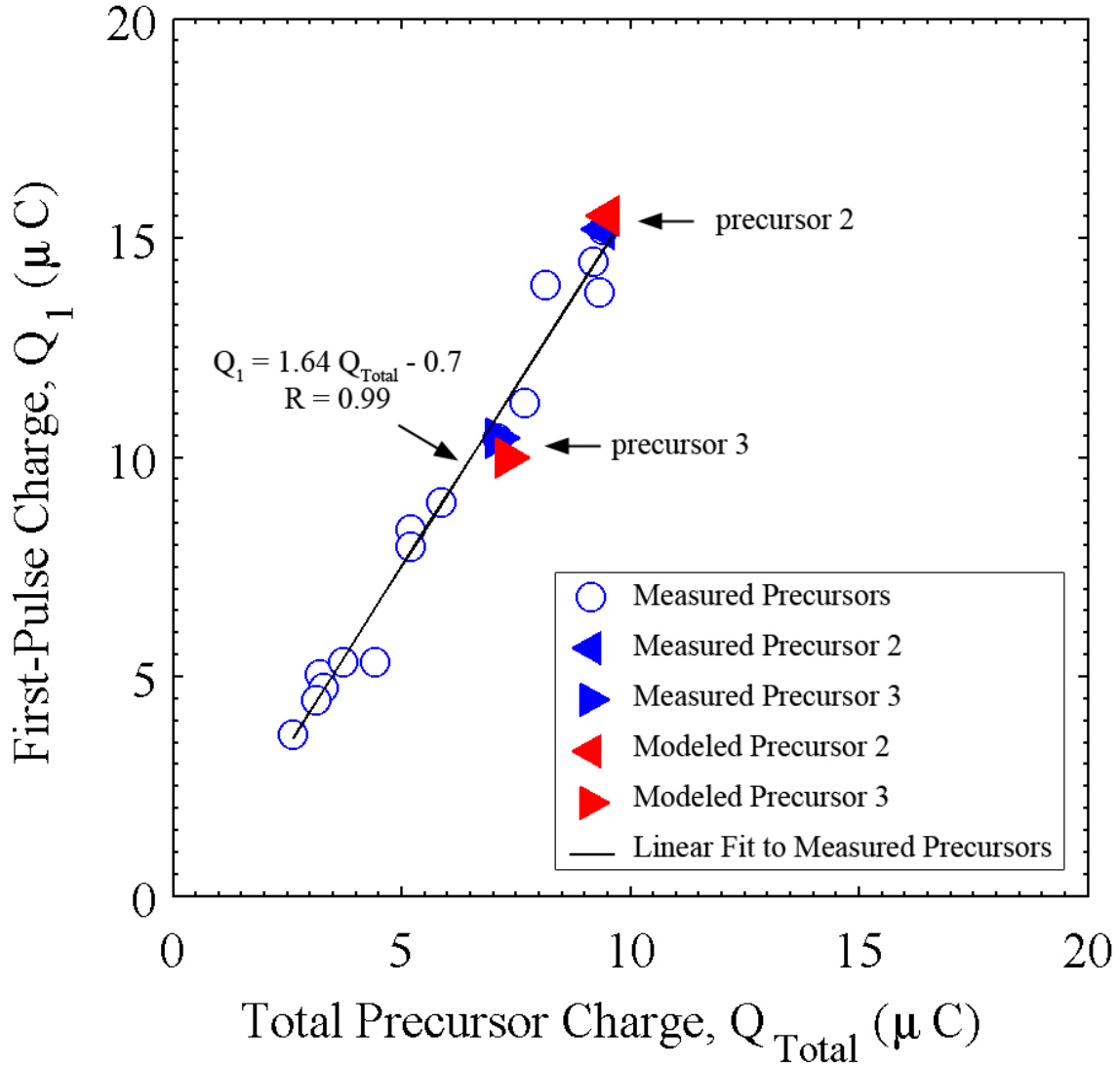


Figure 6-10. A scatter plot of the charge transferred to ground during the initial precursor current pulse versus the total charge transferred to ground by the end of the precursor current signature. Data points are shown for 15 measured precursors (blue circles and triangles, Section 6.3.2), and modeled precursors 2 and 3 (red triangles, Section 6.4). The black line is the linear regression for the 15 measured precursors.

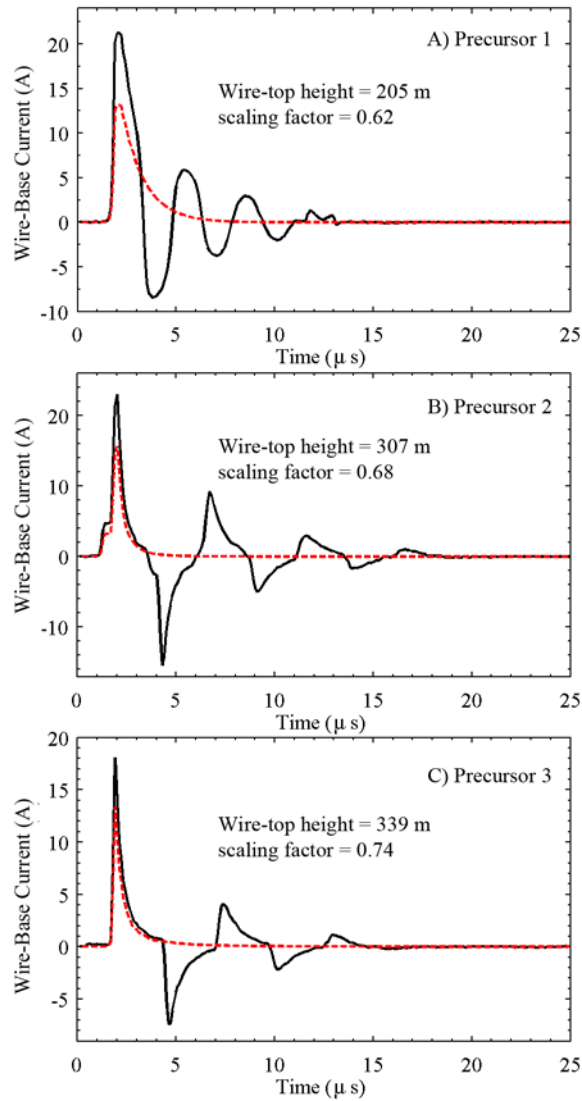


Figure 6-11. The incident current pulses that are used as inputs to the distributed-circuit model shown in Figure 6-12. The red dashed lines are the inputs and the corresponding measurements are shown with black lines for Precursors 1, 2 and 3 in panels A, B, and C, respectively. The incident current pulses are a scaling factor smaller in amplitude than the measured initial pulses (Section 6.4.1).

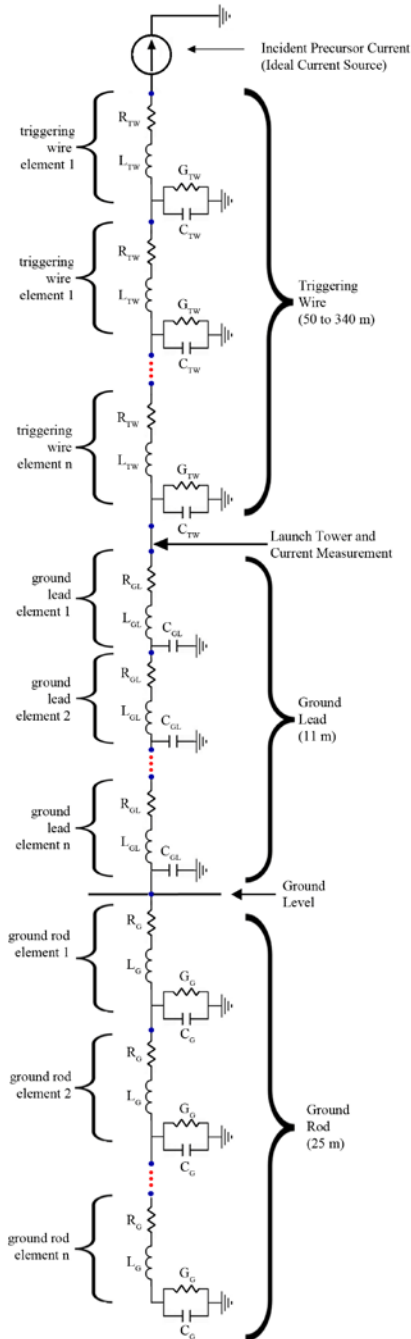


Figure 6-12. The distributed circuit used to model the current propagation on the triggering wire, ground-lead, and ground rod. The precursor incident current is represented by an ideal current source at the triggering-wire top. In the case when the grounding impedance was assumed to be purely resistive, the ground-rod distributed circuit is replaced by a resistor. Current is measured at the junction of the triggering wire and ground lead.

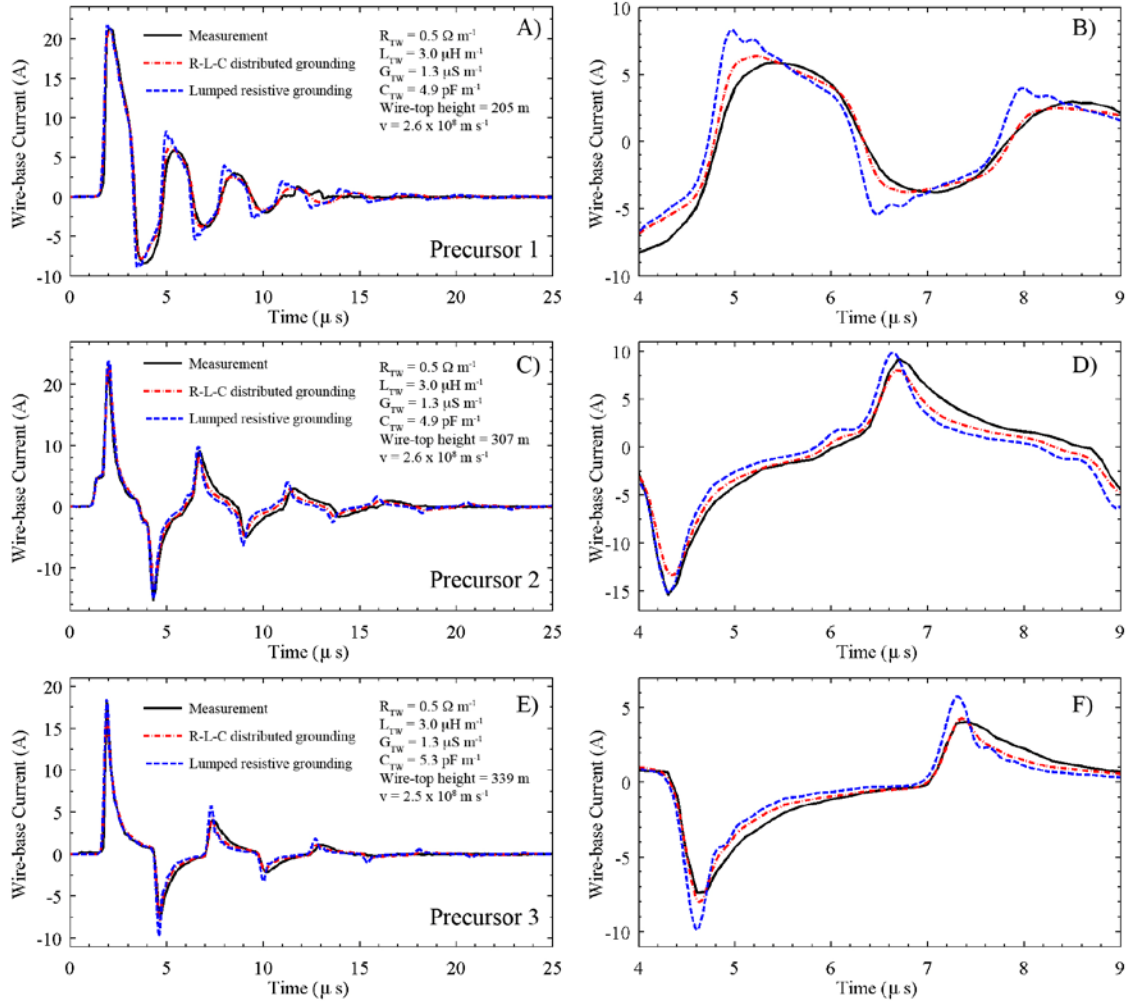


Figure 6-13. Measurement and modeling results for three precursors for two model grounding configurations. The grounding system is modeled as a 25-m transmission line (dash-dot red line) and the grounding system is modeled as a lumped resistor (dashed blue line). Precursors 1, 2, and 3 are shown on a 25- $\mu$ s time scale in panels A, C, and E, respectively. Precursors 1, 2, and 3 are shown on a 5- $\mu$ s time scale in panels B, D, and F, respectively.

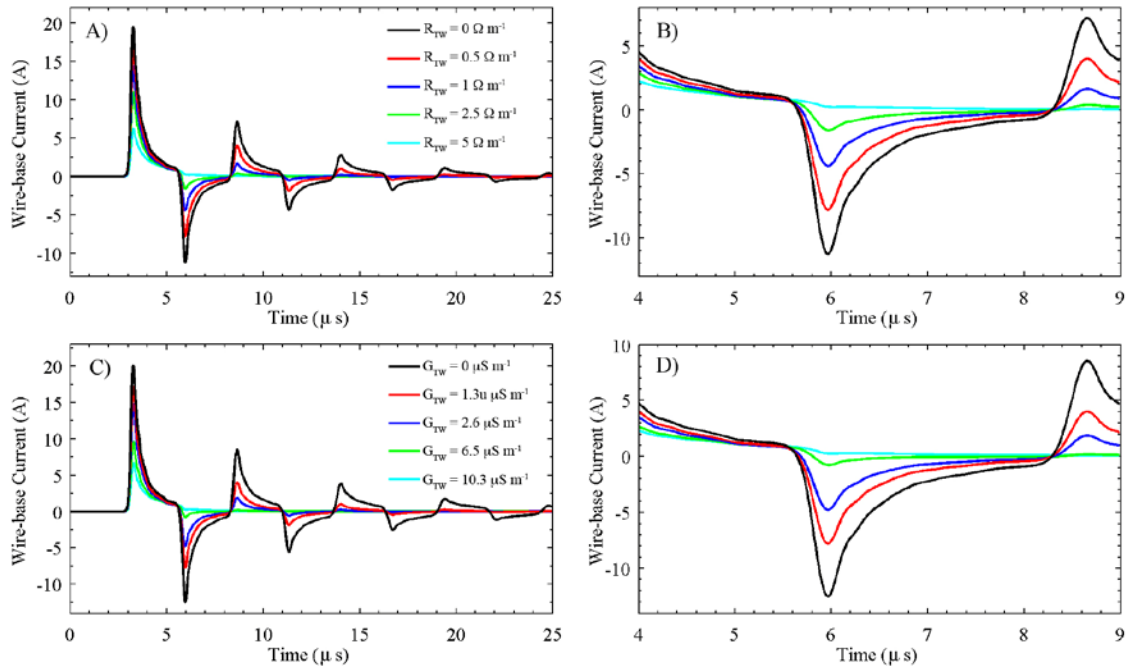


Figure 6-14. The model predictions for precursor 3 with varied values of  $G_{TW}$  and  $R_{TW}$ . The model predictions using different values of  $R_{TW}$  are shown in panels A and B. The model predictions using different values of  $G_{TW}$  are shown in panels C and D. In both cases the grounding system is modeled as a 25-m transmission line. For each case, the left plot (panels A and C) shows the model predictions on a 25- $\mu s$  time scale, and the right plot (panels B and D) shows an expanded 5- $\mu s$  time scale from 4 to 9  $\mu s$ . In each case, increasing values of  $R_{TW}$  or  $G_{TW}$  correspond to the curves with smaller first-peak amplitudes. Note that the measured current signature is not shown here. The red curves are the same model predictions as shown in Figure 6-13.

## CHAPTER 7

### DETERMINATION OF THE ELECTRIC FIELD INTENSITY AND SPACE CHARGE DENSITY VERSUS HEIGHT PRIOR TO TRIGGERED LIGHTNING

The ambient electric field of thunderstorms causes electrical discharge known as corona from various types of sharp objects located on the ground, often creating a space charge layer near ground. This layer produces its own electric field that at ground level opposes the cloud's electric field. Space charge produced by ground corona plays an important role in atmospheric electricity. The usually upward-directed electric field due to negative cloud charges is reduced near ground by the presence of the positive corona space charge layer. A space charge layer (of either polarity) prevents the quasi-static electric field at ground level from exceeding an absolute value of about 5 to 10 kV m<sup>-1</sup>, while the field above the layer can be up to an order of magnitude higher [e.g., Standler and Winn, 1979; Chauzy and Raizonville, 1982; Soula and Chauzy, 1991; Willett et al., 1999]. A space charge layer near ground can influence inferences made from ground-based measurements of quasi-static electric fields regarding cloud-charge structure and lightning parameters. When a significant space charge layer is present near ground, the relatively large and fast field change from a lightning flash typically causes a polarity reversal at ground but not at altitude, and the field recovery following a large and fast field change occurs more rapidly at ground than aloft [e.g., Standler and Winn, 1979; Chauzy and Soula, 1987; Chauzy and Soula, 1989]. Thus, inferences of, for example, aspects of charge transfer and continuing current from electric field measurements at ground may be compromised by the presence of a space charge layer. Additionally, when attempting to artificially initiate (trigger) lightning using the rocket-and-wire technique [Rakov and Uman, 2003, Ch. 7], the electric field at ground is used as an often-inadequate proxy for the unknown triggering field at higher altitudes, and the variable field reduction of the space charge layer reduces the triggering efficiency. Finally, space charge produced by corona at ground may play an important role in

thundercloud electrification (at heights greater than 1 km or so). The lower positive charge center in thunderclouds may develop through accumulation of corona space charge lifted from ground level by conduction or convection currents [e.g., Malan, 1952; Chauzy and Soula, 1999]. Although it would often be advantageous to measure the electric field above the space charge layer for the reasons given above, doing so presents logistical difficulties. On the other hand, the effect of the space charge density on ground-based measurements of electric field might be accounted for in principle if the vertical profile of the space charge layer were known.

This chapter describes a novel method to infer the vertical profiles of space charge density and electric field intensity above ground by comparing modeling and measurements of the ground-level electric field changes caused by elevating grounded lightning-triggering wires. Measurements are presented of the ground-level electric field intensity versus time prior to initiation of the triggered-lightning upward positive leader at distances of 60 m and 350 m for six triggered lightning flashes (named Launches 1 through 6, with the UF event ID for each listed in Table 7-1). The measurements (accounting for precursor charge transfer) are then compared to numerical solutions of Poisson's equation for the electric field change everywhere in the computational domain as the wire is extended upward in assumed space charge layer with an assumed uniform electric field intensity far above this layer. The induced charge on the wire as a function of height is inferred from the model-predicted radial component of electric field along the wire, as is the current from ground that supplies it. Finally, the relationship between the measured pre-launch values of the ground-level electric field and triggering height are analyzed and compared to similar relationships presented by other researchers. In this chapter, a positive electric field at ground corresponds to the electric field vector pointing upward (physics sign

convention). Positive current and negative electric field change at ground correspond to the removal of negative charge from or the deposition of positive charge in the atmosphere.

### 7.1 The Wire Shielding Effect

Panel A of Figure 7-1 illustrates the cloud charge, the space charge layer near ground, and the ground-surface charge assuming that (1) the cloud charge is uniformly distributed on an infinitely thin boundary at constant height of several kilometers with a horizontal extent that is much greater than its height above ground and (2) the space charge layer near ground is horizontally homogeneous. Under these approximations, the lines of equal potential (colored lines in Figure 7-1) are horizontally uniform. Correspondingly, the ambient electric field lines (the negative gradient of the potential, shown as solid black arrows) point vertically from the ground to the cloud (with no horizontal component), and the ambient electric field strength (represented by density of field lines) increases with increasing height in the space charge layer.

Panel B of Figure 7-1 illustrates the ambient electric field profile when a thin and grounded conductor is quickly extended vertically from ground, as is done during the launch of a grounded wire to trigger lightning (this electric field profile is similar to that around a stationary tall object). As the wire ascends, an induced charge develops on the wire surface to cancel the tangential component of the ambient electric field on the surface of the conducting wire [Griffiths, 1981, chap. 2]. The line charge density on the wire surface is proportional to the radial field magnitude at the wire's surface according to Gauss's Law. The ground supplies the induced charge needed to keep the wire at ground potential. Corona from the wire pushes the induced charge radially outwards, creating a 'corona sheath' around the wire extending out several meters. In the modeling, it is assumed that the shielding effect at ground is the same if the charge is on the wire or in the corona sheath. The induced charge on the wire and in the corona sheath creates an electric field outside the wire that distorts the ambient electric field

depicted in Figure 7-1, forcing some of the ambient electric field lines that were vertical before the wire was launched to originate on the surface of the wire (or corona sheath) in the normal (radial) direction instead of originating on the ground. This results in a reduction of the electric field magnitude at ground near the wire.

The induced charge per unit length on the wire (and surrounding electric field intensity) is highest at the top of the ascending wire. Eventually, current pulses at the wire tip (precursors) occur as the air undergoes significant dielectric breakdown [e.g., *Lalande et al.*, 1998; *Willett et al.*, 1999; *Biagi et al.*, 2009]. Each precursor deposits charge in the air (and delivers opposite charge to ground via current on the wire) that causes a field reduction at ground of the same polarity as the field reduction from the wire charges. As described in Section 7.3.3, measurements show that the charge of a single precursor is on average about 34  $\mu\text{C}$ , which can reduce the electric field at ground by up to several tens of  $\text{V m}^{-1}$  or more, depending on the charge height and the horizontal distance of the sensor from the wire, and the number of precursors that occur. If as few as several tens of precursors occur during the wire ascent, the cumulative ground-level electric field change from precursors is significant, and the total electric field reduction at ground during the wire ascent is then a combination of the presence of the induced wire charge, the wire-corona charge in the surrounding air, and the precursor charge in the surrounding air.

## **7.2 Data**

### **7.2.1 Rocket Height and Wire Extension Rate**

The triggering wires were unspooled from the bottom of rockets that are about one meter in length, and it is assumed that the wire-top heights (and wire lengths) were the same as the rocket heights. Rocket trajectories were determined by tracking either the engine plumes or rocket bodies in the high-speed video data. Luminosity at the wire tip from precursors was often

evident and was also used to aid in the trajectory measurements. The rockets do not always ascend purely vertically, and lack of tension or excess slack in a wire could cause wire curvature, especially if the wire were blown by the wind. The straightness and tilt of the wires were determined from the optical image data after the luminous wire explosion during the initial stage of the triggered lightning. None of the six wires studied here exhibited a tilt angle of more than a few degrees or had a significant curvature. It is estimated that the wire tops did not deviate horizontally from the launch tower more than 10 m. The rocket speeds were similar in all six launches. All heights discussed hereafter are relative to ground level. In Launches 1, 3, 4, and 5, the high speed video camera did not begin recording until the rockets were at heights of 23 m, 79 m, 40 m, and 21 m, respectively. For these four launches, estimations were made for the rocket heights prior to the time when the high-speed video records began using a modeled trajectory created from the rocket height of Launch 2, which was tracked from 14 to 304 m. The modeled rocket height and wire extension rate (numerical time derivative of the height) versus time are shown in Figures 7-2A and 7-2B, respectively. Figure 7-2C shows the modeled wire extension rate versus the modeled wire height. The rocket in Launch 2 reached a maximum speed of about  $160 \text{ m s}^{-1}$  when the rocket was at a height of about 80 m.

## **7.2.2 Ground-Level Quasi-Static Electric Field Measurements**

The ground-level quasi-static electric field measurements at 60 m and 350 m are co-plotted with the rocket height on a 5-s time-scale in panels A, B, C, D, E and F in Figure 7-3 for Launches 1, 2, 3, 4, 5, and 6, respectively. The salient features in the ground-level electric field change during the triggered lightning are identified in Launch 1 in Figure 7-3A and summarized in Table 7-1. These features are apparent to varying degree in all six launches. Table 7-2 summarizes the ground level field changes due to precursors for the six launches (Section 7.3.3). The precise time-alignment of the field-mill data to all other data was not straightforward

because the field mill data were not recorded with GPS timing. In order to perform the analysis presented in this chapter, the times when the sustained upward positive leader began in the high-speed video images (recorded with GPS timing and precise to about 100  $\mu\text{s}$ ) were assumed to correspond to the field-mill data points at the onset of the relatively large and fast field change associated with the initiation of the sustained upward positive leader of triggered lightning (placed at time zero in the plots of Figure 7-3). For the data presented in Figure 7-3, the sustained upward positive leaders may have begun any time between 0 s and 0.2 s, and it follows that there is 200 ms timing uncertainty in the analysis.

The following describes the general changes, during the triggering of a lightning flash, in the ground-level electric field within horizontal ranges that are similar to the total height of the triggering wire. Prior to launching the rocket, the ground-level electric field magnitudes at 60 m and 350 m are about the same; they differ at most by 1.1  $\text{kV m}^{-1}$  in Launch 6. Further, the rate of change in the field magnitude before launch at both distances is about the same and relatively low. This fact is primarily a result of launching the wires at the ends of storms when the cloud-recharging rate is relatively slow and there is a low natural-lightning flash rate. The maximum rate of ground-level electric field change is 300  $\text{V m}^{-1} \text{s}^{-1}$  in Launch 2 (at 60 m). The similarity in the field magnitudes and rates of change give an indication of the horizontal homogeneity of the electric field and space charge near ground between the two sensors, located 390 m apart.

Shortly after the rocket launch, the ground-level electric field magnitude at 60 m begins to decrease, but apparently not significantly until the wire top has been lifted to a height between 50 and 75 m. The field reduction shape due to the wire shielding at 60 m begins as convex and transitions to concave when the wire top has been lifted to a height of 150 m. This transition is not observed in Launch 4 because the sustained upward positive leader initiated at a height of

123 m. It is not clear if the extending wire causes significant ground-level electric field reduction at 350 m, at least not until the wire reaches an altitude between 150 and 250 m. The field reduction at 350 m during the wire-top ascent was at most  $500 \text{ V m}^{-1}$  in Launch 1, but prior to launching the rocket the ground-level electric field reduced at a rate of  $200 \text{ V m}^{-1} \text{ s}^{-1}$ .

In all events, the sustained upward positive leader and initial continuous current produced a large field change (identified in panel A of Figure 7.3, henceforth referred to as the “lightning field change”) at both 60 m and 350 m. Table 7-3 presents, for the six triggered lightning flashes, the initial stage (IS) duration, the time interval between the end of the IS and first return stroke (RS), the duration of the return strokes (the time from the first stroke to the end of the final stroke’s current), and total number of return strokes (these times were determined from channel-base current measurement not shown here). The IS durations, as determined from the current records, were always longer than the lightning field change durations that were measured by the field mills, with the exception of Launch 1. The lightning field change was as large as  $-24.5 \text{ kV m}^{-1}$  at 350 m in Launch 4. The lightning field change was always larger at 350 m than at 60 m, and the sum of the field change during the wire ascent and the lightning field change at both distances were similar. After the flash ends, the electric field magnitude at ground ‘recovers’, i.e. begins changing in the positive direction, mainly due to negative space charge generation by corona at ground in response to the sudden onset of negative electric-field of large magnitude [e.g., *Standler and Winn, 1979; Chauzy and Soula, 1987; Chauzy and Soula, 1989*]. Some of the field recovery possibly results from cloud recharging after the triggered lightning. Note that in Figure 7-3, the rate of field recovery is apparently higher when the maximum field excursion due to the lightning field change is higher.

Figure 7-4 presents the measured ground-level electric field plotted versus wire-top height for the six launches at distances from the launch tower of (A) 60 m and (B) 350 m. The first data point in each curve corresponds to the electric field value just before the rocket was launched. The last data point represents the ground-level electric field value and rocket height when the sustained UPL began. It is apparent in Figure 7-4A that the rate of electric field change at 60 m was different in different launches, and the change began mostly after the wire top had reached a height of 50 m. As seen in Figure 7-4B, the ambient electric field change apparently dominates the total electric field at 350 m from the wire until the wire reached a height between 150 and 250 m, perhaps with the exception of Launch 1. As shown in Section 7.3.3, some of the measured field change at ground during the wire ascent was due to precursors, particularly at 60 m. Precursor field changes will be accounted for in the modeling (Section 7.4.3).

### **7.2.3 Precursor Current in the Wire and Corresponding Charge Transfer**

Each launch discussed here resulted in triggered lightning in electric fields of positive-polarity (negative charge overhead), and thus, precursor charge deposited ahead of the wire tip was of positive polarity, and a current wave carrying an equal amount of negative charge was guided towards ground by the triggering wire. The propagation of the current wave on the wire radiates a damped-oscillatory field signature, and a “static” field change at ground is produced from the overall lowering of negative charge from the wire tip to ground, as discussed in Chapter 6. Figure 7-5 presents examples of precursor current and electric field signatures on a 25- $\mu$ s time scale that transferred about 18  $\mu$ C of negative charge from a height of 152 m to ground, and produced a ground-level electric field change of about  $-10 \text{ V m}^{-1}$  at a distance of 60 m from the wire.

In the comparisons between measured and modeled field changes during the wire ascents, the field changes from precursors are first removed from the measured ground-level field change.

Based on the modeling results in Section 6.4, it is assumed here that precursor charge can be represented by a point source at the wire tip. Of the six launches analyzed here, both the wire-base currents and fast electric field changes were adequately measured in Launches 1 and 6. For these two launches, the field change of each precursor at 60 m and 350 m is inferred from the following approximation [Uman 1969, Eq. 3.3]:

$$\Delta E = \frac{2\Delta QH}{4\pi\epsilon_0(H^2 + R^2)^{3/2}} \quad 7-1$$

where  $\epsilon_0$  is the permittivity of free space, H is the wire-tip altitude, R is the horizontal distance between the wire base (launch tower) and the electric field sensor, and  $\Delta Q$  is the total charge transferred to ground. For a given precursor, the quantity  $\Delta Q$  was determined by computing the time integral from the beginning of the current to the time when the oscillations drop below the noise floor. Additionally, Equation 7-1 was used to scale the precursor field changes measured by E2 at a range of 156 m to field change at ranges of 60 m (e.g., Figure 7-5A) and 350 m. For Launches 2 through 5, the current measurement saturated at about 20 A, and the first current peaks of most precursors saturated, making it impossible to determine  $\Delta Q$  from integrating the precursor current at the wire bottom, so the measured field changes from E2 were used to determine  $\Delta Q$  via Equation 7-1. The placement of a plastic dome over the E2 sensor to shield it from rain introduced uncertainty to the sensor's amplitude calibration, so the measured field changes from E2 were calibrated to the inferred field change (using Equation 7-1) from accurate wire-base current measurements for 96 precursors in four launches: Launches 1 (UF09-15), 6 (UF10-25), and two launches otherwise not analyzed here (different than Launches 1 through 6): UF09-12 and UF09-17 (the latter was in the same storm of Launch 1). According to this calibration, the E2 measurements were consistently too high in amplitude by 29%. Table 7-4 presents for the 96 precursor current pulses statistics on the total negative charge lowered to

ground and E2-measured electric field change scaled to 60 m. There was no correlation between the amount of precursor charge deposited ahead of the wire tip and wire-tip height.

### **7.3 Modeling**

This section begins with a description of the model construct and the assumed vertical profiles of space charge density, electric field intensity, and electric potential. Then, examples of possible model outputs are presented. The model parameters that yield electric field change predictions that best fit the measured electric field changes are determined for each launch, and thereby the vertical profiles of space charge density, electric field intensity, and electric potential are inferred. Finally, the model predictions of the radial electric field along the wire as a function of height for Launch 1 are examined.

#### **7.3.1 Model Description**

The electric field structure is assumed to have cylindrical symmetry centered on the vertical wire, allowing the three-dimensional field structure to be modeled in two dimensions. The triggering wire is infinitely thin in the model. The model domain is a square ‘slice’ of the three-dimensional space, with the left side being the axis of symmetry. The following five conditions are imposed: (1) the total vertical and horizontal (radial) extent of the model space each is 3 km, (2) the vertical wire extension begins in the lower-left corner at ground, and continues up along the left boundary, (3) the boundaries at ground (bottom side) and along the wire are at zero potential, (4) the horizontal (radial) derivative of the electric potential (the negative of the radial electric field) is zero on the right boundary and on the left boundary vertically above the wire top, and (5) the potential along the top boundary (at  $z = 3$  km) is defined by Equation 7-4 (described below).

The space charge density profile versus altitude is assumed to decay exponentially. This choice was based primarily on the rocket soundings of the electric field versus height with

relatively high spatial resolution that were presented in the work of *Willett et al.* [1999], and an exponentially decaying space charge density profile is the simplest realistic profile with the minimum number of free parameters to test in the computationally intensive model. Prior to launching the rocket, the height profiles of the exponentially decaying space charge, the corresponding electric field as a function of  $z$ , and the electric potential as a function of  $z$  are described by the following three relations, respectively:

$$\rho(z) = \epsilon_0 \frac{\exp(-z/d)}{d} (E_\infty - E_0) \quad 7-2$$

$$E(z) = E_\infty - \exp(-z/d)(E_\infty - E_0) \quad 7-3$$

$$V(z) = d(E_\infty - E_0)[1 - \exp(-z/d)] - E_\infty z \quad 7-4$$

The equations for  $\rho(z)$  and  $V(z)$  are consistent with the equation for  $E(z)$  via Gauss's Law

$\rho(z) = \partial\epsilon_0 E(z)/\partial z$  and the definition of the electric potential  $V(z) = -\int_0^z E(z')dz'$ , respectively.

The two adjustable parameters of the model are: the rate of charge decrease with height (e-folding length)  $d$  and the electric field magnitude far above the space charge layer  $E_\infty$ . The ground-level electric field when the wire is first launched,  $E_0$ , is a measured value. The electric potential is found first by numerically solving Poisson's equation (or Laplace's equation for the zero space charge case) using the finite-element method. The electric field is then found by taking the negative of the gradient of the electric potential. The initial finite-element mesh was refined many times using higher-order finite elements with the most grid points located near ground and along the left boundary where the wire was placed.

Because of the computationally intensive nature of the Poisson solver, the modeling was done for only three values each of the two free parameters,  $E_\infty$  (20, 40 and 60 kV m<sup>-1</sup>) and  $d$  (67, 100 and 200 m), as well as the zero space charge case ( $d$  is set to zero), for the six initial

measured ground-level electric field values  $E_0$  (ranging from 3.2 to 7.6 kV m<sup>-1</sup>). For example, Figure 7-6 presents  $\rho(z)$ ,  $E(z)$ , and  $V(z)$  for the nine combinations of  $E_\infty$  and  $d$  and  $E_0 = 6$  kV m<sup>-1</sup>. For the zero space charge case, the electric field prior to launching the rocket is vertical and is equal to the measured field at the ground  $E_0$  for all  $z$ . The vertical profiles are inferred from the solution that provided the best least-squares fit to the time series of electric field measured at the 60 m range.

### 7.3.2 Model Predictions

Figure 7-7 presents the model-predicted, ground-level electric field change at (A) 60 m and (B) 350 m for the zero space charge case and for the nine cases of exponentially decaying space charge, all for  $E_0 = 6$  kV m<sup>-1</sup>. The corresponding measurements for Launch 1 are also shown (although the  $E_0$  value at 350 m was about 6.1 kV m<sup>-1</sup> versus 6 kV m<sup>-1</sup> assumed in calculations). The model-predicted ground-level electric field change is lowest when zero space charge was assumed: about -1 kV m<sup>-1</sup> at 60 m and -100 V m<sup>-1</sup> at 350 m. The second-smallest predicted ground-level field change is for the lowest space charge density at ground (corresponding to highest  $d = 200$  m and smallest  $E_\infty = 20$  kV m<sup>-1</sup>): about -1.4 kV m<sup>-1</sup> at 60 m and 0.1 kV m<sup>-1</sup> at 350 m. The largest model-predicted field change is for the highest space charge density at ground (corresponding to smallest  $d = 67$  m and highest  $E_\infty = 60$  kV m<sup>-1</sup>): about -4.9 kV m<sup>-1</sup> and -0.5 kV m<sup>-1</sup> at 60 m and 350 m, respectively. In all of the predicted ground-level field changes at 60 m for zero space charge and the nine combinations of  $E_\infty$  and  $d$ , there is a point of inflection when the wire top reaches a height of about 130 m. An inflection point is not evident in the modeled field change curves at 350 m, although presumably there would be one if the wire reached a height of 700 m.

### 7.3.3 Model Fit

Figure 7-8, panels (A) through (F), present for Launches 1, 2, 3, 4, 5, and 6, respectively, the original measured field change at 60 m, the measured field change with the precursor field changes removed (referred to as the precursor-adjusted measurement), and also the model prediction that best matches the precursor-adjusted measurement according to the best least-squares fit. The values of  $E_0$  (assumed to be equal to the measured value),  $E_\infty$ , and  $d$  corresponding to the best-fitting model predictions, along with the space charge density at ground are given in each plot. For each of the plots in Figure 7-8, a vertical arrow points to the height at which the first precursor field change was removed from the measurement. Below these heights the original measured curves and the precursor-adjusted measured curves are identical. In each launch, the overall field change from precursors, several hundred  $\text{V m}^{-1}$ , is small relative to the overall field change due to the wire shielding effect, several  $\text{kV m}^{-1}$ . The field adjustments for precursors appear as positive-going steps, although the field change for many precursors is too small to be evident in the plots of Figure 7-8. Accounting for precursor field changes has the effect of reducing the total field change. Table 7-5 summarizes the parameters that produced the best-fitting model predictions for each launch, as well as the model-predictions of ground-level space charge density, the ambient vertical electric field for the height at which the sustained UPL initiated (these heights are given in Table 7-1), and the electric potential traversed by the wire. The modeling results indicate that the ambient electric field at the wire-tip height was lower and the electric potential traversed by the wire was larger when the sustained UPL initiated at higher altitudes. No attempt was made to fit modeled electric field changes to the measured electric field changes at 350 m since any wire-shielding effect at this distance was not clearly observable.

### 7.3.4 Model Predicted Line Charge Density

In addition to predicting the ground-level electric field, the model yields the vertical (z-component) and radial electric field near the surface of the wire. From these fields, the corresponding charge per unit length that must exist on the wire and/or corona sheath as a function of height can be inferred. Figure 7-9 presents examples of the model-predicted height profiles of the radial electric field along the wire at a radius of 5 m (bottom axis) and the approximate charge density (top axis) that must exist along the wire to produce the radial electric field according to Gauss's Law when the input parameters were  $E_{\infty} = 40 \text{ kV m}^{-1}$  and  $d = 100 \text{ m}$ , and  $E_0 = 6 \text{ kV m}^{-1}$ . Each of the four curves in Figure 7-9 is the model-predicted radial electric field and corresponding charge per unit length from 0 m to 300 m at four different times, when the wire top was at heights of: 60 m, 135 m, 210 m, and 285 m. The charge per unit length is calculated as follows. A Gaussian cylinder of a few meters height and a few meters radius has its axis co-located with the wire, and  $\epsilon_0 \vec{E}$  is integrated over the lateral surface of the cylinder to yield the charge inside the cylinder. For all locations of the Gaussian cylinder, except at the top of the wire, the electric flux out the top and bottom circular surfaces is negligible, leading to a charge per unit length  $\lambda(z) = 2\pi\epsilon_0 r E_r(z)$  (top axis of Figure 7-9), where  $E_r$  is found to vary as  $r^{-1}$  out to about 10 m. At the top of the wire, the electric flux out the top surface of the Gaussian cylinder is of the same order of magnitude as the flux out the cylindrical side surface, so the actual charge per unit length at the top of the wire is two or three times that plotted in Figure 7-9. The exact value determined depends on the grid size of the model calculations, which has a practical lower limit.

The model predicts that the radial electric field magnitude and charge density at any given height are highest when the wire first reaches that height, thereafter decreasing slightly as the

wire continues ascending. The model-predicted radial electric field (at  $r = 5$  m) and charge density (underestimated near the wire tip) shown in Figure 7-9 reach maxima of about  $210 \text{ kV m}^{-1}$  and  $60 \text{ } \mu\text{C m}^{-1}$ , respectively, at a height of 270 m when the wire top is at 285 m. The model predicts that the radial electric field near the wire and corresponding charge per unit length increases with increasing values of  $E_\infty$  and decreasing values of  $d$ . Note that the non-smooth nature of the curves is due to unevenly spaced finite-element mesh points.

The model predicts that there is a total charge along the wire of about 6.5 mC when the wire top is at a height of 285 m. The current required to supply the charge (the rate of change of total charge on wire as the wire extends upward) increases steadily as the wire ascends to a height of 135 m, reaching a level of about 3 mA, and continues to increase for higher wire heights, although at a slower rate because the wire extension rate is decreasing (Figure 7-2).

The model predicts that the radial electric field magnitude is highest about 10 meters below the top of the wire. The predicted decrease of radial electric field in the upper 10 m or so of wire is due to the electric field becoming more vertical, and less radial, near the wire top. The radial field does not drop to zero above the maximum wire-top height because there is some radial component of electric field above the wire at a radial distance of 5 m (there should be radial electric field everywhere except directly along the wire axis), and to some extent because of insufficient mesh refinement. The model predicts that the vertical electric field at 5-m radius increases from small compared to the radial field some meters below the wire top to a maximum at the wire top, above which the z-directed field decreases.

#### **7.4 Discussion**

The measurements of the ground-level electric field change during the vertical extension of a thin, grounded wire are similar to previous reports. *Willett et al.* [1999] reported higher-magnitude but similarly shaped field changes at a distance of about 30 m from their launcher, or

half the distance at which the measured field change presented here were made. For their ‘flight 6’ (as seen in their Figure 6), *Willett et al.* [1999] reported that the electric field began at about  $7 \text{ kV m}^{-1}$  and the field changed during the wire extension (up to 307 m) by a little over  $-7 \text{ kV m}^{-1}$ , becoming slightly negative before the UPL initiated. For the launches analyzed in this Chapter, the largest measured field change during a wire extension was  $-3.4 \text{ kV m}^{-1}$  for Launch 1. The lightning field change of ‘flight 6’ in *Willett et al.* [1999] was about  $-7 \text{ kV m}^{-1}$ , and the combined field change from the wire ascent and triggered lightning was about  $-14 \text{ kV m}^{-1}$ . *Liu et al.* [1994] reported a similar quasi-static electric field change signature measured 75 m from the launcher during a triggering attempt with positive charge overhead. The field change during the wire ascent was about  $3.5 \text{ kV m}^{-1}$  (as seen in their Figure 2).

Figure 7-10 presents a scatter plot of the ground-level electric field magnitude when the wire-trailing rocket was launched versus the height at which the sustained UPL developed (triggering height). The two quantities show a strong linear relationship with a correlation coefficient of  $-0.85$ . *Hubert et al.* [1984] reported a strong power-law relationship (correlation coefficient of  $-0.82$ ) between the triggering heights (from about 100 to 600 m) and ground-level electric field magnitudes (between  $4$  and  $13 \text{ kV m}^{-1}$ ) for 35 triggered flashes in Langmuir Laboratory in New Mexico. The power law relation of *Hubert et al.* [1984] is also shown in Figure 7-10 (they did not report data points). The results in Figure 7-10 indicate that for the same electric field at ground lightning can be triggered at a lower triggering height at the ICLRT than at Langmuir Laboratory. In explanation of these observations, there may have been less space charge present in the vicinity of the triggering experiments at Langmuir than at the ICLRT, or the electric field magnitudes of *Hubert et al.* [1984] may have been enhanced by the mountainous local topography. It is worth noting that *Horii and Nakano* [1995] reported for

winter triggered-lightning studies at Kahokugata site in Japan that no clear correlation was observed between the triggering height and the initial ground level electric field for either positive or negative lightning polarity.

As seen in Figure 7-8, there is good agreement between the model-predicted and precursor-adjusted measured ground-level electric field at 60 m from the wire, when an exponentially decaying space charge profile is assumed, particularly in Launches 1, 4 and 5. There is nearly perfect agreement between measurement and model for Launch 5. Interestingly, there was a 1-cm air gap in the ground lead for Launch 5, although it is unclear how the measurement would differ if the air gap were not present. The rate at which the measured electric field magnitude initially decreases is well modeled for Launches 1, 4 and 5. For Launches 2 and 3, the measured field change when the wire is at a higher altitude is larger than the model predicts. This discrepancy could well be due to the uncertain time alignment between the rocket trajectory and ground level field change. As noted in Section 7.3.2, it was assumed that the sustained upward positive leaders began when the lightning field changes in the field mill records began (time zero in the plots of Figure 7-3). However, the sustained upward positive leaders may have begun between 0 s and 0.2 s, introducing an uncertainty of 200 ms in the data time alignment. The timing uncertainty means that the wire may have been launched up to 200 ms later than was assumed in the present analysis and the computed field versus height curves may be shifted horizontally to lower wire-top heights. For example, in Launch 2 the electric field increases (as seen in Figures 7-4 and 7-8) for wire-top heights from about 14 m to 60 m. The 200 ms timing uncertainty allows the wire launch to begin when the field maximum occurred, in which case there would probably be a better match of the model prediction to the measurement, although perhaps for a different space charge profile.

The radial electric field of the model-predicted line charge along the wire is large enough to produce corona. The wire has a diameter of  $2 \times 10^{-4}$  m, and if the minimum electric field strength necessary to produce corona is assumed to be  $1 \text{ MV m}^{-1}$  [e.g., *Kodali et al.*, 2005; *Maslowski and Rakov*, 2006], then a line-charge density as low as  $11 \text{ nC m}^{-1}$  will produce corona. For a line-charge density of  $60 \text{ } \mu\text{C m}^{-1}$  (the maximum model-prediction shown in Figure 7-9), the radial electric field drops below  $200 \text{ kV m}^{-1}$  (the minimum electric field for corona propagation according to *Griffiths and Phelps* [1976]) for a radius of about 5.4 m. The model indicates that for all wire launches, the induced charge on the wire expanded radially via corona on the order of five meters. However, the location of the wire/corona-sheath charge does not affect the model predictions as long as that corona sheath charge magnitude is essentially the same as would be found on the wire (or on a grounded wire of any radius) in the absence of corona. It is possible that wind advection or conduction current removes a part of the charge created by corona from the vicinity of the wire, in which case corona resupplies the removed charge with additional charge. The removed charge would then be supplementary to the charge required to keep the wire at ground potential, and would enhance the overall electric field decrease measured at ground beyond what the model would predict (after accounting for precursor charge). The supplementary charge effect may explain some of the divergence of the model-predictions and precursor-adjusted measurements of electric field change that typically begins around the wire heights when the first precursor begins (Figure 7-8).

Another possible source of supplementary charge is the rocket-motor exhaust, as previously suggested by *Fieux et al.* [1978]. The rocket-motors used in the experiments are specified to have a 1.2-s burn time, or about half the typical time the wire ascends before triggering lightning (Figure 7-3). Any potential charge deposition by the motor exhaust is

thought to have negligible effect on the measurements for the following reason: If charge deposition by the motor exhaust were significant, one would expect a discontinuity in the measured field reduction during the wire extension when the motor extinguishes at a time 1.2 s after launching the wire; such discontinuities are not observed.

The choice to use an exponentially decaying space charge density, and the parameters  $E_\infty$  and  $d$ , was based on the rocket soundings of the vertical electric field versus altitude in the work of *Willett et al.* [1999]. The rocket soundings of *Willett et al.* [1999] indicated that the electric field aloft increased exponentially with height up to heights of tens to hundreds of meters, above which it became more or less constant. All other reports of measurements of the electric field aloft found in the literature indicate it increases with height, although not necessarily exponentially. The true space charge profiles through which the wires ascended may not have varied with height exponentially, or even monotonically. Further, the model solutions are not unique to the space charge profiles that were assumed; other space charge density profiles versus height may yield similar or better model predictions. The non-unique nature of the model predictions is obvious in Figure 7-7, which shows that the model predicted ground-level electric field change with  $d = 100$  m and  $E_\infty = 40$  kV m<sup>-1</sup> is nearly the same as the model prediction with  $d = 200$  m and  $E_\infty = 60$  kV m<sup>-1</sup>. In fact, for Launch 3, the model prediction with  $E_\infty = 60$  kV m<sup>-1</sup> and  $d = 200$  m fits the measurement only slightly better than the model prediction with  $E_\infty = 40$  kV m<sup>-1</sup> and  $d = 100$  m. Similarly, for Launch 6, the model prediction with  $E_\infty = 40$  kV m<sup>-1</sup> and  $d = 100$  m fits the measurement only slightly better than the model prediction with  $E_\infty = 60$  kV m<sup>-1</sup> and  $d = 200$  m.

The good agreement between the model-predicted field change and precursor-adjusted measured field change, especially for Launches 1, 4 and 5, indicates that the assumption made

here regarding the uncertainties in the inter-measurement timing, supplementary charge creation along the wire, and the exponentially decaying space charge profiles are not grossly inaccurate. The analysis at least shows that the triggering wires extended through space charge layers of significant density, such that the atmospheric electric field increased significantly with height. For example, for Launch 1,  $E_0$  was  $6 \text{ kV m}^{-1}$ , the wire reached a height of 230 m before the sustained upward positive leader began, and the wire caused a ground-level electric field change of  $-3.2 \text{ kV m}^{-1}$ . The model-predicted ground-level electric field change for the same  $E_0$  and wire height (Figure 7-7) with zero space charge was only about  $-700 \text{ V m}^{-1}$ , or a factor of four less than the measured field change.

Table 7-1. Salient values of the quasi-static ground-level electric fields and the upward positive leader (UPL) initiation height.

Launch	Flash ID	Ground-level field at launch (kV m <sup>-1</sup> )		Ambient field change rate prior to launch (kV m <sup>-1</sup> s <sup>-1</sup> )		Total field reduction between launch and UPL initiation (kV m <sup>-1</sup> )		Total lightning field reduction (kV m <sup>-1</sup> )		UPL initiation height (m)
		60 m	350 m	60 m	350 m	60 m	350 m	60 m	350 m	
		1	UF09-15	6.0	6.1	-0.2	-0.2	3.4	0.5	
2	UF09-21	3.2	3.1	0.3	0.2	2.4	0.0	10.3	13.8	304
3	UF09-26	5.5	5.3	0.0	0.0	3.0	0.3	12.9	16.2	232
4	UF09-30	7.2	8.1	0.0	0.0	2.2	0.0	22.7	24.5	123
5	UF09-42	7.6	7.2	0.0	0.0	2.5	0.1	13.7	15.9	161
6	UF10-25	5.1	4.0	0.0	0.0	2.9	0.2	8.8	10.2	233

Table 7-2. The number of precursors, the height at which they first occurred, and the total ground-level field change they produced.

Launch	Number of precursors	Height of first precursor (m)	Total field reduction from precursors (kV m <sup>-1</sup> ) <sup>a</sup>	
			60 m	350 m
			1	12
2	36	229	0.28	0.07
3	24	168	0.67	0.13
4	10	79	0.17	0.10
5	37	83	0.32	0.02
6	22	147	0.15	0.03

a) Distances scaled from E2 measurement at 156 m from wire.

Table 7-3. The initial stage (IS) duration, the time interval between the end of the IS and the first return stroke, and the duration of the return stroke stage. The duration of the return stroke stage is defined as the time from the fast rise of the first return-stroke current to the end of the final return-stroke current, including any continuing current. There were no return strokes in Launches 1, 2 and 6.

Launch	IS stage duration (ms)	Time between IS and 1st return stroke (ms)	Number of return strokes	Return-stroke stage duration (ms)
1	161	-	-	-
2	552	-	-	-
3	534	57.6	5	541
4	238	138	1	216
5	630	631	1	199
6	210	-	-	-

Table 7-4. Salient statistics of precursor charge and electric field change (sample size of 96).

Value	Charge Lowered to Ground ( $\mu\text{C}$ )	Field Reduction at 60 m ( $\text{V m}^{-1}$ ) <sup>a</sup>
Arithmetic Mean	33.9	27.1
Standard Deviation	23.5	16.0
Geometric Mean	26.9	22.2
Median	27.8	24.0
Min	4.8	4.2
Max	151.7	86.9

a) Distance scaled from E2 measurement at 156 m from wire.

Table 7-5. Model parameters, the corresponding space charge density at ground, and the electric field and the electric potential at the triggering height. These values were calculated using Equations 7-2, 7-3 and 7-4 (Section 7.4.1).

Launch	$E_0$ ( $\text{kV m}^{-1}$ ) <sup>a</sup>	$E_\infty$ ( $\text{kV m}^{-1}$ )	d (m)	$\rho(z=0)$ ( $\text{nC m}^{-3}$ )	E at triggering height ( $\text{kV m}^{-1}$ )	V at triggering height ( $\text{kV m}^{-1}$ )
1	6.0	40	67	4.5	39	-4.1
2	3.2	20	100	1.5	19	-3.0
3	5.5	60	200	2.4	43	-3.9
4	7.2	60	67	7.0	51	-2.3
5	7.6	60	100	4.6	50	-1.3
6	5.1	40	100	3.1	36	-3.2

a) At a distance of 60 m from the launch tower, equal to the measured value.

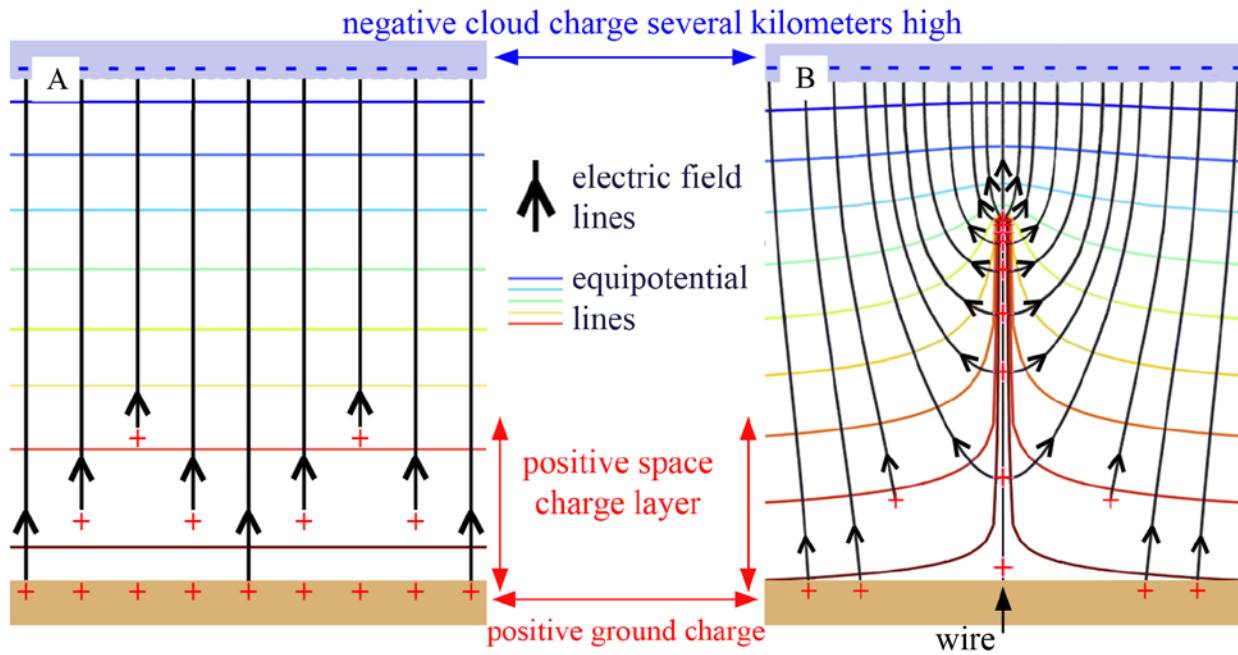


Figure 7-1. Schematic illustrations of the ambient electric field before and after the extension of a triggering wire. (A) An approximation of the electric field between negative thundercloud charge that is several kilometers above ground and ground surface. The vertical electric field, shown with black arrows is a function of height in the space charge layer ('red plus' symbols). The horizontal equipotential lines (representing equipotential planes in 3-D space) are further apart in the space charge layer than in the space-charge free region. (B) The electric field with the grounded triggering wire present.

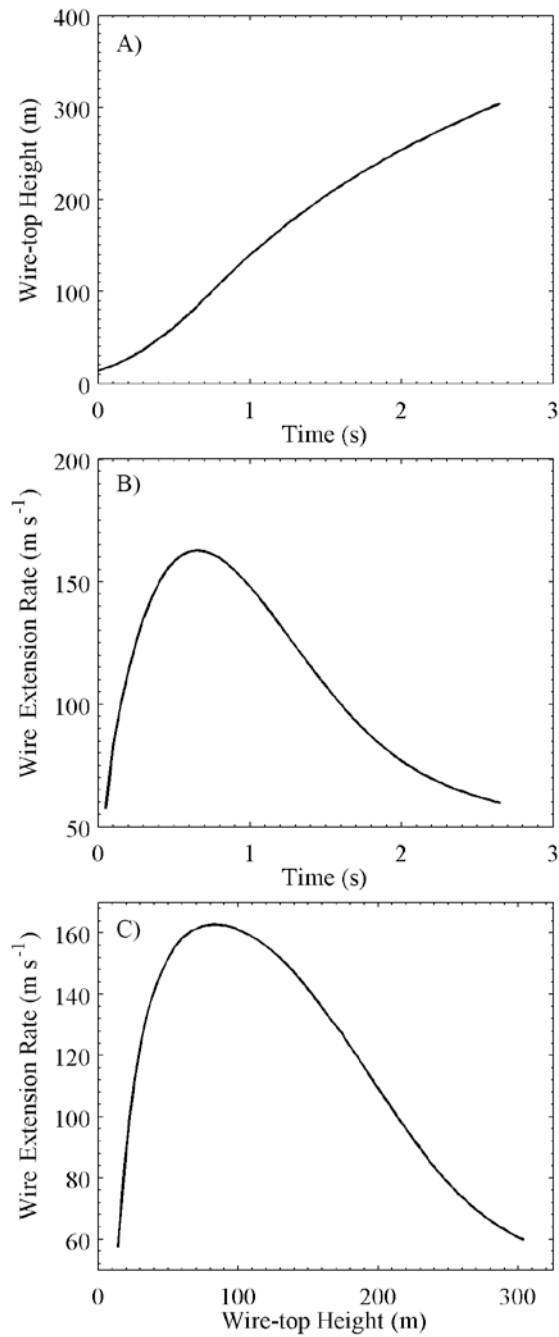


Figure 7-2. The model wire trajectory. (A) The modeled wire-top height versus time. (B) The modeled wire extension rate versus time. (C) The modeled wire extension rate versus the modeled wire-top height. The minimum wire height is the top of the launch tubes, or a height of 14 m.

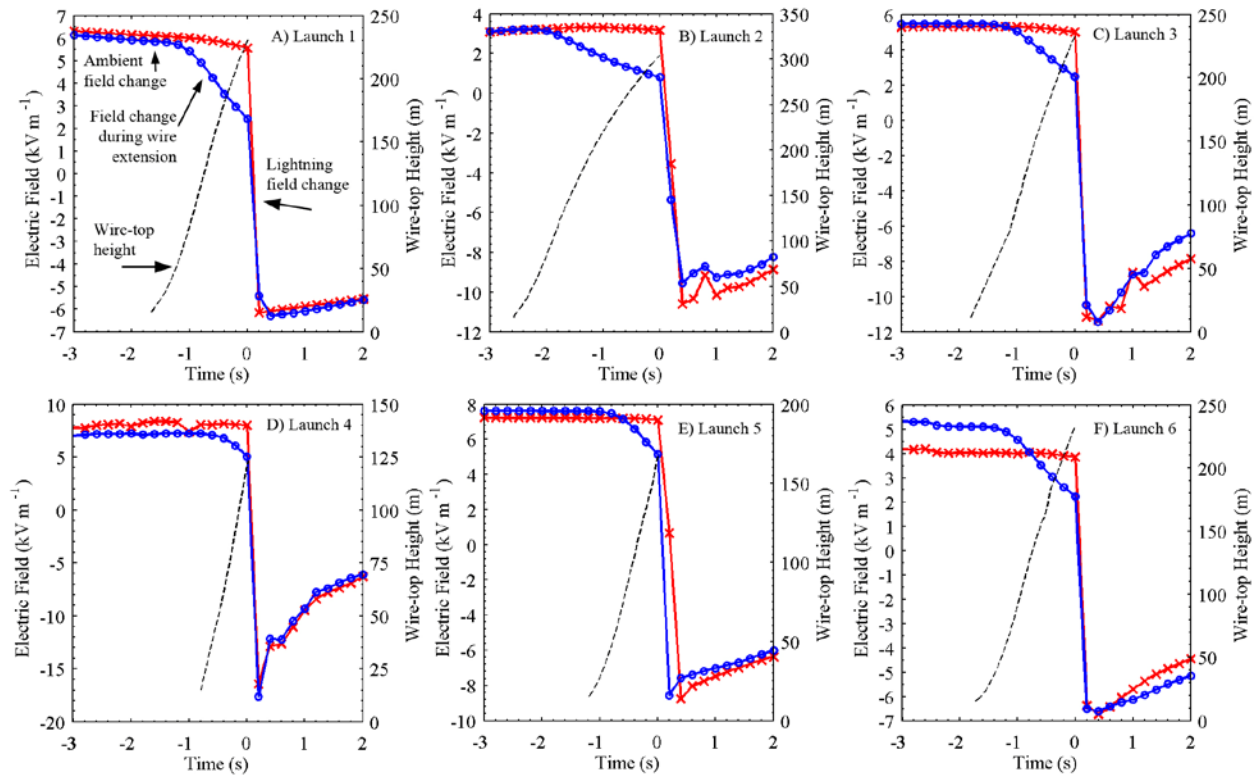


Figure 7-3. The ground-level electric field changes and wire-top heights versus time for Launches 1 through 6. The ground-level electric field changes at 60 m are shown with solid blue line with circles (left vertical scale), the 350 m are shown with solid red lines with x symbols (left vertical scale), and the wire-top heights are shown with dashed black lines (right vertical scale). Salient features in the electric field change that are evident in all launches are identified in panel (A) for Launch 1. In each panel, time zero corresponds to the lightning field change and the last wire-top height measurement.

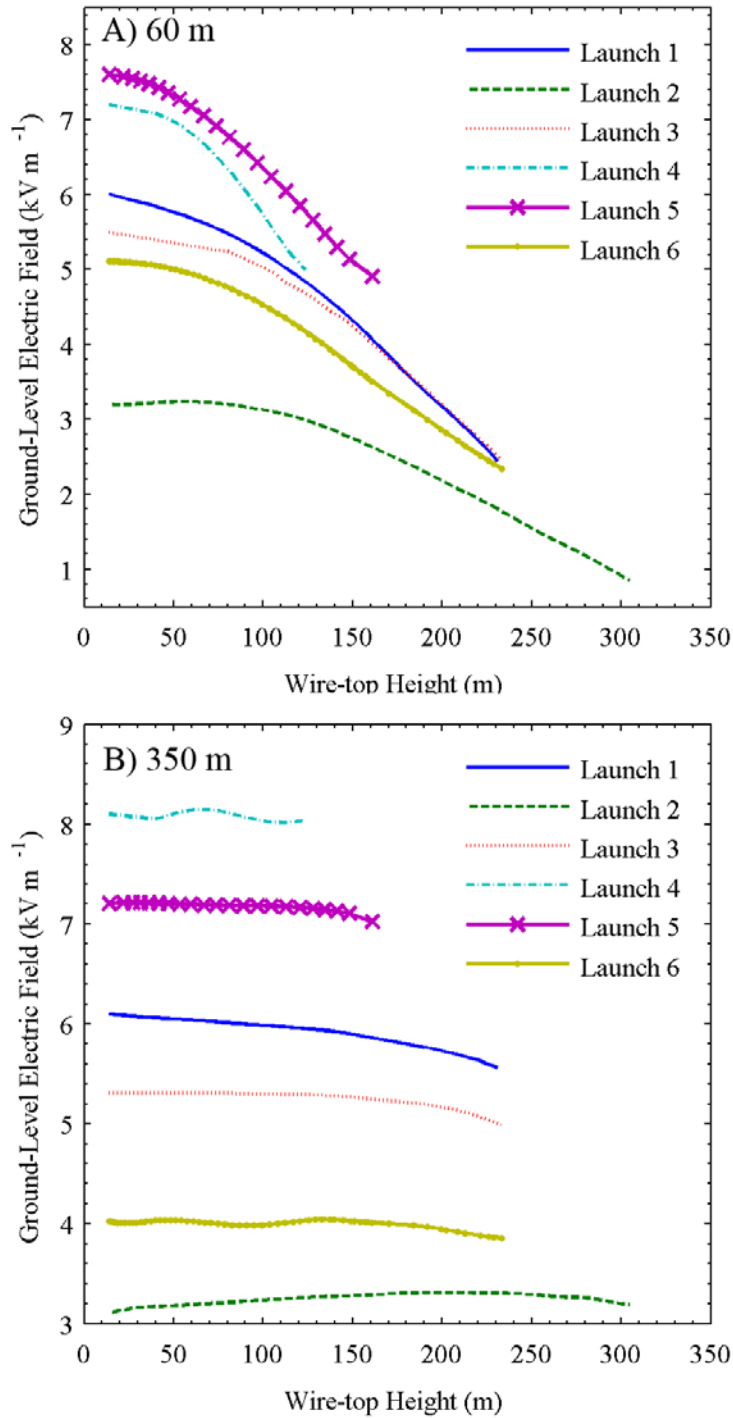


Figure 7-4. Field change versus wire-top heights for Launches 1 through 6. Panel A shows the field changes at 60 m, and Panel B shows the field changes at 350 m. Note that the vertical scales of electric field in the two plots are different.

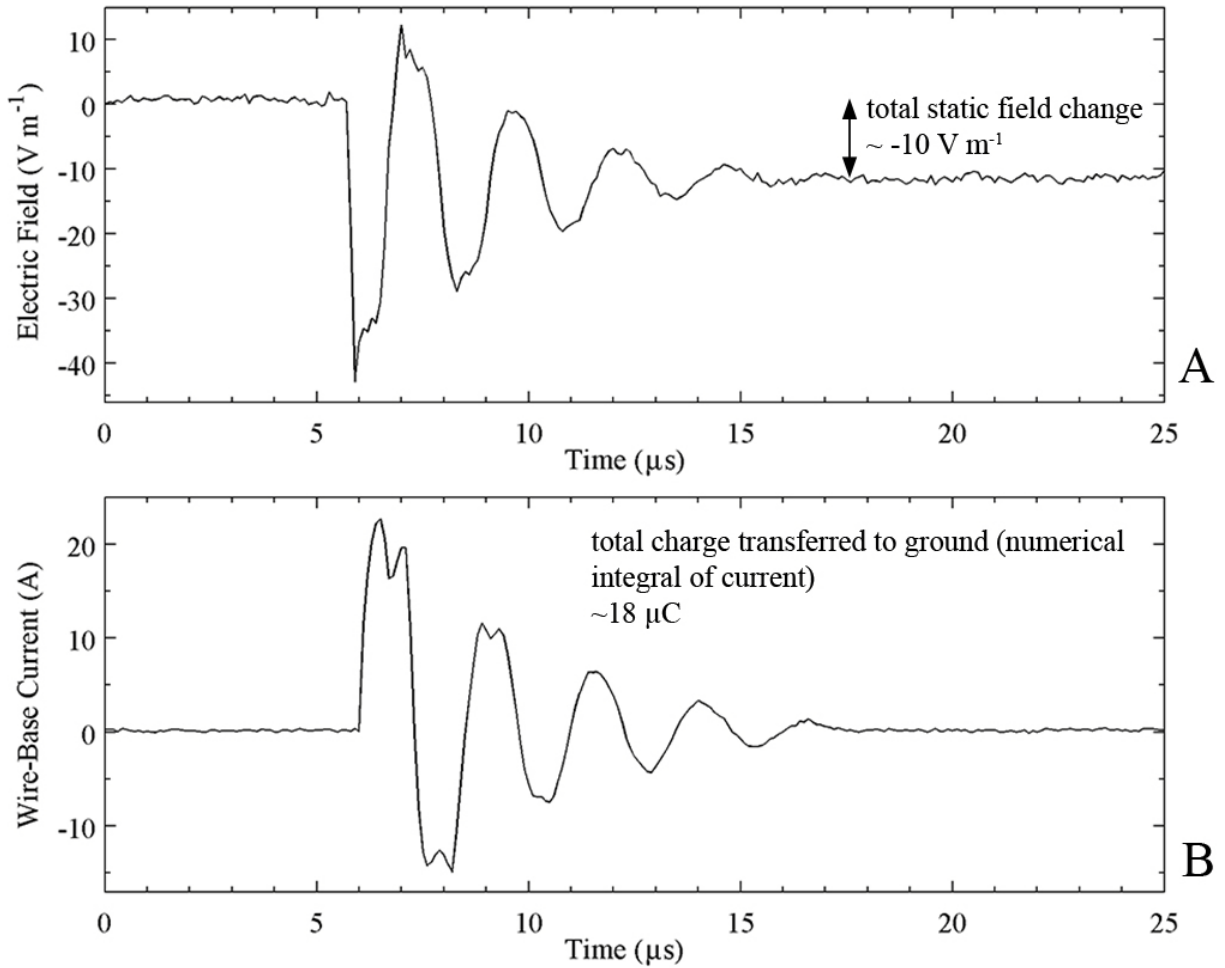


Figure 7-5. An example of a precursor that produced a static electric field change. Panel A shows the ground-level electric field change measured at 156 m (by E2) but range-scaled by Equation 7-1 to a horizontal distance of 60 m from wire. Panel B shows the corresponding wire-base current. The  $18 \mu\text{C}$  of negative charge transferred to ground during this precursor produced an overall field change at 60 m of about  $-10 \text{ V m}^{-1}$ .

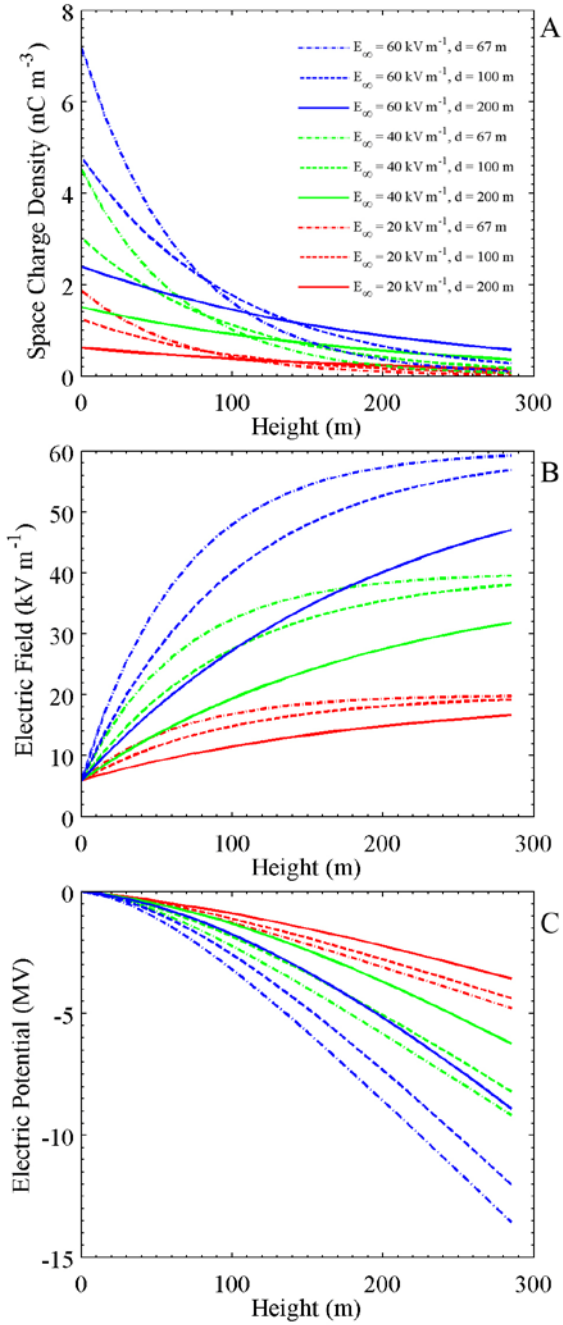


Figure 7-6. The vertical profiles of space charge density, electric field magnitude, and electric potential for the nine combinations of  $d$  and  $E_\infty$  values and  $E_0 = 6 \text{ kV m}^{-1}$ . Panel A shows the space charge density, Panel B shows the electric field, and Panel C shows the electric potential. A common legend is shown on the top panel.

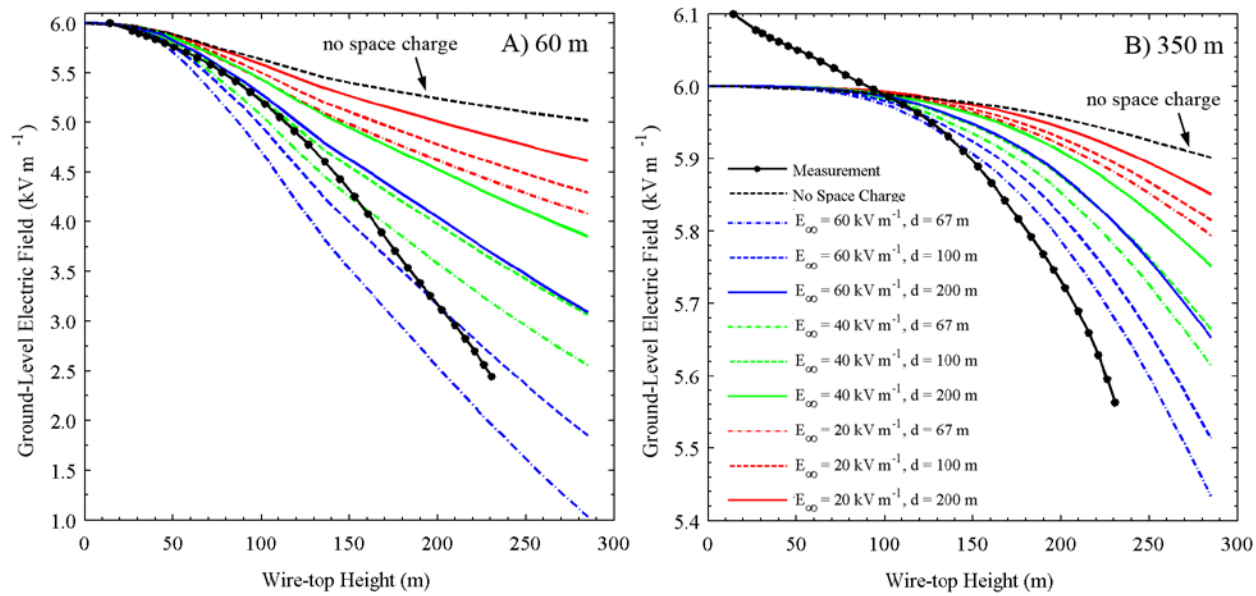


Figure 7-7. The model-predicted ground-level field changes for no space charge and the nine cases of exponentially decaying space charge density for  $E_0 = 6 \text{ kV m}^{-1}$ . Panel A shows the field changes at 60 m, and Panel B shows the field changes at 350 m, with a common legend shown in panel B. The measured field change for event 060409-2 at both distances is shown for comparison. Note the different vertical scales of electric field in (A) and (B).

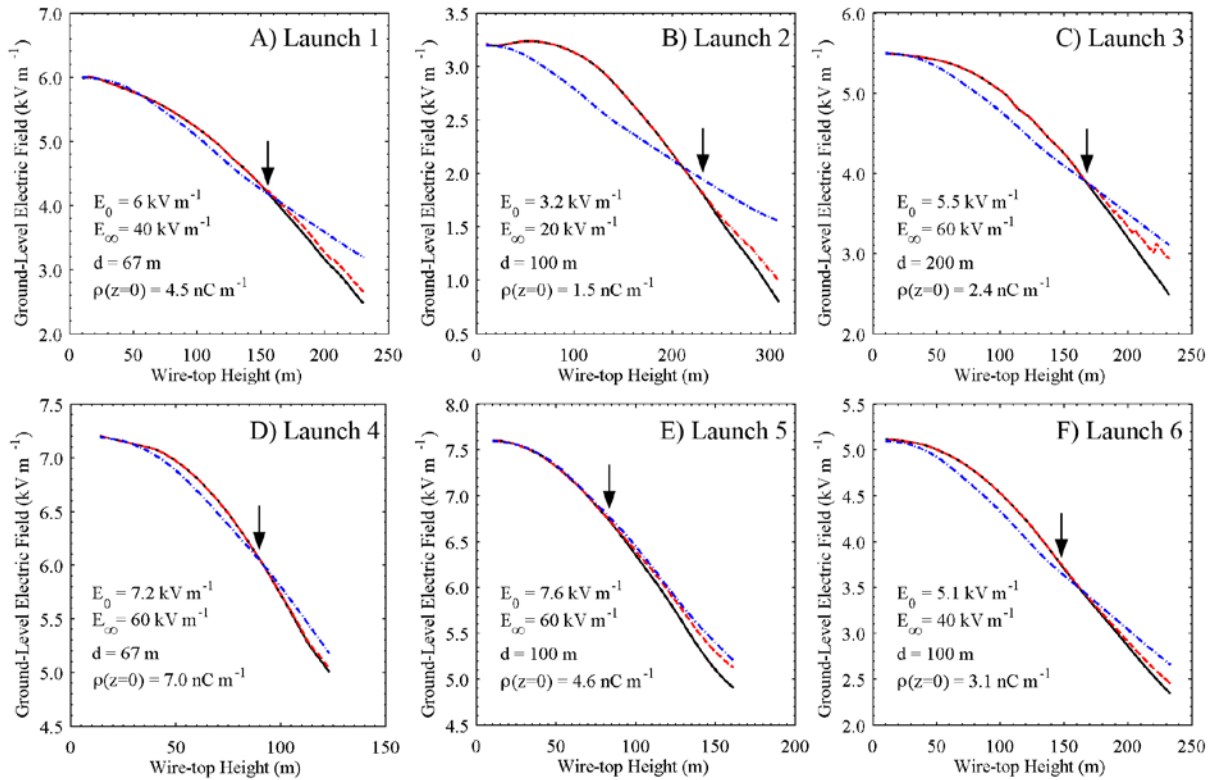


Figure 7-8. The model predictions that best fit the measured electric field changes for Launches 1 through 6. The measured field changes at 60 m are shown with solid black lines, the precursor-adjusted measurements are shown with dashed red lines, and the model-predicted field changes are shown with dot-dashed blue lines. The values of  $E_0$  (assumed to be equal to the measured value),  $E_\infty$ ,  $d$ , and  $\rho(z=0)$  (the space charge density at ground) corresponding to the best model fit are shown in the bottom left of each plot. Note that the plots have different height and electric field scales. The vertical arrows point to the wire-top height at which the first precursor is removed.

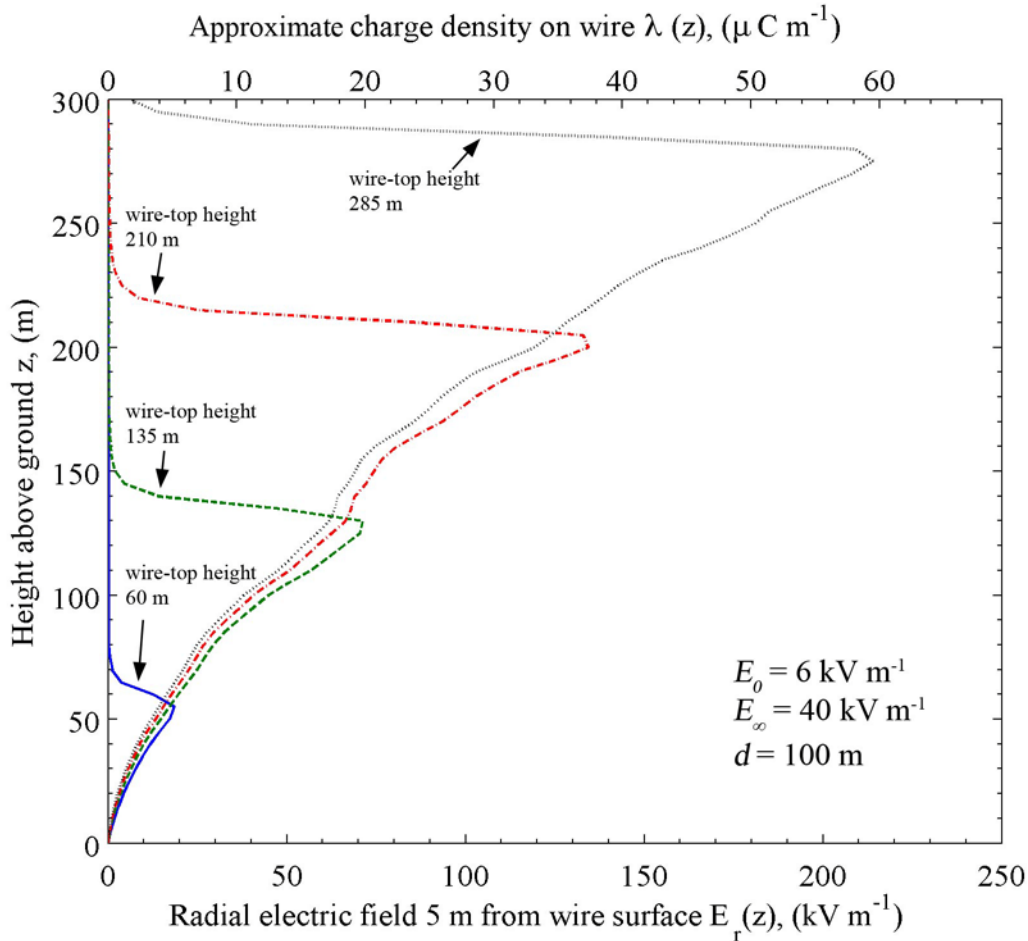


Figure 7-9. Examples of the model-predicted height profiles of the radial electric field 5 m from the wire and equivalent approximate line charge density. The induced charge densities (top scale) are inferred from the radial electric field (bottom scale) using Gauss's law: values of charge density near the wire top are underestimated because there is vertical component of electric field not taken into account in these calculations (Section 7.4.4). Each curve is a 'snapshot' of the radial electric field and charge density along the wire when the wire top is at a certain height. The calculated radial electric field varies as  $1/r$  from more than 10 m to the wire's surface in the assumed absence of corona, except near the top of the wire. The radial field does not drop to zero above the maximum wire-top height because there is some radial component of electric field above the wire at a radial distance of 5 m (one would expect a purely vertical field only along the wire's longitudinal axis).

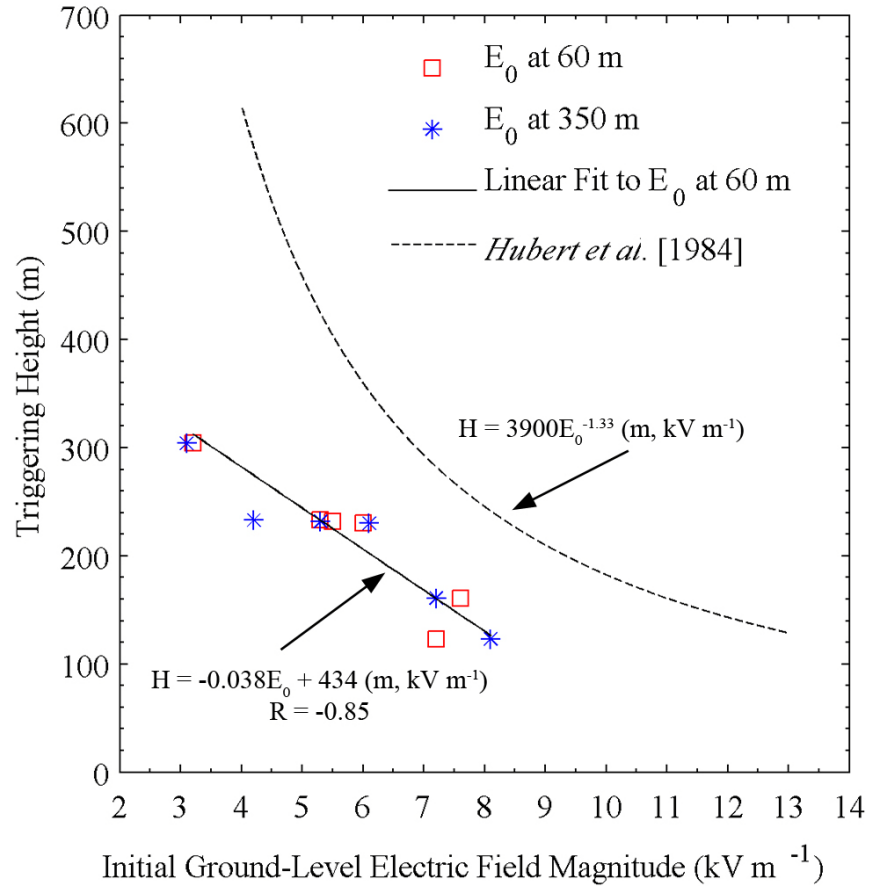


Figure 7-10. Triggering height versus initial ground-level electric field magnitude.

## CHAPTER 8 SUMMARY OF RESULTS AND RECOMMENDATIONS FOR FUTURE RESEARCH

### 8.1 Summary

The work that has been presented was made possible by several key additions to the measurement infrastructure at the ICLRT. The relatively sensitive current sensor (II-VLS) and electric field sensor (E2), both made possible by the use of an amplifier designed and constructed by the author, played an important role in resolving the low-level current and electric field pulses that occurred during the times when the dart-stepped leaders and upward positive connecting leaders were imaged (Chapter 5). The II-VLS and E2 sensors allowed for the precursor signatures in current and electric field to be recorded with high amplitude resolution. The precursor current signatures served as the basis for the modeling of transient current propagation on the triggering wire in Section 6.4. The precursor current and electric field signatures measured using the II-VLS and E2 sensors made possible important corrections to the measured ground level electric field changes in the analysis of Section 7.4. Additionally, new types of current-pulse behavior were detected with the II-VLS sensor, namely the ‘quasi-periodic’ pulses that occur with regular intervals of hundreds of microseconds to several milliseconds, and have amplitudes that vary regularly in time (Section 6.2.2).

The Positive Lightning Experiment (PLE) network of Digital Storage Oscilloscopes (DSO) played a key role in acquiring the data reported in this work. In multiple instances, the PLE DSO network provided data for the wire ascent phase and initial phase in triggered lightning in which no return strokes occurred and the Multiple Station Experiment (MSE) DSO did not trigger. There were also some cases when the return stroke, and thus the MSE trigger time, occurred several seconds after the wire launch. For these cases, the MSE did not record the current and electric field data during the wire ascent.

The most important additions to the ICLRT observational instruments were the high-speed video cameras, which were essential to all of the work presented here. The high-speed video cameras have made possible major advances in the understanding of lightning leader propagation and attachment processes. The Photron SA1.1, operating at a framing speed of 300 kfps ( $3.3 \mu\text{s}$  per frame) has provided the first images showing details of the stepped development of an upward positive leader from a triggering wire (Section 5.2) that is synchronized to wire-base current. The Photron has provided the first images in which the negative leader stepping mechanisms, namely the space stem and space leader, were both spatially and temporally resolved (Section 5.3). These mechanisms have been observed in two downward negative dart-stepped leaders (Section 5.3.1) in different classically triggered lightning flashes, and for a downward stepped leader breaking down virgin air in an altitude triggered flash (Section 5.3.2). The observations of the stepping mechanisms show that negative lightning leaders and negative laboratory spark leaders propagate via the same mechanism, albeit on different scales of length, time, and voltage.

The Photron has provided the first photographic images of the upward positive connecting leaders and the downward leaders in 15 return strokes in triggered lightning, including one for a return stroke in an altitude triggered flash (Section 5.4). The upward and downward leaders were only a few meters to several tens of meters apart when they were imaged and, in one remarkable image recorded by a Photron (Figure 5.4), the tip of a downward dart-stepped leader could be seen about 40 m above ground, and about 15 m from an upward positive connecting leader, the latter being about 16 m in length. In this image, the descending-leader streamer zone appears to be in contact with the upward connecting leader, and a space stem or space leader is evident directly between the two. The image presented in Figure 5.4 shows with great resolution

filamentary corona streamers emanating from several points along the leader, including the leader tip, and the bottom (cathode end) of the space stem/leader below the leader tip. The high-speed video cameras have made possible the direct observations of aborted leader channels, or precursors, as the wire ascends (Section 6.2.1). The Phantom camera was used in 2009 to track the rocket ascension in time, thereby providing a simple and accurate way to determine the wire length versus time (Section 7.3.1).

The accurate measurement of the wire lengths via high-speed video made possible the research presented in Chapters 6 and 7. In Chapter 6, the current, electric field, and optical signatures associated with the sudden electrical breakdown processes (precursors) that occurred at the top of the copper wires used to artificially trigger lightning were examined. The analysis was limited to data collected in 2009, since the II-VLS and E2 sensors were not operational in 2008. Of the tens of thousands of pulses in current and electric field that were recorded, a total of 410 were analyzed in detail. Luminosity at the wire tip was observed for 339 of the 410 precursors and, in seven cases, discharge channels developed to lengths of 3 m to 8 m over times of several hundred microseconds.

Precursors were found to occur at remarkably different rates and with behavior not previously observed. For example, in launch (UF09-11), before the sustained upward positive leader initiated, it is estimated that between 5,000 and 10,000 precursors occurred (one every few hundred microseconds). The peak current amplitude was generally one to about 100 amperes (Figure 6-4), and the amplitudes formed an ‘envelope’ that varied with some periodicity. In the following launch (UF09-12), which took place only 18 minutes later, there was a short period containing rapidly occurring precursors with amplitudes of about an ampere, followed by a 380 ms interval during which no precursors occurred, and then a 680-ms interval during which 41

precursors occurred before the sustained upward positive leader was initiated (Figure 6-5). It is not clear why precursors occur with different rates or why their amplitudes may vary periodically. Different wires may extend in different vertical profiles of electric field, or the humidity in the air through which the wire travels may play a role. Corona processes require a higher electric field strength in air with high humidity than in air with lower humidity [e.g., *Griffiths and Phelps, 1976; Gallimberti, 1977*].

Negative-polarity precursor currents were observed in a single wire launched with predominately positive charge overhead. Unfortunately, no high-speed video was acquired for this launch, so the heights at which they occurred was not known, and no images of associated luminosity were acquired. Interestingly, the currents of the observed negative-polarity precursors did not appear much different in rate and shape from those of the positive-polarity precursors. Considering that individual negative leader steps seem to develop only via the space stem and space leader mechanism, whereas individual positive leader steps seem to extend incrementally [*Rakov and Uman, 2003, Section 5.3.2*], one might expect the current signatures for the two polarities to be different, at least in shape.

The precursor current pulse propagation speeds on the triggering wire were measured for 271 precursors. The speed was about 10 to 20% less than the speed of light, and decreased with increasing wire-top height, from about  $2.8 \times 10^8 \text{ m s}^{-1}$  to about  $2.3 \times 10^8 \text{ m s}^{-1}$  for wire-top heights from about 80 m to about 340 m (Figure 6-8). The less-than-light speeds were attributed to an increased capacitance per unit length of the triggering wire system resulting from the presence of a corona sheath having a radius much larger than the wire radius, while the inductance per unit length is unchanged since the longitudinal current flows solely in the wire.

In Section 6.4, the triggering wire and its grounding system were modeled as uniform transmission lines in an attempt to reproduce the measured wire-base current signatures for three precursors occurring in the same launch at different wire-tip heights. The model predictions matched the measured wire-base precursor current signatures very well, although the former seemed to lack the observed attenuation of high frequency signal components. For each precursor that was modeled, the current pulse was made to propagate in the model (by adjusting the capacitance per unit length) at the speed that was measured in Section 6.3.1. The good agreement between the signatures of the model predictions and the measurements validates the method by which the speeds were measured. For each precursor that was modeled, the incident input current pulse used as model input was a unipolar pulse that was essentially the same as the first pulse of the measured signature, but with an assumed power-law decay following the current peak. Since the first pulse of the precursor signature measured at ground is the superposition of the incident wave and a reflected wave at ground, it is larger in amplitude than the current pulse arriving at ground (and could be potentially different from the input pulse in shape) which itself is the input current attenuated from its initial value by propagating down the wire. It was found that the input current needed to be reduced in amplitude in order that the modeled current peaks matched in amplitude the measured current peaks. The corollary of this observation is that the measured current at ground is not the same as the current pulse created by the electrical breakdown at the wire tip. The modeling showed that: (1) the triggering wire characteristic impedance is between 600 and 800  $\Omega$ , (2) the 25-m ground-rod grounding impedance for the peak precursor current is about 100  $\Omega$ , while the DC grounding resistance is 20  $\Omega$ , (3) the current pulses propagate in the low-loss mode with an attenuation constant that is

approximately frequency and height independent, and is  $8.2 \times 10^{-4}$  Neper  $\text{m}^{-1}$ , and (4) the current reflection coefficient at ground for peak precursor current is approximately 0.9.

In Chapter 7, the ground-level quasi-static electric field at distances of 60 m and 350 m during six wire launches that resulted in triggered lightning were examined in detail. For these six launches, the ground-level electric fields ranged from 3.2 to 7.6  $\text{kV m}^{-1}$ , and the triggering heights ranged from 123 to 304 m. From wire-launch time to lightning-initiation time, the ground-level electric field reduction at 60 m ranged from 2.2 to 3.4  $\text{kV m}^{-1}$ , with little ground-level electric-field reduction being observed at 350 m. The precursors in these six launches were found to produce an appreciable fraction of the total field change measured at ground. For example, in Launch 1, the total field change measured at 60 m was 3  $\text{kV m}^{-1}$ , and the precursors that occurred during the wire launch were expected to have been responsible for about 670  $\text{V m}^{-1}$  (23%) of this field change.

In Section 7.4, the vertical profiles of space charge density and electric field intensity above ground were inferred by comparing modeling and measurements of the ground-level electric field changes caused by elevating grounded lightning-triggering wires. A Poisson equation solver simulated the ground-level electric field changes as the zero-radius grounded wires extend in assumed vertical profiles of space charge density and electric field intensity that varied by an exponential relation, and for the case when there was no space charge (i.e., the solution to Laplace's equation was also determined). As expected, the solution to Laplace's equation yielded field changes much smaller than those measured, ruling out the possibility that no space charge was present above ground. The model reproduced the measured ground-level electric field changes when the assumed space charge density decayed exponentially with altitude, with ground-level charge densities between 1.5 and 7  $\text{nC m}^{-3}$ , space charge exponential

decay height constants ranging from 67 to 200 m, and uniform electric field intensities far above the space-charge layer ranging from 20 to 60 kV m<sup>-1</sup>. However, the model generally predicted too much field change for low wire heights, and too little field change for greater wire heights. It is possible that a steady, low-level current (glow corona) from the wire tip deposited charge continuously as the wire ascended, in a manner similar to the charge deposition by precursors, which caused the measured field to change more than would be expected without such a current. The addition of a milliampere-scale current measurement at the wire base would be helpful in determining if this were the case.

The line charge density along the triggering wire was inferred from the modeled radial electric field for the case when  $E_0 = 6 \text{ kV m}^{-1}$ ,  $E_\infty = 40 \text{ kV m}^{-1}$ , and  $d = 100 \text{ m}$ . For this case, the radial electric field predicted by the model implies the existence of a corona sheath that increases in radius with increasing wire height, having a maximum radius of about 5 m at 285 m above ground. The line charge density on the wire or contained by the corona sheath would increase steadily from less than 1  $\mu\text{C m}^{-1}$  to about 60  $\mu\text{C m}^{-1}$  at wire heights from 1 m to 285 m.

Finally, for the six launches examined in Chapter 7, there was strong linear relationship between the triggering height and the ground-level electric field at launch time, with a correlation coefficient of -0.85. The triggering heights decreased from about 304 m to 123 m for ground-level electric field values increasing from about 3.2 kV m<sup>-1</sup> to 8.1 kV m<sup>-1</sup>, respectively. The triggering heights for a given field value were much lower than what would be expected from the relationship given in *Hubert et al.* [1984] for lightning triggered at the summit of Mount South Baldy in the Magdalena Mountains in central New Mexico at about 3.23 km above sea level.

## 8.2 Recommendations for Future Research

The various observations and modeling discussed in this work point to new paths of research to follow, some of which are discussed next.

**Lightning leaders.** A detailed study of laboratory spark leaders that develop step-wise via the space leader mechanism (gaps greater than 2 m length and with long voltage rise times) using microsecond or sub-microsecond high-speed video and synchronized x-ray measurements might help to clarify the location and time of x-ray production in lightning and long laboratory spark leaders. X-ray film or other simple but sensitive x-ray sensors should be placed inside of the body and nose of the rockets. The detectors from launches in which only precursors occur, and in which precursors and an initial stage occur can be checked for x-ray detection. This may prove to be an inexpensive and simple way to determine if x-rays are produced by precursors and/or the upward positive leader. The rectangular-shaped intercepting wire that was used in 2008 may have produced some kind of geometric field enhancement above the tower, and encouraged the development of upward positive connecting leaders. It would be interesting to erect a grounded ring above or around the launch tube assembly and see if more upward positive connecting leaders are imaged. Steps and stepping mechanisms may develop over longer time scales in the downward negative stepped leader produced in altitude triggered lightning than in natural downward negative stepped leader from a cloud. This makes the downward negative leader in altitude triggered lightning well suited for the study of stepping mechanisms with high-speed video cameras.

**Transient current pulse propagation on triggering wires.** The modeling performed in Section 6.4 can be made more sophisticated by making the electrical parameters functions of height. Such a model would likely reproduce better the measured current signatures, and might render the frequency-dependence of the grounding impedance unnecessary (Figure 6-13). The

modeling performed in Section 6.4 can also be extended to include the upward positive leader channel so as to infer the leader's electrical characteristics. One might expect that a corona sheath will not form around the vertically extended triggering wire in fair weather electric fields. If a corona sheath were not present, then transient current pulses would be expected to propagate on the triggering wire at the speed of light. It would be interesting to inject current pulses into the base of a wire launched in fair weather to test if this is true. An attempt should be made to predict wire lengths from the oscillatory current pulses at the beginning of the upward positive leader; that is, measure the peak to peak time, and multiply by the expected speed at that height.

**Electric field change during extension of triggering wires.** The modeling in Chapter 7 can be constrained further with additional ground-level electric field measurements at different ranges and measurements of the wire-base current on milliampere and possibly microampere levels. Non-zero radius upward extending conductors should be considered in future modeling of the wire-shielding effects. The experiment should be performed in fair weather electric fields, which is on the order of a  $100 \text{ V m}^{-1}$  at ground, and is understood to decrease exponentially with height [e.g., *Gish*, 1944; *Volland*, 1984; *MacGorman and Rust*, 1998; *Rakov and Uman*, 2003]. If the vertical electric field profile,  $E(z)$ , does indeed decrease exponentially, then a comparison of the measured and modeled ground level field change may serve as an independent confirmation of the relations of  $E(z)$  given by *Gish* [1944] and *Volland* [1984], and as validation for the model presented in Chapter 7. Finally, alternative methods of extending vertically grounded wires to heights of tens of meters, such as using crossbows and using rockets propelled by pressurized gas, should be explored so that this experiment can be performed without triggering lightning.

## LIST OF REFERENCES

- Alexandrov, N. L., and E. M. Bazelyan (1996), Simulation of long-streamer propagation in air at atmospheric pressure, *J. Phys. D: Appl. Phys.*, 29, 740-53.
- Alexandrov, N. L., and E. M. Bazelyan (1999), Ionization processes in spark discharge plasmas, *Plasma Sources Sci. Technol.*, 8, 285-94.
- Baba, Y., and V. A. Rakov (2003), On the transmission line model for lightning return stroke representation, *Geophys. Res. Lett.*, 30(24), doi:10.1029/2003GL018407.
- Baba, Y., and V. A. Rakov (2005), On the mechanism of attenuation of current waves propagating along a vertical perfectly conducting wire above ground: Application to lightning, *IEEE Trans. Electromagn. Compt.*, 47(3), 521-532, doi:10.1109/TEM.2005.850690.
- Bacchiega, G., A. Gazzani, M. Bernardi, I. Gallimberti, and A. Bondiou-Clergerie (1994), Theoretical modeling of the laboratory negative stepped-leader, *Int. Conf. on. Lightning and Static Elec.*, Mannheim, Germany.
- Ballarotti, M. G., M. M. F. Saba, O. Pinto Jr. (2005), High-speed camera observations of negative ground flashes on a millisecond-scale, *Geophys. Res. Lett.*, 32, L23802, doi:10.1029/2005GL023889.
- Bazelyan, E. M., and Y. P. Raizer (1998), *Spark Discharge*, CRC Press, Boca Raton, Fla.
- Bazelyan, E. M., and Y. P. Raizer (2000), *Lightning Physics and Lightning Protection*, Inst. of Phys., Bristol, UK.
- Bazelyan, E. M., E. N. Brago, and I. S. Stekol'nikov (1961), The large reduction in mean breakdown gradients in long discharge gaps with an oblique-sloping voltage wave, *Sov. Phys.*, 5.
- Bazelyan, E. M., B. N. Gorin, and V. I. Levitov (1978), *Physical and engineering foundations of lightning protection*, Gidrometeoizdat, St. Petersburg, Russia, 1978.
- Beasley, W. H., M. A. Uman, and P. L. Rustan (1982), Electric fields preceding cloud-to-ground lightning flashes, *J. Geophys. Res.*, 87, 4883-4902.
- Berger, K., and E. Vogelsanger (1966), Photographische Blitzuntersuchungender Jahre 1955-1963 auf dem Monte San Salvatore, *Bull. Schweiz. Elektrotech. Ver.*, 57, 599-620.
- Berger, K., and E. Vogelsanger (1969), New results of lightning observations, In *Planetary Electrodynamics*, eds. S.C. Coroniti, and J. Hughes, pp. 489-510, New York, Gordon and Breach.
- Berger, K., R. B. Anderson, and H. Kroninger (1975), Parameters of lightning flashes, *Electra*, 80, 223-37.

- Biagi, C. J., K. L. Cummins, K. E. Kehoe, and E. P. Krider (2007), National Lightning Detection Network (NLDN) performance in southern Arizona, Texas, and Oklahoma in 2003–2004, *J. Geophys. Res.*, *112*, D05208, doi:10.1029/2006JD007341.
- Biagi, C. J., D. M. Jordan, M. A. Uman, J. D. Hill, W. H. Beasley, and J. Howard (2009), High-speed video observations of rocket-and-wire initiated lightning, *Geophys. Res. Lett.*, *36*, L15801, doi:10.1029/2009GL038525.
- Biagi, C. J., M. A. Uman, J. D. Hill, D. M. Jordan, V. A. Rakov, and J. Dwyer (2010), Observations of stepping mechanisms in a rocket-and-wire triggered lightning flash, *J. Geophys. Res.*, *115*, D23215, doi:10.1029/2010JD014616.
- Bondiou, A., and I. Gallimberti (1994), Theoretical modeling of the development of the positive spark in long gaps, *J. Phys. D: Appl. Phys.*, *27*, pp. 1252-1266.
- Boys, C. V. (1926), Progressive lightning, *Nature*, *118*, 749-50.
- Boys, C. V. (1928), Progressive lightning, *Nature*, *122*, 310-11.
- Boys, C. V. (1929), Progressive lightning, *Nature*, *124*, 54-55.
- Brook, M., N. Kitagawa, and E. J. Workman (1962), Quantitative study of strokes and continuing currents in lightning discharges to ground, *J. Geophys. Res.*, *67*, 649-69.
- Brook, M., G. Armstrong, R. P. H. Winder, B. Vonnegut, and C. B. Moore (1961), Artificial initiation of lightning discharges, *J. Geophys. Res.*, *66*, 3967-9.
- Chauzy, S., and P. Raizonville (1982), Space charge layers created by coroneae at ground level below thunderclouds: Measurements and modeling, *J. Geophys. Res.*, *87*, C4, 3143-8, 2C0065.
- Chauzy, S. and S. Soula (1987), General interpretation of surface electric field variations between lightning flashes, *J. Geophys. Res.*, *92*, D5, 5676-84, 7D0018.
- Chauzy, S., and S. Soula (1989), Ground coroneae and lightning, *J. Geophys. Res.*, *94*, D11, 13,115-9.
- Chazy, S., and S. Soula (1999), Contribution of the ground corona ions to the convective charging mechanism, *Atmos. Res.*, *51*, 279-300.
- Chauzy, S., J.-C. Medale, S. Prieur, and S. Soula (1991), Multilevel measurement of the electric field underneath a thundercloud: 1. A new system and the associated data processing, *J. Geophys. Res.*, *96*, D12, 22319-26.
- Chen, M., N. Takagi, T. Watanabe, D. Wang, Z.-I. Kawasaki, and X. Liu (1999), Spatial and temporal properties of optical radiation produced by stepped leaders, *J. Geophys. Res.*, *104*, doi:10.1029/1999JD900846.

- Chen, M., T. Watanabe, N. Takagi, Y. Du, D. Wang, and X. Liu (2003), Simultaneous observations of optical and electrical signals in altitude-triggered negative lightning flashes, *J. Geophys. Res.*, *108*, D8, doi:10.1029/2002JD002676.
- Clarence, N. D., and D. J. Malan (1957), Preliminary discharge processes in lightning flashes to ground, *Q. J. R. Meteorol. Soc.*, *83*, 161–172.
- Cooray, V. (1993), A model for subsequent return strokes, *J. Electrostat.*, *30*, 343-54.
- Crawford, D.E., V. A. Rakov, M. A. Uman, G. H. Schnetzer, K. J. Rambo, M. V. Stapleton, and R. J. Fisher (2001), The close lightning electromagnetic environment: dart-leader electric field change versus distance. *J. Geophys. Res.*, *106*, 14909–14917.
- Cummer, S. A., and M. Stanley (1999), Submillisecond resolution lightning currents and sprite development: Observations and implications, *Geophys. Res. Lett.*, *26*(20), 3205-8, 1999GL003635.
- Cummer, S. A., N. Jaugey, J. Li, W. A. Lyons, T. E. Nelson, and E. A. Gerken (2006), Submillisecond imaging of sprite development and structure, *Geophys. Res. Lett.*, *33*, L04104, doi:10.1029/2005GL024969.
- Davis, D. A., and P. Laroche (1999), Positive leaders in rocket-triggered lightning: propagation velocity from measured current and electric field derivative at ground. In *Proc. 11<sup>th</sup> Int. Conf. on Atmospheric Electricity*, Guntersville, Alabama, 158-61.
- Davis, S. M. (1999), Properties of lightning discharges from multiple-station wideband electric field measurements, Ph. D. dissertation, University of Florida, Gainesville.
- DeCarlo, B. A., V. A. Rakov, J. E. Jerauld, G. H. Schnetzer, J. Schoene, M. A. Uman, K. J. Rambo, V. Kodali, D. M. Jordan, G. Maxwell, S. Humeniuk, and M. Morgan (2008), Distribution of currents in the lightning protective system of a residential building - Part I: Triggered-lightning experiments, *IEEE Trans. Pow. Deliv.*, *23*(4), doi:10.1109/TPWRD.2008.917894.
- Depasse, P. (1994), Statistics on artificially triggered lightning, *J. Geophys. Res.*, *99*, 18515-22.
- Domens, P., A. Gilbert, J. Dupuy, and B. Hutzler (1991), Propagation of the positive streamer-leader system in a 16.7 m rod-plane gap, *J. Phys. D Appl. Phys.*, *24*, 1748-57.
- Dwyer, J. R. (2004), Implications of X-ray emission from lightning, *Geophys. Res. Lett.*, *31*, L12102, doi:10.1029/2004GL019795.
- Dwyer, J. R., et al. (2004), Measurements of X-ray emission from rocket-triggered lightning, *Geophys. Res. Lett.*, *31*, L05118, doi:10.1029/2003GL018770.
- Dwyer, J. R., H. K. Rassoul, Z. Saleh, M. A. Uman, J. Jerauld, and J. A. Plumer (2005a), X-ray bursts produced by laboratory sparks in air, *Geophys. Res. Lett.*, *32*, L20809, doi:10.1029/2005GL024027.

- Dwyer, J. R., et al. (2005b), X-ray bursts associated with leader steps in cloud-to-ground lightning, *Geophys. Res. Lett.*, 32, L01803, doi:10.1029/2004GL021782.
- Dwyer, J. R., Z. Saleh, H. K. Rassoul, D. Concha, M. Rahman, V. Cooray, J. Jerauld, M. A. Uman, and V. A. Rakov (2008), A study of X-ray emission from laboratory sparks in air at atmospheric pressure, *J. Geophys. Res.*, 113, D23207, doi:10.1029/2008JD010315.
- Evens, W. H., and R. L. Walker (1963), High speed photographs of lightning at close range, *J. Geophys. Res.*, 68, 4455-61.
- Eybert-Berard, A., L. Barret, and J. P. Berlandis (1986), Campagne foudre aux ETATS-UNIS Kennedy Space Center (Florida), Programme RTLP 85\* (in French), STT/ASP 86-01, Centre d'Etudes Neclaire de Grenoble, Grenoble, France.
- Fieux, R., C. Gary, and P. Hubert (1975), Artificially triggered lightning above land, *Nature*, 257, 212-4.
- Fieux, R. P., C. H. Gary, B. P. Hutzler, A. R. Eybert-Berard, P. L. Hubert, A. C. Meesters, P. H. Perroud, J. H. Hamelin, and J. M. Person (1978), Research on artificially triggered lightning in Fance, *IEEE Trans. Pow. Appar. Syst.*, PAS-97, 725-33.
- Fischer, R.J., G. H. Schnetzer, R. Thottappillil, V. A. Rakov, M. A. Uman, and J. D. Goldberg (1993), Parameters of triggered-lightning flashes in Florida and Alabama, *J. Geophys. Res.*, 98, 22887-902.
- Gallimberti, I. (1977), The development of long sparks and the influence of humidity, *Electra*, 53, 103-13.
- Gallimberti, I (1979), The mechanism of the long spark formation, *J. Physique*, 7(40), 7-193.
- Gallimberti, I., G. Bacchiega, A. Bondiou-Clergerie, and P. Lalande (2002), Fundamental processes in long air gap discharges, *C. R. Physique*, 3, doi:10.1016/S1631-0705(02)01414-7.
- Gish, O. H. (1994), Evaluation and interpretation of the columnar resistance of the atmosphere, *Terr. Magn. Atmos. Elec.*, 49, 159-68.
- Golde, R. H. (1947), Occurrence of upward streamers in lightning discharges, *Nature*, 160, 395-6.
- Gomes, C., V. Cooray, and C. Jayaratne (1998), Comparison of preliminary breakdown pulses observed in Sweden and in Sri Lanka, *J. Atmos. Solar Terr. Phys.*, 60, 975-979.
- Goodlet, B. L. (1937), Lightning, *J. Inst. Elec. Eng.*, 81, 1.
- Gorin, B, N, and A. V. Shkilev (1984), Measurements of lightning currents at the Ostankino tower, *Elektrichestvo*, 8, 64-5.

- Gorin, B. N., V. I. Levitov, and A. V. Shkilev (1976), Some principles of leader discharge of air gaps with a strong non-uniform field, *IEE Conf. Publ.*, 143, 274–278.
- Griffiths, D. J., (1981), Introduction to Electrodynamics, Prentice-Hall, Upper Saddle River, New Jersey.
- Griffiths, R. F., and C. T. Phelps (1976), The effects of air pressure and water vapor content on the propagation of positive corona streamers and their implications to lightning initiation, *Q. J. R. Meteorol. Soc.*, 102, 419-26.
- Gu, S., W. Chen, J. Chen, H. He, and G. Qian (2010), Observations of the streamer-leader propagation processes of long air-gap positive discharges, *IEEE. Trans. Plasm. Sci.*, 38(2), doi:10.1109/TPS.2009.2037004.
- Gurevich, A. V., G. M. Milikh, and R. Roussel-Dupre´ (1992), Runaway electron mechanism of air breakdown and preconditioning during a thunderstorm, *Phys. Lett. A*, 165, 463–468.
- Gurevich, A. V., G. M. Milikh, and J. A. Valdivia (1997), Model of X-ray emission and fast preconditioning during a thunderstorm, *Phys. Lett. A*, 231, 402–408.
- Hagenguth, J. H. (1947), Photographic study of lightning, *Trans. Am. Inst. Electr. Eng.*, 66, 577–85.
- Hagenguth, J. H., and J. G. Anderson (1952), Lightning to the Empire State Building Pt. 3, *Trans AIEE*, 71, 641-9.
- Hill, J. D., M. A. Uman, and D. M. Jordan (2011), High-speed video observations of a lightning stepped leader, *in production J. Geophys. Res.*, paper 2011JD015818.
- Hill, J. D., M. A. Uman, M. Stapleton, D. M. Jordan, A. M. Chebaro, and C. J. Biagi (2010), Attempts to create ball lightning with triggered lightning, *J. Atmos. Sol-Terr. Res.*, 72, 13, 913-25, doi:10:1016/j.ASTP.2010.04.009.
- Hoffert, H. H. (1889), Intermittent lightning flashes, *Proc. Phys. Soc.*, 10, 176-180.
- Horii, K. (1982), Experiment of artificial lightning triggered with rocket, *Memoirs of the Faculty of Engineering Nagoya University*, 34, No. 1, 77-112.
- Horii, K., and G. Ikeda (1985), A consideration on success conditions of triggered lightning, *Proc. 18<sup>th</sup> in. Conf. on Lightning Protection*, paper 1-3, Munich, Germany.
- Horii, K., and M. Nakano (1995), Artificially triggered lightning. In *Handbook of Atmospheric Electrodynamics*, Vol. 1. eds. H. Volland, pp. 151-66, Boca Raton, Florida: CRC Press.
- Howard, J. (2009), Lightning propagation and ground attachment processes from multiple-station electric field and x-ray measurements, University of Florida, Gainesville, FL.

- Howard, J., M. A. Uman, C. Biagi, D. Hill, V. A. Rakov, and D. M. Jordan (2011), Measured close lightning leader-step electric field-derivative waveforms, *J. Geophys. Res.*, *116*, D08201, doi:10.1029/2010JD015249.
- Howard, J., M. A. Uman, J. R. Dwyer, D. Hill, C. Biagi, Z. Saleh, J. Jerauld, and H. K. Rassoul (2008), Co-location of lightning leader x-ray and electric field change sources, *Geophys. Res. Lett.*, *35*, L13817, doi:10.1029/2008GL034134.
- Howard, J., M. A. Uman, C. Biagi, D. Hill, J. Jerauld, V. A. Rakov, J. Dwyer, Z. Saleh, and H. Rassoul (2010), RF and X-ray source locations during the lightning attachment process, *J. Geophys. Res.*, *115*, D06204, doi:10.1029/2009JD012055.
- Hubert, P. (1984), Triggered lightning in France and New Mexico, *Endeavour*, *8*, 85-9.
- Hubert, P., and G. Mouget (1981), Return stroke velocity measurements in two triggered lightning flashes, *J. Geophys. Res.*, *86*, 5253-61.
- Hubert, P., P. Laroche, A. Eybert-Berard, and L. Barret (1984), Triggered lightning in New Mexico, *J. Geophys. Res.*, *89*, D2, 2,511-21, 3D1983.
- Idone, V. P. (1990), Length bounds for connecting discharges in triggered lightning, *J. Geophys. Res.*, *95*, 20409-16.
- Idone, V. P. (1992), The luminous development of Florida triggered lightning, *Res. Lett. Atmos. Electr.*, *122*, 23-8.
- Idone, V. P. (1995), Microscale tortuosity and its variation as observed in triggered lightning channels, *J. Geophys. Res.*, *100*(D11), 22943-56, 95JD02458.
- Idone, V. P., and R. E. Orville (1984), Three unusual strokes in a triggered lightning flash, *J. Geophys. Res.*, *89*, 7311-7316, doi:10.1029/JD089ID05P07311.
- Idone, V. P., and R. E. Orville (1988), Channel tortuosity variation in Florida triggered lightning, *Geophys. Res. Lett.*, *15*, 645-8.
- Idone, V. P., R. E. Orville, P. Hubert, L. Barret, and A. Eybert-Berard (1984), Correlated observations of three triggered lightning flashes, *J. Geophys. Res.*, *89*, 1385-94.
- Imece, A. F., D. W. Durbak, H. Elahi, S. Kolluri, A. Lux, D. Mader, T. E. McDermott, A. Morched, A. M. Mousa, R. Natarajan, L. Rugeles, and E. Tarasiewicz, "Modeling guidelines for fast front transients," *IEEE Trans. on Power Delivery*, *11*(1), 493-501, Jan. 1996.
- Jerauld, J. (2007), Properties of natural cloud-to-ground lightning inferred from multiple-station measurements of close electric and magnetic fields and field derivatives, Ph.D. dissertation, University of Florida, Gainesville, FL. (Available at <http://purl.fcla.edu/fcla/etd/UFE0021279>)

- Jerauld, J., V. A. Rakov, M. A. Uman, K. J. Rambo, and D. M. Jordan (2005), An evaluation of the performance characteristics of the U.S. National Lightning Detection Network using triggered lightning in Florida, *J. Geophys. Res.*, *110*, D19106, doi:10.1029/2005JD005924.
- Jerauld, J., M. A. Uman, V. A. Rakov, K. J. Rambo, and G. H. Schnetzer (2007), Insights into the ground attachment process of natural lightning gained from an unusual triggered-lightning, *J. Geophys. Res.*, *112*, D13113, doi:10.1029/2006JD007682.
- Jerauld, J., Uman, M. A., Rakov, V. A., Rambo, K. J., Jordan, D. M., and Schnetzer, G. H. (2008), Electric and magnetic fields and field derivatives from lightning stepped leaders and first return strokes measured at distances from 100 to 1000 m, *J. Geophys. Res.*, *113*, D17111, doi:10.1029/2008JD010171.
- Jordan, D. M., V. A. Rakov, W. H. Beasley, and M. A. Uman (1997), Luminosity characteristics of dart leaders and return strokes in natural lightning, *J. Geophys. Res.*, *102*, 22025-32.
- Jordan, D. M., V. P. Idone, R. E. Orville, V. A. Rakov, and M. A. Uman (1995), Luminosity characteristics of lightning M components, *J. Geophys. Res.*, *100*, 25695-700.
- Jordan, D. M., V. P. Idone, V. A. Rakov, M. A. Uman, W. H. Beasley, and H. Jurenka (1992), Observed dart leader speed in natural and triggered lightning, *J. Geophys. Res.*, *97*, 9951-7
- Kayser, H. (1884), Uber blitzphotographien, *Ber. Konigliche Akad. Berlin*, 611-615.
- Kitagawa, N., and M. Brook (1960), A comparison of intracloud and cloud-to-cloud discharges, *J. Geophys. Res.*, *65*, 1189-201.
- Kitagawa, N., M. Brook, and E. J. Workman (1962), Continuing currents in cloud-to-ground lightning discharges, *J. Geophys. Res.*, *67*, 637-47.
- Kito, Y., K. Horii, Y. Higashiyama, and K. Nakamura (1985), Optical aspects of winter lightning discharges triggered by the rocket-wire technique in Hokuriku district of Japan, *J. Geophys. Res.*, *90*, 6147-57.
- Kodali, V., V. A. Rakov, M. A. Uman, K. J. Rambo, G. H. Schnetzer, J. Schoene, and J. Jerauld (2005), Triggered-lightning properties inferred from measured currents and very close electric fields, *J. Atmos. Res.*, *76*, doi:10.1016/j.atmosres.2004.11.036.
- Koshak, W., and E. P. Krider (1989), Analysis of lightning field changes during active Florida thunderstorms, *J. Geophys. Res.*, *94*(D1), doi:10.1029/JD094ID01P01165.
- Kong, X. Z., X. S. Qie, Y. Zhao, and T. Zhang (2009), Characteristics of negative lightning flashes presenting multiple-ground terminations on a millisecond-scale, *Atmos. Res.*, *91*, doi:10.1016/j.atmosres.2008.03.025.
- Krehbiel, P. R. (1981), An analysis of the electric field change produced by lightning, Ph.D. thesis, University of Manchester Institute of Science and Technology, Manchester, England.

- Krehbiel, P. R., M. Brook, and R. McCrory (1979), An analysis of the charge structure of lightning discharges to the ground, *J. Geophys. Res.*, *84*, 2432-56.
- Krider, E. P., and C. G. Ladd (1975), Upward streamers in lightning discharges to mountainous terrain, *Weather*, *30*, 77-81.
- Krider, E. P., C. D. Weidman, and R. C. Noggle (1977), The electric field produced by lightning stepped leaders, *J. Geophys. Res.*, *82*, 951-60.
- Lalande, P., A. Bondiou-Clergerie, P. Laroche, A. Eybert-Berard, J.-P. Berlandis, B. Bador, A. Bonamy, M. A. Uman, and V. A. Rakov (1998), Leader properties determined with triggered lightning techniques, *J. Geophys. Res.*, *103*(D12), 97JD02492.
- Laroche, P., A. Eybert-Berard, and L. Barret (1985), Triggered lightning flash characterization, paper presented at the 10th International Aerospace and Ground Conference on Lightning and Static Electricity, Paris, France, pp. 231-239.
- Laroche, P., V. Idone, A. Eybert-Berard, and L. Barret (1991), Observations of bi-directional leader development in a triggered lightning flash, *paper presented at the Proc. Int. Conf. on Lightning and Static Electricity*, Cocoa Beach, Florida, pp.57/1-10.
- Laroche, P., A. Eybert-Berard, L. Barret, and J. P. Berlandis (1988), Observations of preliminary discharges initiating flashes triggered by the rocket and wire technique, *paper presented at the 8<sup>th</sup> International Conference on Atmospheric Electricity*, Uppsala Univ., Swed. Nat. Sci. Res. Counc., Uppsala, Sweden, June 13-16.
- Larsen, A. (1905), Photographing lightning with a moving camera, *Ann. Rept. Smithsonian Inst.*, 119-27.
- Loeb, L. B., and J. M. Meek (1941), *The mechanism of the electric spark*, Stanford, CA, USA, Stanford University Press.
- Les Renardieres Group (1972), Research on long air gap discharges at Les Renardieres, *Electra*, *23*, 53-157.
- Les Renardieres Group (1974), Long air gap discharges at Les Renardieres: 1973 results, *Electra*, *35*, 49-156.
- Les Renardieres Group (1977), Positive discharge in long air gaps at Les Renardieres: 1975 results and conclusions, *Electra*, *53*, 31-153.
- Les Renardieres Group (1981), Negative discharges in long air gaps at Les Renardieres, *Electra*, *74*, 67-216.
- Leteinturier, C., C. Weidman, and J. Hamelin (1990), Current and electric field derivatives in triggered lightning return strokes, *J. Geophys. Res.*, *95*, 139-46.

- Leteinturier, C., J. H. Hamelin, and A. Eybert-Berard (1991), Sub-microsecond characteristics of lightning return-stroke currents, *IEEE Trans. Electromagn. Compat.*, 33, 351-7.
- Liu, X. -S., and Y. Zhang (1998), Review of artificially triggered lightning in China, *Trans. IEE Japan*, 118-B(2), 170-5.
- Liu, X. -S., C. Wang, Y. Zhang, Q. Xiao, D. Wang, Z. Zhou, and C. Guo (1994), Experiment of artificially triggering lightning in China, *J. Geophys. Res.*, 99, 10727-31.
- Lu, W., Y. Zhang, X. Zhou, X. Qie, D. Zheng, Q. Meng, M. Ma, S. Chen, F. Wang, and X. Kong (2009), Simultaneous optical and electrical observations on the initial processes of altitude-triggered negative lightning, *Atmos. Res.*, 9, doi:10.1016/j.atmosres.2008.01.011.
- MacGorman, D. R. and W. D. Rust (1998), *The Electrical Nature of Thunderstorms*, New York, Oxford University Press.
- Mach, D. M., and W. D. Rust (1997), Two-dimensional speed and optical risetime estimates for natural and triggered dart leaders, *J. Geophys. Res.*, 102, 13,673–13,684.
- Malan, D. J. (1952), Les decharges dans l'air et la charge inferieure positive d'unnage orageux, *Ann. Geophys.*, 8, 285-401.
- Malan, D. J., and H. Collens (1937), Progressive lightning, Pt. 3: The fine structure of lightning return strokes, *Proc. Roy. Soc. (London)*, A162, 175-203.
- Malan, D. J., and B. F. J. Schonland (1947), Progressive lightning Pt 7: Directly correlated photographic and electrical studies of lightning from near thunderstorms, *Proc. Roy. Soc. (London)*, A191, 513-23.
- Marshall, R. A., and U. S. Inan (2005), High-speed telescopic imaging of sprites, *Geophys. Res. Lett.*, 32, L05804, doi:10.1029/2004GL021988.
- Maslowski, G., and V. A. Rakov (2006), A study of the lightning channel corona sheath, *J. Geophys. Res.*, 111, D14110, doi:10.1029/2005JD006858.
- Mata. C. T., M. I. Fernandez, V. A. Rakov, and M. A. Uman (2000), EMTP modeling of a triggered-lightning strike to the phase conductor of an overhead distribution line, *IEEE Trans. Pow. Del.*, 15(4), 1175-81.
- McEachron, K. B. (1939), Lightning to the Empire State Building, *J. Franklin Inst.*, 227, 149–217.
- McEachron, K. B. (1941), Lightning to the Empire State Building, *Trans. AIEE*, 60, 885-89.
- Morrow, R., and J. J. Lowke (1997), Streamer propagation in air, *J. Phys. D: Appl. Phys.*, 30, 614-27.

- Moss, G. D., V. P. Pasko, N. Liu, and G. Veronis (2006), Monte Carlo model for analysis of thermal runaway electrons in streamer tips in transient luminous events and streamer zones of lightning leaders, *J. Geophys. Res.*, *111*, A02307, doi:10.1029/2005JA011350.
- Moudry, D. R., H. C. Stenbaek-Nielsen, D. D. Sentman, and E. M. Wescott (2002), Velocities of sprite tendrils, *Geophys. Res. Lett.*, *29*(20), doi:10.1029/2002GL015682.
- Murray, N. D., E. P. Krider, and J. C. Willett (2005), Multiple pulses in dE/dt and the fine-structure of E during the onset of the first return strokes in cloud-to-ocean lightning, *Atmos. Res.*, *76*, doi:10.1016/j.atmosres.2004.11.038.
- Nag, A., and V. A. Rakov (2009), Electric field pulse trains occurring prior to the first stroke in negative cloud-to-ground lightning, *IEEE Trans. Electromagn. Compat.*, *51*(1), doi:10.1109/TEM.2008.2005488.
- Nag, A., S. Mallick, V. A. Rakov, J. Howard, C. J. Biagi, D. Hill, M. A. Uman, D. M. Jordan, K. J. Rambo, J. Jerauld, B. A. DeCarlo, K. L. Cummins, and J. A. Cramer (2011), Evaluation of NLDN performance characteristics using rocket-triggered lightning data acquired in 2004-2009, *J. Geophys. Res.*, *116*, D02123, doi:10.1029/JD014929.
- Nagai, Y., S. Kawamata, and Y. Edano (1982), Observation of preceding leader and its downward traveling velocity in Utsunomiya district, *Res. Lett. Atmos. Electr.*, *2*, 53-6.
- Nakamura, K., K. Horii, M. Nakano, and S. Sumi (1992), Experiments on rocket triggered lightning, *Res. Lett. Atmos. Electr.*, *12*, 29-35.
- Nakamura, K., K. Horii, Y. Kito, A. Wada, G. Ikeda, S. Sumi, M. Yoda, S. Aiba, H. Sakurano, and K. Wakamatsu (1991), Artificially triggered lightning experiments to an EHV transmission line, *IEEE Trans. Pow. Del.*, *6*, 1311-8.
- Newman, N. M. (1958), Lightning discharge channel characteristics and related atmospheric, In *Recent Advances in Atmospheric Electricity*, ed. L. G. Smith, 475-84, New York, Pergamon Press.
- Newman, M. M. (1965), Use of triggered lightning to study the discharge channel, In *Problems of Atmospheric and Space Electricity*, 482-90, New York, Elsevier.
- Newman, M. M., and J. D. Robb (1977), Protection of aircraft, In *Lightning, vol. 2: Lightning Protection*, ed. R. H. Golde, 659-96, London, Academic Press.
- Newman, M. M., J. R. Stahmann, J. D. Robb, E. A. Lewis, S. G. Martin, and S. V. Zinn (1967), Triggered lightning strokes at very close range, *J. Geophys. Res.*, *72*, 4761-4.
- Nguyen, C. V., A. P. J. van Deursen, E. J. M. van Heesch, G. J. J. Winands, and A. J. M. Pemen (2010), X-ray emission in streamer-corona plasma, *J. Phys. D: Appl. Phys.*, *43*, doi:10.1088/0022-3727/43/2/025202.

- Nudnova, M. M, and A. Yu. Starikovskii (2008), Streamer head structure: role of ionization and photoionization, *J. Phys. D: Appl. Phys.*, *41*, doi:10.1088/0022-3727/41/23/234003.
- Olsen, R. C., D. M. Jordan, V. A. Rakov, M. A. Uman, and N. Grimes (2004), Observed one-dimensional return stroke propagation speeds in the bottom 170 m of a rocket-triggered lightning channel, *Geophys. Res. Lett.*, *31*, L16107, doi:10.1029/2004GL020187.
- Olsen, R. C., V. A. Rakov, D. M. Jordan, J. Jerauld, M. A. Uman, and K. J. Rambo (2006), Leader/return-stroke-like processes in the initial stage of rocket-triggered lightning, *J. Geophys. Res.*, *111*, D13202, doi:10.1029/2005JD006790.
- Ortega, P., P. Domens, A. Gibert, B. Hutzler, and G. Riquel (1994), Performance of a 16.7 m air rod-plane gap under a negative switching impulse, *J. Phys. D Appl. Phys.*, *27*, doi:10.1088/0022-3727/27/11/019.
- Ortega, P., F. Heilbronner, F. Ruhling, R. Diaz, and M. Rodiere (2005), Charge-voltage relationship of the first impulse corona, *J. Phys. D: Appl. Phys.*, *38*, doi:10.1088/0022-3727/38/13/021.
- Orville, R. E. (1968), Photograph of a close lightning flash, *Science*, *162*, 666–667.
- Orville, R. E., and V. P. Idone (1982), Lightning leader characteristics in the Thunderstorm Research International Program (TRIP), *J. Geophys. Res.*, *87*, doi:10.1029/JC087IC13P11177.
- Peek, F. W. (1929), Dielectric phenomena in high voltage engineering, New York, NY, USA, McGraw-Hill, pp. 52-80.
- Proctor, D. E., R. Uytendogaardt, and B. M. Meredith (1988), VHF radio pictures of lightning flashes to ground, *J. Geophys. Res.*, *93*, 10.1029/JD093ID10P12683.
- Qie, X., and X. Kong (2007), Progression features of a stepped leader process with four grounded leader branches, *Geophys. Res. Lett.*, *34*, L06809, doi:10/1029/2006GL028771.
- Qie, X., S. Soula, and S. Chauzy (1994), Influence of ion attachment on the vertical distribution of the electric field and charge density below a thunderstorm, *Ann. Geophys.*, *12*, 1,218-28.
- Raether, H (1964), Electron avalanches and breakdown in gases, London, UK, Butterworths.
- Rahman, M., V. Cooray, N. A. Ahmad, J. Nyberg, V. A. Rakov, and S. Sharma (2008), X rays from 80-cm long sparks in air, *Geophys. Res. Lett.*, *35*, L06805, doi:10.1029/2007GL032678.
- Rakov, V. A. (1998), Some inferences on the propagation mechanisms of dart leaders and return strokes, *J. Geophys. Res.*, *103*, 1879–87.
- Rakov, V. A. (2001), Transient response of a tall object to lightning, *IEEE Trans. Electromagn. Compat.*, *43*(4), 654-61.

- Rakov, V. A. (2007), Lightning Return Stroke Speed, *J. Lightning. Res.*, *1*, 80-9.
- Rakov, V. A., and M. A. Uman (1990), Some properties of negative cloud-to-ground lightning flashes versus stroke order, *J. Geophys. Res.*, *95*, 5447-53.
- Rakov, V. A., and M. A. Uman (1998), Review and evaluation of lightning return stroke models including some aspects of their application, *IEEE Trans. Electromagn. Compat.*, *40*, 403-26.
- Rakov, V. A., and M. A. Uman (2003), *Lightning: Physics and Effects*, Cambridge Univ. Press, New York.
- Rakov, V. A., M. A. Uman, and R. Thottappillil (1994), Review of lightning properties determined from electric field and TV observations, *J. Geophys. Res.*, *99*, 10745-50.
- Rakov, V. A., M. A. Uman, G. R. Hoffman, M.W. Masters, and M. Brook (1996), Bursts of pulses in lightning electromagnetic radiation: observations and implications for lightning test standards, *IEEE Trans. on EMC*, *38*(2), 156–164.
- Rakov, V.A., D. E. Crawford, K. J. Rambo, G. H. Schnetzer, M. A. Uman, and R. Thottappillil (2001), M-component mode of charge transfer to ground in lightning discharges, *J. Geophys. Res.*, *106*, 22817-31.
- Rakov, V. A., M. A. Uman, M. I. Fernandez, C. T. Mata, K. T. Rambo, M. V. Stapleton, and R. R. Sutil (2002), Direct lightning strikes to the lightning protective system of a residential building: triggered-lightning experiments, *IEEE Trans. Pow. Del.*, *17*(2), 575-86.
- Rakov, V. A., D. E. Crawford, V. Kodali, V. P. Idone, M. A. Uman, G. H. Schnetzer, and K. J. Rambo (2003), Cutoff and reestablishment of current in rocket-triggered lightning, *J. Geophys. Res.*, *108*, D23, doi:10.1029/2003JD003694.
- Rakov, V. A., V. Kodali, D. E. Crawford, J. Schoene, M. A. Uman, K. J. Rambo, and G. H. Schnetzer (2005), Close electric field signatures of dart leader/return stroke sequences in rocket-triggered lightning showing residual fields, *J. Geophys. Res.*, *110*, D07205, doi:10.1029/2004JD005417.
- Rakov, V. A. et al. (1998), New insights into lightning processes gained from triggered-lightning experiments in Florida and Alabama, *J. Geophys. Res.*, *103*, D12, 14117-30, 97JD02149.
- Reess, T., P. Ortega, A. Gibert, P. Domens, and P. Pigolet (1995), An experimental study of negative discharge in a 1.3 m point-plane air gap: The function of the space stem in the propagation mechanisms, *J. Phys. D Appl. Phys.*, *28*, doi:10.1088/00223727/28/11/011.
- Rhodes, C., and P. R. Krehbiel (1989), Interferometric observations of a single stroke cloud-to-ground flash, *Geophys. Res. Lett.*, *16*, 1169-72, doi:10.1029/GL016i010p01169.

- Roychowdhury, J. S., and D. O. Pederson, (1991), Efficient transient simulation of lossy interconnect, *Proc. 28<sup>th</sup> ACM/IEEE Design Automation Conference*, San Francisco, CA, USA, 740-5.
- Roychowdhury, J. S., A. R. Newton, D. O. Pederson (1994), Algorithms for the transient simulation of lossy transmission lines, *IEEE Trans. Computer-Aided Design of Int. Circuits and Sys*, 13(1), 96-104.
- Saba, M. M. F., O. Pinto Jr., N. N. Solorzano, and A. Eybert-Berard (2005), Lightning current observation of an altitude-triggered flash, *Atmos. Res.*, 76, 402-11, doi:10.1016/j.atmosres.2004.11.005.
- Saba, M. M. F., O. Pinto, I. R. C. A. Pinto, F. J. Pissolato, A. Eyert-Berard, A. Lefort, C. Potvin, L. F. Heine, and S. Chauzy (2000), An international center for triggered and natural lightning research in Brazil, *Proc. 2000 Int. Lightning Detection Conf.*, paper 40, Tucson, Arizona, U.S.A.
- Saba, M. M. F., K. L. Cummins, T. A. Warner, E. P. Krider, L. Z. S. Campos, M. G. Ballarotti, O. Pinto Jr., and S. A. Fleenor (2008), Positive leader characteristics from high-speed video observations, *Geophys. Res. Lett.*, 35, L7802, doi:10.1029/2007GL033000.
- Sadiku, M. N. O. (1994), *Elements of Electromagnetics*, Sounders College, Orlando, FL.
- Saleh, Z., J. Dwyer, J. Howard, M. Uman, M. Bakhtiari, D. Concha, M. Stapleton, D. Hill, C. Biagi, and H. Rassoul (2009), Properties of the X-ray emission from rocket-triggered lightning as measured by the Thunderstorm Energetic Radiation Array (TERA), *J. Geophys. Res.*, 114, D17210, doi:10.1029/2008JD011618.
- Saraiva, A. C. V., M. M. F. Saba, O. Pinto Jr., K. L. Cummins, E. P. Krider, and L. Z. S. Campos (2010), A comparative study of negative cloud-to-ground lightning characteristics in São Paulo (Brazil) and Arizona (United States) based on high-speed video observations, *J. Geophys. Res.*, 115, D11102, doi:10.1029/2009JD012604.
- Schoene, J., M. A. Uman, and V. A. Rakov (2010), Return Stroke Peak Current versus Charge Transfer in Rocket-Triggered Lightning, *J. Geophys. Res.*, 115, D12107, doi:10.1029/2009JD013066.
- Schoene, J., M. A. Uman, V. A. Rakov, K. J. Rambo, J. Jerauld, and G. H. Schnetzer (2003), Test of the transmission line model and traveling current source model with triggered lightning return strokes at very close range, *J. Geophys. Res.*, 108, D23, 4737, doi:10.1029/2003JD003683.
- Schoene, J., M. A. Uman, V. A. Rakov, K. J. Rambo, J. Jerauld, C. T. Mata, A. G. Mata, D. M. Jordan, and G. H. Schnetzer (2009), Characterization of return-stroke currents in rocket-triggered lightning, *J. Geophys. Res.*, 114, D03106, doi:10.1029/2008JD009873.
- Schonland, B. F. J. (1928), The interchange of electricity between thunderclouds and the earth, *Proc. Roy. Soc. London, Ser. A*, 118, 252-262.

- Schonland, B. F. J. (1956), The lightning discharge, in *Handbook of Physics*, vol. 22, pp. 576–628, Springer, Berlin.
- Schonland, B. F. J., and H. Collens (1934), Progressive lightning, *Proc. Roy. Soc. (London)*, *A143*, 654-674.
- Schonland, B. F. J., D. J. Malan, and H. Collens (1935), Progressive lightning, part 2: The discharge mechanisms, *Proc. R. Soc., Ser. A*, *152*, 595–625.
- Shao, X. M., P. R. Krehbiel, R. J. Thomas, and W. Rison (1995), Radio interferometric observations of cloud-to-ground lightning phenomena in Florida, *J. Geophys. Res.*, *100*, 2749-83, doi:10.1029/94JD01943.
- Soula, S. and S. Chauzy (1991), Multilevel measurement of the electric field underneath a thundercloud: 2. Dynamical evolution of a ground space charge layer, *J. Geophys. Res.*, *96*, D12, 22,327-36, 91JD02032.
- Standler, R. B., and W. P. Winn (1979), Effects of coronae on electric fields beneath thunderstorms, *Quart. J. R. Met. Soc.*, *105*, 285-302.
- Stanley, M., P. Krehbiel, M. Brook, C. Moore, and W. Rison (1999), High speed video of initial sprite development, *Geophys. Res. Lett.*, *26*(20), 3201-4, 1999GL010673.
- Stenbaek-Nielsen, H. C., and M. G. McHarg (2008), High time-resolution sprite imaging: Observations and implications, *J. Phys. D. Appl. Phys.*, *41*, doi:10.1088/00223727/41/23/234009.
- Stolzenburg, M., T. C. Marshall, W. D. Rust, and D. L. Bartels (2002), Two simultaneous charge structures in thunderstorm convection, *J. Geophys. Res.*, *107*, D18, doi:10.1029/2001JD000904.
- Theethayi, N., and V. Cooray (2005), On the representation of the lightning return stroke as a current pulse propagating along a transmission line, *IEEE Trans. Power Delivery*, *20*(2), doi:10.1109/TPWRD.2004.839188.
- Thomas, R. J., P. R. Krehbiel, W. Rison, H. E. Edens, G. D. Aulich, W. P. Winn, S. R. McNutt, G. Tytgat, and E. Clark (2007), Electrical activity during the 2006 Mount St. Augustine volcanic eruptions, *Science*, *315*, No. 5815, pg. 1097, doi:10.1126/science.1136091.
- Thomson, E. M., M. A. Uman, and W. H. Beasley (1985), Speed and current for lightning stepped leaders near ground as determined from electric field records, *J. Geophys. Res.*, *90*, 8136-42.
- Toland, R. B., and B. Vonnegut (1977), Measurement of maximum electric field intensities over water during thunderstorms, *J. Geophys. Res.*, *82*, 438-40.
- Trichel, G. W. (1938), The mechanism of the negative point to plane corona near onset, *Phys. Rev.*, *54*.

- Uman, M. A. (1969), *Lightning*, Dover Publications Inc., McGraw-Hill Book Company, New York.
- Uman, M. A. (1987), *The Lightning Discharge*, Academic Press, Orlando.
- Uman, M. A., D. F. Seacord, G. H. Price, and E.T. Pierce (1972), Lightning induced by thermonuclear detonations, *J. Geophys. Res.*, 77, 1591-6.
- Uman, M. A., D. K. McLain, R. J. Fisher, and E. P. Krider (1973), Currents in Florida lightning return strokes, *J. Geophys. Res.*, 78, 3530-7.
- Uman, M. A., et al. (1996), 1995 Triggered lightning experiment in Florida, *Proc 10<sup>th</sup> Int. Conf. on Atmos. Elec.*, Osaka, Japan, pp. 644-7.
- Uman, M. A., V. A. Rakov, K. J. Rambo, T. W. Vaught, M. I. Fernandez, D. J. Cordier, R. M. Chandler, R. Bernstein, and C. Golden (1997), Triggered-lightning experiments at Camp Blanding, Florida (1993-1995), *Trans. IEE Japan*, 117-B, 446-52.
- Uman, M. A., J. Schoene, V. A. Rakov, K. J. Rambo, and G. H. Schnetzer (2002), Correlated time derivatives of current, electric field intensity, and magnetic flux density for triggered lightning at 15 m., *J. Geophys. Res.*, 107, D13, doi:10.1029/2000JD000249.
- Visacro, S. and A. De Conti (2005), A distributed-circuit return-stroke model allowing time and height parameter variation to match lightning electromagnetic field waveform signatures, *Geophys. Res. Lett.*, 32, L23805, doi:10.1029/2005GL024336.
- Volland, H. (1984), Atmospheric electrodynamics. In *Physics and Chemistry in Space*, vol. II, eds. L. J. Lanzerotti and J. T. Wasson, New York: Springer-Verlag.
- Wagner, C. F. (1967), Lightning and transmission lines, *J. Franklin Inst.*, 283, 558–594.
- Wagner, C. F., and A. R. Hileman (1958), The lightning stroke (1), *AIEE Trans.*, 80(3), 622-42.
- Walker, T. D., C. J. Biagi, J. D. Hill, D. M. Jordan, M. A. Uman, H. J. Christian (2009), Optical spectra of triggered lightning, *Eos Trans. AGU*, Vol. 91, Abstract No. AE21A-0297, San Fransisco, December 15, 2009.
- Walker, T. D., J. D. Hill, D. M. Jordan M. A. Uman and H. Christian (2010), Physical characteristics of triggered lightning determined by optical spectroscopy, *Eos Trans. AGU*, Vol. 91, Abstract No. AE23A-05, San Fransisco, December 14, 2010.
- Walter, B. (1902), Ein photgraphischer apparat zur genaueren analyse des blitzes, *Physik. Z.*, 3, 168-72.
- Walter, B. (1903), Uber die entstehungsweise des blitzes, *Ann. Physik.*, 10, 393-407.
- Walter, B. (1910), Uber doppelaufnahmen von Blitzen, *Jahrbuch Hamb. Wiss. Anst.*, 27(5), 81-118.

- Walter, B. (1912), Stereoscopische blitzaufnahmen, *Physik. Z.*, *13*, 1082-84.
- Walter, B. (1918), Über die ermittlung der zeitlichen aufeinanderfolge zusammengehöriger blitze sowie über ein bemerkenswertes beispiel dieser art von entladungen, *Physik. Z.*, *19*, 273-9.
- Wang, M. C., and E. E. Kunhardt (1990), Streamer dynamics, *Phys. Rev. A.*, *42*(4), 42-50.
- Wang, D., and N. Takagi (2011), A downward positive leader that radiated optical pulses like a negative stepped leader, *J. Geophys. Res.*, *116*, D10205, doi:10.1029/2010JD015391.
- Wang, D., N. Takagi, T. Watanabe, V. A. Rakov, and M. A. Uman (1999a), Observed leader and return-stroke propagation characteristics in the bottom 400 m of the rocket triggered lightning channel, *J. Geophys. Res.*, *104*, doi:10.1029/1999JD900201.
- Wang, D., V. A. Rakov, M. A. Uman, N. Takagi, T. Watanabe, D. E. Crawford, K. J. Rambo, G. H. Schnetzer, R. J. Fisher, and Z. I. Kawasaki (1999b), Attachment process in rocket-triggered lightning strokes, *J. Geophys. Res.*, *104*, 2143-50.
- Wang, D., V. A. Rakov, M. A. Uman, M. I. Fernandex, K. J. Rambo, G. H. Schnetzer, and R. J. Fisher (1999c), Characteristics of the initial stage of negative rocket-triggered lightning, *J. Geophys. Res.*, *104*, D4, 4213-4222.
- Wang, D., N. Takagi, T. Watanabe, V. A. Rakov, M. A. Uman, K. J. Rambo, and M. V. Stapleton (2005), A comparison of channel-base currents and optical signals for rocket-triggered lightning strokes, *J. Atmos. Res.*, *76*, doi:10.1016/j.atmosres.2004.11.025.
- Wang, D., and N. Takagi (2011), A downward positive leader that radiated optical pulses like a negative stepped leader, *J. Geophys. Res.*, *116*, D10205, doi:10.1029/2010JD015391.
- Warner, T. A., R. E. Orville, J. L. Marshall, and K. Huggins (2011), Spectral (600-1050 nm) time exposures (99.6  $\mu$ s) of a lightning stepped leader, *J. Geophys. Res.*, *116*, doi:10.1029/2011JD015663.
- Weber, L. (1889), Über Blitzphotographien, *Ber. Konigliche Akad. Berlin*, 781-784.
- Weidman, C. D., and E. P. Krider (1978), The fine structure of lightning return stroke wave forms, *J. Geophys. Res.*, *83*, C12, 6239-6247.
- Weidman, C. D., and E. P. Krider (1979), The radiation field waveforms produced by intracloud lightning discharge processes, *J. Geophys. Res.*, *84*, 3159-3164.
- Willet, J. C (1992), Rocket-triggered-lightning experiments in Florida, *Res. Lett. Atmos. Electr.*, *12*, 37-45.
- Willet, J. C., D. A. Davis, and P. Laroche (1999), An experimental study of positive leaders initiating rocket-triggered lightning, *Atmos. Res.*, *51*, 189-219.

- Willett, J. C., J. C. Bailey, V. P. Idone, A. Eybert-Berard, and L. Barret, (1989), Submicrosecond intercomparison of radiation fields and currents in triggered lightning return strokes based on the transmission-line model, *J. Geophys. Res.*, *94*, 13,275-86.
- Willett, J. C., V. P. Idone, R. E. Orville, C. Leteinturier, A. Eybert-Berard, L. Barret, and E. P. Krider (1988), An experimental test of the "transmission-line model" of electromagnetic radiation from triggered lightning return strokes, *J. Geophys. Res.*, *93*, D4, 3867–3878.
- Williams, E. R., M. E. Weber, and R. E. Orville (1989), The relationship between lightning type and convective state of thunderclouds, *J. Geophys. Res.*, *94*, 13213-20.
- Winands, G. J. J., Z. Liu, A. J. M. Pemen, E. J. M. van Heesch, and K. Yan (2008), Analysis of streamer properties in air as function of pulse and reactor parameters by ICCD photography, *J. Phys. D: Appl. Phys.*, *41*, doi:10.1088/0022-3727/41/23/234001.
- Workman, E. J., M. Brook, and N. Kitagawa (1960), Lightning and charge storage, *J. Geophys. Res.*, *65*, 1513-7.
- Yokoyama, S., K. Miyake, T. Suzuki, and S. Kanao (1990), Winter lightning on Japan Sea Coast – development of measuring system on progressing feature of lightning discharge, *IEEE Trans. Pow. Del.*, *5*, 1418–25.
- Yoshida, S., C. J. Biagi, V. A. Rakov, J. D. Hill, M. V. Stapleton, D. M. Jordan, M. A. Uman, T. Morimoto, T. Ushio, and Z. –I. Kawasaki (2010), Three-dimensional imaging of upward positive leaders in triggered lightning using VHF broadband digital interferometers, *Geophys. Res. Lett.*, *37*, L05805, doi:10.1029/2009GL042065.
- Yoshida, S., C. J. Biagi, V. A. Rakov, J. D. Hill, M. V. Stapleton, M. A. Uman, T. Morimoto, T. Ushio, Z. –I. Kawasaki, and M. Akita (2011), VHF radiation sources associated with precursors and ICC pulses of rocket-and-wire triggered lightning, *Int. Conf. Atmos. Elec.*, Rio de Janeiro.
- Zhang, Q., X. Qie, Z. Wang, T. Zhang, and J. Yang (2009), Simultaneous observation on electric field changes at 60 m and 550 m from altitude-triggered lightning flashes, *Radio Science*, *44*, RS1011, doi:10.1029/2008RS003866.
- Zhang, Y., W. Lu, J. Li, W. Dong, D. Zheng, and S. Chen (2009), Luminosity characteristics of leaders in natural cloud-to-ground lightning flashes, *Atmos. Res.*, *91*, doi:10.1016/j.atmosres.2008.01.013.
- Zundl, T. (1994), First results of the coordinated lightning current and LEMP measurements at the Peissenberg tower, Paper R1c-09, *Proc. 22<sup>nd</sup> Int. Conf. on Lightning Protection, Budapest, Hungary*.

## BIOGRAPHICAL SKETCH

Christopher John Biagi was born in Tucson, Arizona in 1980. He received a Bachelor of Science degree in physics in 2003 from the University of Arizona. Shortly afterwards, he took a research assistant position at the Institute for Atmospheric Physics at the University of Arizona. Chris subsequently earned a Master of Science in atmospheric science in 2006 from the University of Arizona. Thereafter, he moved to Florida to join the Lightning Research Group at the University of Florida, where he worked toward a Ph.D. at the International Center for Lightning Research and Testing from 2006 to 2009. He earned a second Master of Science degree in 2008 and a Ph.D. in 2011, both in electrical and computer engineering from the University of Florida. Chris has authored five peer-reviewed journal publications, and been a co-author on nine others. He has been author or co-author on 21 papers in conference proceedings, and on three technical reports.